

UNIVERSITY OF BIRMINGHAM

NANOPARTICLES WITH NON-EQUILIBRIUM STRUCTURES SYNTHESIZED BY PHYSICAL WAYS

By

YU XIA (夏雨)

A thesis submitted to the University of Birmingham for the degree of

DOCTOR OF PHILOSOPHY

Nanoscale Physics Research Laboratory

School of Physics and Astronomy

University of Birmingham

Birmingham, UK

November 2022

UNIVERSITY OF
BIRMINGHAM

University of Birmingham Research Archive

e-theses repository

This unpublished thesis/dissertation is copyright of the author and/or third parties. The intellectual property rights of the author or third parties in respect of this work are as defined by The Copyright Designs and Patents Act 1988 or as modified by any successor legislation.

Any use made of information contained in this thesis/dissertation must be in accordance with that legislation and must be properly acknowledged. Further distribution or reproduction in any format is prohibited without the permission of the copyright holder.

Abstract

Synthesizing nanoparticles with nonequilibrium structures and shapes is full of significance not only due to the excellent catalytic performance, but also because of the role on the understanding of crystal growth. This work focuses on the nanoparticle preparation through physical routes and the structural characterisation using scanning transmission electron microscopy (STEM). Magnetron-sputtering gas condensation method was employed to prepare population-tunable platinum (Pt) tetrahedral and octahedral nanoparticles with mass-selection. The growth pathway of tetrahedral Pt nanoparticles was simulated based on the experimental conditions and the STEM images. The same strategy was employed to prepare nickel-platinum (Ni-Pt) nanoparticles from alloys to core-shells by tuning preparation conditions. In the presence of Ni atoms during the growth stage, Ni-Pt nanoparticles formed with icosahedral and decahedral structures, which show robust structural stability observed by in-situ heating. Joule heating is a novel nanoparticle synthesis, which was utilized to fabricate metal nanoparticles and metallic phosphides within second in this thesis. Thanks to the ultrafast heating and cooling rates of the Joule heating synthesis, both stacking faults and metastable structures were remained in the as-prepared nanoparticles. Pt doped ruthenium nanoparticles with a face-centered cubic structure prepared using flash Joule heating was demonstrated for the application of electrocatalytic hydrogen evolution reaction with ultralow overpotentials and small Tafel slopes. The synthesis techniques shown in this thesis have implications for catalysts preparation.

Acknowledgments

Time sure flies that witness my efforts and growth on the academic road. There are many persons giving their helping hands for supporting my study.

I would like to thank Dr. Ziyou Li for her patient guidance and heuristic discussions not only on my studies but also on the career planning. Her encouragements motivate me to overcome barriers on my study road.

My supervisor Dr. Wolfgang Theis for his great patience with his discussions and guidance throughout my PhD.

A special gratitude must be shown to Prof. Jun Yuan from the University of York for his efforts to teach me the transmission electron microscopy and his understanding of the nanoparticle growth.

I would like to thank Dr. Alexander J. Pattison for his patience with the microscope. Dr. Patrick James Harrison for his patient training on the cluster source and the microscope.

Diana Nelli and Prof. Riccardo Ferrando from the Università degli Studi di Genova for their simulation on the growth of tetrahedral and octahedral platinum nanoparticles.

As a student of the Joint PhD Training Program offered by the University of Birmingham (UoB) and Southern University of Science and Technology (SUSTech), I would like to express my heartfelt gratitude to my supervisor Prof. Hsinglin Wang at SUSTech, for his supervision and supports as well as to UoB and SUSTech for their support for my studies in both universities.

I would like to thank my colleagues at SUSTech, particularly Dr. Shaoqing Chen, Zian Xu and Chuanlai Jiao who share me with their knowledges and skills on the electrochemical tests. Dr. Jian Zhu for his helps and cooperations on the synthesis of catalysts.

And, of course, I would like to thank my families for their unwavering supports and encouragements.

Authors' Publications

1. **Y. Xia**, P. Harrison, I.M. Ornelas, H.L. Wang, Z.Y. Li. HAADF-STEM image analysis for size-selected platinum nanoclusters. *Journal of Microscopy*, 279, **2020**, 229-233.
2. **Yu Xia**, Diana Nelli, Riccardo Ferrando, Jun Yuan & Z. Y. Li. Shape control of size-selected naked platinum nanocrystals. *Nature Communications*, 12, **2021**, 3019.
3. Benben Wei, **Yu Xia**, Shaoqing Chen, Hsing-Lin Wang. Modified separator with nitrogen-doped high-graphitized carbon for lithium-sulfur batteries. *Electroanalysis*, 34, **2022**, 1472-1477.

In preparation:

1. Decahedral and icosahedral Ni-Pt nanoparticles with core-shell or alloy structures prepared by magnetron-sputtering gas-condensation. Yu Xia, Wolfgang Theis and Hsinglin Wang.
2. Single-Pt-atom Ru hosts alloy promoting hydrogen evolution reaction. Yu Xia, Wolfgang Theis and Hsinglin Wang.
3. Ruthenium phosphides with stacking faults prepared by the flash Joule heating for hydrogen evolution reaction. Yu Xia, Wolfgang Theis and Hsinglin Wang.

List of Figures

Figure 1.2.1 Strategies to enhance the catalytic activity of nanoparticles. 2

Figure 1.2.1 Geometric and electronic structures of single atom, clusters and nanoparticles... 4

Figure 1.2.2 Illustrations of nonequilibrium shapes 4

Figure 1.2.3 Schematic illustrations of metal nanoparticles. 8

Figure 1.3.1 Schematic illustrations of how the capping agents direct the growth of a single-crystal seed made of an FCC metal. 11

Figure 1.3.2 The curves of the concentration of atoms and the reaction time in the general synthetic ways for size and shape control of metal nanoparticles. 11

Figure 1.3.3 Carbothermal shock synthesis of nanoparticles on carbon supports. 12

Figure 1.3.4 HAADF-STEM image of L10 intermetallic nanoparticles. 13

Figure 1.3.5 Schematics of reaction chambers used for common reactive vapor deposition methods. 14

Figure 1.4.1 A schematic illustration of the synthesis and structure of nanoparticles. 16

Figure 1.4.2 Schematic diagram of the pulsed laser ablation setup, which the nanoparticles are cooled by gases. 17

Figure 1.4.3 Schematic illustration of spark discharge generator. 18

Figure 1.4.4 Schematic structures of the cluster source used to deposit mass-filtered nanoparticles. 19

Figure 1.4.5 schematics of magnetron sputtering head and the process of nucleation and growth of clusters. 22

Figure 1.4.6 Scheme of the mass selector. 23

Figure 1.5.1 A schematic of a typical TEM and the applications of in-situ microscopy for imaging and spectroscopy…… ..... ……...27

Figure 1.5.2 Signals generated by the interaction of high-energy electrons with the sample. 28

Figure 1.5.3 Typical imaging modes of TEM and STEM with an annular bright field detector and a high-angle annular dark-field (HAADF) detector…… ..……29

Figure 1.5.4 Schematics of spherical aberration in the lens and Ray diagrams of a commercial

Cs-corrector system (CEOS). 31
Figure 1.5.5 Schematic of EDX and EELS signal generation……..... 33
Figure 1.5.6 Schematic of high-loss edge extraction from EELS… 37
Figure 1.5.7 Schematic convolution of the observed edge……..... 39
Figure 1.5.8 Flow chart of EELS analysis. 41
Figure 1.6.1 Schematic illustration of the HER energetics, polarization curves, and Tafel plots. 44
Figure 1.6.2 Schematic mechanism of hydrogen evolution on the surface of an electrode. ... 45
Figure 2.1.1 Example of extracting the intensity of background..... 50
Figure 2.1.2 Batch extracting the background intensity of nanoparticles. 50
Figure 2.1.3 The interface of home-made program. 51
Figure 2.1.4 Factors impacting the integrated intensity..... 52
Figure 2.1.5 Pt_{561} particles size-analysis by the home-programed script. 53
Figure 2.1.6. Mean integrated intensity as a function of cluster size in the range from Pt_{147} to Pt_{20000}. 55
Figure 2.2.1 Pt nanoparticles prepared with the sputtering power of 10 W, 30 W, and 75 W. 57
Figure 2.2.2 Mass spectra of Pt nanoparticles prepared by 10 W, 40 W, and 75 W. 59
Figure 2.2.3 Pt nanoparticles grown at room temperature with the condensation length at 10 cm and 25 cm..... 60
Figure 2.2.4 Mass spectra of Pt nanoparticles with different condensation lengths..... 61
Figure 2.2.5 Mass spectra of Pt nanoparticles prepared with different argon gas flow rates. . 62
Figure 2.2.6 Impacts of gas flow rate (pressure of the chamber) on the formation of Pt particles. 63
Figure 2.2.7 Pt Decahedra with different sizes. 65
Figure 2.2.8 Influences of the chamber wall's temperature on the morphology of nanoparticles. 66
Figure 2.2.9 No size-filtered Pt nanoparticles prepared under different temperature of the chamber's walls. 67

Figure 2.2.10 Projected area distribution of Pt nanoparticles prepared at room temperature (RT) or -140 ℃. 68
Figure 2.2.11 Size-filtered Pt nanoparticles prepared under different temperature of the chamber's walls. 71
Figure 2.2.12 Pt nanoparticles fabricated using the Sputtering power of (a) 10 W, (b) 75 W, and (c) 135 W on the 2-inch Pt target. 72
Figure 2.2.13 Pd nanoparticles grown in the chamber, which was cooled down by the liquid nitrogen. 73
Figure 2.2.14 Size-selected Pd_{12000} nanoparticles prepared without cooling the chamber temperature. 75
Figure 2.2.15 Size distribution of Pd particles measured by the integrated intensity. 76
Figure 2.2.16 Dendritic Pt particles fabricated in the chilled chamber... 76
Figure 2.2.17 No size-selected Pt nanoparticles prepared without LN2 cooling and with LN2 cooling. 77
Figure 2.3.1 Illustrations of tetrahedral and octahedral particles covered by {111} facets. 79
Figure 2.3.2 Excess energy of different structural motifs and schematic representation of the growth sequence. 79
Figure. 2.3.3 The typical shaped Pt_{5000} nanoparticles imaged using HAADF-STEM..... 82
Figure 2.3.4 Libraries of HAADF-STEM images of an atomic model of tetrahedral nanoparticles and octahedral nanoparticle. 83
Figure. 2.3.5 Controlling size and shape of Pt nanoparticles. 85
Figure 2.3.6 The procedure of imaging Pt nanoparticles for structure identification. 87
Figure 2.3.7 Representative HAADF-STEM images of experimental Pt nanoparticles with 'other structures. 88
Figure 2.3.8 Influence of He flow rate on the formation of Pt nanoparticles. 92
Figure 2.3.9 Growth pathway from truncated octahedral, to octahedral and to tetrahedral shaped nanoparticles. 93
Figure 2.3.10 Growth simulation at 600 K and flux of 0.1 atoms/ns. 96

Figure. 2.3.11 Snapshots from growth simulations at T=900 K and deposition rate of 1 atom/ns. 99
Figure. 2.3.12 Growth simulation at 800 K and flux of 0.1 atoms/ns. 99
Figure 2.3.13 Pt_{1415} nanoparticles prepared using a 1-inch target. 100
Figure 2.3.14 Mass spectra of Pt nanoparticles fabricated without He gas and different Ar gas flow rates. 101
Figure 2.3.15 Three sizes of Pt nanoparticles and their percentages. 102
Figure 2.3.16 Pt_{5000} nanoparticles and the population distribution. 103
Figure 2.4.1 The representative Pd nanocrystals with octahedral, decahedral, and icosahedral structures. 105
Figure 2.4.2 HAADF-STEM image, size distribution, and population distribution of Pd12000 nanocrystals. 106
Figure 2.4.3 Influence of sputtering power on the structure of Pd_{3800} nanocrystals. 107
Figure 2.4.4 Naked Pd_{3800} nanoparticles oxidized in the air. 109
Figure 2.4.5 HAADF-STEM images of Pd_{12000} decahedron and octahedron under the electron beam irradiation. 110
Figure 2.4.6 Ni clusters prepared using 10 W. Clusters mainly show an icosahedral structure. 111
Figure 2.4.7 Pure Ni clusters prepared using 50 W and mass-selected with the nominal size of 5000 Ni atoms. 112
Figure 2.4.8. Decahedra, decahedra, fcc structures (octahedra, and tetrahedra). 113
Figure 2.5.1. In-situ heating chip. 114
Figure 2.5.2 An temperature setting of the in-situ heating holder. 115
Figure 2.5.3 Direct visualisation of thermal transformation of Pt_{2057} tetrahedral nanoparticles with in-situ heating experiment and comparison with the simulation. 117
Figure 2.5.4. Size-dependent melting temperature of platinum shapes v.s. their sizes. 120
Figure 2.5.5 Melting analysis of tetrahedron. 122
Figure 2.5.6 Melting analysis of octahedron. 123

Figure 2.5.7 Electron irradiation on a Pt decahedron. 126
Figure 2.5.8 Pt_{10000} octahedra under the electron irradiation. 127
Figure 3.1.1 Atomic models of Ni-Pt nanoparticles. 131
Figure 3.1.2 Simulated HAADF-STEM images of Marks decahedra and tetrahedra. 132
Figure 3.1.3 HAADF-STEM images of Ni-Pt nanoparticles. 133
Scheme 3.1 Equipment illustration of the cluster source using magnetron-sputtering. 133
Figure 3.2.1 Photograph of the dual target holder used in this chapter. 134
Figure 3.2.2 Ni-Pt nanoparticles were prepared at room temperature with the same aggregation length. 135
Figure 3.2.3 25 cm and 19 cm were utilized as the condensation length of Ni and Pt targets. 136
Figure 3.2.4 Size distribution of Ni-Pt nanoparticles with a mass selection 5.0×10^5 amu. 138
Figure 3.2.5 Ni-Pt nanoparticles, which the condensation lengths of Ni and Pt targets were 25 cm and 19 cm, respectively. 140
Figure 3.2.6 Size distribution of Ni-Pt nanoparticles using the condensation lengths of 25 cm and 19 cm for Ni target and Pt target, respectively. 142
Figure 3.2.7 Elemental mappings of Ni-Pt nanoparticles with core-shell structures. 143
Figure 3.3.1 Mass spectra of nanoparticles prepared with various sputtering powers. 145
Figure 3.3.2 Elemental mappings of Pt-rich nanoparticles (Ni30W/Pt50W). 147
Figure 3.3.3 Elemental mappings of Pt-rich nanoparticles (Ni75W/Pt50W). 148
Figure 3.3.4. Linear distribution of elements in Pt-rich nanoparticles (Ni75W/Pt50W). 149
Figure 3.3.5 Ni-Pt alloys (1.0×10^6 amu) prepared with a longer condensation length of Ni atoms (25 cm) than that of Pt atoms (22 cm). 150
Figure 3.3.6 Size distribution of Ni-Pt alloys (Ni30W/Pt50W) with a mass selection of 1.0×10^6 amu. 152
Figure 3.3.7 Size distribution of Ni-Pt alloys with a mass selection of 1.0×10^6 amu (Ni75W/Pt50W). 152
Figure 3.4.1 Elemental mappings of Ni-rich nanoparticles. 153

Figure 3.4.2 Atomic fraction of Ni-Pt nanoparticles, which were prepared under the argon flow rate of 90 sccm. 154
Figure 3.4.3 Size distribution of Ni-Pt nanoparticles (Ni30W/Pt30W). 155
Figure 3.4.4 HAADF-STEM images of Ni-rich nanoparticles (Ni30W/Pt30W mass-filter with 1.0×10^6 amu). 156
Figure 3.4.5 Size distribution of Ni-Pt nanoparticles (Ni75W/Pt30W with a mass selection of 1.0×10^6 amu). 158
Figure 3.4.6 Images of Ni75W/Pt30W (a mass with 1.0×10^6 amu). 158
Figure 3.4.7 Images of core-shell Ni-Pt nanoparticles size selected from the Ni75W/Pt30W with a mass of 3.2×10^5 amu. 159
Figure 3.4.8 Size distribution of Ni75W/Pt30W mass selected with a mass of 3.2×10^5 amu. 160
Figure 3.5.1 Structural evolution of Ni-Pt nanoparticles by in-situ heating. 162
Figure 3.5.2 Changes of integrated intensities and areas of nanoparticles shown in Figure 3.5.1. 164
Figure 3.5.3 Structural evolution of Ni-Pt nanoparticles by in-situ heating. 166
Figure 3.5.4 The ratio of Feret's diameter of nanoparticles. 167
Figure 3.5.5 Core-shell nanoparticles (Pt30W-Ni75W) exposed in the air for 8 months. 168
Figure 3.5.6 Storage stability of Pt-Ni nanoparticles with core shell structures. 170
Figure 3.5.7 Core-shell nanoparticles (Pt30W-Ni75W) stored in the air for 13 months. 171
Figure 3.5.8 The structural stability of Ni-Pt nanoparticles in the long-term (one-year) storage. 172
Figure 3.5.9 Ni-Pt alloys (*Ms*=3.2×10^5 amu, Pt30W and Ni 75W) stored in air for 12 months. 173
Figure 3.5.10 Examples of background-subtracted, deconvoluted and normalized Ni $L_{3,2}$ edges in core-shell Ni-Pt nanoparticles. 173
Figure 4.1.1 Wettability of water, ethanol, and N, N-dimethyl formamide (DMF) on the carbon films. 177

Figure 4.1.2 Carbothermal shock synthesis of nanoparticles on carbon films. 178
Figure 4.1.3. Influences of solvents on the size of Ru nanoparticles growing on carbon fibers synthesized by flash Joule heating. 179
Figure 4.1.4. XRD spectra of Ru and Pt-doped Ru alloys. 181
Figure 4.1.5. XRD spectra of 5 at% Pt atom doping Ru nanoparticles. 182
Figure 4.1.6. Pure Ru nanoparticles (Ru2A) growing on the surface of carbon fibers. 183
Figure 4.1.7. Images and size distributions of $Ru_{95}Pt_5$ nanoparticles prepared using 3A with 100 ms. 184
Figure 4.1.8. $Ru_{95}Pt_5$ nanoparticles prepared using 4A with 100 ms. 184
Figure 4.1.9. Pure Ru nanoparticles (Ru2A) prepared with a current of 2A. 185
Figure 4.1.10. HAADF-STEM and EDX mapping images of $Ru_{95}Pt_5$ with an fcc structure. 186
Figure 4.1.11. HAADF-STEM images of $Ru_{95}Pt_5$ with an hcp structure. 187
Figure 4.1.12. Structural Recognition of $Ru_{95}Pt_5$ nanoparticles from the HAADF-STEM images. 188
Figure. 4.2.1. Schematic of the flash Joule heating using cylinder electrodes..... 189
Figure 4.2.2. Schematic of the flash Joule heating synthesis. 190
Figure 4.2.3. PtCo nanoparticles prepared using flash Joule heating with a current pulse of 500 ms. 192
Figure 4.2.4. PtCo alloy nanoparticles and single-Pt/Co-atoms dispersed in carbon hosts... 193
Figure 4.2.5. Structural characterisation of as-prepared MoC nanoparticles. 194
Figure 4.3.1. Unite cells of phosphides prepared by the flash Joule heating method. 196
Figure 4.3.2. Size description of RuP_x nanoparticles..... 197
Figure 4.3.3. The EDX mappings of one Ru*P*x nanoparticle. 197
Figure 4.3.4. Structural characterisation of ruthenium phosphide nanoparticles (RuP_x)..... 199
Figure 4.3.5. Chemical state measurement of as-prepared ruthenium phosphide nanoparticles. 200
Figure 4.3.6. XRD of as-prepared tungsten phosphide nanoparticles. 201

Figure 4.3.7. STEM images and the EDS mappings of WP nanoparticles. 203
Figure 4.3.8. Atomic resolution STEM images of WP. 204
Figure 4.3.9. High-resolution XPS of P 2p (a) and W 4f (b) in the as-prepared WP and WC_x. 204
Figure 4.4.1. Single-Pt-atoms Ru nanoparticle with an FCC and an HCP structures. 206
Figure 4.4.2. WP nanoparticle with stack faults. 208
Figure 4.5.1. Calibration of the reference electrodes. 209
Figure 4.5.2. HER activity measurements in acidic and alkaline electrolytes. 212
Figure 4.5.3. Comparison of overpotentials at η_{10} and Tafel slopes of recently reported Ru or Pt-contained electrocatalysts for HER. 213
Figure 4.5.4. Durability tests by the accelerated cyclic voltammetry tests. 216
Figure 4.5.5. Structure of RuPt(1:1). 217
Figure 4.5.6. HER performance tests of RuPt(1:1)_FCC and RuPt(1:1)_HCP. 217
Figure 4.5.7. High-resolution XPS of $Ru_{95}Pt_5$ and $Ru_{90}Pt_{10}$ nanoparticles before and after HER tests. 219

List of Tables

Table 1.1 Comparison between EDS and EELS. 34

Table 2.1. Parameters of the as-prepared Pt nanoparticles with different cooling time for the chamber by the LN_2 68

Table 2.2 Comparison between tetrahedra/truncated tetrahedra and truncated octahedra of the same size. 81

Table 2.3. Sampling data for nanoparticle shape identification. 87

Table 3.1 Parameters of atomic models of Ni-Pt nanoparticles with core-shell structures ... 131

Table 3.2. Parameters of Ni, Pt with faced-center cubic structures. 137

Table 3.3. Sizes of nanoparticles shown in Figure 3.2.3. 137

Table 3.4. Preparation conditions of core-shell nanoparticles with a mass selection of 1.0×10^6 amu. 160

Table 4.1. Summary of recently reported Ru or Pt-contained catalysts for HER in 1 M KOH electrolyte. 214

Table 4.2. Summary of recently reported Ru or Pt-contained catalysts for HER in 0.5 M H_2SO_4 electrolyte. 215

List of Abbreviations

STEM ..... Scanning Transmission Electron Microscopy

TEM..... Transmission Electron Microscopy

SEM..... Scanning Electron Microscopy

HAADF ..... High Angle Annular Dark Field

BF ..... Bright Field

EDX/EDS ..... Energy Dispersive X-ray spectroscopy

EELS..... Electron Energy-Loss Spectroscopy

XPS..... X-ray Photoelectron Spectroscopy

XRD..... X-ray Diffraction

SNR ..... Signal/Noise Ratio

WL..... White line

Pt..... Platinum

Ru ..... Ruthenium

Ni ..... Nickel

FCC..... Face-Centered Cubic

HCP ..... Hexagonal Close-Packed

TOF..... Time-of-Flight

DMF ..... N, N-dimethyl Formamide

HER ..... Hydrogen Evolution Reaction

OER ..... Oxygen Evolution Reaction

LSV..... Linear Sweep Voltammetry

CV..... Cyclic Voltammetry

EIS ..... Electrochemical Impedance Spectrum

WE..... Working Electrode

RE..... Reference Electrode

CE..... Counter Electrode

RHE ..... Reversible Hydrogen Electrode

NHE.....Normal Hydrogen Electrode

PDF.....Powder Diffraction File

ICSD .....International Crystal Structure Database

Contents

Chapter 1. Backgrounds and literature reviews 1
1.1 Motivation 1
1.2 Introduction of nonequilibrium nanoparticles 4
1.3 Chemical synthesis of nanoparticles 9
1.3.1 Colloidal methods 10
1.3.2 Carbothermic reduction synthesis 12
1.3.3 Chemical vapor phase deposition 14
1.4 Physical ways of nanoparticles preparation 16
1.4.1 Pulsed laser ablation 16
1.4.2 Spark discharge generation 18
1.4.3 Magnetron sputtering used in this thesis 18
1.5 Scanning transmission electron microscope 27
1.5.1 Imaging in STEM mode 29
1.5.2 Spherical aberration of electromagnetic lens 30
1.5.3 Spectroscopy (EELS/EDX) 33
1.5.4 Data acquisition and processing in this thesis 35
1.6 Hydrogen evolution reaction by electrocatalysis 42
Chapter 2. Tetrahedral and octahedral nanoparticles fabrication using the magnetron-sputtering method 48
2.1. Size measurement of nanoparticles using an ImageJ's script 48
2.2. Preparation conditions of nanoparticles using the cluster source 56
2.2.1. Sputtering power 56
2.2.2. Condensation zone length 59
2.2.3. Gas flow rates (pressure) 61
2.2.4. Influence of temperature on the growth of particles 65
2.2.5. Formation of aggregated particles 71
2.3. Tetrahedral and octahedral Pt nanoparticles 77
2.3.1. Octahedral and tetrahedral Pt nanoparticles 78
2.3.2 Preparation conditions of tetrahedral Pt nanoparticles 84

2.3.3 Shape identification using the STEM images 86
2.3.4. Growth mechanism by simulations 89
2.3.5. Tetrahedra prepared by a small target 100
2.4. Palladium and Nickel nanoparticles 103
2.4.1. Octahedral palladium nanoparticles 104
2.4.2. Nickel nanoparticles: From an icosahedron to an octahedron 111
2.5. Structure stability of Pt nanoparticles 113
2.6 Conclusion 128
Chapter 3. Ni-Pt alloyed and core-shell nanoparticles 129
3.1. Atomic models of Ni-Pt nanoparticles and the corresponding simulated STEM images 129
3.2. Condensation lengths of targets 133
3.3. Pt-rich Ni-Pt alloys 144
3.3.1. Mass spectra of Ni-Pt nanoparticles 145
3.3.2. Elemental contents and mappings of Pt-rich nanoparticles 146
3.3.3. Size distribution of Pt-rich nanoparticles 150
3.4. Ni-rich Ni-Pt core-shell nanoparticles 153
3.4.1. Elemental contents and mappings of Ni-Pt nanoparticles 153
3.4.2. Size distribution of Ni-rich nanoparticles 155
3.5. Structural stability of Ni-Pt nanoparticles 161
3.5.1. Thermal stability 161
3.5.2. Structural stability of core-shell nanoparticles 167
3.6. Conclusion 175
Chapter 4. Nanoparticles synthesis using Joule heating 176
4.1. Structure controlled synthesis of single-Pt-atoms Ru nanoparticles by carbothermal shock 177
4.1.1. Influence of solvent on the nanoparticle sizes 177
4.1.2 Structure-controlled synthesis of Pt-doped Ru nanoparticles 180
4.2. Nanoparticle synthesis using flash Joule heating synthesis 188
4.3. Metallic phosphides synthesis 194
4.3.1 Ruthenium phosphide 196
4.3.2 Tungsten phosphide 200
4.4. Stacking faults in the nanoparticles 205

4.5. Catalytic performances of Ru-based nanoparticles 209
4.6 Conclusion 220
Chapter 5. Conclusion and outlook 221
Reference 225

Chapter 1. Backgrounds and literature reviews

1.1 Motivation

Over the past few decades, significant progress has been made in enhancing the catalytic properties of metal nanoparticles, particularly in the field of electrocatalysis. This type of catalysis is based on electrochemical reactions such as water-splitting, oxygen reduction, and carbon dioxide reduction and so forth [1–4]. Especially, the oxygen reduction reaction (ORR) is crucial for the proton exchange membrane fuel cells (PEMFC), which can offer eco-friendly energy without any pollution to the environmental. It has been demonstrated that metal nanoparticles exhibit remarkable catalytic reactivity due to the metal atoms present at edges, corners, and facets[5–9]. For instance, Pt_3Ni nanoparticles with icosahedral shapes exhibit higher catalytic activity of ORR compared to their octahedral counterparts[10], while octahedral nanoparticles consisted of {111} facets exhibit better catalytic performance than other shapes[11]. Strains created by structure defects in nanoparticles, e.g. twin boundaries and stacking faults, can promote the catalytic reaction. However, achieving precise control over the shape and structure of nanoparticles, e.g. with nonequilibrium structures, remains a challenge, and further efforts are needed to develop efficient synthesis methods. Firstly, it is essential to fabricate size-controlled nanoparticles with specific shapes, which can serve as model systems to establish a correlation between the number of catalytic sites on the nanoparticles and their catalytic performances. Moreover, surface cleanness is vital to ensure that all the atoms on the surface of nanoparticles are exposed to catalytic reactions. However, it remains challenging to prepare

naked nanoparticles with specific structures and shapes[12]. Another challenge of catalysts preparation is to lower the costs of catalyst preparation, which is essential for commercialization. Hence, developing an economical synthesis method for nanoparticles is significant. An ideal synthesis method should be time-saving and low-cost. Currently, nanoparticle preparation methods are energy-intensive and time-consuming. Finally, it is vital for metal nanoparticles to retain their structural stability under storage and reaction conditions, including high temperatures.

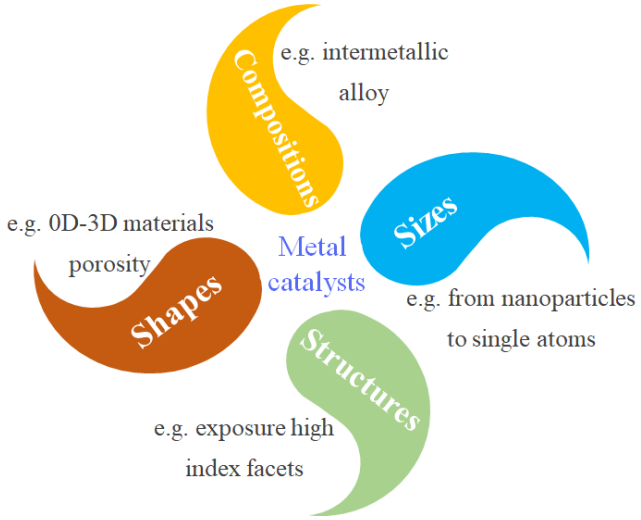


Figure 1.1.1. Strategies to enhance the catalytic activity of nanoparticles.

This thesis aims to make contributions to the field of physical nanoparticle synthesis, focusing on four strategies for optimizing nanoparticles: composition, size, structure, and shape, as shown in Figure 1.1.1. Magnetron sputtering gas condensation was employed to prepare size-selected nanoparticles with naked surfaces and specific shapes. Firstly, tetrahedral Pt nanoparticles were prepared with controlled population growth. The observed tetrahedra are not the equilibrium shapes obtained by the Wulff construction. A novel growth mechanism was

developed to interpret the tetrahedron formation through simulations. Furthermore, the research involved the preparation of nickel-platinum (Ni-Pt) nanoparticles from alloys to core-shell structures. It was observed through spherical aberration corrected scanning transmission electron microscopy (Cs-STEM) that Ni-Pt nanoparticles formed not only with octahedral, and tetrahedral shapes, but also with decahedral and icosahedral shapes, which were induced by the introduction of nickel atoms. Both types of as-prepared naked nanoparticles can assist in exploring catalytic mechanisms through cut-of-edge technologies, e.g. in-situ techniques. The thermal stability of these nanoparticles was also investigated using in-situ heating, which revealed that truncated octahedral shapes were the most thermodynamically stable structures for Pt nanoparticles compared to other shapes. Furthermore, Ni-Pt nanoparticles showed stable icosahedral and decahedral structures at elevated temperatures, but exhibited unstable structures in long-term storage in air due to atom diffusion.

The Flash Joule heating method is a newly developed synthesis approach that offers significant time and energy savings in producing a range of nanoparticles, including metal nanoparticles, carbides, and phosphides. This study employed this technique to synthesize Pt-doped ruthenium nanoparticles with energetically unfavorable structures, as well as to generate carbides and phosphides as further examples. The prepared nanoparticles were observed to exhibit stacking faults, as seen in their structural images. Metastable structures were demonstrated to yield superior catalytic performance, as exemplified by the application of Pt-doped Ru nanoparticles in hydrogen evolution reaction.

1.2 Introduction of nonequilibrium nanoparticles

Clusters or nanoparticles are aggregates of a few to many millions of atoms or molecules[7]. Generally, particles whose size in any direction is less than 100 nm are called as nanoparticles[13]. Considering the difference of electronic structures, nanoparticles can be classified in three groups: single atoms, clusters, and nanoparticles (Figure 1.1.1)[8]. When atoms exist in isolation, their electrons occupy discrete energy levels in atomic orbitals. However, when N atoms combine to form a cluster through covalent or metallic bonding, the energy spacing between levels become narrow due to overlapping atomic orbitals of the outermost electrons. As the number of atoms in a nanoparticle increases, the energy levels of the atoms become closely spaced, forming a continuum or energy band[14]. Normally, the nanoparticle with 1-3 nm in diameter is called a cluster, which corresponding to a few hundred atoms[15].

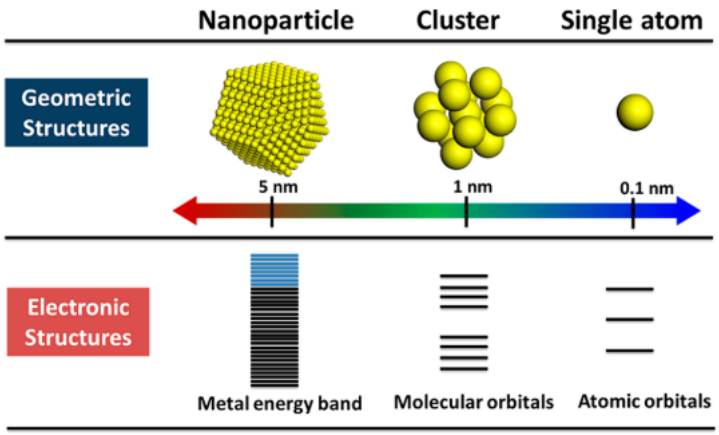


Figure 1.2.1. Geometric and electronic structures of single atom, cluster and nanoparticle. Figure and caption taken from Ref[8].

Metal nanoparticles can grow with various shapes, terminated by different facets. When a nanoparticle is formed, its overall Gibbs free energy is the combination of the bulk Gibbs free

energy and the surplus Gibbs free energy that arises from the surface[16]:

$$dG = dG_{bulk} + \gamma\, dA, \tag{1-2-1}$$

where A is the surface area and the γ is the specific surface free energy (per unit area). The specific surface energy refers to the amount of energy necessary to create a surface by breaking a particular number of atomic bonds in a crystal structure. In a nanoparticle with a constant number of atoms the entire surface area determines the total Gibbs free energy, which is calculated through the integration of γdA across the surface of the nanoparticle. This implies that a nanoparticle will adopt an equilibrium shape when its total surface free energy is at a minimum. In a crystalline nanoparticle, the specific surface energy varies with different atomic arrangements, resulting in different crystallographic planes possessing unique energies. The structure and shape that are in thermodynamic equilibrium will enable the nanoparticle to be at the minimum Gibbs free energy globally. Conversely, non-equilibrium structures and shapes of the nanoparticle can form, which will correspond to local minima of the Gibbs free energy, as shown in Figure 1.2.2(a),

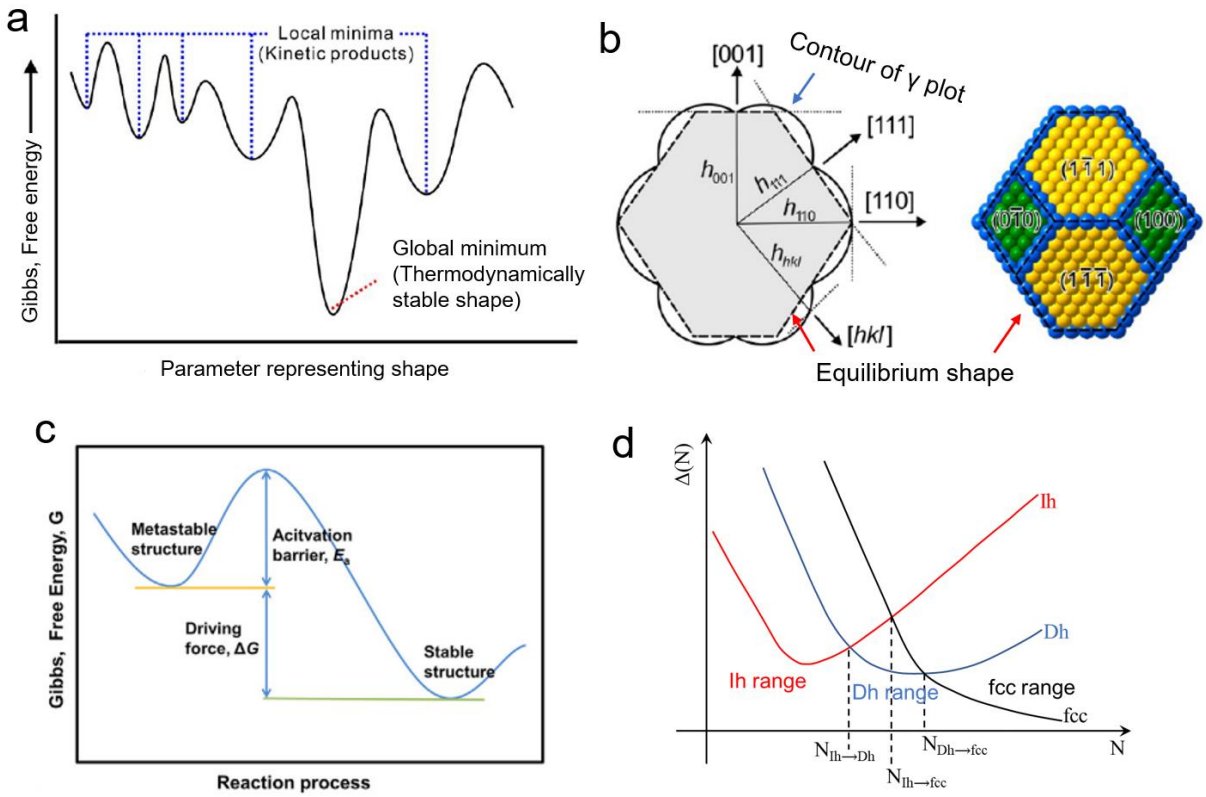


Figure 1.2.2. (a) Nanoparticles with various shapes. The shape with the lowest Gibbs free energy is the thermodynamic equilibrium shape. (b) Illustration of the Wulff construction. Two-dimensional section of a polar plot of the specific surface free energies of an fcc crystal oriented along [1$\bar{1}$0] as built by the Wulff theorem. The inner envelope denoted by dashed lines corresponds to the equilibrium shape of the nanocrystal. A three- dimensional atomic model corresponding to the equilibrium shape is shown on the right. (c) Free energy diagram illustrating the transition from a metastable phase to a stable phase. (d) Qualitive behaviour of excess energy (Δ) for crystalline (fcc), icosahedron (Ih), and decahedron (Dh) clusters. Figure (a-b) and the corresponding captions taken from [16], Figure c and its caption taken from [17], and Figure d and its caption taken from [15].

The equilibrium shapes of nanoparticles, which have minimum total surface energy, are predicted by the Wulff constructions[18] and the modified Wulff constructions[19].

$$h_{hkl} = \lambda \gamma_{hkl} \tag{1-2-2}$$

The shape of the Wulff construction shown in Figure 1.2.2(b) can be described using the expression (1-2-2) stating that the normal distance, h_{hkl}, from the center of the nanoparticle to the facet of $\{hkl\}$ is proportional (with factor λ) to the orientation-dependent specific surface

free energy[20,18]. In accordance with this theorem, the Wulff construction commences by creating a polar plot that depicts the specific surface free energies (γ_i) as a function of orientation. Each radius vector (h_i) on the plot corresponds to its respective specific surface free energy (γ_i). Subsequently, at the intersection point with the polar plot, a short-dashed line is drawn perpendicular to each vector, as illustrated by Figure 1.2.2(b). This procedure is repeated for all the different directions represented by the crystal axes, culminating in a closed polyhedron within the polar plot. This polyhedron yields the equilibrium shape of the nanocrystal. Figure 1.2.2(b) illustrates a nanoparticle based on the Wulff construction, which exhibits {111}, and {100} surfaces.

The growth kinetics also plays a significant role on the morphology formation of clusters[20]. For instance, there is a competition between the rate of atomic deposition and diffusion on the surfaces of clusters, which impacts on the growth rates of different facets[21–24]. This competition was observed in the wet-chemical synthesis that the capping polymer was used to alter the surface free energies of clusters[25,26,27]. Cubic iron (Fe) nanoparticles prepared by the magnetron-sputtering gas condensation method was the first example that the kinetic growth modes of {100} and {110} surfaces were interpreted the formation process of cubic Fe nanoparticles[24]. The growth way of nanoparticles formed with different growth rates on different facets is called as the kinetic Wulff construction. Nevertheless, the Gibbs free energy of the kinetic product is greater than that of the thermodynamic product. Nanoparticles with a kinetic shape can transition to their equilibrium shape (i.e., thermodynamic shape) under specific conditions, such as annealing at elevated temperatures, as shown Figure 1.2.2(c).

Figure 1.2.3 shows nanoparticles are built by {111}, {100}, or a combination of both types (e.g. cuboctahedron, octahedron and tetrahedron in Figure 1.2.3(b,c,h). The nanoparticles forming into crystalline structures including the octahedron, the tetrahedron, and the truncated octahedron (e.g. cuboctahedron) do not suffer from the strain of twin boundaries in the growth. The twin boundary storing energies by creating internal strains, builds the morphologies of nanoparticles[19,28], such as the decahedron and icosahedron (Figure 1.2.3d-f).

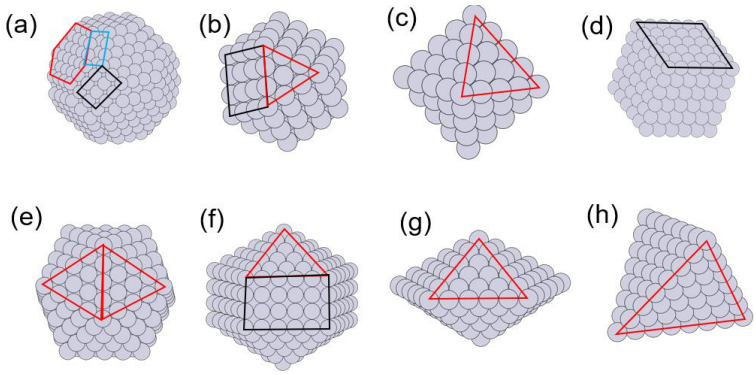


Figure 1.2.3. Schematic illustrations of metal nanoparticles. (a) Wulff shape; (b) cub-octahedron; (c) octahedron; (d) cube with (100) planes; (e) icosahedron; (f)decahedron with (100) facets; (g) decahedron without (100) facets, and (h) tetrahedral shape. The red triangles, black squares, and the blue square represent {111}, {100}, and {110} facets, respectively.

Theoretical calculations define the excess energy[15] of a nanoparticle as the energy in excess of the same N atoms in a perfect bulk crystal, as described in equation (1-2-3). This excess energy is used to compare the stability of nanoparticles of a given size (N). Here, E_b represents the binding energy of the nanoparticle, while ε_{coh} denotes the cohesive energy per atom in the bulk, which is the energy difference between the agglomeration of atoms to form a crystal nanoparticle and their isolated state[15].

$$\Delta(N)=\frac{E_b(N)-N\varepsilon_{coh}}{N^{2/3}} \qquad (1\text{-}2\text{-}3)$$

The binding energy refers to the energy difference between the isolated state of atoms and their combined state as a particle ($E_b = E_{particle} - NE_{at}$), where E_{at} is the energy of an isolated atom. In general, the binding energy E_b of a nanoparticle with size N can be grouped with volume and surface contributions that are expressed by the empirically equation (1) [15,20]:

$$E_b(N) = aN + bN^{2/3} + cN^{1/3} + d \quad (1\text{-}2\text{-}4)$$

There are four terms in the equation (1-2-4), where a through d are material and shape-dependent coefficients. The exponents of N depend on the geometric dimensions of contributors, for example, the contributor of volume has 3 dimensions, therefore, N's exponent is 3/3. The parameter a is simply the cohesive energy ε_{coh} in crystal nanoparticles. When the size of the nanoparticle approaches infinity, which means the nanoparticle approaches a bulk, b is close to the excess energy $\Delta(N)$. Surface and twin boundary energies contribute to b. c, and d are contributed by edge and corner atoms of nanoparticles, respectively. Figure 1.2.2d gives the relationship between the excess energy of a nanoparticle and its size for different shapes, which indicates that icosahedra could be the most favorable structures at small sizes (e.g. around 100 atoms for Pt clusters), while truncated octahedron nanoparticles are expected for large sizes[29]. This finding is consistent with the predictions of the Wulff construction.

1.3 Chemical synthesis of nanoparticles

Numerous methods have been invented to prepare metal nanoparticles, which are grown by atoms nucleation or condensation[30]. Depending on the metal atoms sources, the synthetic strategies can be classified into chemical and physical methods. The chemical methods utilize

metal salts as precursors, while the physical method uses bulk materials as the atom sources.

1.3.1 Colloidal methods

Colloidal or wet-chemical methods prepare metal nanoparticles by reducing metal salt precursors in colloids or solutions. In order to control the shape of nanoparticles, surfactants or capping agents ranging from organic molecules to ionic salts and polymers are employed to bind to the surfaces of nanoparticles, controlling the growth rate of specific facets of nanoparticles[16] as shown in Figure 1.3.1. Figure 1.3.2 illustrates general colloidal strategies of nanoparticle preparation, where size and shape of nanoparticles depend on the growth under thermodynamic control or kinetic control as determined by various synthetic conditions[16,31]. In addition, the colloidal synthesis can control the structures of nanoparticles to grow in energy-unstable structures, such as ruthenium nanocrystals with a face-centered cubic structure[32] and cobalt nanoparticles with a hexagonal close-packed lattice[33]. There are many advantages of colloidal syntheses, such as simple equipment, easy operation of the synthetic procedures, and large quantities of products[34]. However, the shortcomings of colloidal synthesis are also the capping agents that block the reactants to access the catalytically active sites on the surfaces of nanoparticles[35]. What's worse, capping agents sometimes take place side reactions in catalytic conditions or poison partly or fully the catalysts[35,36].

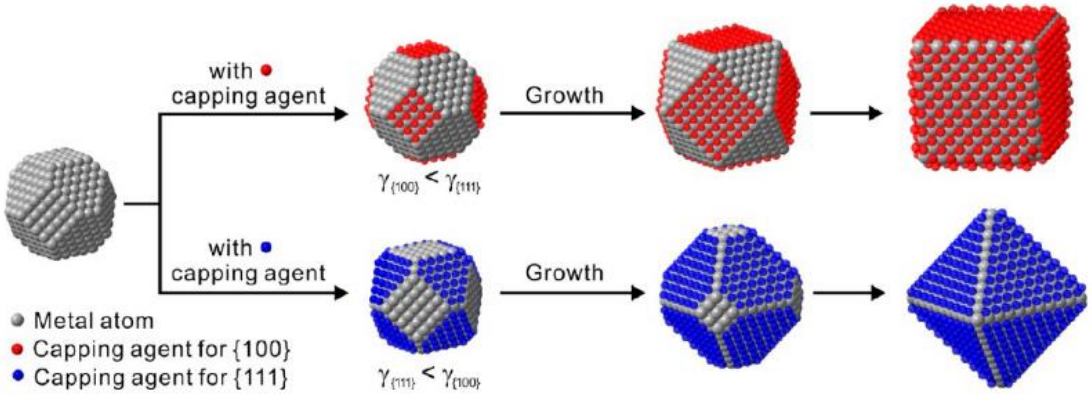


Figure 1.3.1. Schematic illustrations of how the capping agents direct the growth of a single-crystal seed made of an FCC metal. The shape of resultant nanocrystals can be manipulated in a controllable fashion through the introduction of a capping agent (represented by red or blue dots) that can selectively bind to a specific type of facet, altering the order of surface free energies and eventually leading to the formation of a nanocube enclosed by {100} facets and an octahedron enclosed by {111} facets, respectively. Figure and caption taken from Ref.[16].

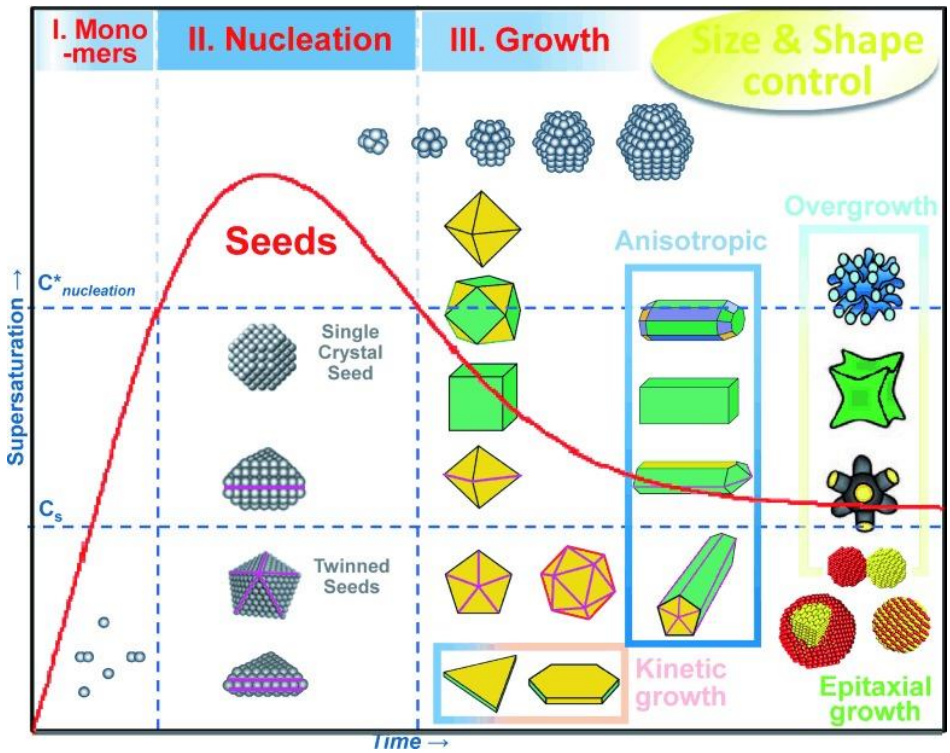


Figure 1.3.2. The curves of the concentration of atoms and the reaction time in the general synthetic ways for size and shape control of metal nanoparticles. Figure and caption taken from Ref.[31].

1.3.2 Carbothermic reduction synthesis

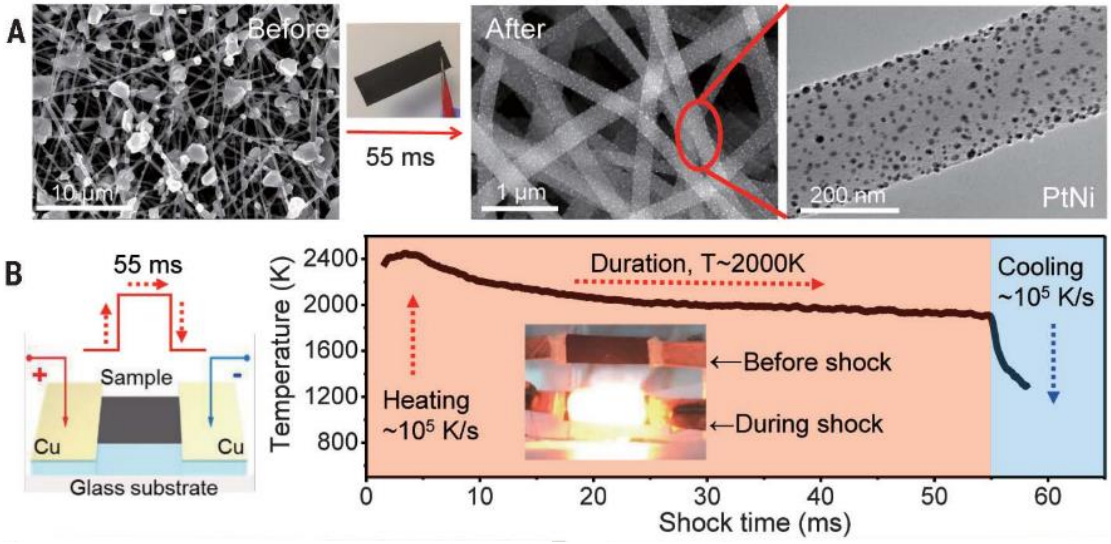


Figure 1.3.3. Carbothermal shock synthesis of nanoparticles on carbon supports. (A) Microscopy images of microsized precursor salt particles on the carbon nanofiber (CNF) support before thermal shock, as well as the synthesized, well-dispersed (PtNi) nanoparticles after shock heating. (B) Sample preparation and the temporal evolution of temperature during the 55-ms thermal shock. Figure and caption taken from Ref.[37].

Carbothermic reduction synthesis utilizes carbon and/or reduction gases (e.g. hydrogen, ammonia) to reduce metallic salts into metal nanoparticles[37] or metallic carbides[38] under high temperatures. However, the reduced metal atoms are susceptible to aggregate into large sizes by diffusion in high-temperature annealing. Recently, the carbothermal shock synthesis[37,39] was utilized to prepare nanoparticles, which are carbothermically reduced at ultrahigh temperature (e.g. 3000 K) through the Joule heating generated by a current in a short time (milliseconds). The shock heating can limit the atom diffusion and narrow the size distributions of nanoparticles[37,40]. Taking advantage of the flash heating and cooling rates of carbothermal shock synthesis, not only high-entropy-alloy nanoparticles[37], but also ordered intermetallic nanoparticles with the $L1_0$ structure[41] can be synthesized (Figure 1.3.4(a)). Doping carbon

materials with nitrogen (N)[42] or sulfur (S)[43] atoms is another effective strategy to hinder the metal atoms diffusion through the strong chemical binding between the metal atoms and the doped elements (N or S)[44]. With the help of sulfur-anchoring synthesis, the intermetallic Pt-based nanoparticles shown in Figure 1.3.4(b) were fabricated.

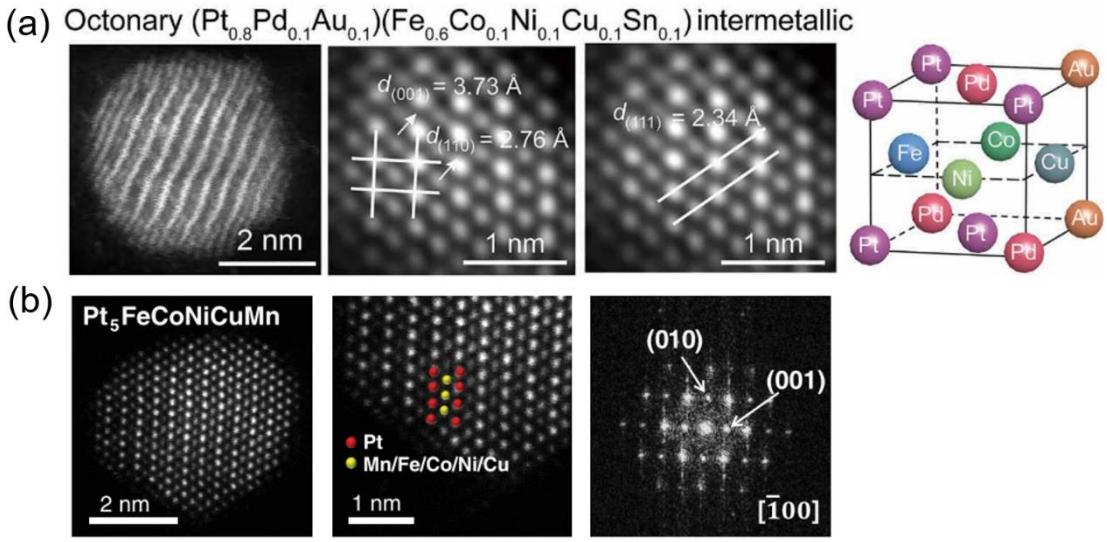


Figure 1.3.4. HAADF-STEM image of $L1_0$ intermetallic nanoparticles. Figure (a) and caption adapted from Ref.[41]. Figure (b) and caption taken from Ref.[43].

1.3.3 Chemical vapor phase deposition

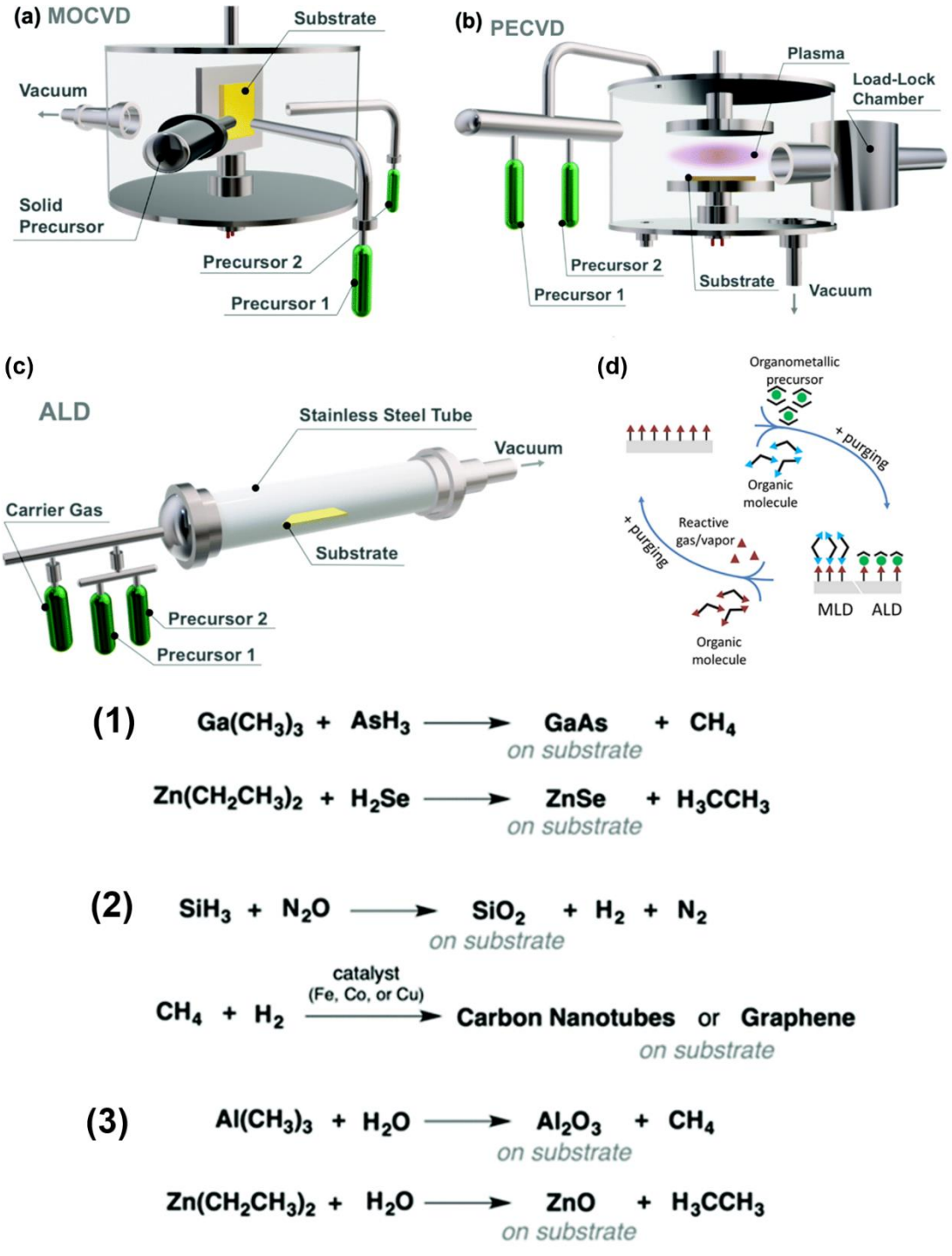


Figure 1.3.5. Schematics of reaction chambers used for common reactive vapor deposition methods. Representative (a) chamber and (1) deposition reactions used in metal–organic chemical vapor deposition (MOCVD). Representative (b) chamber and (2) deposition reactions used in plasma-enhanced chemical vapor deposition (PECVD). Representative (c) chamber and (3) deposition reactions used in atomic layer

deposition (ALD). (d) Reaction mechanism of atomic/molecular layer deposition (ALD, MLD). Figure (a-c) and caption adapted from Ref.[45]. Figure (d) and caption adapted from Ref.[46].

Synthesis of nanoparticles using vapor phase deposition is achieved by chemical reactions of the vapor-phase molecules to nucleate on the surface of supports/substrates[47]. Figure 1.3.5 gives three typical strategies of vapor phase depositions with illustrations of the corresponding apparatus and examples of deposition reactions. Molecular or organometallic precursors are volatilized by heating (or other energies, such as the high energy electrons) under reduced pressure[45]. The chemical vapor synthesis, such as thermal chemical vapor deposition (TCVD), metal–organic chemical vapor deposition (MOCVD), and plasma-enhanced chemical vapor deposition (PECVD), can fabricate doped or multi-component nanoparticles by introducing multiple precursors. Atomic/molecular layer deposition (ALD/MLD), as shown in Figure 1.3.5(c), is achieved by reacting the reactant and counter-reactant precursors sequentially with a repeating algorithm of pulse-purge-pulse cycles as shown in Figure 1.3.5(d). Therefore, ALD/MLD not only can prepare pure nanoparticles, but also can fabricate core-shell nanoparticles[48]. The disadvantage of chemical vapor phase deposition is the slow deposition rates (0.01 Å/s to 2 Å/s) in comparison with the physical vapor deposition methods (5 Å/s to 10 Å/s)[45].

Nanoparticles prepared using the abovementioned methods grow into Wulff constructions controlled by thermodynamics, which means it is difficult to fabricate nanoparticles with nonequilibrium structures or shapes.

1.4 Physical ways of nanoparticles preparation

In physical vapor phase deposition, bulk or powder materials are vaporized into a background gas and then the vapor is condensed by a cold gas into nanoparticles[47]. Depending on the means of evaporation, there are four approaches: thermal evaporation, pulsed laser ablation, spark discharge generation, and ion sputtering.

In thermal evaporation, target materials which have low melting points, are placed in the crucible. Due to the difference in melting, evaporation, and boiling points of the different target materials, they should be heated separately with individually set temperatures for controlling the compositions of alloy nanoparticles[49].

1.4.1 Pulsed laser ablation

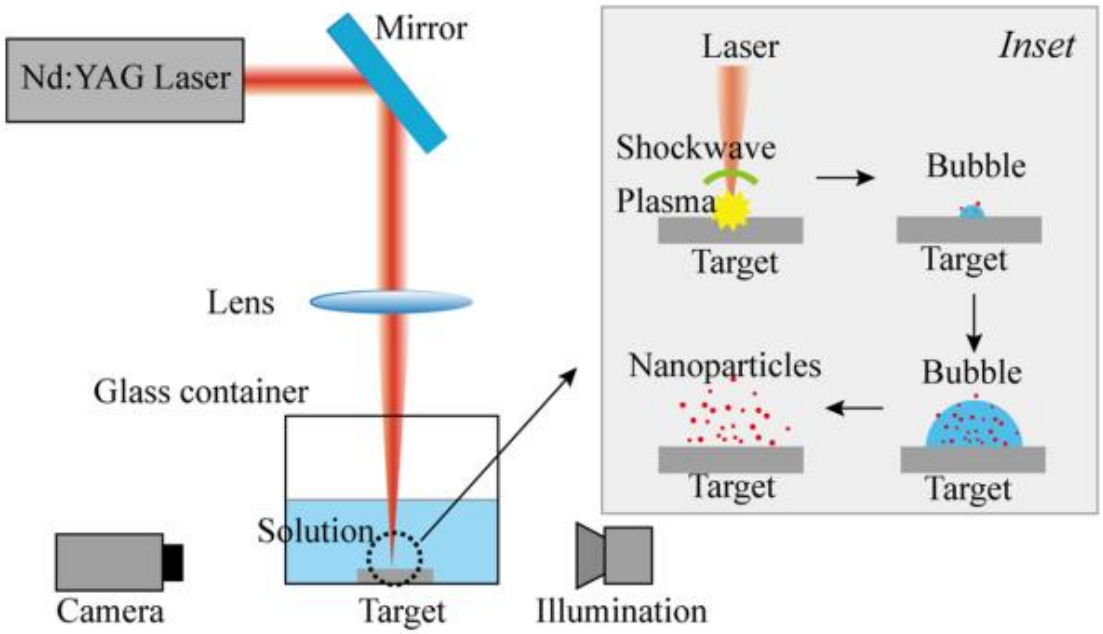


Figure 1.4.1. A schematic illustration of the synthesis and structure of nanoparticles. Figure and caption adapted from Ref.[50].

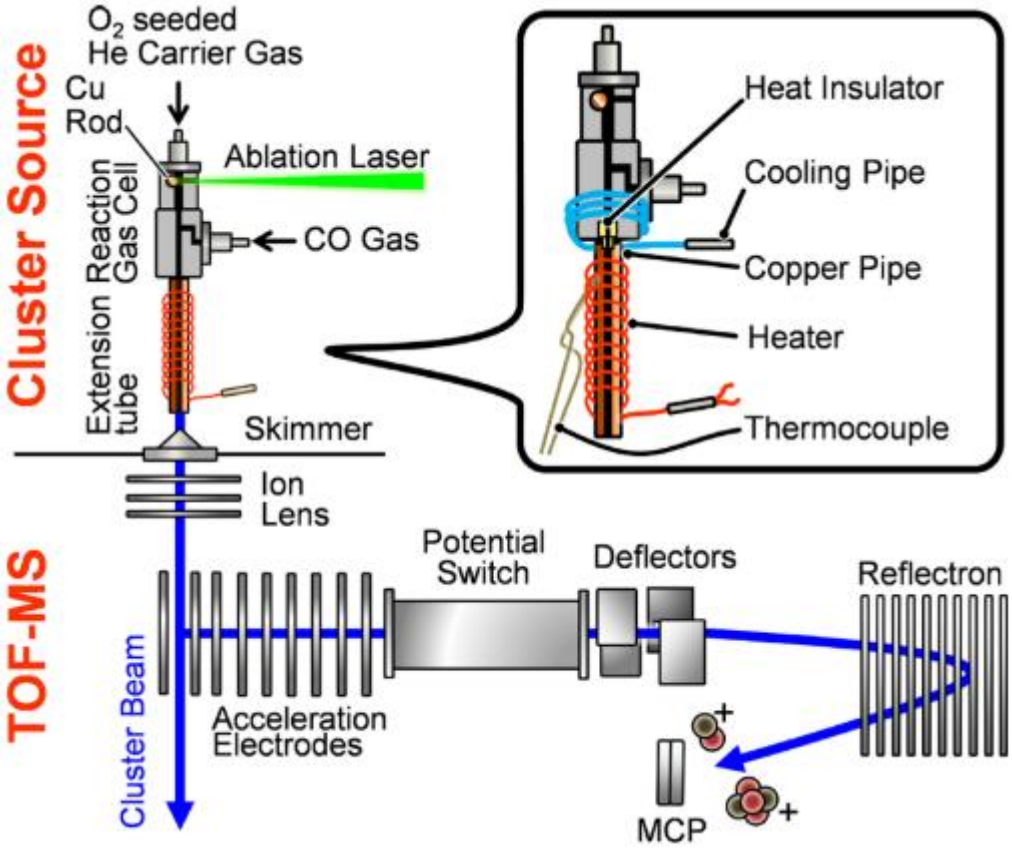


Figure 1.4.2. Schematic diagram of the pulsed laser ablation setup, which the nanoparticles are cooled by gases. Figure and caption taken from Ref.[51].

In pulsed laser deposition, the target is ablated by laser to generate atoms as shown in Figure 1.4.1. As high energy density (e.g. 12.7 J/cm^2) is available with ablation lasers[50], a wide range of materials from metals to oxides can be sputtered. Depending on the cooling medium (gas or liquid), the pulsed laser ablation can be divided into two classes. For example, using water to quench the sputtered silver atoms can build nanoparticles with a high density of stack faults, which promote largely the performance of the hydrogen evolution reaction[52]. However, it is difficult to control the size and morphology of nanoparticles[50]. Figure 1.4.2 shows an experimental setup where gases are used to cool down the nanoparticles[51]. With the time-of-flight mass selector (TOF-MS), the sizes of nanoparticles can be filtered before deposition.

1.4.2 Spark discharge generation

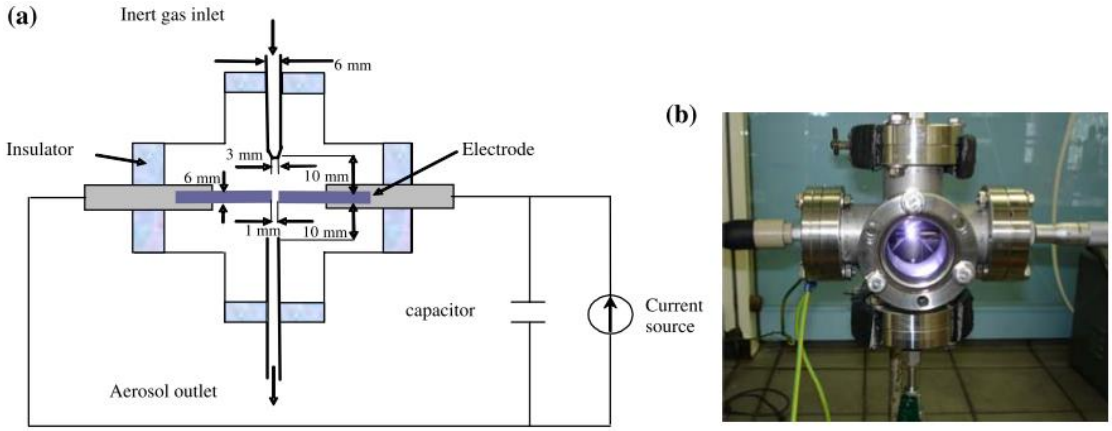


Figure 1.4.3 Schematic illustration of spark discharge generator (a) and the photograph of the equipment (b). Figure and caption adapted from Ref.[53].

The spark discharge (Figure 1.4.3) is ignited by gases applying a high voltage on the electrodes with a small gap, forming a plasma channel with a ultrahigh temperature (20000 K)[54]. The electrode materials are evaporated at ultrahigh temperature. Sizes, morphologies, and the mass production rate depend on the physical properties of electrode materials, such as thermal conductivity, evaporation enthalpy, the boiling point, the gas pressure, and the energy per spark[53].

1.4.3 Magnetron sputtering used in this thesis

Magnetron sputtering, as one of ion beam methods, uses a plasma to bombard the target to generate atoms[55]. The plasma can be ignited by direct current (DC) for conductive targets or radio frequency (RF) for insulator targets. Gases[56], e.g. argon and helium, are usually employed to condense the sputtered atoms into nanoparticles that deposit on substrates directly. Liquid mediums[57] and molten salt[50] can also be used to disperse and stabilize nanoparticles. Our

group's cluster source (Figure.1.4.4) with a time-of-flight (TOF) mass filter can prepare size-selected nanoparticles. This cluster source consists of three sections as shown in Figure 1.4.4, followed with a deposition chamber (not shown in Figure 1.4.4). Nanoparticles are formed in the sputtering and aggregation chamber, where the walls can be cooled down by liquid (e.g. liquid nitrogen or water) for building a stable temperature environment inside the chamber. It is possible to prepare nanoparticles with nonequilibrium shapes by slowing down the diffusion of atoms on the surface of clusters[24].

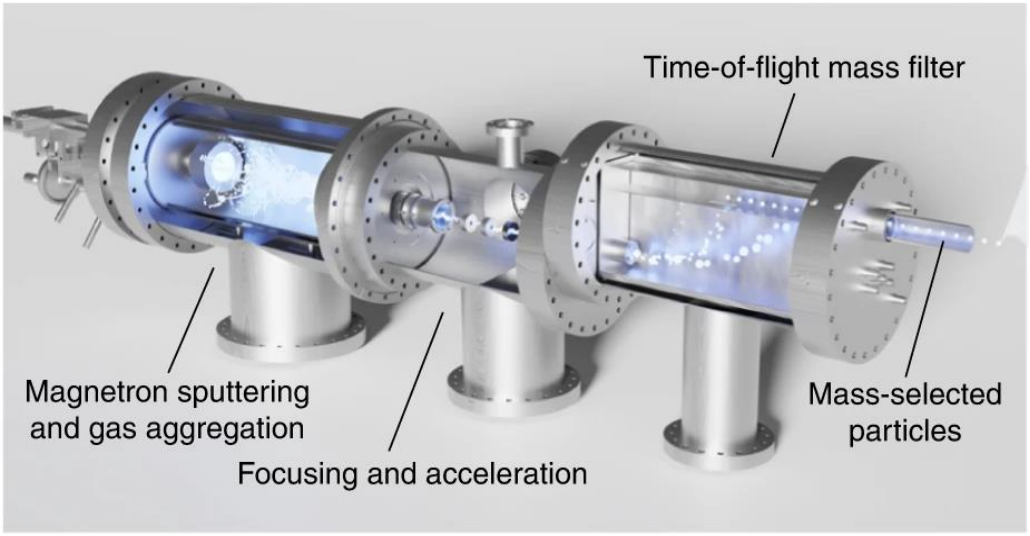


Figure 1.4.4. Schematic structures (from left to right) of the cluster source used to deposit mass-filtered nanoparticles. Figure and caption taken from Ref.[58].

Figure 1.4.5 shows the structure of DC magnetron sputtering head (a) and the picture of a head with a platinum target (b). As showing in Figure 1.4.5 (a), the high voltage (e.g. 300 V) is applied on the anode and the target connects with the ground. Two circular magnets are placed behind the target to constrain the trajectories of electrons and ions. When exposed to a high voltage electric field **E** (e.g. 300 V/0.003 m = 10^5 V/m), the argon atoms - with an ionization energy of 15.7 eV - will become ionized into Ar+ ions and electrons at the beginning. The Ar^+

ions will be accelerated by the electric field to bombard the surface of the target. When Ar+ ions – with several hundred eV (typical ion energies 200-600 eV) - bombard the surface of target, various processes occur. A fraction of Ar+ ions can physically penetrate the near-surface region, while the others are backscattered, becoming neutral recoil Ar atoms from target with an average kinetic energy of several eV. As the Ar^+ ions sputter the target, secondary electrons are emitted and accelerated away from the cathode (target), gaining sufficient energy to excite and ionize the Ar atoms by collisions, leading to the production of plasma[59]. The energies of incident Ar+ ions are transferred to electrons and lattice atoms of target through collisions[60,61]. When atoms at the surface are removed from the solid target, they are known as sputtered atoms. Taking a copper target as an example, the sputtered process can be described as $Ar^+ + Cu \longrightarrow Cu^+ + Ar$ [Ref.62]. Figure 1.4.5 (c) demonstrates schematically the process of the cluster formation[63]. The sputtered atoms and inert gases (e.g. Ar or He) will collide with each other, which is called as "Three-body-collisions" ($2M + Ar \longrightarrow M_2 + Ar$, where M is a sputtered metal atom), forming a diatomic metal cluster in the gas phase. Then clusters grow by metal atom attachment ($Mn + M \longrightarrow M_{n+1}$). The newly formed clusters can be charged by collisions with plasma ions and electrons. Additional processes for modifying the charge state of clusters in a plasma include ionization by electron impact, recombination of electrons with positively charged clusters, and thermoemission of electrons from the cluster surface[64]. Small clusters typically have a lower ionization potential compared to their corresponding atoms and diatoms. Consequently, ionization of such clusters can occur at relatively low electron temperatures or typical electron energies at which ionization of atoms or adatoms does not occur. Thus, clusters

present in a plasma can contribute to the formation of free electrons. Additionally, metallic nanoparticles and clusters can emit and accept electrons from the surrounding plasma, thereby acquiring positive or negative charges. Under high temperatures of metallic particles or clusters, they acquire a positive charge, while under low temperatures, they exhibit a negative charge[64]. The following growth process consists of coagulation ($M_n + M_m \longrightarrow M_{n+m}$) and coalescence ($M_N + xM \longrightarrow M_{N+x-y} + yM$)[64]. When two clusters collide, they can merge into a bigger one through coagulation. However, this process is limited by the repulsion of charges present on the clusters, which hinder clusters of same charge polarity to approach each other. In addition to causing the merging of clusters, the coagulation process also results in an increase in the temperature of the newly formed cluster. This is because the larger size of the newly formed cluster possesses a smaller binding energy ($E = n\varepsilon_0 - An^{2/3}$, where n is the size of cluster in atoms, ε_0 is the binding energy of atoms in bulk, A is the surface area of cluster) than the combined energy of the smaller clusters that coagulated. Consequently, the excess energy is released as the cluster surface is created. The other way of cluster growth is through coalescence. The growth of clusters occurs by passing through an atomic vapour. The sputtered atoms land on the nascent clusters to form larger size clusters. Meanwhile, the surface atoms of clusters have probabilities to evaporate from the clusters as, during the coalescence, the atoms absorb enough energy to overcome the binding energy of a bound atom on the nanoparticle surface (e.g. 2.38 eV for Pt atoms on (111) facet in bulk)[63,65]. The atom evaporation rate from the surface of a cluster is related with the size of clusters, the sputtered atom number density in the vapor, the temperature of the clusters, and the binding energy for surface atoms of cluster. The

interplay between the clusters and the vapour leads to the evaporation of small clusters because the rate of evaporation is higher than the rate of atom attachment. Conversely, the larger clusters continue to grow because the rate of atom attachment is higher than the rate of evaporation. This results in a decrease in the number of clusters. The rate of cluster growth in this scenario is slower compared to the coagulation process and exhibits a sharp dependence on temperature. The final size of clusters exiting the condensation chamber is determined by experimental parameters, including the chamber pressure, the magnetron power, gas compositions and gas flow rates, condensation zone length, pumping rates and cooling mode[55].

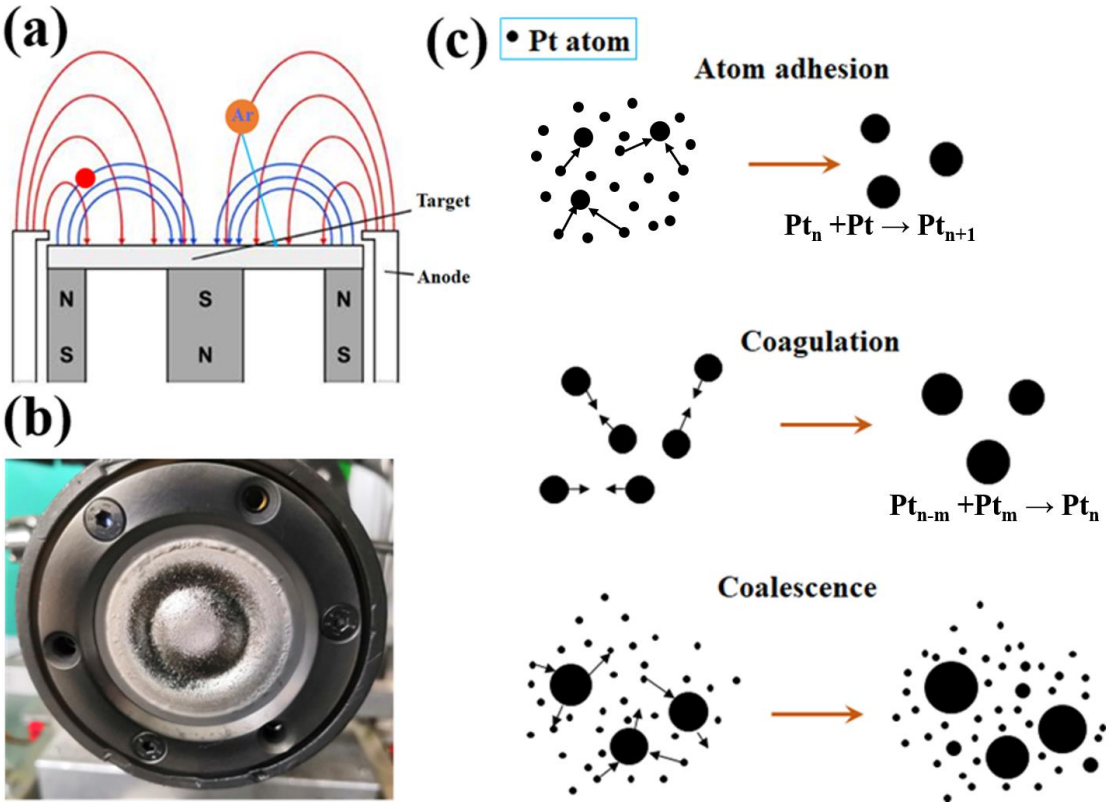


Figure 1.4.5. (a) schematics of magnetron sputtering head (orange lines: electric field lines, blue lines: magnetic induction lines); (b) photon of magnetron sputtering head with a platinum target; (c) the process of nucleation and growth of clusters. Figure (a) and (c) adapted from Ref.[63] (taking Pt atoms as an example).

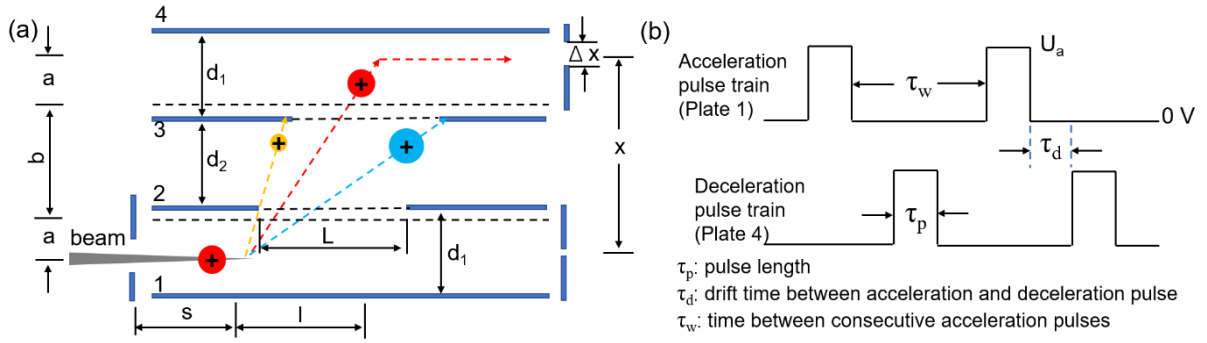


Figure 1.4.6. (a) Scheme of the mass selector (radius of circles represent the size of nanoparticles, the symbol "+" indicates positive charge and the slope of the dotted line denotes the accelerated velocity of nanoparticles); l: length of the nanoparticles displacing along the beam direction, x: vertical displacement between entrance and exit slit centres, L: the opening length of the windows on plate 2 and plate 3, Δx: the width of exit slit, a: beam offset traversed during the high voltage pulse, b: length of the field free region, d_1/d_2: plate separations, s: length of the portion of the ion beam which cannot be used as it would introduce field distortions. (b) Schematic illustration of the high voltage pulses. Figure and caption adapted from Ref.[66].

For the investigation of size dependences of nanoparticle properties, it is of crucial importance to be able to deposit nanoparticles with a narrow size distribution. Therefore, a mass selection is desirable before deposition. A lateral time-of-flight mass selector (TOF) that can select charged nanoparticles for their masses is installed in the cluster source of Birmingham (Figure 1.4.4)[66]. Figure 1.4.6 (a) shows the schematic of the mass filter described in the reference[66]. The mass filter consists of four separated plates. For choosing nanoparticles from the cluster beam, the pulsed voltages are applied on the plates to build the pulsed electric field (Figure 1.4.6(b)). The ion nanoparticles with a velocity $\boldsymbol{v_0}$ parallel to the beam direction are accelerated by the electric field between plate 1 and plate 2 perpendicular to the original beam flight direction, obtaining a velocity $\boldsymbol{v_m}$ perpendicular to the beam direction, while an opposite electric field between plate 3 and plate 4 decelerates the ion nanoparticles. By setting the same width of the time interval (τ_w) between consecutive acceleration pulses and the drift time (τ_d)

between the acceleration and deceleration pulses, the mass of selected nanoparticles is m_0 ($m_0 = \frac{qU_a}{d_1 x} \cdot \tau_p \cdot (\tau_p + \tau_d)$) by moving a displacement of x ($x = a + b + a$) as shown in Figure 1.4.6(a) to pass through the selector.

The mass selection process of the TOF is described by mathematical expressions as followings. The resulting motion of a charged (q) nanoparticle (mass=m_0) is shown in the following equations:

$$W_0 = q\left(\frac{a}{d_1} \cdot U_a\right) = q \cdot U_p \,, \tag{1-4-1}$$

where W_0 is the energy of this nanoparticle gained from the electric filed within the pulse length of τ_p, U_a is the voltage applied on the plate 1, U_p is the electric potential difference between the displacement a covered by this nanoparticle, d_1 is the distance gap between plate 1 and plate 2. Due to the uniform electric field between the plate 1 and 2, the obtained energy (W_0) of the nanoparticle also can be calculated by:

$$W_0 = \vec{F} \cdot a = (\overrightarrow{a_c} \cdot m_0) \cdot \frac{1}{2}\overrightarrow{a_c}\tau_P^2 \,, \tag{1-4-2}$$

where $\vec{F}$ is the electric field force applied on this nanoparticle and $\overrightarrow{a_c}$ is the corresponding accelerated velocity.

$$\overrightarrow{a_c} = \frac{\vec{F}}{m} = \frac{q}{m}\frac{U_a}{d_1} \tag{1-4-3}$$

Bringing eq.(1-3-3) and eq.(1-3-1) into eq. (1-3-2), a new relationship is yielded:

$$\tau_p = \frac{2a}{\sqrt{2qU_{p/m_0}}} \tag{1-4-4}$$

$$v_m = \sqrt{2qU_p \,/\, m_0} \tag{1-4-5}$$

If the nanoparticle can be filtered by the TOF, it will pass from plate 1 to plate 3. Then, it will experience deceleration between plate 3 and plate 4 due to an opposing electric field with the

same strength with the electric field between plate 1 and plate 2. Therefore, the movement distance of mass-filtered nanoparticle can be expressed as:

$\boldsymbol{x}_m = \boldsymbol{v}_m(\tau_p/2) + \boldsymbol{v}_m\tau_d + \boldsymbol{v}_m(\tau_p/2) = a + b + a = x$ (1-4-6)

where b is the length of the field free region (Figure 1.3.6a), where it takes $\tau_d = {}^{b}/_{v_m}$ to pass through. The nanoparticle with a mass m_0 can be filtered when x_m is equal with x. Given the parameters employed in the mentioned above equations, the structure size of the TOF apparatus remain constant. Hence, by modulating the signals (U_a) administered to the plates, the size of the nanoparticles that traverse the TOF can be regulated, with the mass of filtered nanoparticles being determined using equations (1-4-4) to (1-4-6):

$$m_0 = \frac{qU_a}{d_1 x} \cdot \frac{\tau_p}{\tau_p+\tau_d} \cdot \left(\tau_p + \tau_d\right)^2 = \frac{qU_a}{d_1 x} \cdot \tau_p \cdot \left(\tau_p + \tau_d\right), \quad (1\text{-}4\text{-}7)$$

where the interval time (τ_w) separating successive acceleration pulses is set to be equivalent to the drift time (τ_d) between acceleration and deceleration pulses. The eq. (1-3-7) tells that nanoparticles can be selectively deposited by adjusting the lengths of τ_p and τ_d. Meanwhile, the nanoparticle moved a distance of l_p along the initial incident direction, which is parallel to the plane of the plates.

$$l_P = \left(\tau_p + \tau_w\right) \cdot v_0 = \left(\frac{2a}{\sqrt{2qU_{p/m_0}}}\right) v_0 + (s+l), \quad (1\text{-}4\text{-}8)$$

where s represents the length of the ion beam that cannot be utilized due to field distortion, while l denotes the displacement length of the ion beam package. Obviously, the distance traversed by nanoparticles along the beam direction is proportional to the square root of their mass $\sqrt{m_0}$. If the opening length (L) of the windows on plate 2 and plate 3 is sufficiently large, nearly 100% of nanoparticles in the beam can be transferred into the region between plate 3 and

plate 4.

The transferred beam is composed of nanoparticles with varying masses. If a charged nanoparticle has a mass greater than m_0 (indicated by the blue circle in Figure 1.4.6a), it will travel a longer distance l_p along the beam direction than a nanoparticle with mass m_0. Conversely, a smaller nanoparticle (designated by yellow in the figure) will have a shorter displacement l_p along the beam direction.

For a nanoparticle with a mass m_N originated from the same beam of nanoparticle with the transmitted size m_0, the nanoparticle m_N will obtain an energy W_N from the electric field (eq. 1-4-2).

$$W_N = \frac{m_0}{m_N} \cdot W_0 \tag{1-4-9}$$

Therefore, the nanoparticle m_N will gain a velocity v_N along the electric field direction:

$$v_N = \frac{m_0}{m_N} \cdot v_m \tag{1-4-10}$$

The displacement of nanoparticle m_N perpendicular to the beam direction can be calculated as:

$$x_N = \frac{m_0}{m_N} \cdot x_m \tag{1-4-11}$$

Taking the derivative of eq. (1-3-8) with respective to the mass m, the mass resolution R can be obtained by:

$$\left.\frac{dx_N}{dm_N}\right|_{m_N=m_0} = -\frac{m_v}{m_N^2} \cdot \chi|_{m_N=m_0} = -\frac{x}{m_0} \tag{1-4-12}$$

The exit aperture with a width Δx selectively isolates a range of masses from the laterally dispersed mass distribution. The width of this mass range is determined by $R = m/\Delta m = x/\Delta x$. The lateral displacement distance in the cluster source of Birmingham is 184 mm and the mesh opening length (L) on plate 2 and plate 3 is 120 mm. The exit slit was chosen with 8 mm for

the preparation of nanoparticles in this thesis. Therefore, the theoretical value of R = 184/8 = 23.

For controlling the landing energy of nanoparticles, the bias can be applied on the substrate. In this thesis, the landing energy of as-prepared nanoparticles was set at a kinetic energy of no more than 1 eV per atom.

1.5 Scanning transmission electron microscope

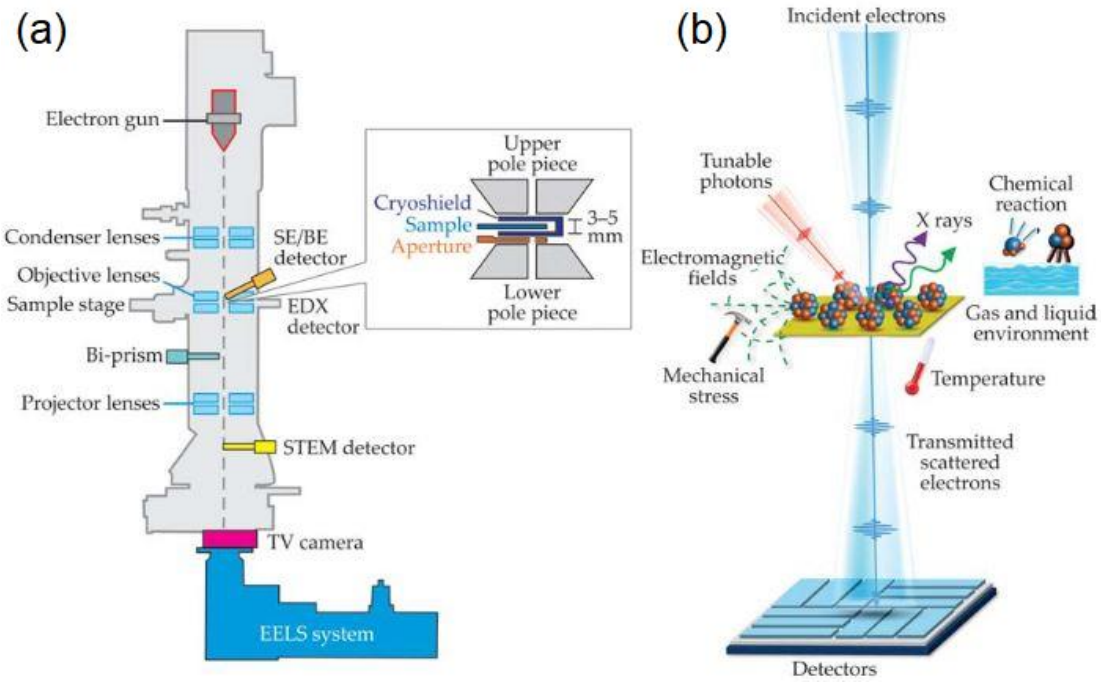


Figure 1.5.1. A schematic of a typical TEM (a) and the applications of *in-situ* microscopy for imaging and spectroscopy (b). A high-resolution analytical microscope usually is installed with detectors for collecting the energy-dispersive X-ray spectroscopy (EDX), secondary and backscattered electron (SE/BE), off-axis electron holography (bi-prism), and electron energy-loss spectroscopy (EELS). Figure and caption taken from Ref.[67].

Transmission electron microscopy (TEM), as shown in Figure 1.5.1(a), benefiting from the advantages of high-energy electrons, *e.g.* strong interaction with matter and versatile operations through the use of electromagnetic lenses, has been developed into powerful and versatile tools

to probe the information of materials at atomic scales[67]. Figure 1.5.1 illustrates the prevalent TEM techniques that have been employed in materials research from image acquisition to energy-related spectroscopy. Combining advanced sample holders and cutting-edge detectors, *in-situ* TEM techniques (Figure 1.5.1(b)) enable researchers to trace material growth and structural transformation processes during the working conditions. For the image acquisition and chemical analysis, the signals generated by the high energy beam interacting with specimen as shown in Figure 1.5.2 need to be collected and utilized effectively. For example, the characteristic X-rays and the inelastically scattered electrons, which carry characteristic energies of elements, can be used to identify the chemical information of specimen. Meanwhile, TEM and scanning TEM (STEM) images are formed by the direct beam and elastically scattered electrons.

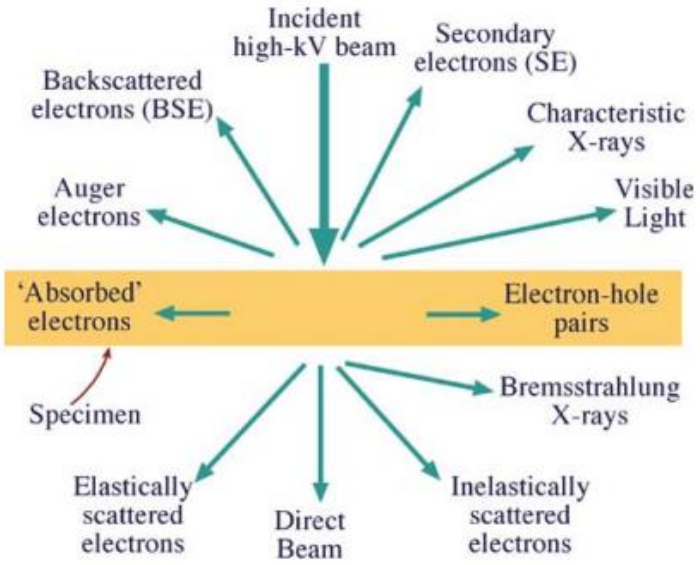


Figure 1.5.2. Signals generated by the interaction of high-energy electrons with the sample. The directions indicate the most signals. Figure and caption taken from Ref.[68].

1.5.1 Imaging in STEM mode

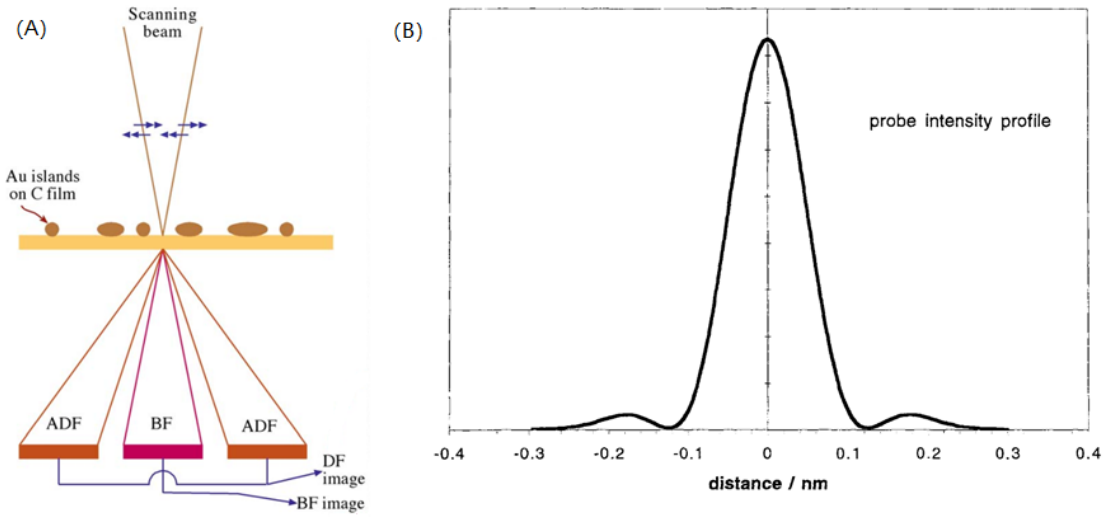


Figure 1.5.3. (A) Typical STEM mode with an annular bright field (BF) detector and an annular dark-field (ADF) detector. Figure(A) and caption taken from Ref.[68]. (B) The intensity profile of the illuminating probe at Scherzer defocus for the HB603U STEM. Figure(B) and caption taken from Ref [69].

Conventional TEM uses a parallel beam to illuminate specimen where the amplitude and phase of the electron beam are changed. The image of specimen can be created from the amplitude and phase of the electron beam. The amplitude contrast has two types, which are called mass-thickness contrast and diffraction contrast[68]. The phase-contrast image in TEM mode is built by the interference of two or more beam waves that have differential phase.

In STEM mode (Figure 1.5.3), the electron beam is converged by a condenser lens into a point to scan the samples at atomic scale. The scan beam is deflected by the atomic nuclei, taking place the Rutherford scattering. A real-space image of specimen can be assembled by summing the scattered electrons collected by an annular field detector (ADF). The image intensity ($I(\vec{R})$) is described mathematically as a convolution of a specimen ($f(\vec{R})$) with the probe amplitude distribution $P(\vec{R})$[70]: $I(\vec{R}) = f(\vec{R}) \otimes |P(\vec{R})|^2$, where $\vec{R}$ is two-dimensional position vector in real

space. For high angle ADF, the image intensity I($\vec{R}$) has a relationship with the screened Rutherford scattering Z^n (n=1.7 ~ 2)[71]. Therefore, STEM images are called as Z-contrast images. From the mathematical expression of the image intensity, it is obvious that the resolution of STEM images depends on the probe beam P($\vec{R}$), which is converged by an electromagnetic lens onto the specimen.

1.5.2 Spherical aberration of electromagnetic lens

The electromagnetic lens in STEM system, analogous with the optical lens, have many defects, such as special aberration, chromatic aberration, and astigmatism[68]. Astigmatism can be easily corrected by small octupoles named stigmators. Chromatic aberration occurs due to the different focal lengths of different energy electrons passing through a lens[72]. However, the chromatic aberration makes minor influence on the resolution of microscopy compared with the impacts of the spherical aberration. As shown in Figure 1.5.4 (a), the spherical wavefront (the electron behaves as wave) of the off-axis rays from a source *P* suffers from more strongly bending toward the axis than that of rays close to the axis. This distortion is called as spherical aberration, making the point object image as a disk in the Gaussian image plane (the image plane), blurring the details of the object and reducing the resolution of STEM.

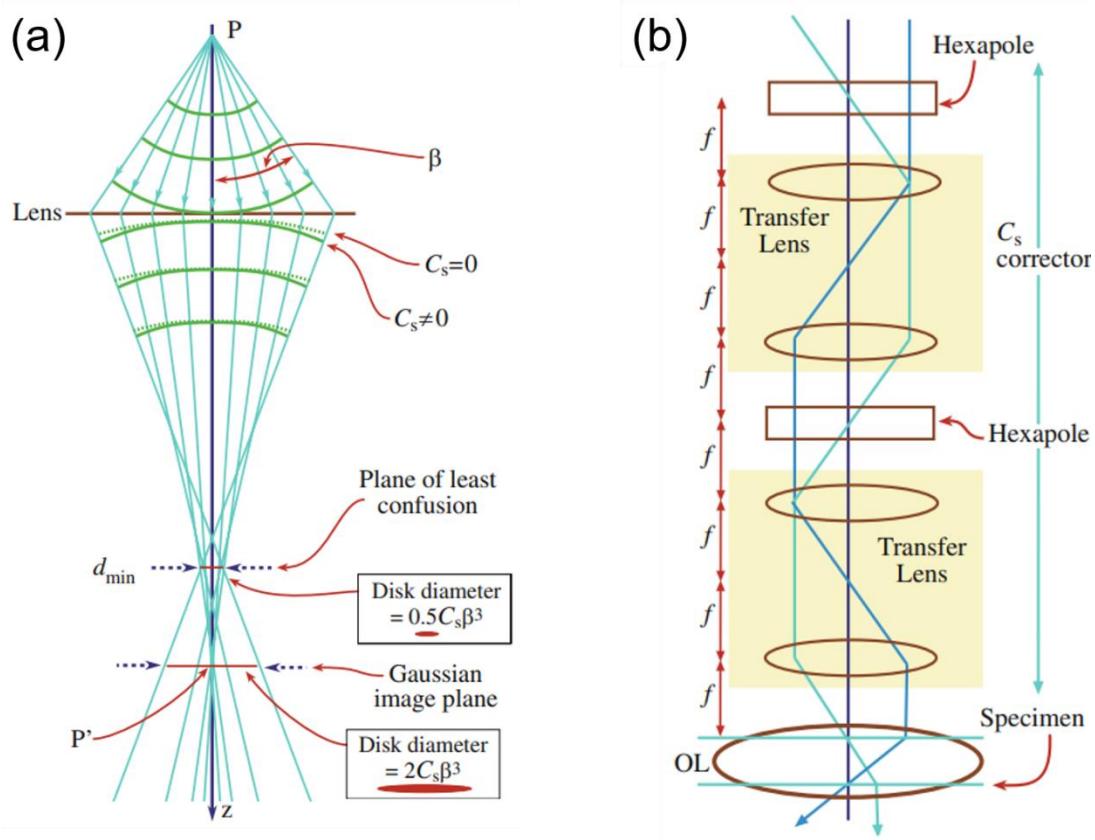


Figure 1.5.4 (a) Schematics of spherical aberration in the lens that the off-axis rays are bent more toward the axis than those close to the axis. The point object P is imaged at P' in the Gaussian-image plane. (b) Ray diagrams of a commercial Cs-corrector system (CEOS) with hexapole and two transfer round-lens doublets. Figure and caption taken from Ref.[68].

Generally, an electromagnetic lens in TEM can be regarded as an optical lens, while the specimen can be described as $f(\vec{R})$, which $\vec{\boldsymbol{R}}$ is a point in the specimen with the coordinate of (x, y). The lens, mathematically, can be expressed into a function $h(\boldsymbol{r})$, which is known as the point-spread function. Therefore, the image of the specimen can be described as $f(\vec{R})$ⓧ$h(\vec{R})$, or it can be expressed in the reciprocal space ($\vec{\boldsymbol{K}}$) of $\vec{\boldsymbol{R}}$ as $F(\vec{\boldsymbol{K}})\cdot H(\vec{\boldsymbol{K}})$ using the $F(\vec{\boldsymbol{K}})$ and $H(\vec{\boldsymbol{K}})$, which are the Fourier transforms of $f(\vec{R})$ and $h(\vec{R})$, respectively. In an STEM system, the $H(\vec{\boldsymbol{K}})$ is known as the probe amplitude distribution[69,70] $P(\vec{R}) = \int A(\vec{K})e^{i\gamma(\vec{K})}\cdot e^{i(\vec{K}\cdot\vec{R})}\,d\vec{K}$. $A(\vec{K})$ is the amplitude in the condenser lens back focal plane that $A(\vec{K})$ is equal with 1 inside the aperture

and 0 outside. $\gamma(\vec{K})$ is the condenser lens transfer function phase factor. Without a probe aberration corrector, the transfer function $\gamma(\vec{K})$ can be approximated as $\gamma = \frac{\lambda}{2}\left(\Delta f K^2 + \frac{1}{2}C_s\lambda^2K^4\right)$, where Δf is the defocus and the C_s is the lens spherical aberration coefficient. Therefore, the resolution of STEM is impacted heavily by the aberration of the lens.

For compensating the spherical aberration, the C_s-corrector is installed after the lens (condenser lens in STEM system or objective lens in TEM). Figure 1.5.4(b) shows the CEOS system built by Haider and colleagues, which consists of hexapoles and other transfer lenses[73]. The hexapole consists of six equal electrodes, which are arranged symmetrically and applied alternating voltages. There are two lenses with the same focal length (f) placed between the hexapoles as shown in Figure 1.5.4(b). These two objective lenses located at the middle of hexapoles make the first hexapole image on the second. Therefore, the primary aberrations of the first hexapole can be compensated by the second hexapole. Meanwhile, the spherical aberration C_s induced by hexapoles can be adjusted as opposite values to that of the objective lens[73,74]. By controlling the applied voltages on the hexapoles, the whole spherical aberration of the hexapoles and round lenses can be eliminated well. With the help of the spherical aberration corrector reducing the C_s of condenser lenses, the probe beam of STEM can be focused to a fine spot (e.g. around 50 pm)[75], which improves the resolution of HAADF-STEM images.

1.5.3 Spectroscopy (EELS/EDX)

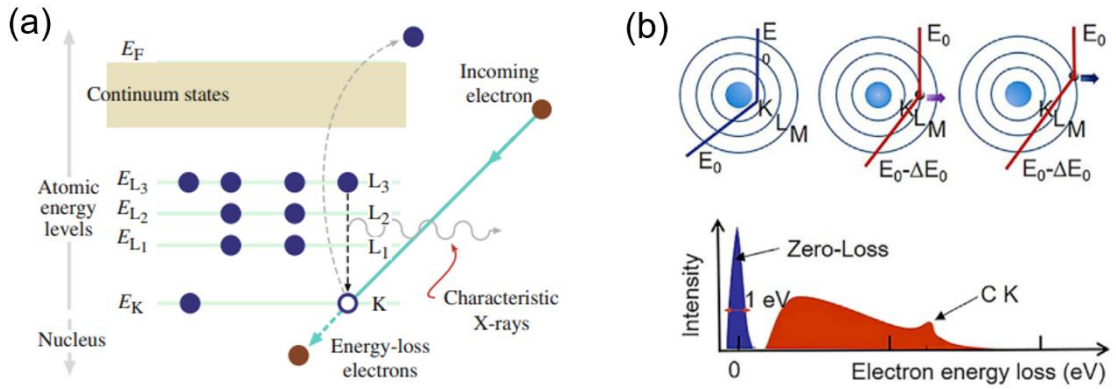


Figure 1.5.5. (a) Schematic of EDX signal generation. Figure(a) and caption taken from Ref.[68]. (b) Schematic of EELS signal generation. Figure(b) and caption adapted from Ref [76].

Various signals as shown in Figure 1.5.2 that are generated by the electron-specimen interactions can also be utilized for chemical analysis via energy-dispersive X-ray spectroscopy (EDX) and electron energy-loss spectroscopy (EELS). Figure 1.5.5 (a) shows the generation of an X-ray photon that an electron hole, created by the ejection of an inner shell electron (e.g. K shell), is occupied by an electron from an outer shell (e.g. L shell)[68]. The wavelength of the X-ray is described by Moseley's law (λ = B/(Z-C)^2, which *B* and *C* are constants and *Z* is the atomic number). Therefore, there is a specific energy (wavelength) for each characteristic X-ray line, which identifies the element. However, EDX does not work well for elements with low atomic number (*e.g.* lithium or beryllium) due to insufficient energy of their X-rays for detection or no X-ray emission because of a lack of electrons in L-shell (e.g. hydrogen or helium). What's more, the intensity of X-rays should be sufficient for detection in that the concentration of elements in the specimen should be higher than a certain level.

Table 1.1 Comparison between EDS and EELS .Table taken from Ref.[76]

	EDS in TEM	EELS in TEM
Signal-to-background ratio	high	medium or low
Thickness requirements	both thin and thick	thin
Detection efficiency	low	high
Element range	better for heavy elements	better for light elements
Specimen at high temperature	does not work	works
Energy resolution	low	high
Signal interference from TEM column and grid	yes	no
Information provided	only chemical	chemical and electronic
Ease of use	simple	complex
Ease of interpretation	simple	complex
Carbon contamination sensitive	no	yes

EELS collects electrons passing through the specimen to analyse the energy distribution, which includes energy-loss electrons and no energy-loss electrons. The energy-loss electrons carry a rich amount of information concerning the electronic structure of the specimen atoms. Analysing the EELS can reveal the valence state of specimen atoms, the nearest-neighbor atomic structure, the dielectric response, the free-electron density, and the specimen thickness[68]. A typical EEL spectrum can be separated into low-loss part and high-loss part. The low-loss (~50 eV) region includes the zero-loss peak, containing single-electron scattering (2-20 eV) and plasmon interactions (5-30 eV) with the weakly bound electrons. The high-loss (50-2000 eV) region is created by inner-shell ionizations containing the information of the tightly bound, core-shell electrons and the details about bounding and atomic distribution[68].

Table 1.1 compares EDX with EELS in the detection of elements. Firstly, EDX has better signal/noise ratio (SNR) than the EELS as EELS generally has higher background than EDX. EDX background originates from the braking irradiation in the TEM and bremsstrahlung[77],

while plasmon and multiple scattering make main contributions to the background of EELS. Secondly, EDX plays well to identify heavy elements but is impacted by the signals from the grid; while EELS works well for light elements without the influence of the grid and the fluorescence. Finally, the data analysis of the EDX is more friendly than the EELS, which requires more knowledge to extract the EELS signal from the background.

1.5.4 Data acquisition and processing in this thesis

A JEM-2100F TEM (JEOL) was used to image the nanoparticles in Chapter 2 and 3, while a FEI Titan Themis G2 (60-300 kV) TEM (Thermo Fisher Scientific) was employed for the EDS and EELS of nanoparticles and the image acquisition in Chapter 3 and 4. The JEM-2100F is equipped with a Schottky-type electron gun and a probe C_s corrector (CEOS, GmbH). It was operated with probe size 8C (the probe semi-convergence angle of 20 mrad) and beam current between 140-150 pA. The HAADF-STEM images were acquired with a collection half angle of 62-164 mrad (camera length was set to 100 mm). The Titan Themis G2 uses a X-FEG (extreme field emission gun) electron gun and a monochromator. The beam current was around 100 pA with a probe semi-convergence angle of 25 mrad. A double C_s corrector (CEOS DCOR+ for the probe correction and CEOS CETCOR for the objective lens correction) is installed for improving the spatial resolution. The camera length in Titan Themis G2 was 115 mm (48-200 mrad for the collection angle) for imaging (including acquiring EDS) and 30 mm for EELS with a collection semi-angle of 56.5 mrad. The Titan Themis G2 is also equipped with a Super-X EDS detector with 4 SDDs (Silicon Drift Detectors) and a Gatan Image Filter (GIF, Gatan

Quantum ER/965P) including the ultrafast dual EELS system. The EDS signals are analysed with the Velox software. Data captured by FEI Titan Themis G2 are specifically indicated in this thesis.

The integrated intensity of atoms can be used to describe the size of nanoparticles or the thickness of atomic column with a number of atoms[78,79]. In practice, the projected area is usually used to represent the size of nanoparticles. However, the accuracy of the projected area relies on the sharpness of the boundary recorded in the images. The merit of the integrated intensity is that it is insensitive to the conditions of microscope, such as the magnification and defocus of objective lens. But the integrated intensity calculated from images acquired from different machines cannot be compared directly due to the difference on the electron beam source and the conditions of the alignment, as well as the HAADF detector[80]. The channeling effect should be drawn attention that it amplifies the integrated intensity, which takes place when the electron beam is propagated through the specimen along with the direction parallel or close to a zone axis orientation[80,81]. In this thesis, the integrated intensity of nanoparticles will be extracted from HAADF-STEM images to measure the size of nanoparticles by a home-written script run in ImageJ.

EDX can be processed automatically by software developed by the manufacturer of the EDX detector. The elemental identification can be achieved by peak analysis of the EDS. The intense peak is contributed by X-rays from K, L, or M families, which are the fingerprints of elements. Software can identify artifact peaks such as sum peaks and escape peaks (e.g. a peak at 1.74 keV in the silicon-type detector). In contrast, the spurious peaks, such as Cu signal caused by

the backscattered electrons hitting the Cu-grid, should be excluded manually in the analysis. Small peaks, if they are missed by software, can be added manually, which they may be produced by elements with low contents in the specimen. The best way of avoiding missing elements in the specimen is to increase the counts.

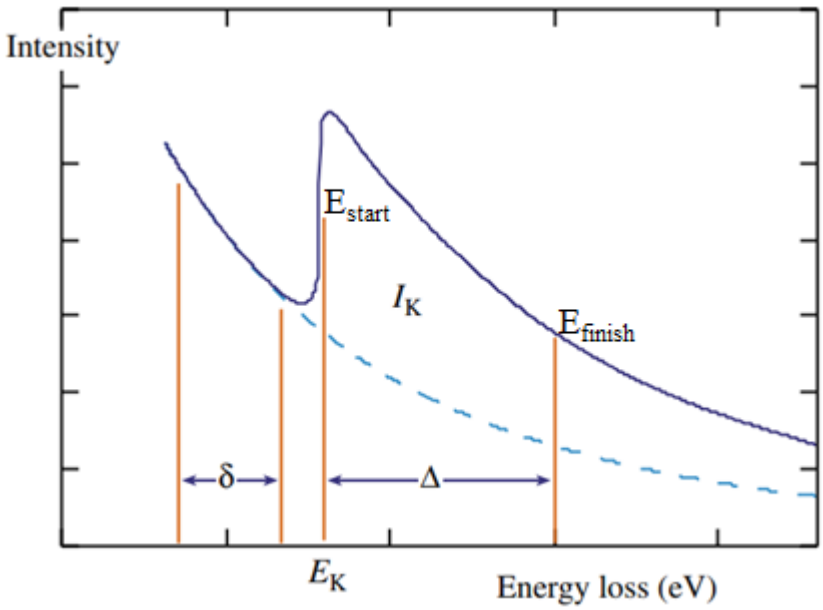


Figure 1.5.6. Schematic of high-loss edge extraction from EELS. The background is confirmed by the dotted blue line, which a pre-edge fitting window δ and a post-edge window Δ are chosen based on the energy E_K of edge to extrapolate the background. The desired edge intensity I_K is extracted by subtracting the background from the total intensity in the window Δ. Figure and caption adapted from Ref. [68].

The quantitative EDX analysis can give out the percent of each element in the specimen based on the Cliff-Lorimer equation: $C_a/C_b=k_{ab}\cdot I_a/I_b$, where C_a and C_b are the percentage of element a and b, respectively. I_a and I_b are the corresponding intensities. The k_{ab} is called as the Cliff-Lorimer factor or k-factor, which is not a constant[68]. A Super-X EDX with 4 silicon drift detectors (Thermo Fisher Scientific) was used to collect the EDX in this thesis and the k-factors are provided by the manufacturer. The background removal and peak integration of the

spectrum can be achieved using the built-in mathematical functions of the software (Velox). For improving the accuracy of the EDX analysis, the holder was kept without tilting during the counts acquisition.

The data analysis of EELS is more complicated than EDX. The main problem is how to extract the edge signals without the background. Figure 1.5.6 shows a general mathematic way to fit the background[68]. The background of a high-loss edge is assumed to have the form of $I=A\,E^{-r}$, where I is the intensity in the channel of energy loss E, and A and r are constants, which are valid over ~100 eV. For ensuring the accuracy of the background using this equation, the energy range is limited. In general, the pre-edge fitting window δ should be in the range of 10-30 % of E_k. The post-edge window Δ, shown in Figure 1.5.6, should have E(finish)/E(start) less than 1.5. There are many expressions used to fit the background, such as the power-law, the exponential, polynomial, or log-polynomial, depending on how well the expression fits the background[68]. In practice, many factors can impact the fitting results, such as the presence of another edge, poor SNR. The linear least-squares fit $\chi^2=\Sigma(y-y_i)^2/y^2$, where $y=\ln I$ and y_i is the counts at energy E_i, is used to evaluate the goodness of fit by an expression. In this thesis, the power-law approach is employed for the background subtraction.

The second step of the EEL spectrum processing is deconvolution, which can remove the single-scattering from the multiple-scattering, illustrated in Figure 1.5.7. Three deconvolution methods are built for the multiple scattering remove[68,77], namely the Fourier_Log method, the Fourier_Ratio technique, and the multiple least-squares fitting. The Fourier_Log method assumes the spectrum is a sum of individual scattering components, including the zero-loss, the

single-scattering, and the double-scattering. The background subtraction is conducted after the deconvolution in the Fourier_Log method. In contrast, the background of the spectrum is removed before doing the Fourier_Ratio deconvolution, which regards the experimental spectrum as a convolution of the ideal single-scattering spectrum with the low-loss spectrum. Multiple least-squares fitting is used for the specimen with non-uniform thickness, using convoluted reference spectra.

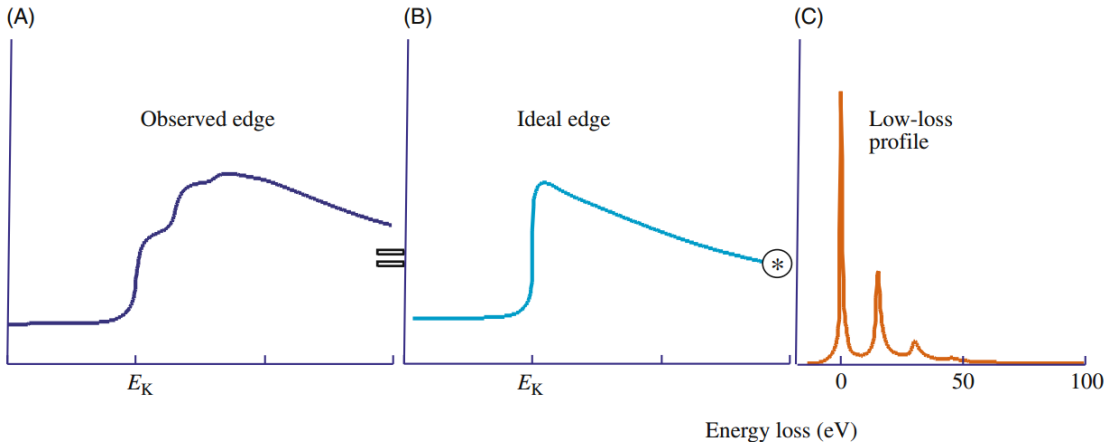


Figure 1.5.7. Schematic convolution of the observed edge. (A) The experimental ionization-edge intensity. (B) The ideal hydrogenic single-scattering ionization edge intensity. (C) The low-loss plasmon intensity profile. Figure and caption taken from Ref.[68].

To improve the accuracy and the efficiency of the EELS analysis, software has been developed, such as the SITools and Spectrum plugins run in Gatan DigitalMicrograph and the open-source Cornell Spectrum Imager[82], which provides the operations such as the background subtraction, energy drift correction, deconvolution, and the derivative the spectrum. Figure 1.5.8 shows the procedure of EELS analysis[83], which is used in this thesis for extracting the white-line (WL) of nickel, which is caused by electrons transferring from occupied 2p states to the unoccupied 3d states that the transition from $2p^{3/2}$ to $3d^{3/2}3d^{5/2}$ and $2p^{1/2}$ to $3d^{3/2}$ and creates the L_3 and L_2 lines,

respectively[77,84]. The oxidation state of nickel can be calculated from the white-line ($L_{2,3}$-edges) ratios, which is correlated with ionicity and *d*-band occupancy[85]. The L_3/L_2 ratio can be obtained by accumulating the intensity of the L_3 and L_2 peaks. The second derivative approach is used to calculate the L_3/L_2 ratio by measuring the area under the positive peaks in the second derivative raw spectrum[86]. Metallic Ni^0 has an L_3/L_2 ratio around 3.2, while the L_3/L_2 ratio of the Ni^{2+} is about 2.8-2.9, lower than that of the metallic state (Ni^0)[87].

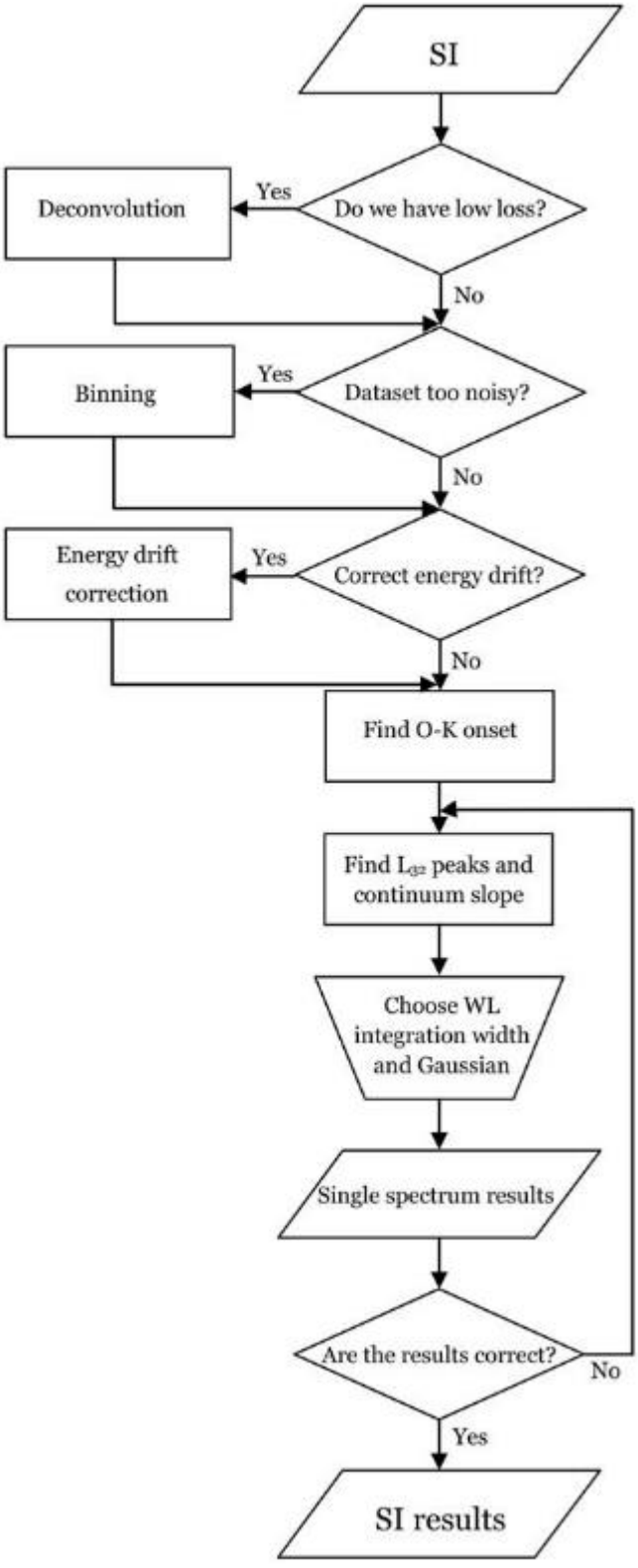


Figure 1.5.8. Flow chart of EELS analysis, stating with a spectrum image (SI) and ending in the results. Figure and caption taken from Ref.**[**83**].**

1.6 Hydrogen evolution reaction by electrocatalysis

The nanoparticles prepared in this thesis will be tested as the catalysts for the hydrogen evolution reaction (HER). HER takes place at the cathode in the electrocatalytic water splitting ($2H_2O$ (aq)→$2H_2$ (g) + O_2 (g), ΔG^0 = +237.2 kJ/mol, ΔE^0 =1.23 V *vs.* normal hydrogen electrode (NHE)), which the hydrogen proton (H^+) is reduced by obtaining electrons to form hydrogen molecules ($2H^+(aq) + 2e^- \rightarrow H_2$ (g))[88,89]. For driving the hydrogen evolution, the activation energy barrier in thermodynamics and kinetics need to be overcome. The thermodynamic potential (E_{HER}) is pH dependent, described by the Nernstian equation[89]:

$$E_{HER} = E^0_{(H_2/H^+)} - \frac{RT}{F} \times \ln\left(a_{H^+} / P_{H_2}^{1/2}\right) = -0.059 \times (PH)\ V\ vs.NHE = 0\ V\ vs.RHE \quad (1\text{-}6\text{-}1)$$

Where $E^0_{(H_2/H^+)}$ is the thermodynamic potential referenced to an NHE, T is the absolute temperature in K (298 K for the room temperature), P_{H_2} is the pressure of hydrogen in standard atmosphere, RHE is the reversible hydrogen electrode, F is faraday constant (96 485 C), R is the ideal gas constant (8.314 J/mol·K), a_{H^+} is the concentration of H^+. For the 0.5 M H_2SO_4 solution, the pH is 0; while the pH is 14 for the 1 M KOH solution in the standard state (1 atm for gases, and T = 298 K).

However, an ohmic potential and the reaction overpotential, in practice, need to be surmounted as shown in Figure 1.6.1(A). The reaction overpotential (η) is brought by the kinetic process. Charge transfer and mass transfer limitations, chemical reactions, and adsorption/desorption contribute the overpotentials. Therefore, the potential of HER should be expressed as:

$$E_i = E_{HER} + iR + \eta \quad (1\text{-}6\text{-}2)$$

Where *i* is the current in the circuit and *R* is the resistance of the circuit.

The current density of the electrochemical reaction ($2H^+(aq) + 2e^- \leftrightarrows H_2$ (g)) is the sum of current density of cathodic and anodic reactions, which can be described by the Butler-Volmer equation[90]:

$$j = j_0 \cdot \left(-e^{-\alpha nF\eta/RT} + e^{(1-\alpha)nF\eta/RT}\right) \quad (1\text{-}6\text{-}3)$$

Where *j* is the current density, j_0 is the exchange current density at the thermodynamic potential, α is the charge transfer coefficient, and *n* is the number of electrons transferred (n=1)[89].

$$\eta = \left(\frac{RT}{n \cdot F j_0}\right) j \quad (1\text{-}6\text{-}4)$$

$$\eta = -\frac{2.3RT}{\alpha nF} log\ j_0 + \frac{2.3RT}{\alpha nF} log\ j = a + b\ log\ j \quad (1\text{-}6\text{-}5)$$

for $\eta \ll 0$ (large cathodic polarization)

$$\eta = -\frac{2.3RT}{(1-\alpha)nF} log\ j_0 + \frac{2.3RT}{(1-\alpha)nF} log\ j = a + b\ log\ j \quad (1\text{-}6\text{-}6)$$

for $\eta \gg 0$ (large anodic polarization)

For the small overpotential ($|\eta| < 10$ mV) near the equilibrium states (j = 0), the equation (1-6-3) is simplified ($e^x \approx 1 + x$) as (1-6-4) that the current density is linear with the overpotential. When the overpotential is out of the equilibrium range (e.g. $|\eta|$> 10 mV), the Butler-Volmer equation can be simplified as the Tafel equation as expressed by (1-6-5) and (1-6-6), which the slope *b* is termed as the Tafel slope[89,90]. Figure 1.6.1(b) displays schematically η-*j* curves of HER that the lower onset overpotential, the lower energy needed by the reaction. The log(*j*)-η curves (Figure 1.6.1(c)) also can be drawn based on η-*j* curves that the linear part of the curve is fitted by $y=a+bx$ to calculate the Tafel slope *b* (mV/decade), which represents the overpotential increment as the current density raises 10 mA/cm^2. The overpotential and the

Tafel slope are employed to evaluate the catalysts that the lower overpotential and the smaller Tafel slope, the higher activity of catalyst in the HER (Figure 1.6.1). Generally, the overpotential for 10 mA/cm^2 is employed as the benchmark to evaluate the catalytic performance of catalysts, which 10 mA/cm^2 approximates the current density expected for a 10% efficient solar-to-fuels conversion device[91,92].

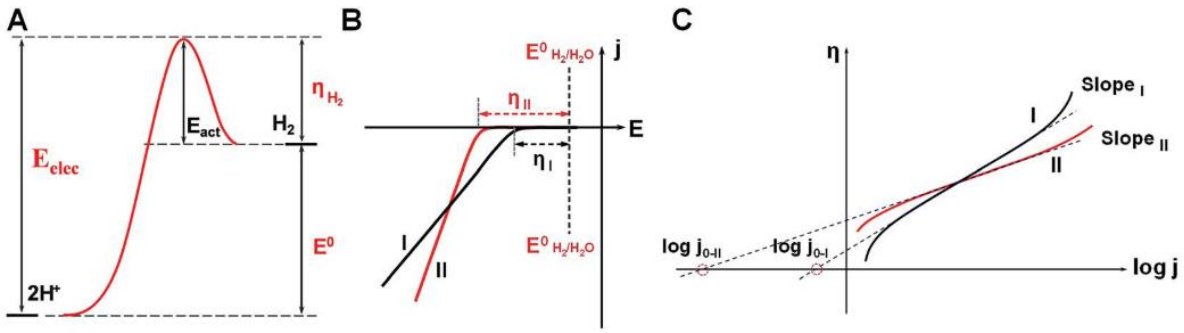


Figure 1.6.1. (A) Schematic illustration of the HER energetics. (B) Schematic HER polarization curves on different electrocatalysts with their onset overpotentials indicated. The small onset overpotential (η_I) means low voltage needed on the reaction. (C) Schematic Tafel plots on different electrocatalysts with the Tafel slopes and exchange current densities indicated. The lower slope (red) and larger exchange current density (j_{0-II}) imply higher catalytic activity. Figure and caption taken from Ref. [89].

In acidic and alkaline media, the electrocatalytic HER takes place through different electrochemical processes as shown in Figure 1.6.2. The Volmer-Heyrovsky or the Volmer-Tafel mechanism are generally accepted to describe the reaction pathways for the HER[89,90,93–95].

Volmer step: $H^+ + e^- \rightarrow H^*$ (acidic medium)

$H_2O + e^- \rightarrow H^* + OH^-$ (alkaline medium)

Heyrovsky step: $H^* + H^+ + e^- \rightarrow H_2$ (acidic medium)

$H_2O + e^- + H^* \rightarrow H_2 + OH^-$ (alkaline medium)

Tafel step: $H^* + H^* \rightarrow H_2$ (both acidic and alkaline medium)

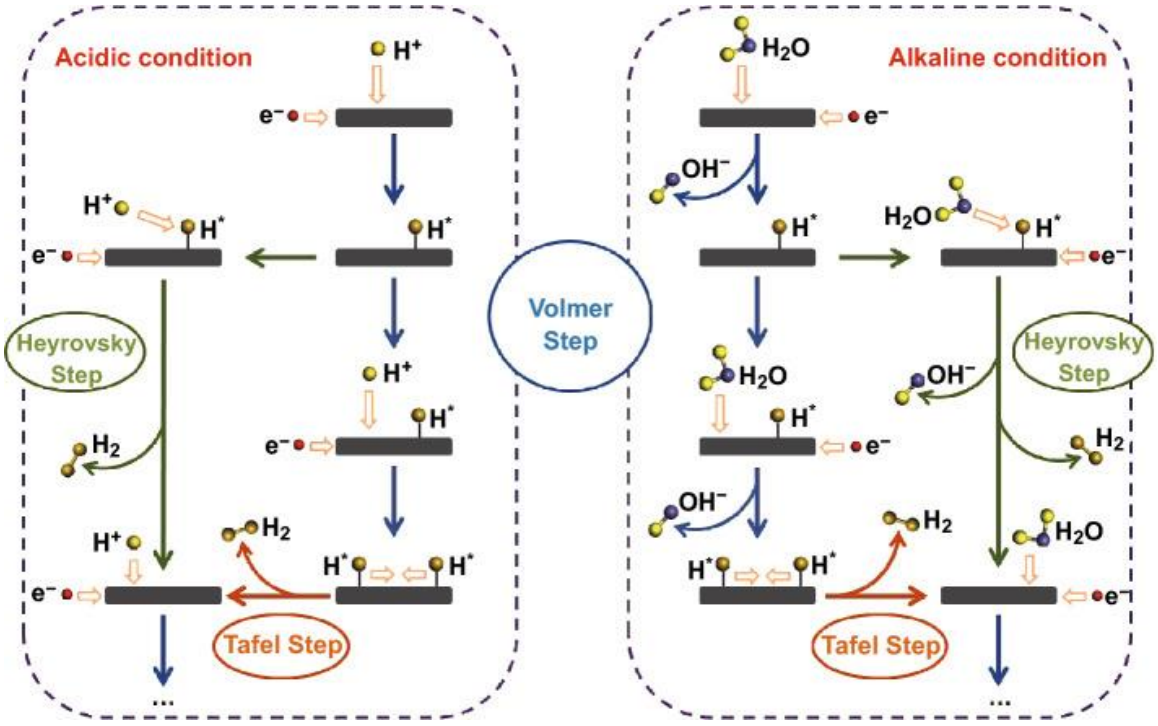


Figure 1.6.2. Schematic mechanism of hydrogen evolution on the surface of an electrode in acidic (left) and alkaline (right) solutions. (H*) is an adsorbed hydrogen atom on the catalyst surface, which * represents the active site. Figure and caption taken from Ref.[95].

Comparing with the HER in the acidic electrolyte, the HER taking place in the alkaline medium involves H_2O dissociation in the Volmer step, which is kinetically sluggish reaction, slower at least two orders of magnitude than in acidic media[93]. Although the noble-metal catalysts (e.g. Pt, Rh, Ir, Ru, and Pd)[89] show low overpotentials and small Tafel slopes in the acidic electrolyte, it is still full of challenge for catalysts to behave well in the alkaline electrolyte. As the half-cell

reaction of the electrocatalytic water splitting, it is more difficult for catalysts to perform with low overpotentials and small Tafel slopes in the OER, which involves four electrons transferring processes. More importantly, non-noble-metal-based catalysts show excellent performances on the OER, which is comparable to the precious metal electrocatalysts[96]. Considering the cost, efficiency, and the performance of electrocatalysts for the water splitting, it is worth developing the HER's catalysts working in the alkaline medium with excellent performances.

For testing the electrocatalytic performances of catalysts, an electrochemical workstation (e.g. CHI 660e or 760e) is utilized to measure the η-j polarization curves using the linear sweep voltammetry in a three-electrode system. There are commonly two types of cells: H-type electrochemical cell with a membrane and cylindrical cell without the membrane. The reference electrode should be calibrated against a Pt electrode in an H_2 saturated working electrolyte before tests. In the acidic media, an Ag/AgCl or a Hg_2SO_4 reference electrode is used; while a Hg/HgO electrode is chosen for the alkaline media. The catalysts are usually prepared into inks using Nafion as the binder and solvents (e.g. water, ethanol, isopropanol). The catalyst inks are loaded on glass carbon electrode or carbon cloth to test the catalytic performance. The ohmic potential can be compensated by testing the resistance ($E_{correction} = E - iR$) using the electrochemical impendence spectroscopy or by the electrochemical workstation[97].

This thesis focuses on the synthesis of nanoparticles with non-equilibrium structures (shapes) using magnetron-sputtering gas condensation method and the flash Joule heating method, respectively. The tetrahedral and octahedral Pt and Ni-Pt nanoparticles are fabricated for the first time in the gas-phase environment that the growth mechanism is simulated and interpreted

(Chapter 2 and 3). Ni-Pt nanoparticles can also grow into icosahedral and decahedral structures that the structural stability is evaluated by the *in-situ* heating and the evolution of Ni valence measured by the EELS (Chapter 3). Thanks to the ultrafast heating and cooling rates of the flash Joule heating synthesis, the structure of ruthenium (Ru) nanoparticles doped by Pt atoms can be controlled from the hexagonal-close-packed (HCP) structure to the face-centered cubic (FCC) structure (Chapter 4). Carbides and phosphides can also be prepared within seconds, which the stacking faults are pinned in the nanoparticles. Finally, the as-prepared nanoparticles are measured for the HER as the example of the applications (Chapter 4).

Chapter 2. Tetrahedral and octahedral nanoparticles fabrication using the magnetron-sputtering method

The magnetron-sputtering gas-condensation method can prepare naked metal nanoparticles with the sizes from single atoms to hundreds of nanometers. Convex (near-spherical) shapes, which are constructed based on the Wulff theorem, are the most common morphology in this method. The way of breaking the thermodynamic equilibrium in the growth will be presented and discussed for producing octahedral and tetrahedral nanoparticles in this chapter. The preparation conditions, such as sputtering powers, temperature, condensation zone length, and target sizes, will be investigated on the impact of the formation of nanoparticles. In this chapter, the data analysis to obtain the size distribution of nanoparticles using a custom ImageJ script is presented. Following this, octahedral and tetrahedral Pt particles, the non-spherical Pd and Ni nanoparticles will be introduced, which are all fabricated using the cluster source. Lastly, *in-situ* heating experiments will be used to investigate the structural stability of octahedral and tetrahedral Pt nanoparticles at high temperature.

2.1. Size measurement of nanoparticles using an ImageJ's script

Measuring the size of nanoparticles accurately and efficiently provides the feedback in optimization cycles for the synthesis of nanoparticles. The state-of-the-art transmission electron microscopes (TEMs) can image nanoparticles with atomic resolution. For example, STEMs with spherical aberration corrector achieve resolution up to 60 pm at 300 kV. However, it is

time-consuming to batch process the STEM images manually to extract the size information of nanoparticles and plot the distribution. The HAADF-STEM images not only give the area of nanoparticles, but also record the scattering intensity of nanoparticles that can be used to weigh nanoparticles because of the incoherent nature of HAADF technique[98,99]. An ImageJ (version 1.52p)-based script was programed for the efficiently and accurately quantitative analysis of numerous nanoparticles in single HAADF images. Compared with other programs based on MATLAB or C++[100,101], this program is user friendly with no special professional knowledge as prerequisite. What's more, the script can give out the coordinates of particles and the corresponding information, such as area, peak intensity, and integrated intensity. For extracting the integrated intensity of nanoparticles from the HAADF-STEM image, the background intensity is estimated based on the neighbor intensity, as shown in Figure 2.1.1. Two encircled curves, the inner and the outer profiles, similar with the boundary of the nanoparticle, were drawn for measuring the local background intensity. The background intensity per pixel area can be calculated by integrating the intensity between the inner and outer profiles and dividing this by the corresponding area of pixels. The integrated intensity of the nanoparticles is derived by subtracting the background intensity from the pixel intensities and summing the value within the boundary. The home-made script, using the plugin facility of ImageJ, allows users to set parameters through an interactive dialog box, such as changing the filters. By batch processing of HAADF-STEM images the integrated intensity of nanoparticles (Figure 2.1.2) and the other corresponding information, such as the area, the peak HAADF intensity and coordinates, are compiled by the program to present the size distribution in histograms (Figure 2.1.3).

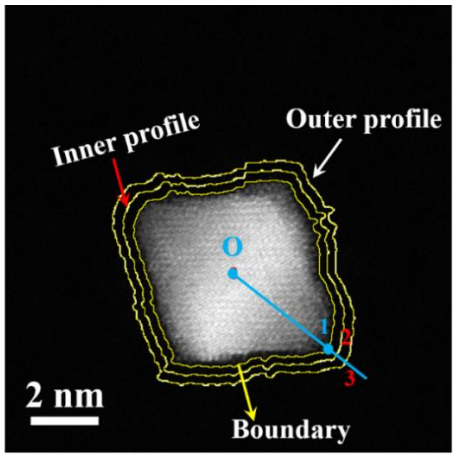


Figure 2.1.1. Example of extracting the local background intensity. Two closed curves were drawn on the outside of the nanoparticle. “O” is the geometric center of the boundary of the nanoparticle. The inner profile and the outer profile were drawn by expanding the area of the boundary with a certain factor. In the home-made ImageJ’s script, the coordinates of the boundary were multiplied by a factor (e.g. 1.1 for the inner and 1.15 for the outer) to generate the coordinates of the inner profile and the outer profile.

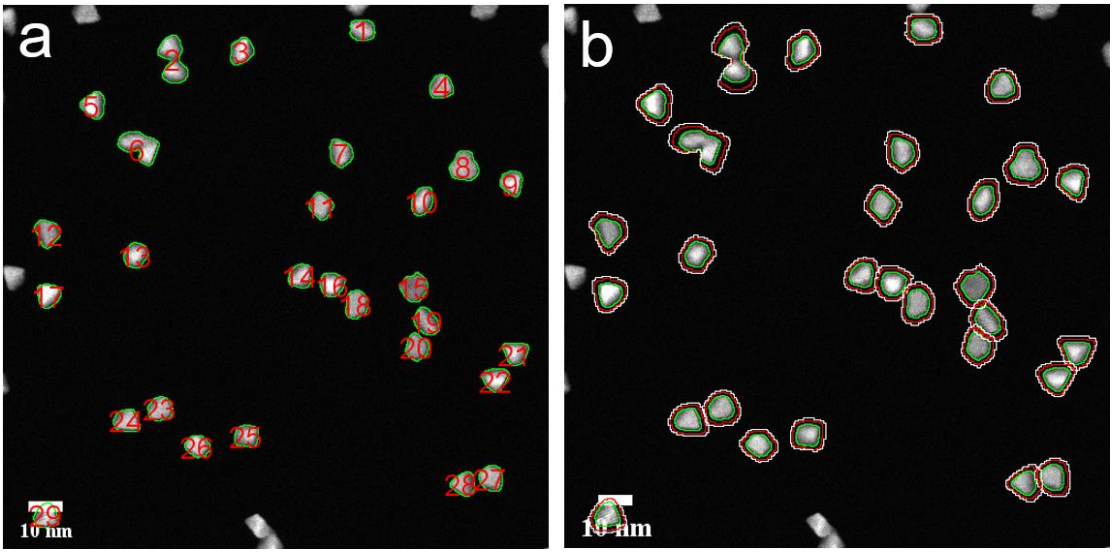


Figure 2.1.2. Batch extracting the background intensity of nanoparticles imaged with 1 M in magnification/0.307 nm per pixel. The contours of nanoparticles were drawn by green with numerical orders (a) and the local backgrounds were calculated based on the red and white curves (b).

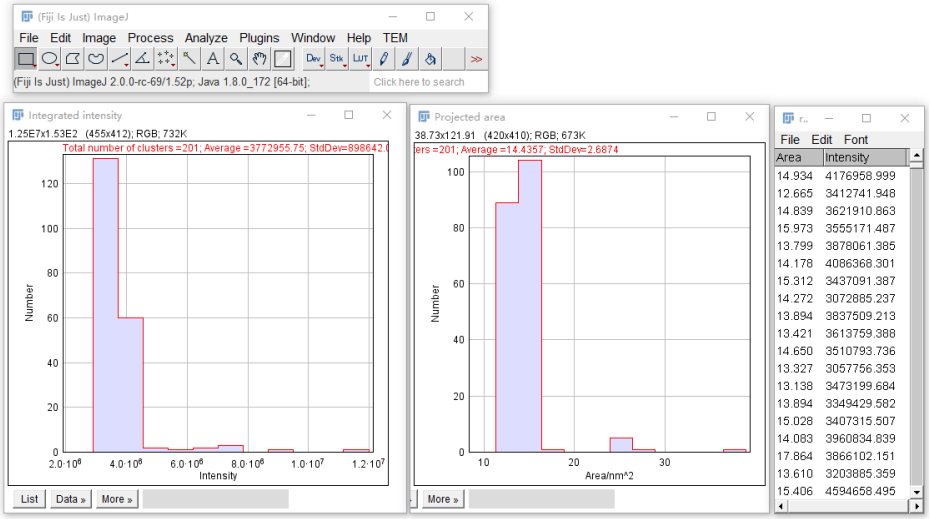


Figure 2.1.3. The interface of the program. The distributions of integrated intensity and projected area are visualised by histograms. The corresponding values are in a list.

The integrated HAADF intensity of nanoparticles was more robust than the projected area and peak intensity when the pixel size of the image and the parameters of filters are altered[102]. Figure 2.1.4(a) shows that projected areas of nanoparticles measured from the same image increased as larger standard deviation of Gaussian filter, σ, was used to blur the image for finding the boundary of nanoparticles, while the change of σ impacts slightly on the results of the HAADF intensity. Changes of imaging pixel size also have minor impact on the integrated intensity, as shown in Figure 2.1.4(b). However, the projected area drops significantly off as the magnification changing from 3M to 600k accompanying the increase of pixel sizes from 1 to 5 Å/pixel, reflecting the poor accuracy of defining the particle boundary at lower magnifications[102].

The parameters of STEM, such as convergence angle and size of the scanning probe beam, the camera length and defocus, can impact on the quality of images[80]. Using this script, the projected area, peak HAADF intensity, and integrated HAADF intensity were discussed as size

descriptors. Figure 2.1.5 illustrates the influence of defocus on the integrated HAADF intensity, peak HAADF intensity, and the projected area of Pt_{561} nanoparticles, as well as the calculated intensity (= projected area × peak intensity). HAADF images were captured by a HAADF detector with identical conditions, except for the defocus changing from -20 nm to +20 nm. A Gaussian blur filter (σ=1) and a threshold (Ostu's method) were employed for the image processing as shown in Figure 2.1.5(b, c). There were 43 Pt_{561} nanoparticles imaged successively with 3.07 Å/pixel from under-defocus to over-defocus in 4 nm defocus steps. The average of integrated intensity of 43 particles, as well as their average projected area, peak intensity, and the calculated intensity are shown in Figure 2.1.5(d). The peak intensity and projected area had broader variations of 12.5 % and 9.3 %, respectively, than 3.6% of the integrated intensity[102]. Interestingly, the calculated intensity shows less dependence on defocus with a change from -3.6% to +2.1%, much smaller than that of the peak intensity and projected area. Therefore, the integrated intensity of particles is the most robust descriptors to measure the size of nanoparticles.

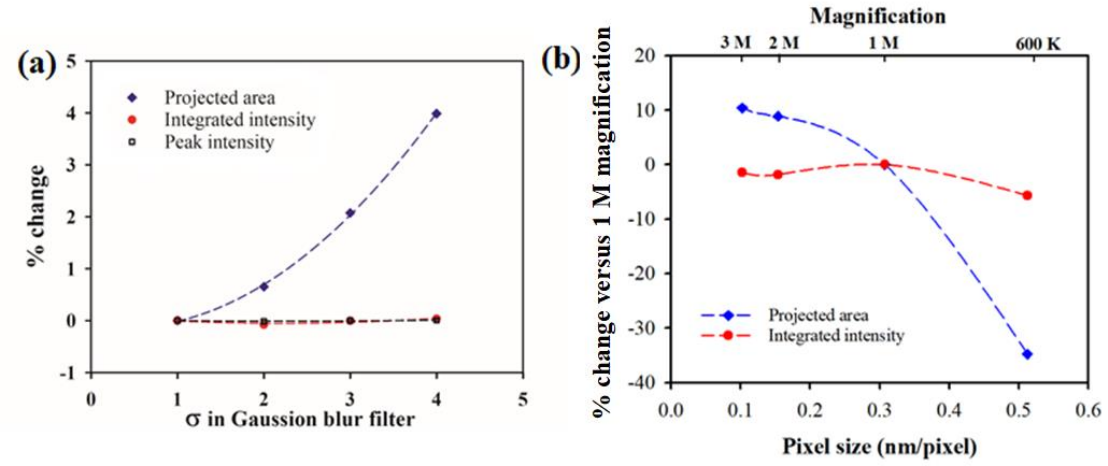


Figure.2.1.4. (a) The relationship between σ, the integrated intensity and the projection area. (b) The influence of imaging magnification and pixel size on the integrated

intensity (red points) and projected area (blue points) of Pt_{561} clusters. The dashed lines are a guide for the eye. Figure and caption taken from Ref[102].

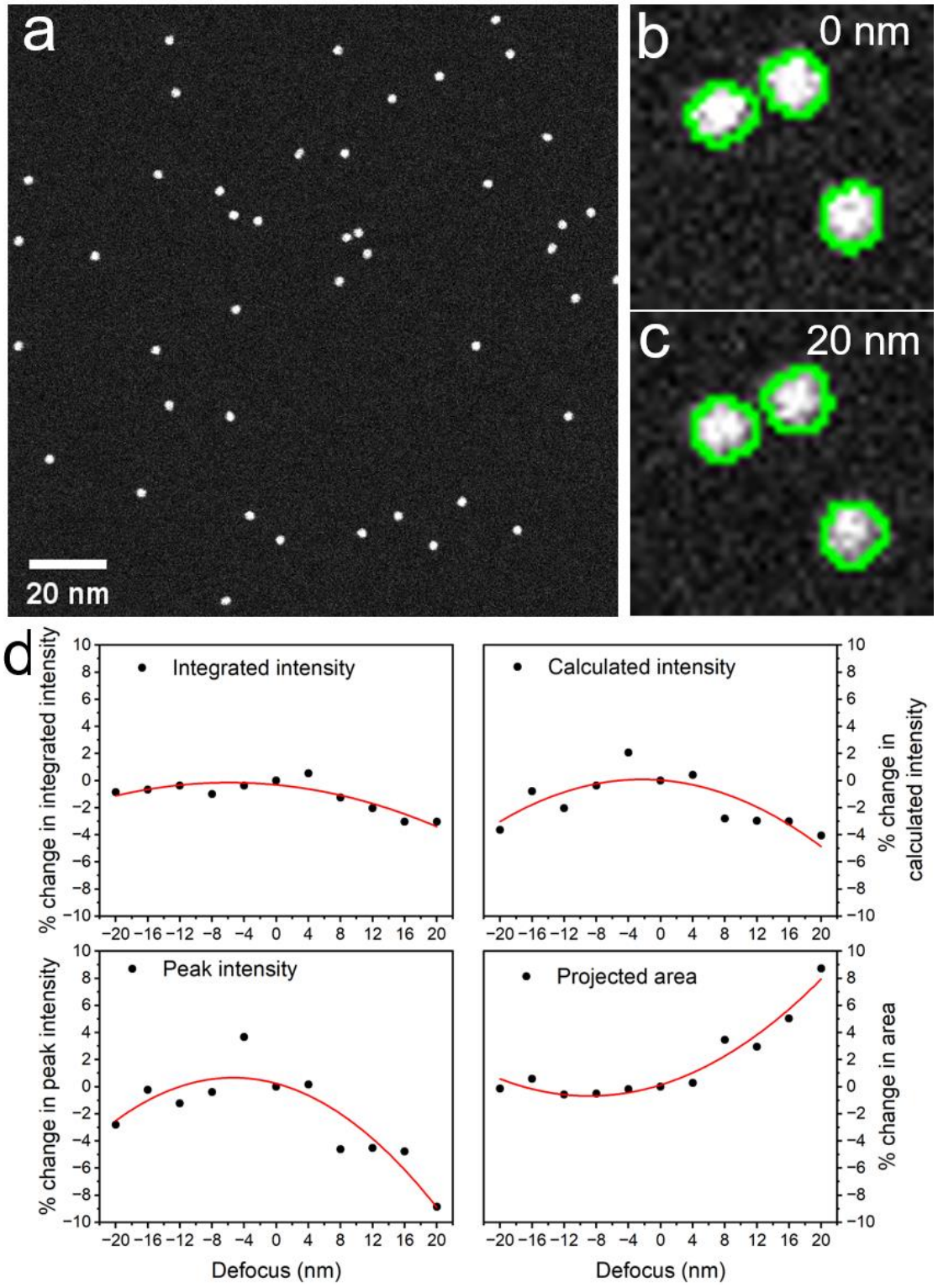


Figure.2.1.5. (a) Pt_{561} particles imaged with the magnification of 1 Mx (512×512 pixels with 0.307 nm/pixel) with defocus=0. The boundaries of clusters determined by the home-programed script: (b) image with 0 nm of defocus and image with +20 nm of

defocus. (d)The average integrated intensity, calculated intensity, peak intensity, and projected area as the defocus change for Pt_{561} clusters in (a). The dashed lines were drawn as a guide to the eye. Figure and caption adapted from Ref [102].

One of the significant applications of the integrated intensity is to measure the size of nanoparticles. Figure 2.1.6(a) depicts a strong linear correlation between the size of the nanoparticles, which were mass-selected using the TOF of the cluster source, and their mean integrated intensity. This linear relationship between the integrated intensity of nanoparticles and their sizes (number of atoms per nanoparticle) can be employed to measure the size of nanoparticles with unknown sizes. Using the same imaging conditions, the HAADF intensities of nanoparticles can be measured, and their unknown size can be determined by substituting the HAADF intensity into this linear function. Additionally, this relationship can also identify particles with different sizes, particularly those captured at low magnification. For example, 339 Pt_{561} nanoparticles were imaged with a magnification of 600k in Figure 2.1.6(b) with the corresponding integrated intensity distribution shown in a histogram in Figure 2.1.6(c). The histogram exhibits three distinct peaks and a line can fit well for the mean integrated intensity of three groups (inset in Figure 2.1.6(c)), indicating that the larger particles were agglomerated by single Pt_{561} nanoparticles. Using the coordinates provided by the script, the doublets and triplets of particles can be easily located in the original image, as shown in Figure 2.1.6(b).

Although there are many abovementioned merits of the integrated intensity as the size descriptor of particles, the demerits should be kept in mind. The HAADF intensity in the recorded images is impacted dramatically by imaging conditions, such as the contrast and brightness of the camera, the condenser lens size, the pixel dwell time[103,80]. Different HAADF

cameras have different saturation limits, which means the HAADF images of particles acquired by different machines cannot compare the size by the integrated intensity. In contrast, the projected area of particles is more universal. Therefore, the projected area is used to describe the size of particles in the following parts.

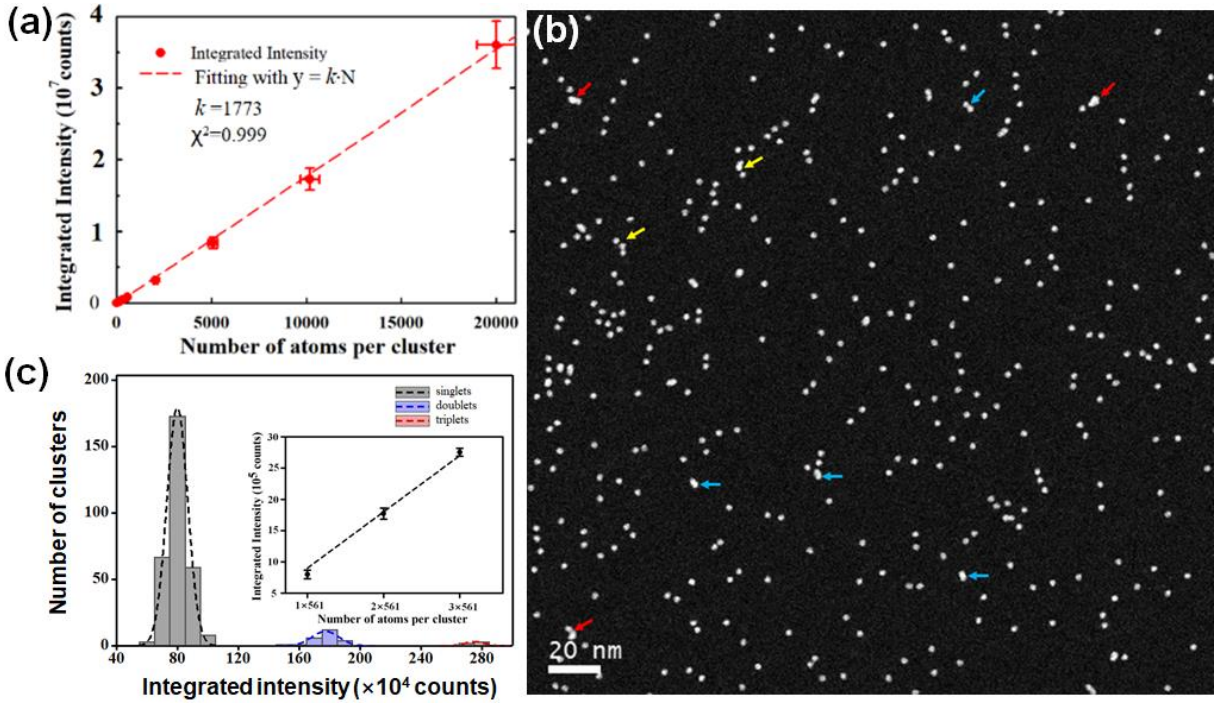


Figure.2.1.6. Mean integrated intensity as a function of cluster size in the range from Pt_{147} to Pt_{20000}. (a)The mass resolution of the time-of-flight filter gives the *x*-axis error bars (±5% of the number of atoms in the clusters) and the standard deviations from Gaussian distribution analysis were used to represent the *y*-axis error bars for the integrated intensity. (b) Pt_{561} clusters imaged by 600k in magnification. (c) Histogram of integrated intensity of Pt_{561} clusters in (b) was displayed and three sizes of clusters were distinguished by the integrated intensity. The inset plot displays the relationship between the size of clusters and integrated intensity. Figure and caption adapted from Ref.[102].

2.2. Preparation conditions of nanoparticles using the cluster source

Magnetron sputtering is utilized as the source of clusters. Operating parameters include the temperature, residence time, atomic vapours in the chamber, and the energy of sputtered atoms, etc., which are interrelated and have significant impacts on the size distribution and the morphology of particles[104,65,55]. This chapter will be discussed in detail about the influences of these conditions on the formation of nanoparticles.

2.2.1. Sputtering power

The sputtering yield is defined as the ratio of the number of atoms removed from the target to the number of ions incident onto the target. When the energy (E) of incident ions surpasses the threshold energy (E_{th}) of sputtering, the sputtering power directly affects the sputtering yield of target[105], which is proportional to $\left[1-(E_{th}\ /\ E)^{1/2}\right]$. When Ar^+ ions were used as bombarding ions, the platinum target and nickel target exhibited threshold energies of 21.23 eV and 20.88 eV, respectively. Hence, under the same sputtering environment (e.g. gas flow rate), elevating the sputtering power can not only augment the incidence of ions bombarding the target but also enhance the sputtering yield, thereby generating a greater number of sputtered atoms. Figure 2.2.1 shows the images of Pt nanoparticles fabricated using sputtering powers of 10 W, 30 W, and 75 W, respectively, with the same Ar gas flow rate (90 sccm). The target was cooled by flowing water, ensuring that the target does not melt and the magnet does not loose magnetization due to high temperature. The population of small clusters dropped visibly as the

discharge power was increased. Based on the size distribution (Figure 2.2.1) of Pt nanoparticles measured using the home-made ImageJ script, small clusters accounted for the majority in the sample prepared with 10 W. In contrast, few small clusters were observed in the sample prepared with 75 W. The particle size distribution (PSD) became narrower as sputtering powers increased from 10 W to 75 W with the full width at half maximum (FWHM) decreasing from about 8 nm at 30 W to around 6 nm at 75 W, indicating high sputtering powers can improve the utilization of sputtered atoms.

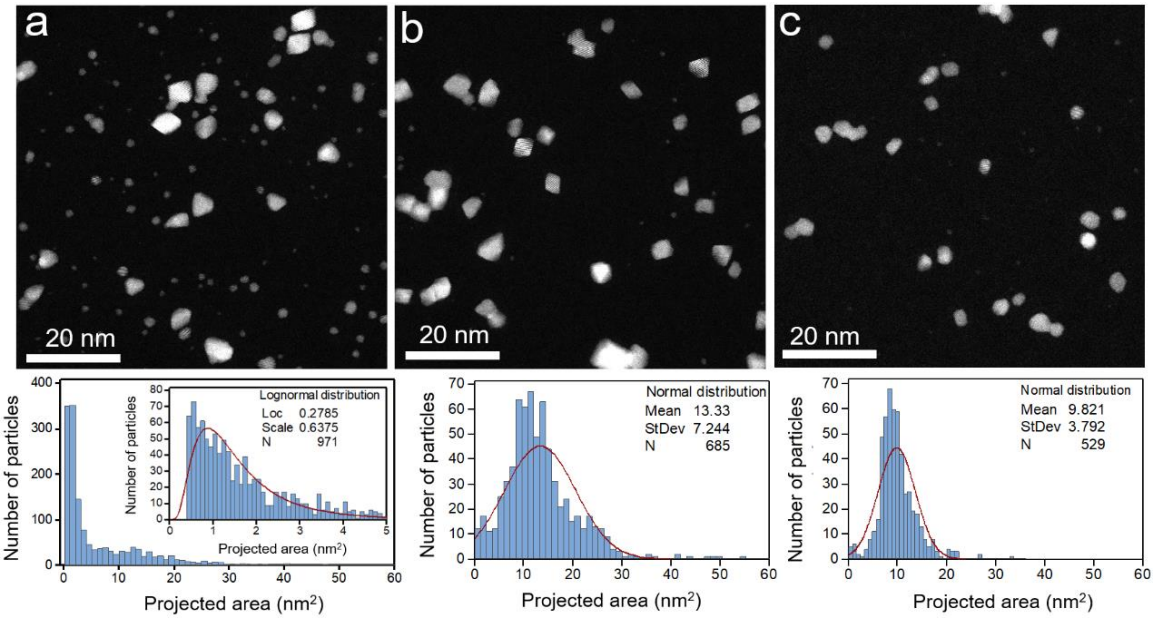


Figure 2.2.1. Pt nanoparticles prepared with the sputtering power of 10 W (a), 30 W (b), and 75 W(c) at the room temperature with an argon flow rate of 90 sccm (around 0.3 mbar) and an aggregation zone length of 25cm. The nanoparticle was collected behind the nozzle of the condensation chamber. As the increase of powers, the size distribution of particles changes from a lognormal mode to a normal mode. All samples were collected with the same deposition time (about 1 s).

The phenomenon of strong sputtering powers yielding narrower size distributions is universally observed independent of those gas flow rate. For example, the similar feature of size distributions of Pt nanoparticles prepared with 10 W, 40 W, and 75 W with the argon gas flow

rate of 150 sccm. Figure 2.2.2 presents the mass spectra collected using the lateral TOF mass filter installed in the cluster source. The peak of the mass spectra moved from about Pt_{700} at 10 W to about Pt_{3000} at 40 W and 75 W. A narrower volcano-curve obtained at 75 W than the counterpart of 40 W suggests the high sputter power (75W) can steer the size distribution of Pt nanoparticles toward the small range. The growth rate ($\frac{dN(t)}{dt}$) of Pt nanoparticles (N(t): number of atoms in a given nanoparticle at time, growing with time t) can be evaluated by the classical nucleation theory, which is expressed by[24,106]:

$$\frac{dN(t)}{dt} = \pi r^2 \left(\rho_{Pt} - \frac{N(t)}{V}\right)\left(\frac{3k_B T_{Pt}}{m_{Pt}}\right)^{1/2} \quad , \tag{2-2-1}$$

$$\rho_{Pt} = \frac{Y_{Pt} I_d / e^-}{\phi_G P_{at} / P_G} \quad , \tag{2-2-2}$$

where the physical meanings of parameters appeared in the above equations are: the radius (r) of the Pt nanoparticle, the number density (ρ_{Pt}) of sputtered Pt atoms, the volume (V) of the sputtered atoms filled in space, the temperature (T_{Pt}) of Pt nanoparticle, the mass (m_{Pt}) of Pt atom, the Pt sputtering yield (Y_{Pt}), the dc current (I_d), the gas flow rate ($\emptyset_G$), the working gas pressure (P_G) and the atmospheric pressure (P_{at}) in the chamber. According to equations (2-2-1) and (2-2-2), an increase in sputtering power can improve the number density of sputtered atoms, which will induce larger sizes of Pt nanoparticles. However, the atmospheric pressure (P_{at}) is also impacted by sputtering power, which the number density of sputtered Pt atoms cannot be continually enhanced as the sputtering power increases. Furthermore, a higher sputtering power restrains the plasma in a narrower zone that leads to a narrower size distribution of nanoparticles[107]. As a result, the mass spectrum of Pt nanoparticles produced at 75 W exhibited a narrower distribution compared to those produced at 40 W.

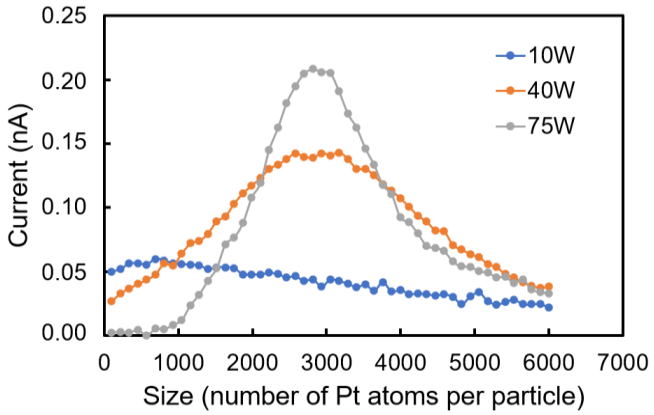


Figure 2.2.2. Mass spectra of Pt nanoparticles, which were prepared at the room temperature by 10 W, 40 W, and 75 W of the sputtering power as the condensation length (25 cm), Ar gas flow rate (150 sccm) and the pressure of the chamber (0.4 mbar) were kept the same.

2.2.2. Condensation zone length

The sputtered atoms from the targets exhibit collisions with cooling gas, forming nucleus and clusters, which grow into large particles by adding free atoms and clusters through random collisions in the sputtering/aggregation chamber[104,63]. This growth process terminates immediately after the particles are carried out the aggregation chamber. Therefore, the condensation zone length, which is the distance from targets to the exit of the aggregation chamber and informs the dwell time of particles in the aggregation chamber, affects the growth of particles. The chamber was not cooled for eliminating the influence of inert gas on the condensation of sputtered atoms. Figure 2.2.3 shows the images of Pt nanoparticles prepared with condensation lengths of 10 cm and 25 cm, respectively. Plenty of clusters were observed in Figure 2.2.3(a), while few of clusters was captured in the sample with a condensation length of 25 cm, indicating that short condensation length is a disadvantage of the growth of particles.

Figure 2.2.3(c) gives the size distribution of Pt nanoparticles with a condensation length of 10 cm, which the most of particles show less than 1 nm in diameter. In contrast, a longer condensation length (25 cm) enables the clusters to grow with a narrow normal size distribution (Figure 2.2.1(c)).

The lateral TOF also can detect the population of clusters formed in the chamber, as shown in Figure 2.2.4, in which the current in the mass spectrum represents the number of positive charged clusters/particles exiting the lateral TOF mass filter.[108] With the increase of condensation length, the spectra became more narrow, indicating the focus on the size distribution of particles.

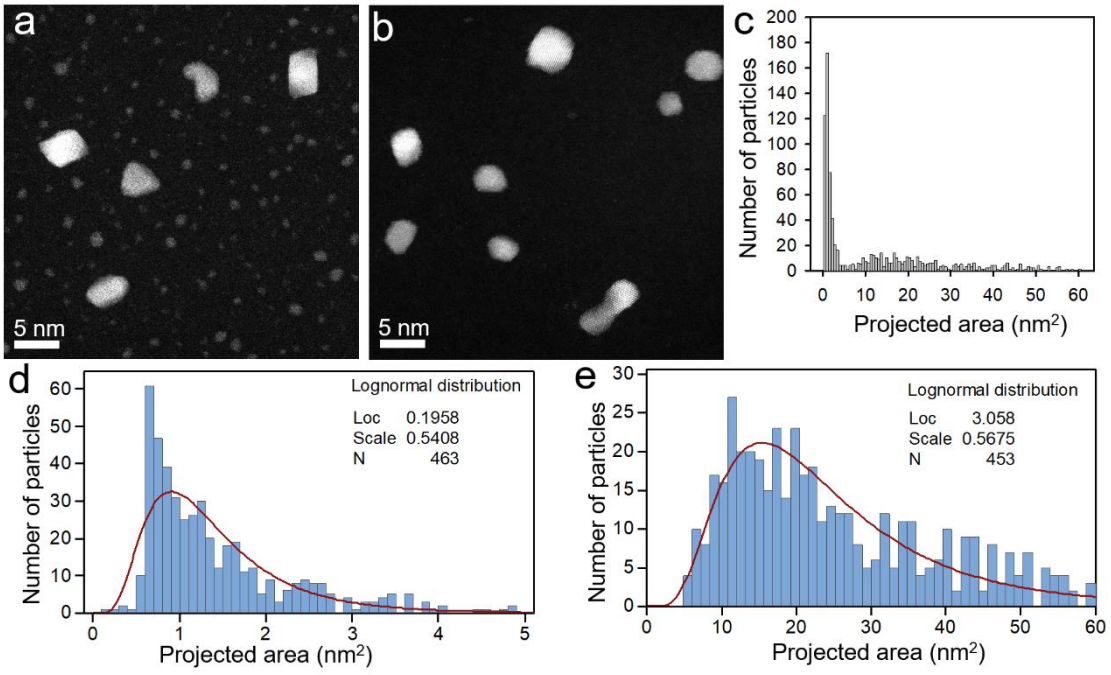


Figure 2.2.3. Pt nanoparticles grown at room temperature with the condensation length at (a) 10 cm and (b) 25 cm; (c) Projected area distribution of particles with a condensation length of 10 cm, which there are two peaks distributed in the range of 0-5 nm^2 (d) and 5-60 nm^2 (e). Log-normal distributions can fit well for particles with a size range of 0-5 nm^2 (d) and 5-60 nm^2 (e). Other parameters included: Ar gas: 90 sccm, pressure in the chamber: 0.38 mbar, the sputtering power: 75 W.

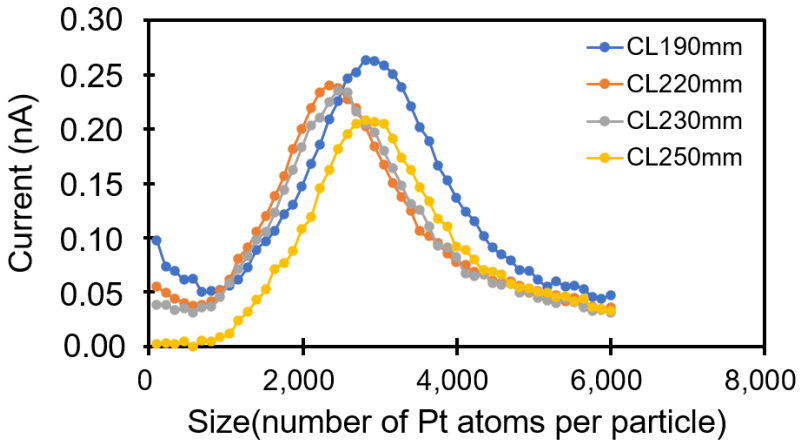


Figure 2.2.4. Mass spectra of Pt nanoparticles, which the preparation conditions were kept the same except the condensation length changing from 19 cm to 25 cm. (Ar gas: 90 sccm, pressure in the chamber: 0.38 mbar, the sputtering power: 75 W)

2.2.3. Gas flow rates (pressure)

Ar gas plays two roles in the growth of nanoparticles: igniting and sustaining the plasma and condensing the sputtered atoms (collisional thermostat). An example of Ar gas flow rates impacting the size distribution of Pt nanoparticles is displayed in Figure 2.2.5. For a given mass distribution f(m) in the beam, the measured current is I(m)=constant×f(m)×T(m), where T(m), the transmission of the mass filter, is proportional to the mass (m) of nanoparticles. Thus, the f(m) is proportional to $\frac{I(m)}{m}$, which became broader as the flow rate was increased. In detail, the peak position of mass spectra increased from less than 1500 atoms per particle to around 3000 atoms per particle, where the gas flow rate was increased from 60 sccm to 200 sccm. An inset image shows the magnified region of Figure 2.2.5(b), where the high value of current/mass suggests the high population of small sizes (less than 500 Pt atoms per cluster). The integration of current/mass is used to represent the number of nanoparticles (Figure 2.2.5(c)), while Figure 2.2.5(d) shows the FWHMs and the peak values of the curves of current/mass. As the Ar gas

flow rate increases from 60 sccm to 120 sccm, both the number of nanoparticles and the FWHM rise. Meanwhile, the beam current reached a maximum when the gas flow rate was 120 sccm, suggesting that 120 sccm was the best condition for the formation of particles with a size of 2500 atoms. As the gas flow rate increased from 120 sccm to 200 sccm, the beam current and the area under the current/mass (Figure 2.2.5(d)) dropped continuously, indicating the decrease of the total number of the formed particles.

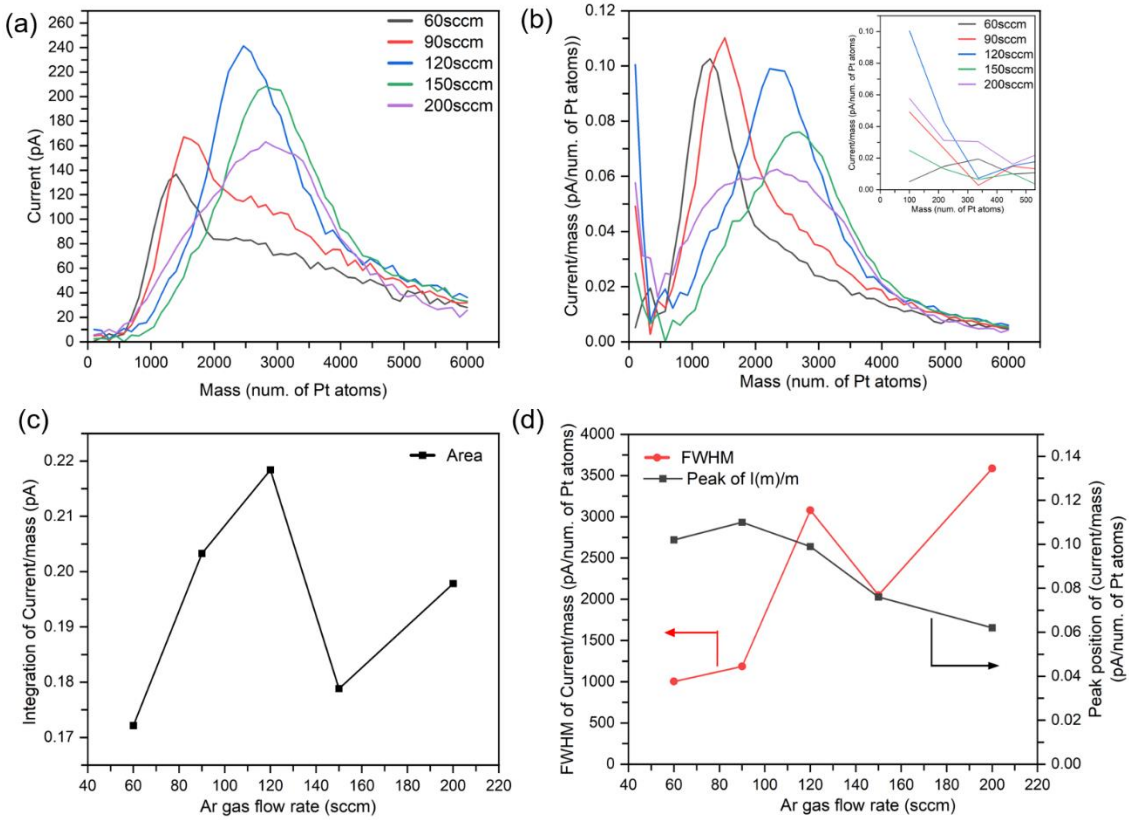


Figure 2.2.5. (a) Mass spectra of Pt nanoparticles prepared with different argon gas flow rates. (b) Impacts of argon gas flow rates on the beam currents and the size of particles at the peak of mass spectra. (c) Areas under the mass spectra, which indicates the total number of particles formed in the chamber.

The size changes of nanoparticles were observed through the STEM images with Ar gas flow rates of 90 sccm, 120 sccm, and 200 sccm, respectively, during the preparation of Pt particles

that were collected behind the nozzle. Figure 2.2.6 shows the HAADF-STEM images of as-prepared Pt nanoparticles, which the population of Pt clusters increased markedly as the increase of Ar flow rates, indicating that the higher gas flow rate builds more clusters, but the number of large particles drop.

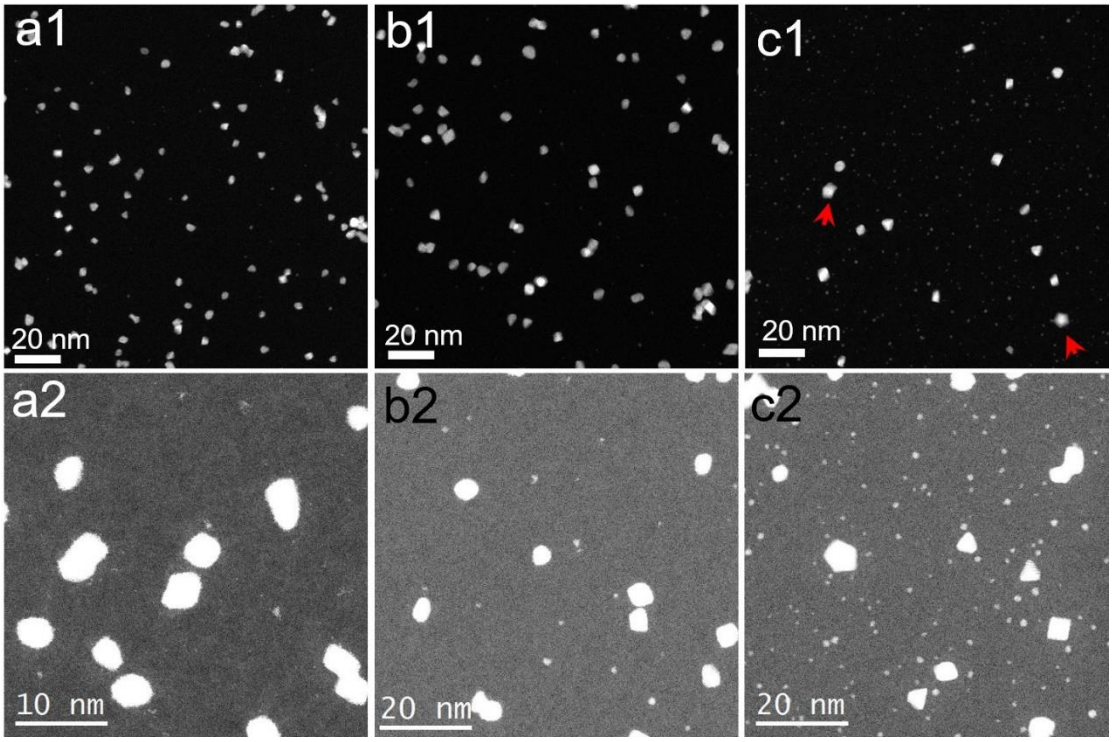


Figure 2.2.6. Impact of gas flow rate (pressure of the chamber) on the formation of Pt particles. (a1-a2) 90 sccm (0.26 mbar); (b1-b2) 120 sccm (0.38 mbar); (c1-c2) 200 sccm (0.50 mbar). Only argon gas was introduced for the particle growth.

It is interesting that decahedra marked by red arrows in Figure 2.2.6(c1) were easily observed in the sample prepared with the Ar gas flow rate of 200 sccm. A normal decahedron consists of five tetrahedra by sharing {111} planes with five twin boundaries as shown in Figure 2.2.7(f), exposing ten {111} facets. There is another decahedral-type, as shown in Figure 2.2.7(d) and (e) with five more faces ({200} facets shown in Figure 2.2.7(e)) than the normal decahedron. The existence of decahedra in the 200 sccm image suggests that the formation of decahedra can

benefit from the high Ar gas flow rates (e.g. 200 sccm), inducing the out-of-equilibrium growth of Pt nanoparticles from a FCC structure to a decahedral shape. The Wulff construction in combination with calculations predicts that a truncated octahedron is the lowest-energy shape for FCC crystals compared to decahedra[109]. Additionally, molecular dynamics simulations predict the structural transformation of small Pt decahedral nanoparticles (887 and 1389-atom) to the FCC structure under high-temperature annealing[110]. Few Pt decahedra observed in other Ar gas flow rates indicates that decahedra are less preferable compared to truncated octahedra. Theoretically, the modified Wulff construction[19] attributes the formation of Pt decahedra to the presence of internal strain caused by twin boundaries, which can reduce the total free energy of Pt nanoparticles. Thus, the growth of Pt decahedra occurs through an out-of-equilibrium pathway, whereas truncated octahedra grow along an equilibrium path. These two growth pathways can be differentiated based on the population of decahedra and truncated octahedra from STEM images of prepared nanoparticles.

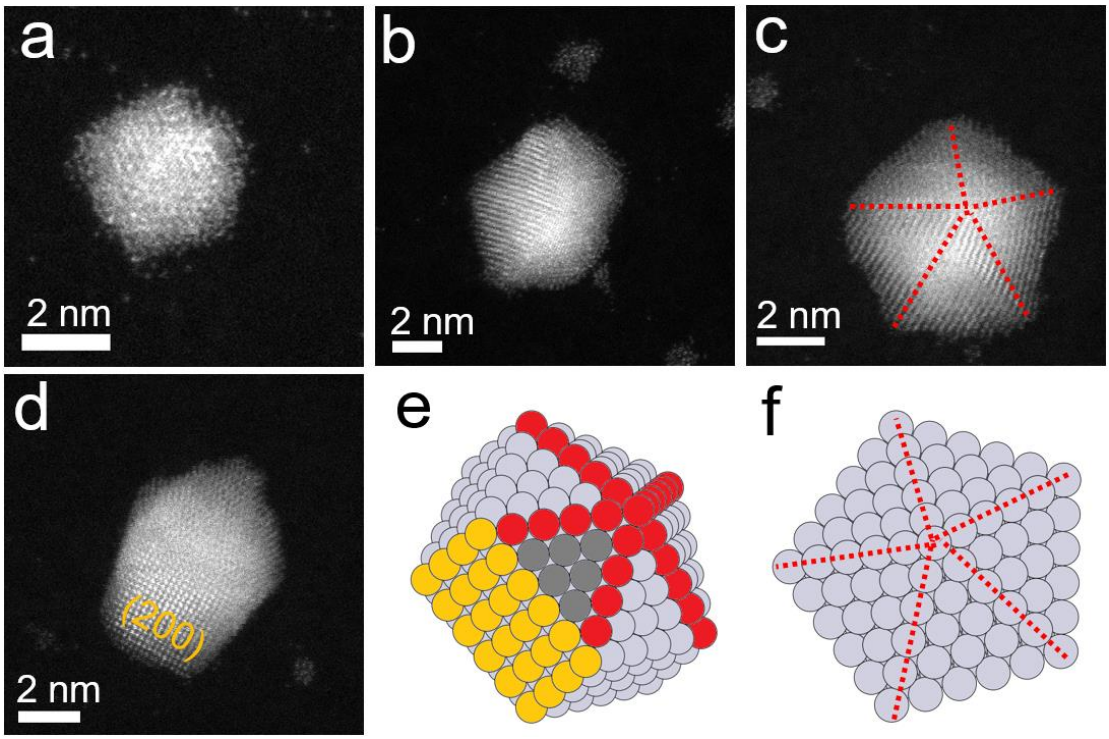


Figure 2.2.7. Decahedra with different sizes prepared at room temperature by the argon flow rate of 200 sccm (0.5mbar in the chamber) and a sputtering power of 75 W (1-inch). The condensation length was 25 cm. (a-c) decahedron without (200) facets; (d)decahedron with 5 (200) facets; (e) A decahedral model with (200) facets, which one of (200) facets was labeled by yellow; (f) An atomic model of decahedron without (200) facets.

2.2.4. Influence of temperature on the growth of particles

The cylindrical sputtering chamber can be cooled by flowing liquid nitrogen (LN_2) in the shroud, colored by blue in Figure 2.2.8(a). For investigating the influence of the temperature on the formation of nanoparticles, the temperature in the chamber was measured using four thermocouples located as shown in Figure 2.2.8(a). An example set of measurements is shown in Figure 2.2.8(b). The measurement point 3 touches the interior wall of the chamber showing the lowest temperature of -140 ℃. In contrast, the highest temperature was measured at point 4 with -17 ℃ which suggests a temperature gradient was built by the gas molecules in the

chamber through exchanging the heat with the wall. The mass spectra (Figure 2.2.8(c)) were recorded through different time-scales of the cooling. It was found that the peak of the mass spectrum moved to small sizes after the chamber was cooled by LN_2 for 5 hours that the temperature of the walls reached -140 ℃. It was confirmed by the HAADF-STEM images (Figure 2.2.9) of Pt nanoparticles collected directly after the nozzle.

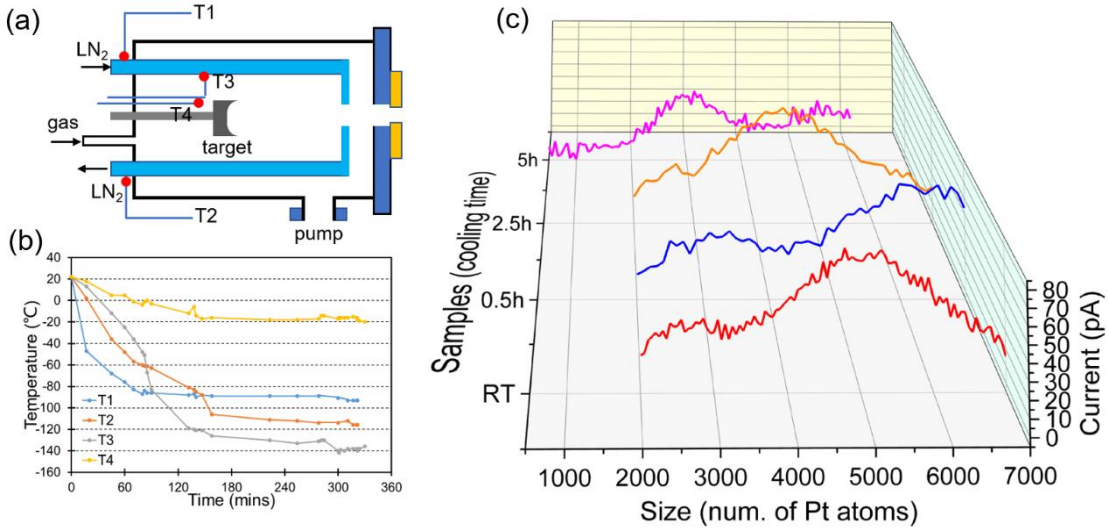


Figure 2.2.8. Influences of the chamber wall's temperature on the morphology of nanoparticles. (a) Location of thermocouples (T1-T4) for the temperature measurement. (b)Temperatures measured by thermocouples versus cooling time. (c) Mass spectra recorded with an argon gas flow rate of 200 sccm and a sputtering power of 75 W for a one-inch Pt target. As the cooling time increases, the peak of spectra moves to small sizes.

The projected areas of the particles were extracted using the home-made script running in the ImageJ, using the same parameters for all HAADF-STEM images. The area distributions are presented in histograms in Figure 2.2.10. There were about 68% of small clusters, whose projected area was smaller than 5 nm^2 (the corresponding diameter was less than 2.5 nm), observed in the sample (Figure 2.2.9(a-c)) prepared at the room temperature, less than that of the sample (Figure 2.2.9(d-f)) prepared in the cooled chamber, where over 81% of small clusters

were produced. It suggests that a low gas temperature can produce more clusters rather than large particles. Apart from the small clusters, the large particles in these two samples demonstrate different size distributions as shown in Figure 2.2.10 (c,d). The particles formed at room temperature show a normal distribution, which the mean projected area was around 25.6 nm^2; while the sizes of particles grown in the cooled chamber can be fitted well by a lognormal distribution[111] with a mean area of $e^{2.489}$=12.1 nm^2. It indicates the low growing temperature caused by the cooled chamber leads to the aggregation of particles in the growing chamber.

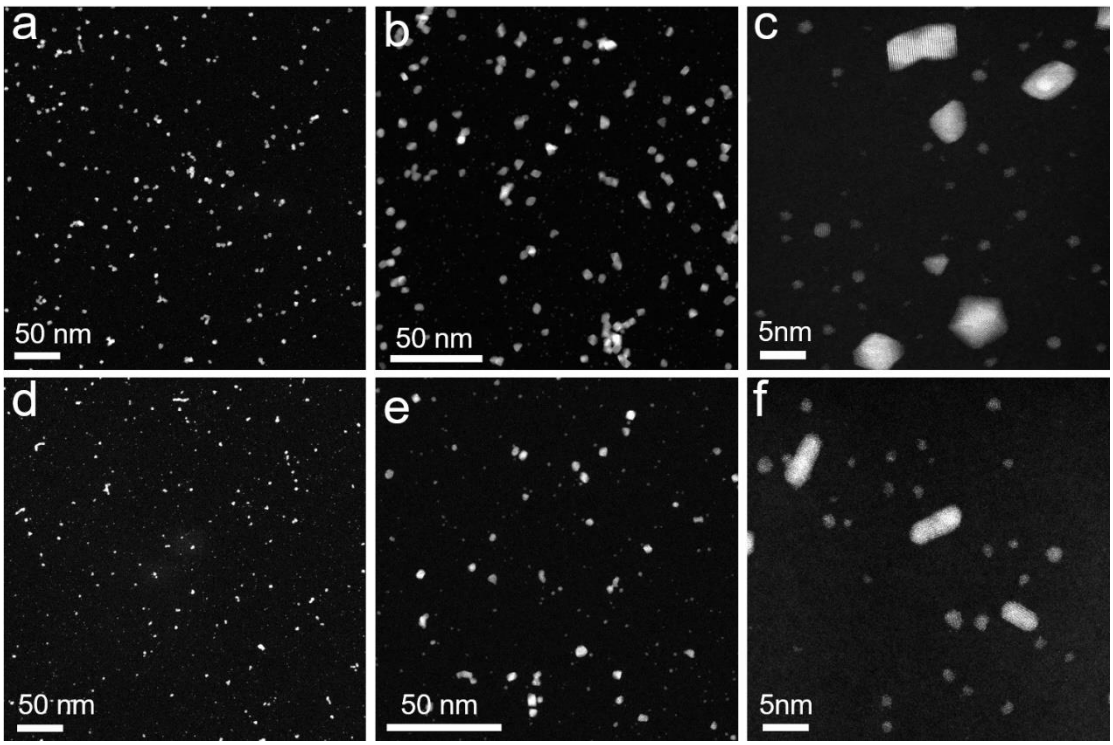


Figure 2.2.9. Pt nanoparticles prepared using a 1-inch Pt target at 75 W, 200 sccm Ar, and 25 cm condensation length. The difference is the temperature of the chamber's walls: (a-c) at room temperature; (d-f) cooled by LN_2 for 5 hours. Particles without mass filtering were collected behind the nozzle.

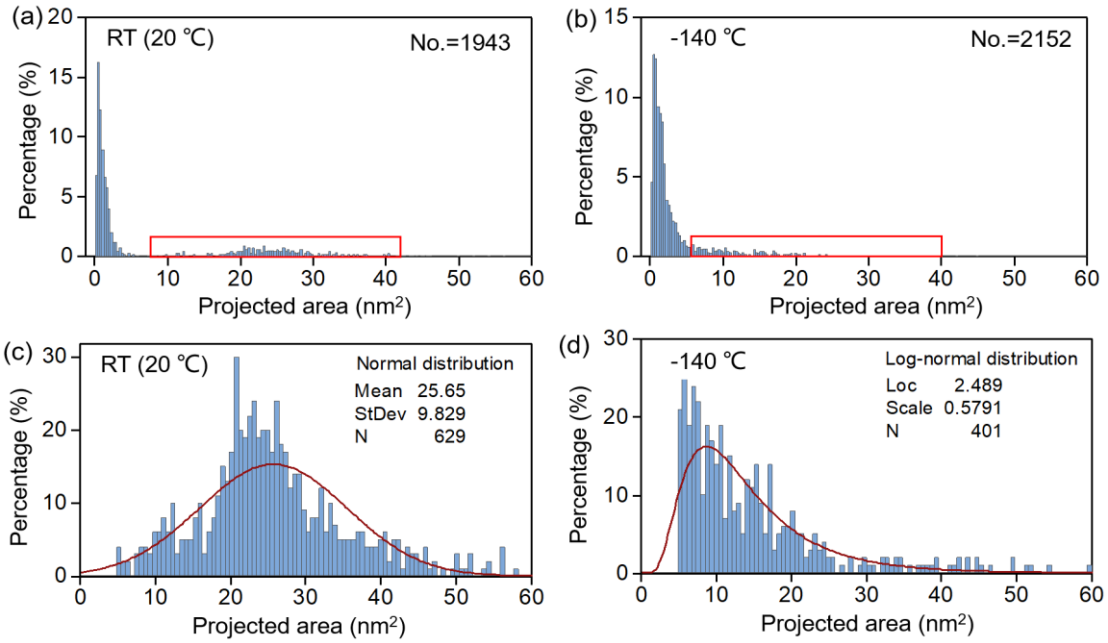


Figure 2.2.10. Projected area distribution of Pt nanoparticles prepared at room temperature (RT) (a,c) or -140 ℃ (b,d), which the images were shown in Figure 2.2.9. The size distribution of large particles was analyzed and presented in (c) and (d), which the particles prepared in cooled chamber displayed a log-normal distribution, different with the particles prepared at room temperature with a normal distribution.

Table 2.1. Parameters of the as-prepared Pt nanoparticles with different cooling time for the chamber by the LN_2

Sample	Cooling time	Temperature of T3	Temperature of T4	Ar (sccm)	Pressure of chamber
S1-Pt_{5000}	No cooling	22 ℃	22 ℃	200	0.42-0.49 mbar
S2-Pt_{5000}	30mins	0 ℃	9 ℃	200	0.42-0.49 mbar
S3-Pt_{5000}	2h30mins	-121 ℃	-17 ℃	200	around 0.45 mbar
S4-Pt_{5000}	2h35mins	-126 ℃	-16 ℃	90	0.22-0.24 mbar
S5-Pt_{5000}	5h	-140 ℃	-17 ℃	200	0.32-0.35 mbar
S6-Pt_{2057}	5h12mins	-140 ℃	-16 ℃	90	0.16-0.18 mbar

For investigating the impacts of temperature on the growing process of Pt nanoparticles, size-selected Pt nanoparticles were deposited on amorphous carbon films of TEM grids. The preparation parameters are recorded in Table 2.1 at different LN_2 cooling times. Figure 2.2.11 presents the morphology of size-selected Pt nanoparticles. No aggregates are observed in Figure 2.2.11(a) and (b), indicating that short cooling time for the chamber plays little impact on the aggregation. Particles in Figure 2.2.11(c) and (d) were fabricated almost at the same time, but the Ar flow rate was decreased from 200 sccm to 90 sccm, inducing the appearance of aggregated particles in (d). A close-up observation of the particles in Figure 2.2.11(d-f) reveals that they are aggregated by two or more small particles, indicating that the aggregation occurred due to particle-particle collisions. Assuming that the particles were flowing and suspended in the buffer gas (e.g. Ar) before aggregation, Brownian diffusion of the particles occurred due to the constant bombardment by surrounding buffer gas atoms. Brownian diffusion refers to the characteristic random wiggling motion of particles in a gas[112]. The Brownian diffusivity D (or diffusion coefficient), which relates the mobility and mix of particles in the gas flow, is evaluated by the Stokes-Einstein expression[112,113]:

$$D = \frac{k_B T C_C}{3\pi\mu\, dp} \ , \qquad (2\text{-}2\text{-}3)$$

where k_B is Boltzmann's constant, T is the gas temperature in K, Cc is the correction parameter for small particles (the Cunningham correction factor), d_p is the particle diameter, and μ is the dynamic viscosity of the gas, which is primarily a function of temperature and weakly depends on pressure.

As the size of particles before aggregating was below 10 nm, the Cunningham correction factor

Cc can be calculated by an empirical formula as shown in eq. (2-2-4)[113,114]:

$$C_c = 1 + \frac{\lambda_g}{d_p}\left[2.514 + 0.800\, exp\left(-0.55\frac{d_p}{\lambda_g}\right)\right], \quad (2\text{-}2\text{-}4)$$

where λ_g is the mean free path of gas atoms in the chamber. The mean free path of background gas (Ar) (λ_g) is given by[114]:

$$\lambda_g = {k_B T}\Big/{\sqrt{2} d_g^2 \pi P}\ , \quad (2\text{-}2\text{-}5)\ [114]$$

where P is the gas pressure, dg is the gas atom diameter (e.g. d_g of Ar atom is about 1.75 Å). For instance, if we assume that the average particle size is 5 nm, then the value of λ_g for Ar atoms is approximately 0.15 cm, and the corresponding Brownian diffusivity, D, is about 17.7 nm^2/s at T=300 K and P=0.2 mbar. However, increasing the gas pressure in the chamber to 0.5 mbar reduces the D value to about 7 nm^2/s due to the shorter λ_g value of 0.06 cm. Furthermore, decreasing the gas temperature to 200 K would result in a reduced λ_g value of 0.1 cm, leading to a lower D of 7.9 nm^2/s. Hence, the low gas pressure and temperature in the chamber could be a possible reason for the formation of aggregation. This is because a low temperature or a high gas pressure will shorten the mean free path (λ_g) of Ar atoms in the chamber, which increases the probability of collisions among the particles. As the cooling process continued for 5 hours and the gas temperature decreased, the mass-selected particles were primarily aggregates (Figure 2.2.11(e-f)). This observation suggests that a lower temperature of the chamber's walls leads to a lower gas temperature, causing coagulation behaviors of Pt particles.

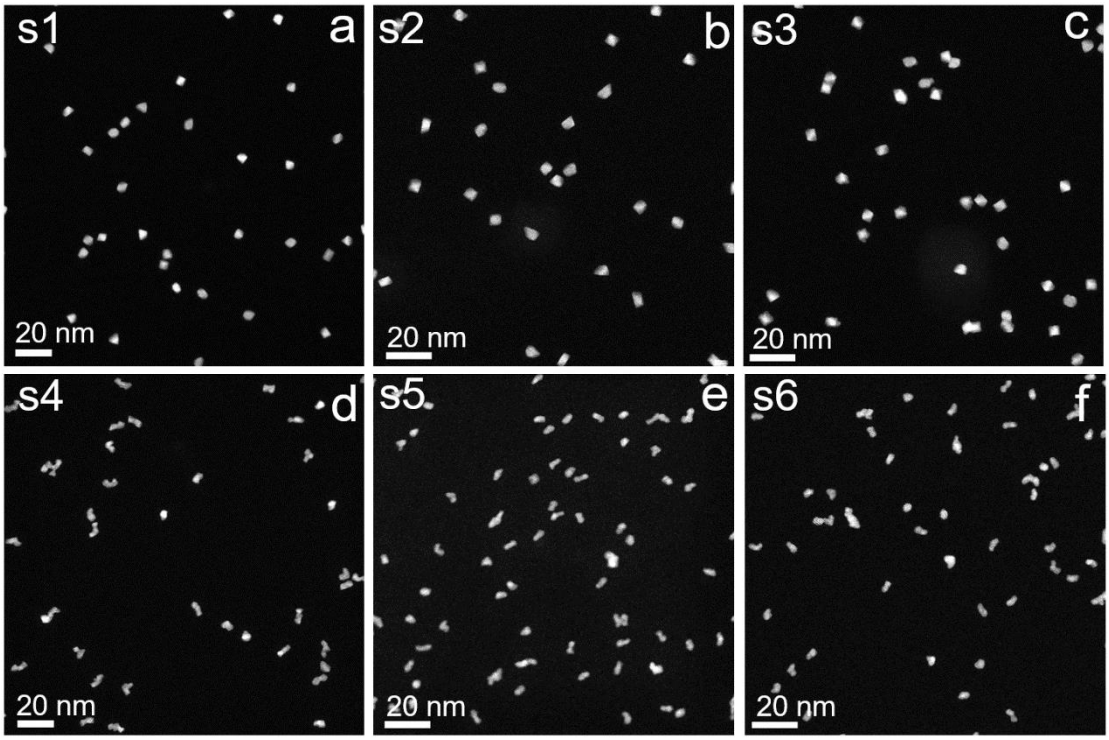


Figure 2.2.11. (a) S1-Pt_{5000}; (b) S2-Pt_{5000}; (c) S3-Pt_{5000}, which was prepared after the argon gas was introduced with 200 sccm for 30 mins; (d) S4-Pt_{5000}, which was prepared following the sample of S3-Pt_{5000} when the argon gas flow rate was changed from 200 sccm to 90 sccm; (e) S5-Pt_{5000}, which was prepared after the flow rates changed from 90 sccm to 200 sccm for 60 mins; (f) S6-Pt_{2057}, which was prepared after the argon gas was altered to 90 sccm for 60 mins.

2.2.5. Formation of aggregated particles

The temperature in the chamber, which can be adjusted by controlling the temperature of the shroud, plays a significant role in nanoparticle aggregations. The size of targets and the intrinsic physical properties also affect the morphology of particles. When a large target, *e.g.* a two-inch target, was sputtered to produce the free atoms in the chamber, the scenario was different. Figure 2.2.12 gives the images of Pt particles that were prepared using a two-inch target in the chamber cooled by LN_2 through 5 hours. The same size of Pt particles (5000 atoms per particle) was selected by the lateral TOF in both Figure 2.2.12(b,c) and Figure 2.2.11(a-e). Few aggregated

particles were observed in Figure 2.2.12 with the sputtering power in the range of 10 to 135 W. However, aggregation took place in Figure 2.2.11 (d-f), which were prepared using a one-inch target. Compared with a one-inch target, not only does the two-inch Pt target have a larger flat area (4 times larger), but it also possesses a stronger magnetic field. When comparing sputtering power, the plasma zone generated by a two-inch target is larger than that of a one-inch target[61]. As the size of the target for sputtering increases, so does the production of sputtered atoms. Additionally, the gas temperature in the chamber would be higher due to the heating effect of the plasma and sputtered atoms when using a larger target for sputtering[64]. A possible explanation for the lack of aggregation in Figure 2.2.12 is that the high atom density and large plasma zone produced by the large target results in a relatively high temperature in the chamber, which prevents particle aggregation during growth. This marked difference in Pt particle morphology is evident between Figure 2.2.11(d-f) and Figure 2.2.12.

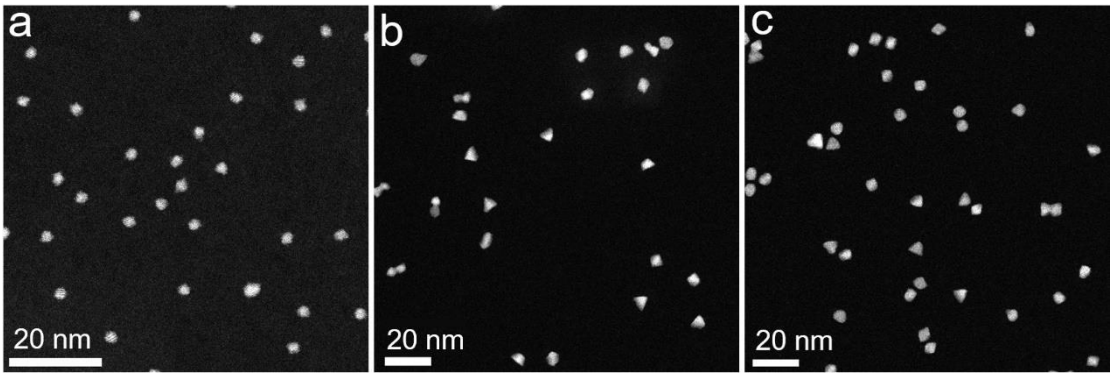


Figure 2.2.12. Pt nanoparticles fabricated using the Sputtering power of (a) 10 W, (b) 75 W, and (c) 135 W on the 2-inch Pt target**.** Before sputtering the target, the chamber was cooled using the flowing liquid nitrogen. Other preparation conditions were: 25 cm for the condensation length; 90 sccm Ar gas; Pt_{561} (a) and Pt_{5000} (b,c) nanoparticles selected by the mass filter.

The physical properties of the target materials, should also be considered in the discussion of

the particle aggregation in the gas phase. The physical properties, including the surface energies, lattice parameters, cohesive energies[115] and binding energies, play significant roles in the formation and growth of particles in the gas phase[15]. A 2-inch palladium target was employed to prepare palladium (Pd) particles in the LN_2-cooled chamber with Pd particles shown in Figure 2.2.13 demonstrating that aggregates were formed. Compared with the chain-like aggregated Pt particles observed in Figure 2.2.11, Pd particles show two types of aggregation morphologies: chain-like and satellite-like shapes, respectively. The chain-like particles, highlighted by yellow arrows, are agglomerates of several small clusters; while the satellite-like shapes were formed by small clusters attached to one large particle, as shown in Figure 2.2.13(c).

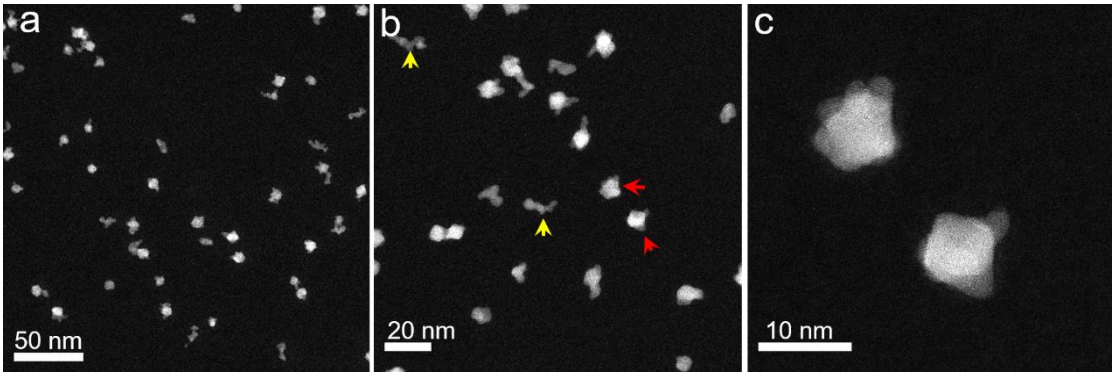


Figure 2.2.13. Pd nanoparticles grown in the chamber, which was cooled down by the liquid nitrogen. The sputtering power was 135 W on the target with 2 inches in diameter with a condensation length of 25 cm. Particles were mass selected with 5000 Pd atoms per particle.

If the chamber was not cooled down by LN_2 and other preparation conditions were no changed, no aggregates were observed as shown in Figure 2.2.14(a), which the mass spectra of Pd particles were presented in (b). In contrast to the mass spectra of Pt particles shown in Figure 2.2.8(c), only one peak was recorded in the mass spectra of Pd particles (Figure 2.2.14b) with

the peak moving large sizes when the chamber was cooled down by LN_2. Meanwhile, the beam current measured by the lateral TOF, dropped sharply from nearly 100 pA at room temperature to less than 40 pA as the chamber wall cooled to -140 ℃. It indicates that the number of nanoparticles formed in the chamber decreased when the gas temperature declined. On the other hand, large Pd nanoparticles (e.g. N>15000 Pd atoms) were detected in the mass spectrum (symbol "Δ"). It could be attributed to more sputtered atoms were absorbed by less formed nanoparticles at low gas temperature by constraining the evaporation of surface atoms in coalescence process. The formation of aggregated Pd particles fabricated by a 2-inch target is supported by the low peak current and broad width in the mass spectrum produced in the cooled chamber.

What does cause Pd nanoparticles to aggregates in the low-temperature chamber, but not Pt nanoparticles? The Pd target bulk possesses a lower surface binding energy (2.81 eV) than the Pt target (5.02 eV)[116]. Given the same preparation conditions, using the same sputtering power will produce a greater number of Pd atoms compared to Pt atoms. Consequently, the density of sputtered Pd atoms in the chamber is higher than that of sputtered Pt atoms. Additionally, the surface energies of Pd nanoparticles are lower than those of Pt nanoparticles[117] (surface energy data from https://legacy.materialsproject.org/). Hence, the concentration of Pd nanoparticles that are formed in the chamber is higher than that of Pt nanoparticles. These factors suggest that Pd nanoparticles have a greater tendency to aggregate than Pt nanoparticles.

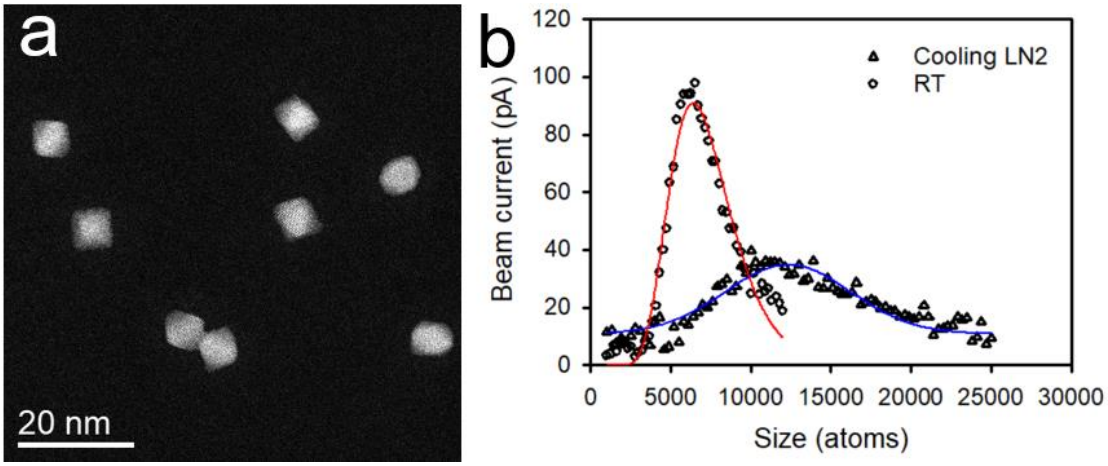


Figure 2.2.14. (a) Size-selected Pd_{12000} nanoparticles prepared without cooling the chamber temperature. (b) The mass spectra of Pd nanoparticles grown in the chamber either cooled by LN_2 (symbols "Δ") or without cooling (symbols "o"). The red and blue curves are the Gaussian fitting results of the spectra.

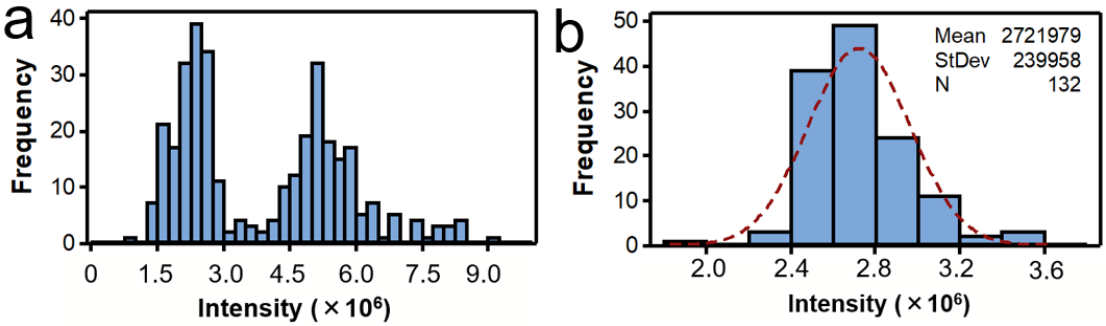


Figure 2.2.15. Size distribution of Pd particles measured by the integrated intensity. (a) preparation in the cooled chamber, (b) growing at room temperature without LN_2 cooling.

Even though there was only one peak recorded in the mass spectrum shown in Figure 2.2.14(b), two peaks were found in the size (integrated intensity) distribution of Pd particles prepared in the cooled chamber (Figure 2.2.15(a)). For Pd particles fabricated at room temperature, there was only one peak in the size distribution (Figure 2.2.15(b)), which was the same as the corresponding mass spectrum. The double peak in the size distribution of Pd particles preparation in the cooled chamber indicates the aggregates carried with two charges, which the

lateral TOF dealt with the aggregates as one whole particle ($\frac{nM}{ne}$)[66,118]. However, the satellite-like Pd nanoparticles were formed by absorbing small clusters, which was not observed in the counterpart Pt particles.

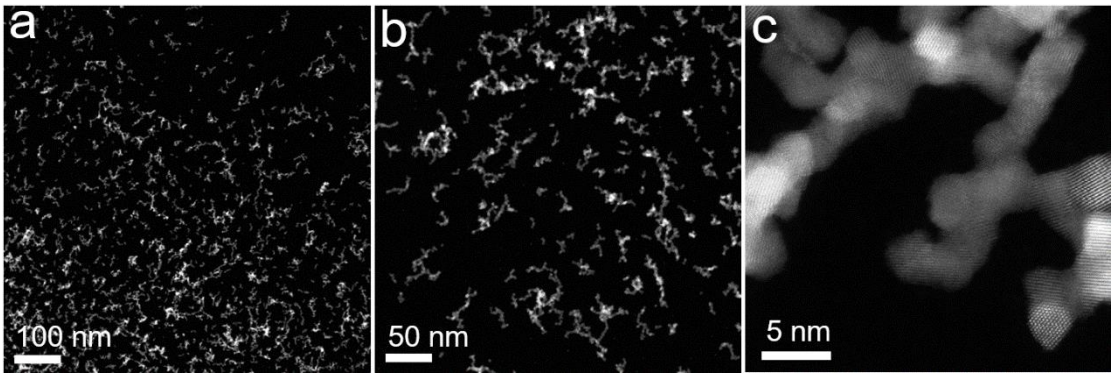


Figure 2.2.16. Dendritic Pt particles fabricated in the LN2 cooled chamber with Ar gas flow rate of 120 sccm (0.23 mbar). A 1-inch Pt target was sputtered with 75 W and the condensation length was 25 cm. Particles from low coverage areas were imaged.

In the case of Pt, many factors impact mutually the formation of dendrites in the gas phase. For example, the length of dendritic Pt particles could be affected by the condensation length and the gas flow rates in the chamber. The dendritic Pt particles in Figure 2.2.16 prepared with 120 sccm of Ar gas had longer dendrites than the sample shown in Figure 2.2.11(d-f), which was fabricated with 90 sccm of Ar gas. When a shorter aggregation length was used, the length of dendrites became shorter (Figure 2.2.17(d-f)). Meanwhile, no satellite-like Pt aggregates were observed in either Figure 2.2.16 or Figure 2.2.17.

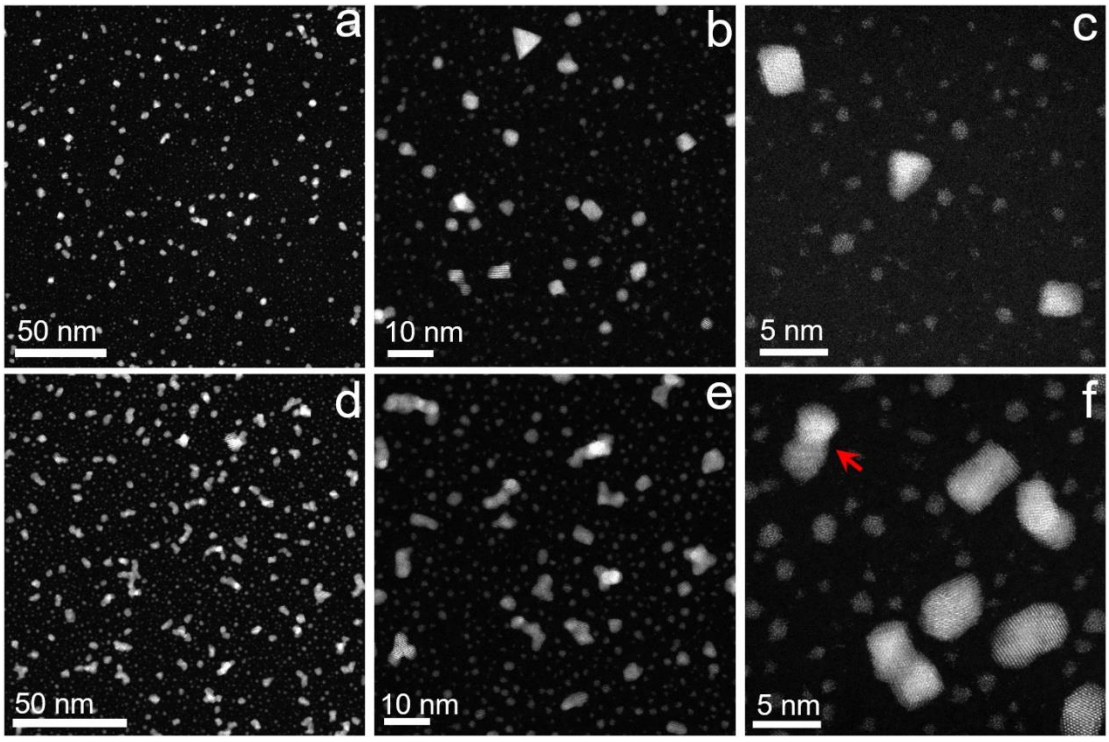


Figure 2.2.17. (a-c) Pt nanoparticles prepared without LN_2 cooling; (d-f) with LN_2 cooling. The Ar gas flow rate was controlled at 90 sccm and the sputtering power was 75 W with a condensation length of 100 mm. The aggregation took place among the large nanoparticles, not the clusters.

2.3. Tetrahedral and octahedral Pt nanoparticles

The technique of shape-directed nanoparticle synthesis has its practical significance due to the extreme importance of size- and shape-controlled nanoparticles to applications. Based on the investigation on the preparation conditions of nanoparticles using the cluster source, breaking the thermodynamics in the growth of nanoparticles can fabricate Pt nanoparticles with out-of-equilibrium shapes. The details in the formation of the non-equilibrium Pt nanoparticles (tetrahedra and octahedra) will be discussed in this section. This work has been published in Ref.[100]: Yu Xia, Diana Nelli, Riccardo Ferrando, Jun Yuan & Z. Y. Li. Shape control of size-

selected naked platinum nanocrystals. Nature Communications, 12, 2021, 3019. I conducted the experimental work. The molecular dynamics simulations of the Pt nanoparticle growth were conducted by Diana Nelli and Richcardo Ferrando. This section is an extended version of the paper.

2.3.1. Octahedral and tetrahedral Pt nanoparticles

The atomic models (Figure 2.3.1) of the octahedral and tetrahedral particles were built using the Atomic Simulation Environment (ASE)[119]. Both octahedra and tetrahedra consist of {111} facets, but the octahedron is four times the volume and twice the surface area compared with the tetrahedron when they have the same edge lengths. Therefore, the octahedron has a larger volume to surface area ratio than the tetrahedron in terms of the same number of atoms per particle.

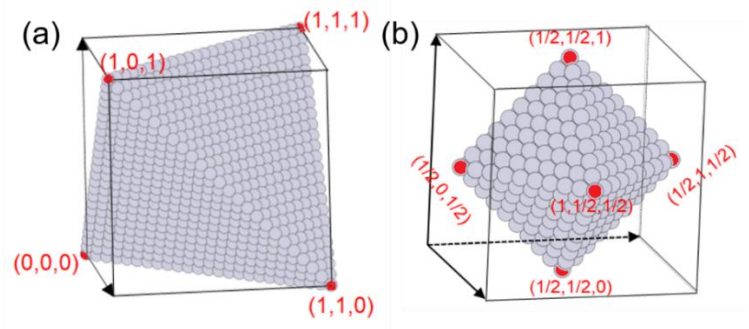


Figure 2.3.1. Illustrations of tetrahedral and octahedral particles covered by {111} facets. The coordinates of the vertex (red points) in the models are given.

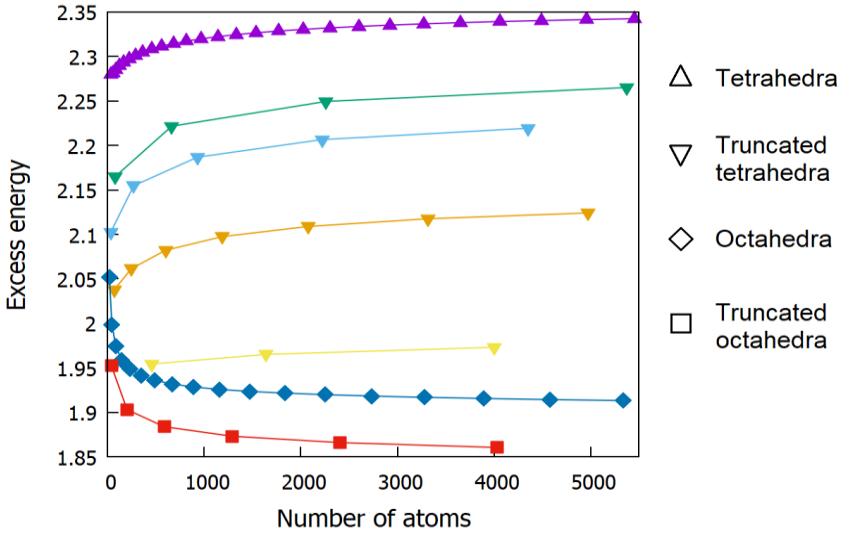


Figure 2.3.2. Excess energy of different structural motifs and schematic representation of the growth sequence. Excess energy E_{exc} as a function of nanoparticle number of atoms N, for regular truncated octahedra (squares), octahedra (diamonds), truncated tetrahedra and tetrahedra (triangles). Lesser and lesser truncations give tetrahedral structures of higher energy. Figure and caption taken from the supplementary material of Ref.[120].

The total excess energy ($\Delta \cdot N^{2/3}$) is computed as the difference between the total binding energy ($E_b(N)$) of the particle and the total cohesive energy ($N\varepsilon_{coh}$) of a bulk system containing the same number (N) of atoms. The excess energy[15] is employed to :

$$\Delta(\mathrm{N})=\frac{E_b(N)-N\varepsilon_{coh}}{N^{2/3}}, \qquad (2\text{-}3\text{-}1)$$

where E_b is the binding energy, ε_{coh} is the cohesive energy per atom in the bulk, N is the number of atoms in nanoparticle. The calculation of Δ involves dividing the total excess energy by $N^{2/3}$, which approximates the number of surface atoms. This allows Δ to approximate the impact of particle shapes on their energy. Among the nanoparticles in Figure 2.3.2 that share the same size, tetrahedra display the greatest excess energy (at the top), followed by truncated tetrahedra, octahedra, and truncated octahedra (which are the closest to the Wulff shape). Nanoparticles grow into the Wulff shape, which is determined by minimizing the total surface free energies

for a given size[20]. Based on the first-principles calculation, nanoparticles conforming to the Wulff construction exhibit the energetically most stable shape[121]. In contrast, those nanoparticles that deviate from such conformity are known as non-equilibrium nanoparticles. Note that the more truncation on the vertex of tetrahedra, the lower the excess energy. It suggests that tetrahedra are by far energetically favourable to form.

Controlling the flow rates of Ar gas and He gas, octahedral and tetrahedral Pt nanoparticles can form in the condensation chamber, as illustrated in Figure 2.3.3 (b) and (f) where show a tetrahedron and an octahedron with a nominal mass of 5000 Pt atoms, respectively. Two simulated HAADF-STEM images (Figure 2.3.3(c, g)) of octahedral and tetrahedral Pt nanoparticles, whose atomic models covered with {111} facets consist of 4495 atoms for the tetrahedron and 4579 atoms for the octahedron built using the ASE[119], were produced using the kinematic-scattering method[122] for the supposed electron beam traveling down along the [011] direction (Figure 1(a, e)). The simulations serve as a reference to confirm the 3D shapes of the experimentally observed Pt nanoparticles shown in Figure 2.3.3 (b, f). Making a close comparison between the experimental images and the simulations, both the contours of the particles and the lattice spacings of {111} planes (2.23 Å in the experiment v.s. 2.26 Å in the simulations) match well. To further quantitatively confirm the identified shapes, the atomic column intensities that reflect the local thickness[98,99,78], were extracted from experimental and simulated images as plotted in Figure 2.3.3 (d, h), respectively. The line profiles of experiments and simulations show the same trend in the variations and mostly match each other, apart from the differences at both ends, which were induced by “missing atoms”. Close comparisons of the

experimental images and the simulations, the “missing atoms” took place at the edges and vertices, indicating the atoms at edges and vertices are unstable. This can be explained by the excess energy shown in Figure 2.3.2 and Table 2 that vertex truncations on octahedral and tetrahedral nanoparticles can reduce the total energy, which is beneficial to the formation of octahedra and tetrahedra.

Table 2.2 Comparison between tetrahedra/truncated tetrahedra and truncated octahedra of the same size. We show the energy difference ΔE between truncated octahedra and tetrahedra/truncated tetrahedra and the excess energy E_{exc} of the two structures under comparison, for some sizes N. We consider three complete perfect tetrahedra (first three rows of the table) and two pairs of truncated tetrahedra with different degrees of truncation (taken from the green and cyan curves of the graph in Figure. 2.3.2, respectively). ΔE and E_{exc} are in eV. Table and caption taken from the supplementary material of Ref.[120].

N	ΔE	E_{exc}	
		TETRAHEDRON/ TRUNCATED TETRAHEDRON	TRUNCATED OCTAHEDRON
2024	-73.911	2.330	1.869
3654	-112.103	2.338	1.865
5456	-148.935	2.342	1.862
2260	-64.970	2.249	1.872
5376	-124.005	2.265	1.861
2220	-57.223	2.206	1.870
4355	-94.881	2.219	1.864

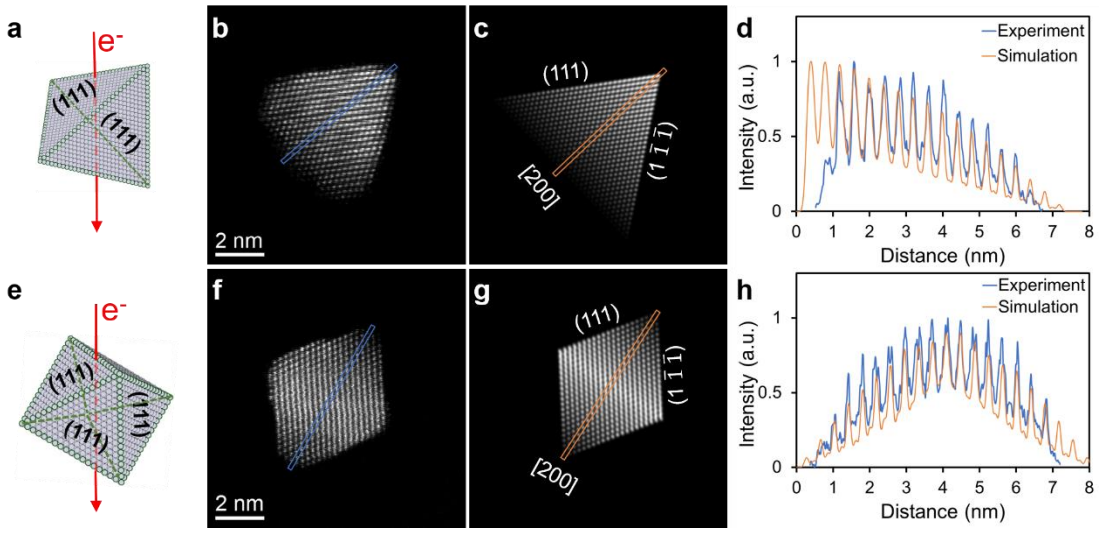


Figure. 2.3.3. The typical shaped Pt_{5000} nanoparticles imaged using HAADF-STEM. (a, e) Schematic representation of tetrahedral and octahedral nanocrystals. The red line indicates the direction of the electron beam traveling along the [011] zone axis of the nanocrystals. The experimental images (b, f) of these nanoparticles are compared with the corresponding simulation (c, g) based on the idealized models of tetrahedron and octahedron as shown in the first column, respectively. The characteristic (111) facets are indicated as well as the [200] direction along which the intensity line profiles are compared in (d) and (h) respectively. Both the image and line profile comparisons show the overall agreement, except that the real nanocrystals have truncated vertices. Figure and caption taken from Ref.[120].

Considering the different landing angles of octahedra and tetrahedra in the deposition, the libraries of HAADF-STEM simulated images were generated by rotating systematically along the x-and y-axis, as the reference of projected images of experimental nanoparticles. Taking Figure 2.3.4 as an example, small differences in the rotating angles can yield significant differences in the projected images. The libraries enable reliable shape identification through comparing the experimental images with the simulations.

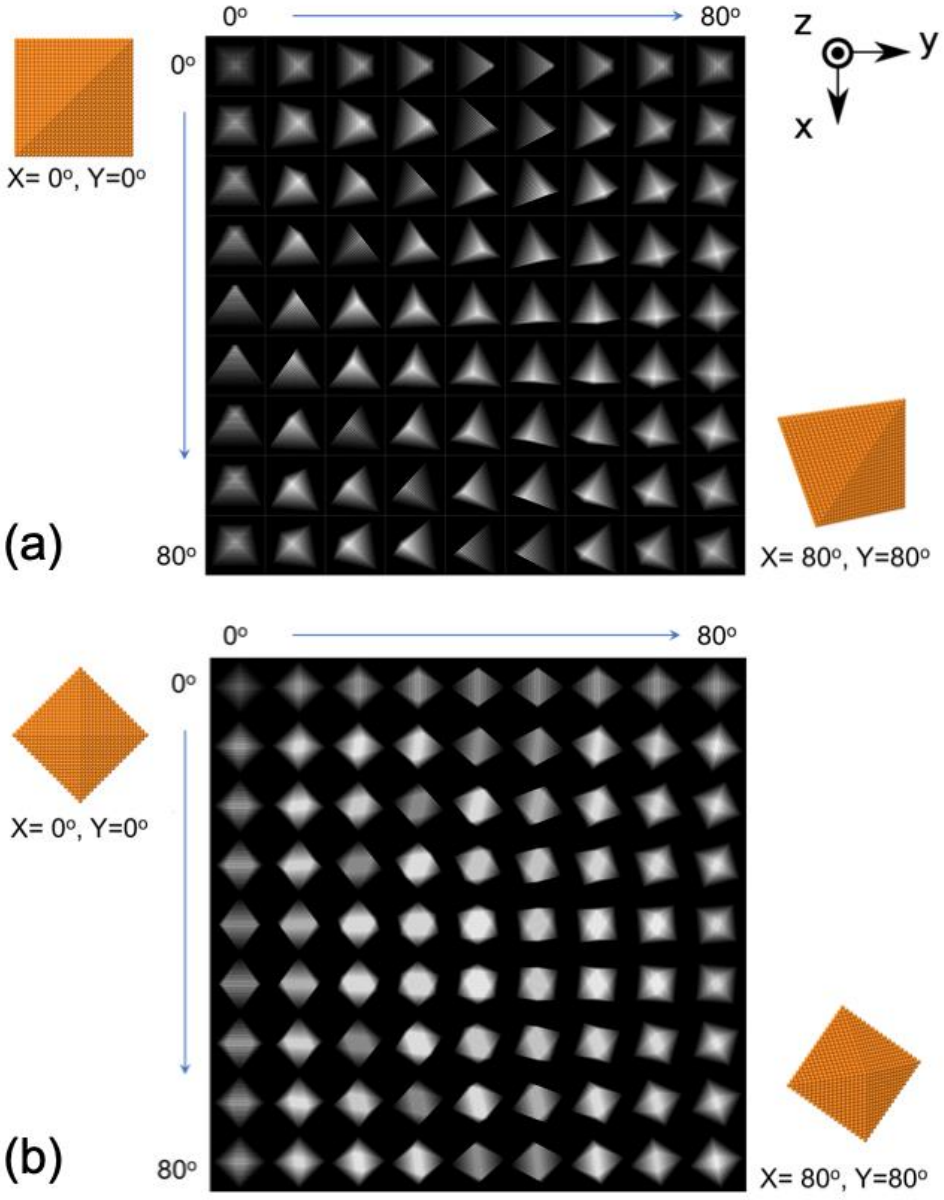


Figure 2.3.4 | Libraries of HAADF-STEM images of an atomic model of (a) tetrahedral nanoparticles with 4459 atoms and (b) octahedral nanoparticle containing 4579 atoms. Both numbers are full shell atom numbers (magical numbers) for tetrahedron and octahedron. STEM images of rotating the atomic models along x-axis and/or y-axis with 10º are shown. Figure and caption taken from the supplementary material of Ref.[120].

2.3.2 Preparation conditions of tetrahedral Pt nanoparticles

As the non-equilibrium octahedral and tetrahedral Pt nanoparticles, which do not conform to the Wulff construction, can be fabricated by the cluster source, there is a potential way to manipulate the shapes of Pt nanoparticles by controlling the experimental conditions. Figure 2.3.5(a) illustrates the fabrication of Pt nanoparticles with non-spherical shapes. Based on the investigation of the influence of preparation conditions on the formation of Pt nanoparticles, 135 W of sputtering power was applied on a 2-inch target with a fixed Ar gas flow rate (90 sccm) to prepare Pt octahedra and tetrahedra. The size distribution of Pt nanoparticles growing in the sputtering chamber was measured by the TOF, with the mass spectra presented in Figure 2.3.5(b). The peak of mass spectra moved from about 2000 to 20000 atoms per particle, but the beam current dropped from nearly 150 pA to around 70 pA as the He gas flow rate was decreased from 145 sccm to 5 sccm. This variation can be elucidated by the classical nucleation theory[106]. The temperature, which regulates the coalescence and interaction of sputtered atoms, is crucial in the formation of nanoparticles. During the sputtering process, Pt atoms are simultaneously cooled by collisions with cooling gas (He gas). Elevating the flow rate of He gas leads to a reduction in the growth rate of the nanoparticle[24,106]. The size of formed Pt nanoparticles is determined by the temperature of Pt nanoparticles and the number density of sputtered Pt atoms. An increase in the flow rate of He gas resulted in a decrease in ρ_{Pt} and a lower temperature of the Pt nanoparticles through collisions with He atoms. This ultimately led to the production of smaller sizes of Pt nanoparticles. For investigating the impacts of He gas on the shapes, the Pt nanoparticles were mass-selected for deposition at their respective peaks

measured in the mass spectra. Figure 2.3.5 (c, d) show images of Pt_{5000} and Pt_{20000} illustrating that the most of particles have octahedral and tetrahedral shapes, respectively. By identifying the shapes of Pt nanoparticles from the HAADF-STEM images, a procedure describes in detail in the following section. The shape distributions of Pt_{3900}, Pt_{5000}, Pt_{10000} and Pt_{20000} were presented in the bar chart (Figure 2.3.5(e)). The most marked variation in Figure 2.3.5(e) is that the population of tetrahedra increased to about 52% but the population of octahedra decreased as the He gas flow rate is reduced to 5 sccm, indicating that the larger Pt nanoparticles have a higher percentage of tetrahedral shapes.

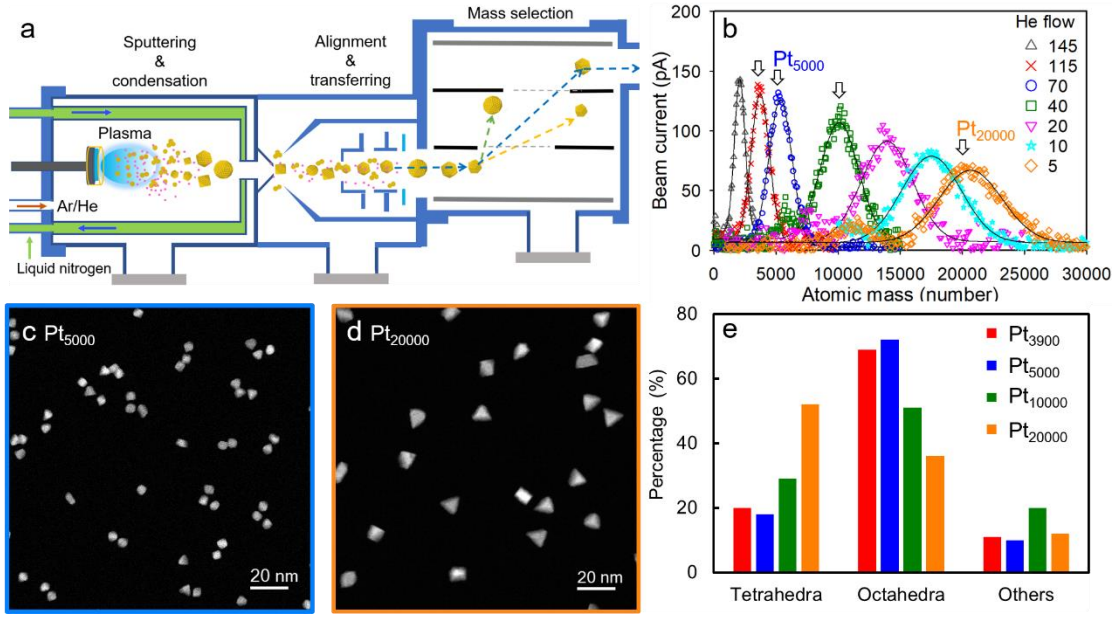


Figure. 2.3.5. Controlling size and shape of Pt nanoparticles. (a) The schematic drawing of magnetron sputtering inert gas condensation beam source used for producing Pt nanoparticles. (b) Mass spectra of Pt nanoparticles produced with the Ar flow rate fixed at 90 sccm and varied He flow rates from 5-145 sccm. HAADF-STEM images of, (c) Pt_{5000} nanoparticles when He flow at 70 sccm, and (d) Pt_{20000} when He flow at 5 sccm, respectively. The corresponding percentages of Pt nanoparticles with certain shapes were shown in (e), together with the data from Pt_{3900} and Pt_{10000} samples (with corresponding He flow at 115 and 40 sccm respectively). Data were taken, with the mass selector, at the peak position of the size distribution as shown in

(b). Other parameters used: sputtering power of 135 W and the condensation length of 250 mm. Figure and caption taken from Ref.[120].

2.3.3 Shape identification using the STEM images

The percentages of different shapes of Pt nanoparticles were determined by identifying the shapes of nanoparticles one-by-one from the STEM images. For reducing the subjective interference of operators, all Pt nanoparticles in a selected region should be identified in the analysis. Figure 2.3.6 shows the procedure that one small zone on the TEM grid was chosen randomly and imaged at low magnification, for example 600 Kx in Figure 2.3.6(a1) for Pt_{5000}. Then higher magnifications, such as 2 Mx in Figure 2.3.6(a2, a3, and b2), were used to capture the nanoparticles at the chosen area in sequence. Comparing the captured images with the simulation in the libraries as shown in Figure 2.3.4, the shapes of nanoparticles were recognized and classified into three groups: octahedra, tetrahedra, and other structures.

It is important to assess the uncertainty of the structure grouping. This was done by selecting three regions in the TEM grids to repeat the above procedures. Table 3 lists the number of shape-classified nanoparticles in each area. The error bars of the percentages were calculated from the statistical results of the same shape in three areas.

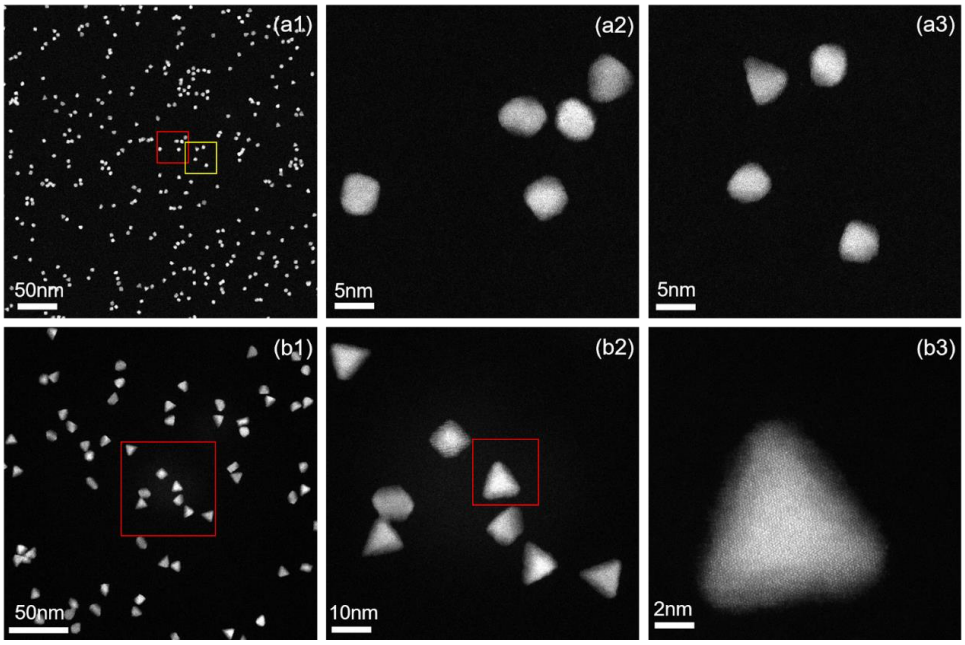


Figure 2.3.6. The procedure of imaging Pt nanoparticles for structure identification. (a1-a3) Pt_{5000}, and (b1-b3) Pt_{20000}. Figure and caption taken from the supplementary materials of Ref.[120].

Table 2.3. Sampling data for nanoparticle shape identification. Table and caption taken from the supplementary material of Ref.[120].

Sample	Regions on the grid (No. of nanoparticles)	Tetrahedron	Octahedron	Others
Pt_{3900} @ 115 sccm	R1(109)	24%	64%	12%
	R2(150)	17%	74%	9%
	R3(100)	19%	75%	6%
	Average(Total no. 359)	20 ±3%	69 ±5%	9 ±3%
Pt_{5000} @ 70 sccm	R1 (284)	19%	73%	8%
	R2 (153)	16%	76%	8%
	R3 (179)	19%	69%	12%
	Average (Total no. 616)	18%± 2%	73%± 4%	10%± 2%
Pt_{10000} @ 40 sccm	R1（91）	30%	53%	17%
	R2（125）	29%	57%	14%
	R3(115)	32%	55%	13%
	Average(Total no.331)	30 ±1%	55 ±2%	15 ±2%
Pt_{20000} @ 5 sccm	R1 (174)	55%	32%	14%
	R2 (329)	50%	40%	10%
	R3 (250)	51%	39%	10%
	Average (total no. 753)	52%± 3%	36%± 4%	12%± 2%

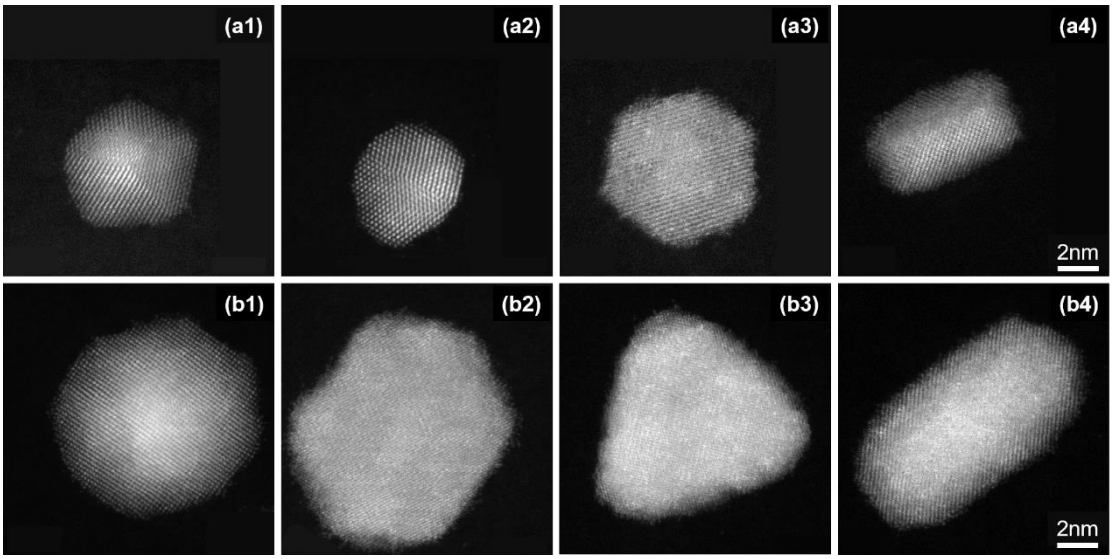


Figure 2.3.7. Representative HAADF-STEM images of experimental Pt nanoparticles with 'other structures'. The images at the upper row are Pt_{5000} nanoparticles and at the bottom row are Pt_{20000} nanoparticles. (a1) a regular five-fold decahedron; (a2) a particle with a twin structure; (a3), (b2) and (b3) particles with flat hexagonal shape and triangular shape; (a4) and (b4) elongated particles; (b1) a rounded shape particle with fcc structure. Figure and caption taken from the supplementary materials of Ref.[120].

Before discussing the growth mechanism of octahedral and tetrahedral nanoparticles, there are small number of nanoparticles classified as "others", as shown in Figure 2.3.7. Twin boundaries were observed in Pt decahedron and twined nanoparticle (Figure 2.3.7a1 and a2), suggesting that stacking faults can be kept in Pt nanoparticles. Columnlike and hexagonal particles are unlike the spherical Pt nanoparticle in Figure 2.3.7 b1, indicating the orientation-limited growth mode. These non-spherical nanoparticles, who do not follow the Wulff construction, suggest the kinetic growth path of Pt nanoparticles in gas-phase[20]. An example of the kinetic growth path can be observed in the nanoparticle presented in Figure 2.3.7a4. The decahedron consists of side surfaces that are bounded by {100} facets. As the nanoparticle grows, Pt atoms preferentially adhere to its ends with {111} facets, resulting in the formation of a nanorod. The low population (around 10%) of "other structures or shapes" also indicate that these shapes and

structures are metastable in energy but were frozen during growth as they were carried out from the condensation chamber. Upon entering the transfer chamber, the aperture and skimmer have reduced the density of nanoparticles and the background pressure. Meanwhile, the charged nanoparticles were aligned by the electric fields of the lenses present in the chamber, thereby reducing the frequency of collisions between them and halting their growth. Furthermore, these metastable crystal nanoparticles remained their shapes due to the low temperature achieved by the cooling gas, which restricts the diffusion of surface atoms.

2.3.4. Growth mechanism by simulations

As shown in the above results, the fraction of octahedral and tetrahedral Pt nanoparticles can be tuned in a range (20-52% for tetrahedra and 36-73% for octahedra). The growth pathway is worth building to understand the shape control for driving the shaped nanoparticles preparation from an art to science.

The Equilibrium Wulff Construction (EWC) or the Kinetic Wulff Construction (KWC) are usually considered when rationalizing the non-equilibrium growth of shape-directed nanocrystals[123,124]. These alone cannot explain the growth competition between octahedra and tetrahedra. It is obvious that both octahedra and tetrahedra are unfavourable surface-to-volume ratios. Moreover, the (111) facets surround the octahedral and tetrahedral shapes, which cannot be explained by the simplistic orientation-directed growth model of KWC. Compared with the octahedron, the tetrahedron has four symmetrical (111) facets to grow. In the magnetron sputtering gas phase environment, free atoms land on the nanoparticles randomly from all

directions, which means no a priori reason leads to the selection growing orientations. For exploring the possible growth pathway, the mass spectroscopy in Figure 2.3.5(b) was analyzed mathematically, as shown in Figure 2.3.8. The area under the mass spectrum, representing the number of detected particles, has a linear relationship with the He gas flow rate. It is apparent that the mass spectra shown in Figure 2.3.5(b) moved to large sizes as the decrease of He gas flow rates. The size of particles at the peak of the mass spectrum can be calculated by an exponential function of He gas flow rates. Taking the first approximation, the inverse of the He flow rate can be interpreted as proportional to the dwell time of the nanoparticles travelling in the condensation chamber[120]. The area under the mass spectrum and the size of particles at the peak were expressed using the inverse of He flow-rate, as shown in Figure 2.3.8(c, d), building the links between the dwell time and the size and number of particles. The number of particles detected by the TOF rose rapidly within short transit time, then stabilized at round a plateau, indicating that the small He flow rate had little impact on the number of particles. The average size of particles increased linearly as the dwell time was increased. It indicates that the increase of the particle size is likely by absorbing adatom on the existing nanocrystals in the condensation zone. Moreover, the symmetrical mass spectra, which were fitted better by the Gaussian rather than log-normal function[111], suggest nanoparticle size increase through He-enhanced two-body collision, rather than particle-particle aggregation, which usually induces either elongated or dendritic shapes[125].

The population of tetrahedra had small variations when the mean nanoparticle sizes less than 5000 atoms. However, the percentage of tetrahedra rose at particle sizes larger than 10000 atoms,

while the number of particles detected in the beam almost did not change. Therefore, it is reasonable to propose an assumption that parts of tetrahedral Pt particles are turned from small octahedra. However, the classical KWC mechanism cannot explain the growth of Pt tetrahedra and octahedra, which both are consisted by {111} facets. The total energy of tetrahedra and octahedra in Table2, as well as the excess energy, demonstrate that tetrahedral nanoparticles deviate farther away from the thermal equilibrium than octahedral nanoparticles, thus the growth of tetrahedra cannot be understood by the EWC. Based on the Wulff construction, the truncated octahedron is the thermodynamically stable shape of Pt nanoparticles, consisting of the lowest-energy facets {111} and {100}[109]. According to the calculation results presented in Figure 2.3.2, it is observed that (truncated) tetrahedral Pt nanoparticles exhibit a higher additional excess energy relative to the truncated octahedra, in comparison to the additional excess energy of the octahedra and relative to the truncated octahedra. This observation implies that the thermal equilibrium shape of Pt nanoparticles, as determined by the Wulff construction, is further from the tetrahedral shape than from the octahedral shape.

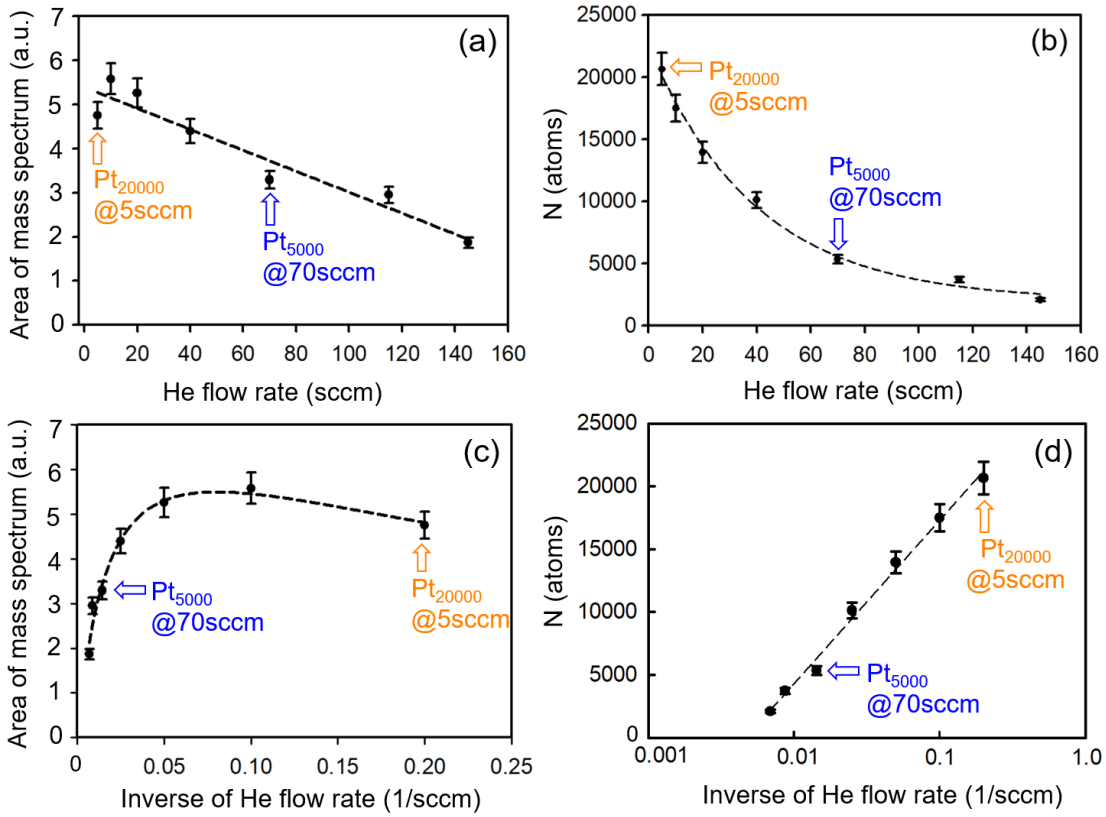


Figure 2.3.8. Influence of He flow rate on the formation of Pt nanoparticles shown in Fig. 2.3.5b. (a) The area (A) covered by the main peak in mass spectra fitted by Gaussian function as a function of He flow rate showing a linear relationship; (b) The number of atoms at the peak position (N) as a function of He flow rate fitted with an exponential function; and (c) The same data as in (a) yet are plotted as a function of inverse of He flow rate, showing a narrow region of nucleation for fast He flow rate and a broad range of no additional nucleation for slow He flow rates. (d) The same data in (b) replotted as a function of the inverse of the He flow rate in the log scale, demonstrating a single relationship. The error bar in the y-axis is from the mass resolution of the mass filter. The arrows point to the growth conditions under which cluster beams showing significant shape transformation from octahedra to tetrahedra. The results demonstrate not only that the shape can be tuned but also the transformation occurs for the nanoparticle beams of similar current but increasing size, suggesting an adatom condensation mechanism. Figure and caption taken from the supplementary materials of Ref.[120].

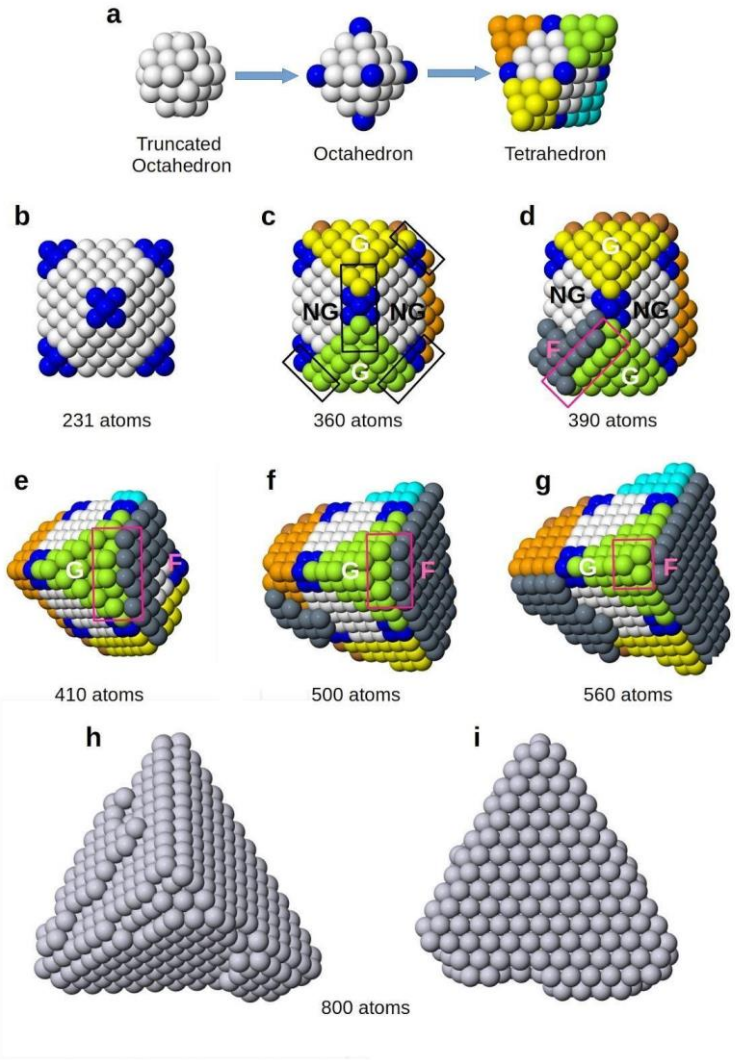


Figure 2.3.9. Growth pathway from truncated octahedral, to octahedral and to tetrahedral shaped nanoparticles. (a) Schematic representation of the two main steps of the growth sequence. A truncated octahedron (white atoms) becomes an octahedron after growth on all (100) facets to complete six vertices (blue atoms). The tetrahedron is then obtained by growing equivalent tips on only four (111) facets of the octahedron over eight, in such a way that octahedral symmetry is broken with a specific pattern. These tips are colored in yellow, green, cyan and orange. (b-g) Snapshots taken for a growth simulation at 400 K and deposition rate of 0.1 atom/ns**.** (b-d) and (e-g) show the same growing nanoparticle from different perspectives. The simulation is started from a truncated octahedron of 201 atoms (white atoms). (b) Octahedral vertices are completed. (c) Non-neighboring growing (G, in yellow and green) facets are formed, separated by non-growing facets (NG). Small tetrahedral edges are formed (enclosed in black rectangles). (d) An island in stacking fault (F, in dark grey) starts to grow at the corner between G and a NG facets, creating a (100)-like fourfold sites (enclosed in the pink rectangle) on which (e) new atoms adsorb and facilitate the

growth of the tetrahedral tips by a self-replicating process (f) which finally leads to the tetrahedral nanoparticle (g), which continues to grow as a tetrahedron (h,i). Figure and caption taken from Ref.[120].

Diana Nelli and Prof. Riccardo Ferrando gave their interpretations on the formation of octahedral and tetrahedral Pt nanoparticles using molecular dynamics (MD) growth simulations[126,127] based on the experimental results presented above[120]. A growth mechanism of defect-mediated symmetry breaking was proposed and simulated using MD where Pt tetrahedra are formed through octahedral-to-tetrahedral shape transformation in a kinetic growth pathway. There are two steps involved in this proposed pathway as schematically shown in Figure 2.3.9. A small truncated octahedron grows into an octahedron and a tetrahedron is formed from the transformation of the octahedron in further growth.

The simulation growth starts from truncated octahedra, which are the equilibrium shape at the high temperature atomic vapour (e.g. 900 K)[15,29]. Free Pt atoms will be condensed by the cooling gas and land on the surface of truncated octahedra. The new-arrived adatoms are adsorbed randomly at the beginning, but adatoms energetically prefer (100) facets by about 0.5 eV compared to (111) facets[120]. As deposited atoms on (111) facets move to (100) facets where they are trapped, truncated octahedra grow to complete their vertices (indicated as blue in Figure 2.3.9) forming complete octahedra[127]. Therefore, these growth steps are driven by the nonequilibrium growth rates of different facets with (100) facets growing fasters than (111) facets, which is called classical KWC[120]. This interpretation is in line with the high percentages of Pt_{3900} and Pt_{5000} octahedral nanoparticles presented experimentally in Figure 2.3.5(e) and Table 3.

However, the KWC model meets difficulties to explain the formation of the tetrahedral Pt nanoparticle from an octahedron covered with all equivalent facets of (111) type, showing the O_h symmetry. Tetrahedral shapes show a T_d symmetry, which is a subgroup of O_h. Four (111) facets disappear in the growth process transitioning an octahedron to a tetrahedron. The snapshots (Figure 2.3.9 and Figure 2.3.10) show the simulation of a Pt_{231} octahedron transitioning to a Pt_{800} tetrahedron, which a subtle mechanism was identified involving stacking faults (dark grey atoms in the snapshots). They were formed by the adatoms at the corner of octahedral surface triggering the shape transformation.

As the truncated octahedron completes its vertices, the growth continues on a random facet of the octahedron by adsorbing adatoms to form steps. Further deposited atoms will be trapped by these steps, which also attract adatoms diffusing from nearby facets. The facet with steps has faster growth rates than its neighbour facets, whose adatoms are depleted due to the diffusion. The facets with fast growth rates are marked as growing (G) facets, which are separated by non-growing (NG) facets with a lower rate, as shown in Figure 2.3.9 c,d.

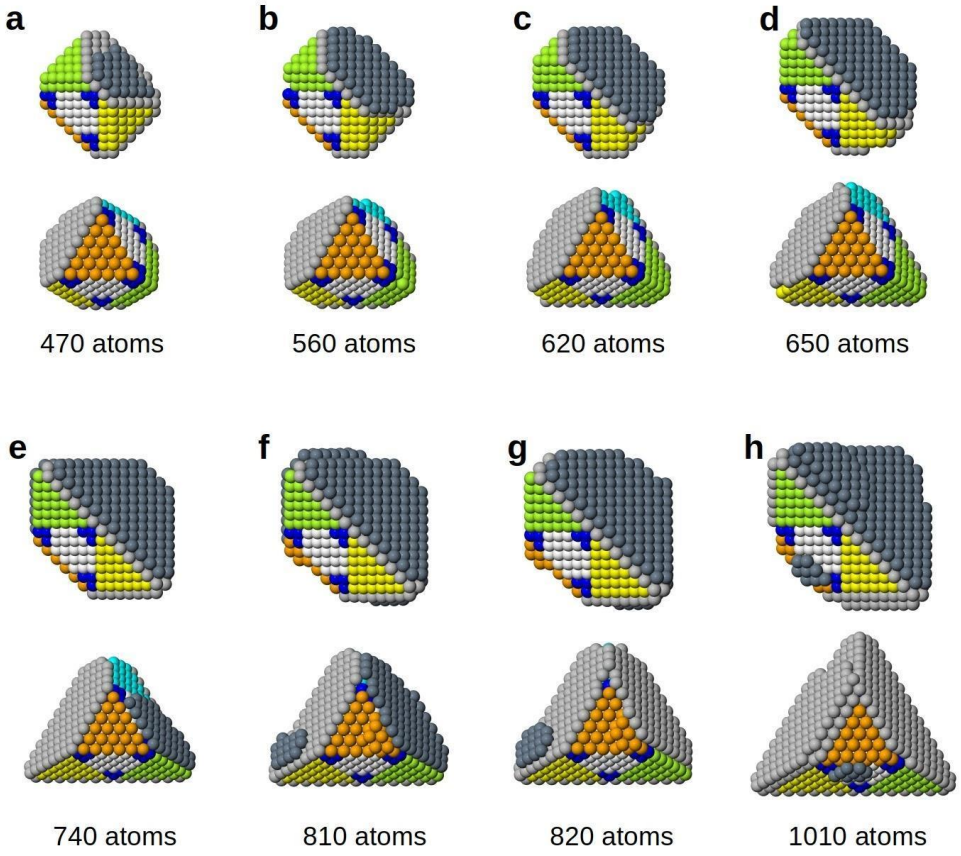


Figure 2.3.10. Growth simulation at 600 K and flux of 0.1 atoms/ns. (a-g) Snapshots are taken at eight different intermediate sizes. For each size, the same structure is shown from two different perspectives. Atoms colored in white correspond to the starting truncated octahedron of 201 atoms, while blue atoms are those completing the octahedral tips on top of it, to form an octahedron of 231 atoms. Atoms in yellow, green, orange and cyan correspond to the tetrahedral tips which would grow on that octahedron of 231 atoms, as in the case of the sequence at 400 K of Figure. 2.3.9. Light grey atoms correspond to further layers in fcc stacking, whereas dark grey atoms are those of islands in hcp stacking. At variance of the sequence at 400 K, growth is still within the octahedral motif up to about a size of (a) 470 atoms, where an island in hcp stacking is formed (atoms in dark grey). (b-d) This island triggers the fast growth of the three tetrahedral tips over four (those in yellow, green and cyan) that have borders in common with it, while the orange tip, which has no faulted islands at its border, does not grow. (e-f) A second faulted island is formed at the border of the orange tip, at its right, and the orange tip starts growing one layer. (g-h) This second faulted island reverts back to fcc stacking, and the growth of the orange tip stops again, no further layers nucleating beyond the second. The final structure is of tetrahedral type, but with three sharp tips and one truncated tip. Note that another small faulted island on the left side of the lower image in (f-g), reverts back to fcc stacking (h)

producing a tetrahedron with one more fcc plane. Figure and caption taken from the supplementary materials of Ref.[120].

The simulations reflect that a tetrahedral edge (marked by a black rectangle in Figure 2.3.9c) is formed as the growth of a layer on the G facet. These sharp tetrahedral edges are preferred energetically by adatoms adsorption on the NG facet. The experimental and computational results on Pt(111) planes[128,129] demonstrate that adatoms on facets are more easily to be trap in the vicinity of edges. Therefore, it is probable for adatoms to nucleate into small islands on NG facets, with preferential site at corners with G facets, where a compact stacking can be formed by atoms occupying edge sites (shown in Figure 2.3.9d).

The following growth pathway determines the final shape of Pt nanoparticles growing into either octahedral or tetrahedral shape. A stacking fault will be built if the new incoming adatoms stack with an ABAB sequence (dark grey atoms in Figure 2.3.9d and Figure 2.3.10a) on the formed island, which is an ABCABC stacking at the corner of the NG facet. This stacking fault constituted an energy trap for new incoming adatoms (Figure 2.3.9e and Figure 2.3.10b). These adatoms self-replicated and accelerated the adsorption growth process that a tetrahedral tip was formed (Figure 2.3.9f, g and Figure 2.3.10c,d,e). The yellow atoms shown in Figure 2.3.10a-d, by comparison, do not form the faulted layer, showing slow and self-limiting growth. The four non-neighbour facets of eight facets grew layer-by-layer taking place on the symmetric placement of the corners between G and NG facets (Figure 2.3.10e,f). This layer-by-layer tip growth is regarded as driven by the fast kinetics, inducing the transformation from an octahedron to a tetrahedron and finally producing the tetrahedral shape (Figure 2.3.9h,i). As the

stacking fault is metastable, the ABAB stacks can revert to the energetically preferred ABCABC stacks during the growth process, as shown in Figure 2.3.10(g, h). This will slow down the growth rate of nearby tetrahedral tips, inducing truncated tetrahedral vertices. Although the stacking fault was not observed in the sample prepared by the gas-phase method, it was found in the tetrahedral Pd nanoparticles synthesized by wet-chemical method, which was fixed by the ligands[24]. Using the same simulation methods, the tetrahedron can grow from a large truncated octahedron (Figure 2.3.11a) and a perfect octahedron (Figure 2.3.11b). These growth simulations of tetrahedra with large sizes confirm the transitions from truncated octahedra to octahedra and then to tetrahedra.

If there is no stacking fault formed or the stacking faults cannot trap atoms effectively, then truncated octahedra will grow into octahedra without further transition to tetrahedra. Figure 2.3.12 gives an example of a truncated octahedron forming at 800 K with a low atom deposition rate (0.1 atom per ns). Compared with the simulation in Figure 2.3.10, the adatoms had higher energies in Figure 2.3.12. Even though the stacking island was formed (dark atoms in Figure 2.3.12), the adatoms cannot be trapped by the fourfold adsorption sites that no tetrahedral tip was formed. Therefore, the transition of octahedra to tetrahedra did not take place.

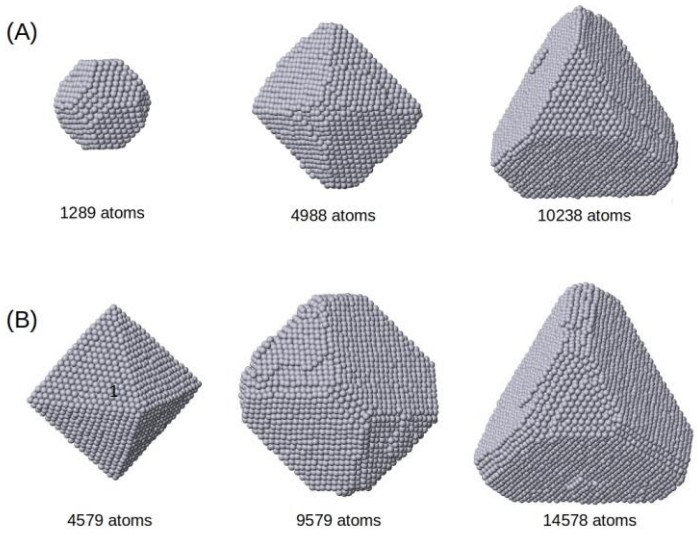


Figure. 2.3.11. Snapshots from growth simulations at T=900 K and deposition rate of 1 atom/ns. (A) the simulation is started from a truncated octahedron of 1289 atoms, which grows to a somewhat asymmetric octahedron for sizes around 5000 atoms and then evolves towards a tetrahedral shape at about 10000 atoms. (B) The simulation starts from a perfect octahedron of about 4600 atoms, then it evolves to a deeply truncated tetrahedron at about 10000 atoms, which becomes sharper growing up to sizes close to 15000 atoms. Figure and caption taken from the supplementary material of Ref.[120].

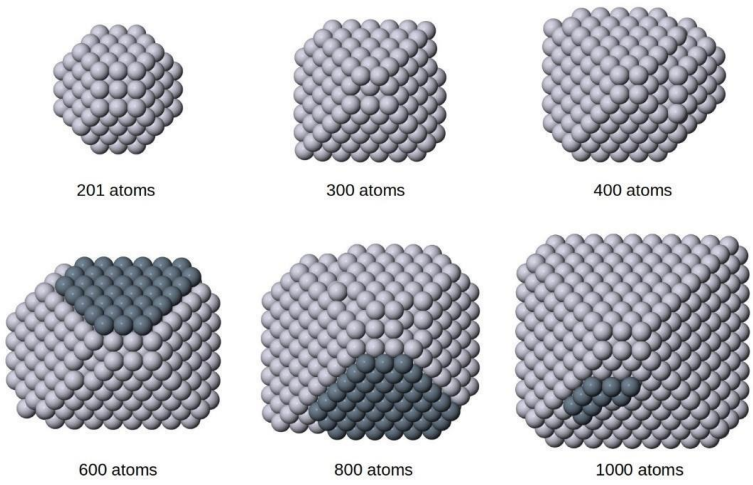


Figure. 2.3.12. Growth simulation at 800 K and flux of 0.1 atoms/ns. The growth starts from the truncated octahedron of 201 atoms, and continues within the octahedral motif up to the final structure at 1000 atoms. All images are taken from the same perspective. Islands in hcp stacking often form (shown by the atoms in dark grey) but they revert

back to the fcc stacking as growth continues. At variance with the lower temperature cases, the fourfold adsorption sites formed at the border of faulted islands are not as effective as atom traps, so that tetrahedral tip growth is not started. Figure and caption taken from the supplementary material of Ref.[120].

2.3.5. Tetrahedra prepared by a small target

The simulations shown before demonstrate that there is a critical size (390 atoms per nanoparticle shown in Figure 2.3.9) above which nanocrystals cannot reach their equilibrium shapes, even with these nanocrystals initially growing from equilibrium shapes. This critical size depends on the growth times, atom density in the chamber, and on temperature.

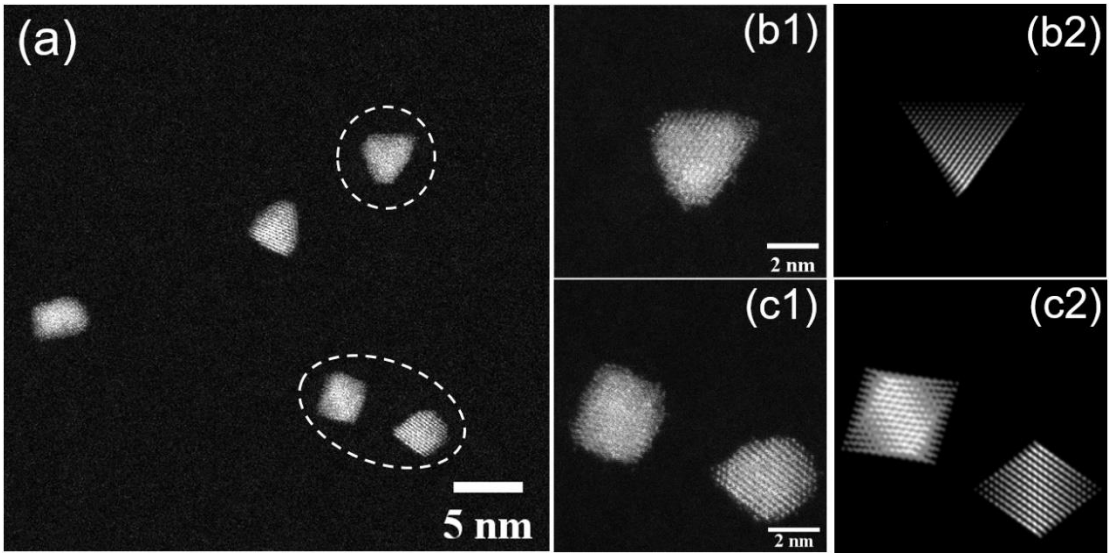


Figure 2.3.13. Pt_{1415} nanoparticles prepared using an one-inch Pt target at room temperature using 75 W and the argon gas flow rate of 90 sccm. (a, b1, c1) experimental images; (b2, c2) simulated images.

Here, a small target (one inch in diameter) was used to prepare tetrahedral Pt nanoparticles as shown in Figure 2.3.13 where both tetrahedral (b1) and octahedral (c1) Pt_{1415} nanoparticles were clearly observed. It demonstrates that tetrahedral Pt nanoparticles can be as small as around 1400 atoms, further supporting experimentally the simulations that the tetrahedra can

transform from the octahedra since small sizes. For successfully preparing octahedral and tetrahedral Pt nanoparticles using the small target, a high sputtering power (e.g. 75 W) is necessary to ensure sufficiently high temperature and atoms density for the growth of the tetrahedra and octahedra. What's more, the room temperature of chamber's walls is the key parameter for small targets, which is different with the scenario of the large target used in the preparation.

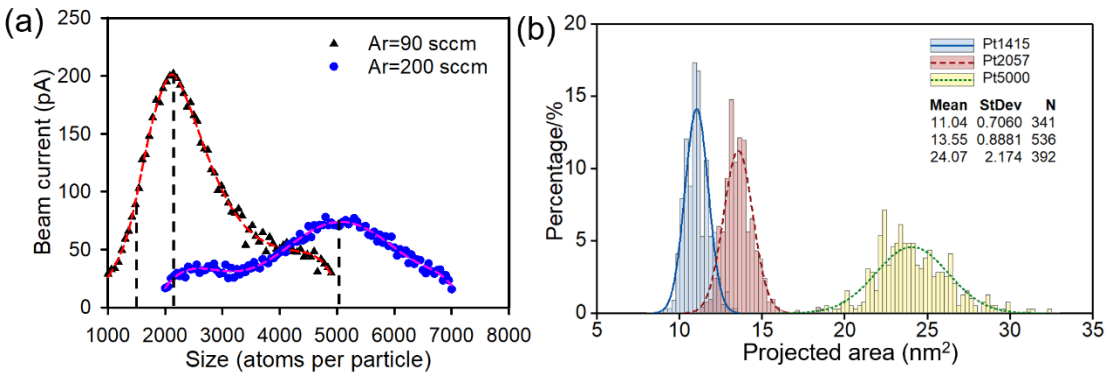


Figure 2.3.14. (a) Mass spectra of Pt nanoparticles fabricated without He gas and different Ar gas flow rates. (b) Size distribution of Pt_{1415}, Pt_{2057}, and Pt_{5000} nanoparticles.

The populations of tetrahedra and octahedra at different sizes in the same mass-spectrum were investigated. Figure 2.3.14(a) shows the mass spectra of Pt nanoparticles prepared using 90 sccm (0.27 mbar) and 200 sccm (0.52 mbar) of Ar gas, respectively. The higher Ar gas flow rate reduced the peak of beam currents of the mass spectrum (blue one), but produced more larger nanoparticles. Nanoparticles with nominal mass of 1415, 2057, and 5000 Pt atoms were mass-selected by the TOF. These size distributions, which was extracted from the STEM images, fitted well by normal functions (Figure 2.3.14(b)). Over three hundred nanoparticles were imaged and shape-identified, done as the same way described in Section 2.3.3. The population distributions of octahedra and tetrahedra are displayed in Figure 2.3.15(d) using bar charts. It

is apparent that Pt_{5000} nanoparticles prepared with 90 sccm of Ar gas had the maximum percentage (47%±3%) of tetrahedra compared with another two sizes of Pt nanoparticles (36%±5% of Pt_{1415} and 27%±5% of Pt_{2057}). This result corresponds with the growth calculations mentioned in Section 2.3.4 that Pt tetrahedra are transformed from the octahedra through the formation of stacking faults in the growth process. Pt_{1415} and Pt_{2057}, and Pt_{5000} nanoparticles were fabricated with the same conditions and the mass spectrum, therefore, Pt_{5000} nanoparticles had higher growth rates than Pt_{1415} and Pt_{2057} because of the same transferring time. It indicates that a higher growth rate is beneficial to the formation of tetrahedral nanoparticles.

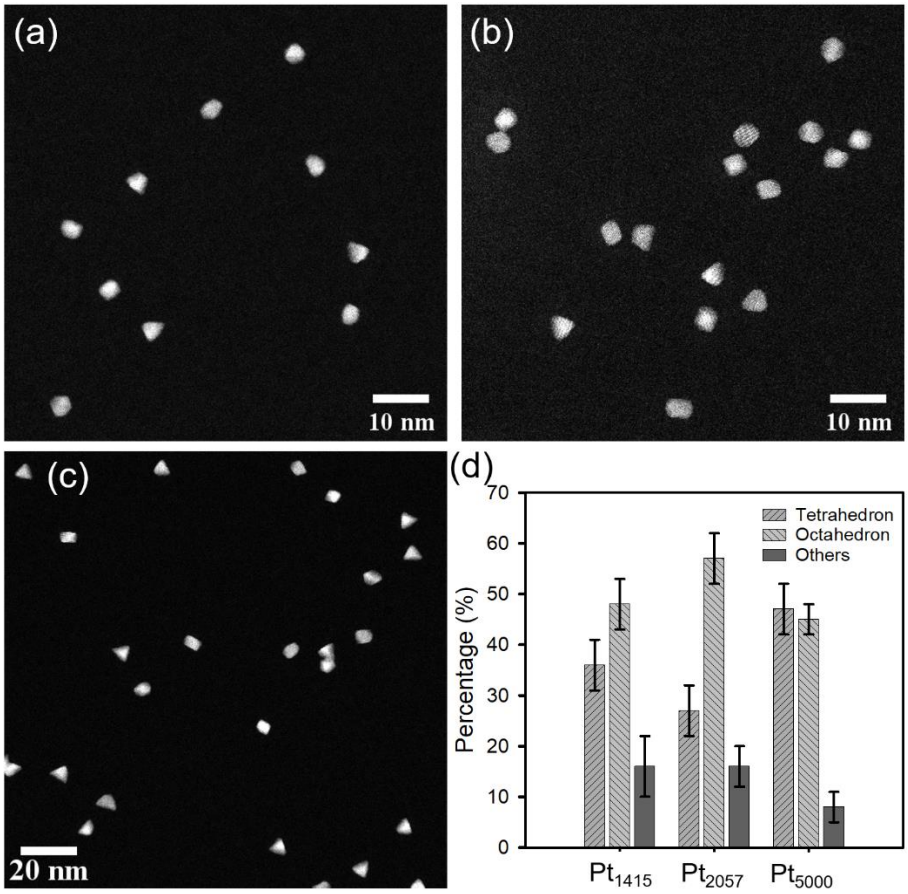


Figure 2.3.15. Three sizes of Pt nanoparticles Pt_{1415} (a), Pt_{2057} (b), and Pt_{5000} (c) were chosen by the mass selector and the HAADF-STEM images and the corresponding percentages of structures were shown in (d), which 394 Pt_{1415} nanoparticles, 334 Pt_{2057} nanoparticles, and 329 Pt_{5000} nanoparticles were shape identification.

It is noticed that there is a small difference (about 9%) on the population of tetrahedra between Pt_{1415} and Pt_{2057} nanoparticles. Considering the overlayed size distributions with blue and red histograms as shown in Figure 2.3.14(b), it is reasonable to propose that Pt_{1415} and Pt_{2057} nanoparticles have similar shape distributions.

The low population of tetrahedra also was discovered in the Pt_{5000} nanoparticles growing in the 200 sccm of Ar gas, which the mass spectrum was drawn by blue in Figure 2.3.14(a) with a lower beam current peak (around 70 pA). Similarly, nearly 400 nanoparticles were shape-identified that there were 10-14% of tetrahedra but the octahedra occupied nearly 80%, much higher than the population of octahedral Pt_{5000} nanoparticles (42-48%) prepared with 90 sccm of Ar gas. This result also matches the relationship of populations of octahedra and the cooling gas flow rates that a high cooling flow rate would induce a higher population of Pt octahedra due to the longer transmit time.

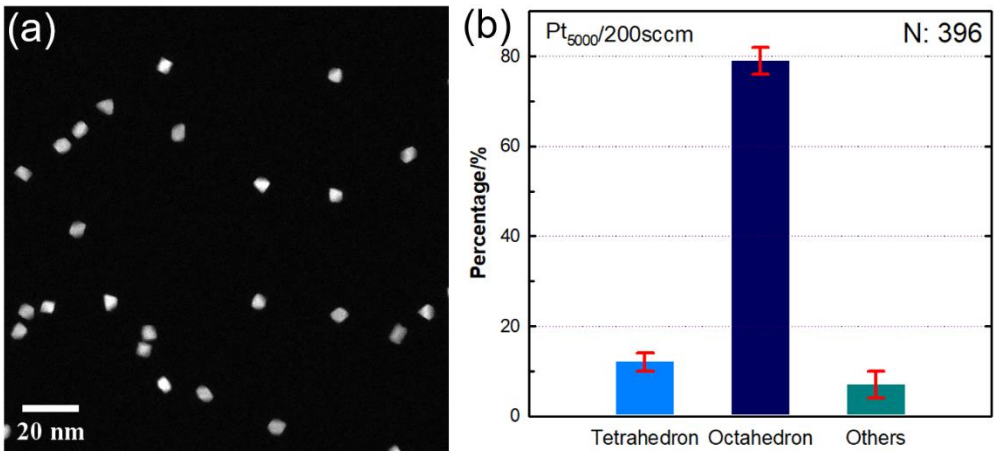


Figure 2.3.16. Pt_{5000} nanoparticles (a) were prepared with 200 sccm of Ar gas flow rate; (b) shape population distribution.

2.4. Palladium and Nickel nanoparticles

Pd and Ni nanoparticles were synthesized using the cluster source. Octahedral shape was

obtained by applying high sputtering powers for both Pd and Ni nanoparticles. In addition to the octahedral shape, decahedral and icosahedral Pd nanoparticles were formed in the gas phase, even though their populations were only 10% in total. Interestingly, only icosahedral shapes of Ni nanoparticles were prepared when the sputtering power was 10 W. In contrast, Ni nanoparticles were formed with multi-structures, such as icosahedral, decahedral, tetrahedral, and octahedral shapes, where the sputtering power was increased to 75 W. It demonstrates that high sputtering power has completely opposite influences on the shapes of Ni and Pd nanoparticles that high sputtering powers lead to high populations of icosahedral and decahedral Pd nanoparticles, but low populations of Ni icosahedra.

2.4.1. Octahedral palladium nanoparticles

There are several reports on the preparation of Pd nanoparticles using magnetron-sputtering gas condensation[125,130,131], but the structure and shape formation of Pd nanoparticles by the gas phase synthesis have not been thoroughly investigated. Figure 2.4.1 shows the atomic resolution HAADF-STEM images of octahedral (a, d), decahedral (b, e), and icosahedral (c, f) Pd nanoparticles, which were prepared in the cluster source with power of 135 W and an Ar gas flow rate of 90 sccm at room temperature. Using the lateral TOF, the particles with sizes of nominally 3800 (a-c) and 12000 (d-f) Pd atoms were mass-selected to deposit on TEM grids for structural investigation. For shape identification of Pd nanoparticles, simulated STEM images were generated as shown in Figure 2.4.1(g-i), for an example. The shapes of Pd nanoparticles were recognized by close matches of the contours and the intensity variations

between the experimental Pd images and the simulations. However, the "missing atoms" truncate the edges and vertices of Pd nanoparticles in Figure 2.4.1, especially in octahedral shapes (a, d), which indicates the instability of atoms at the edges and vertices.

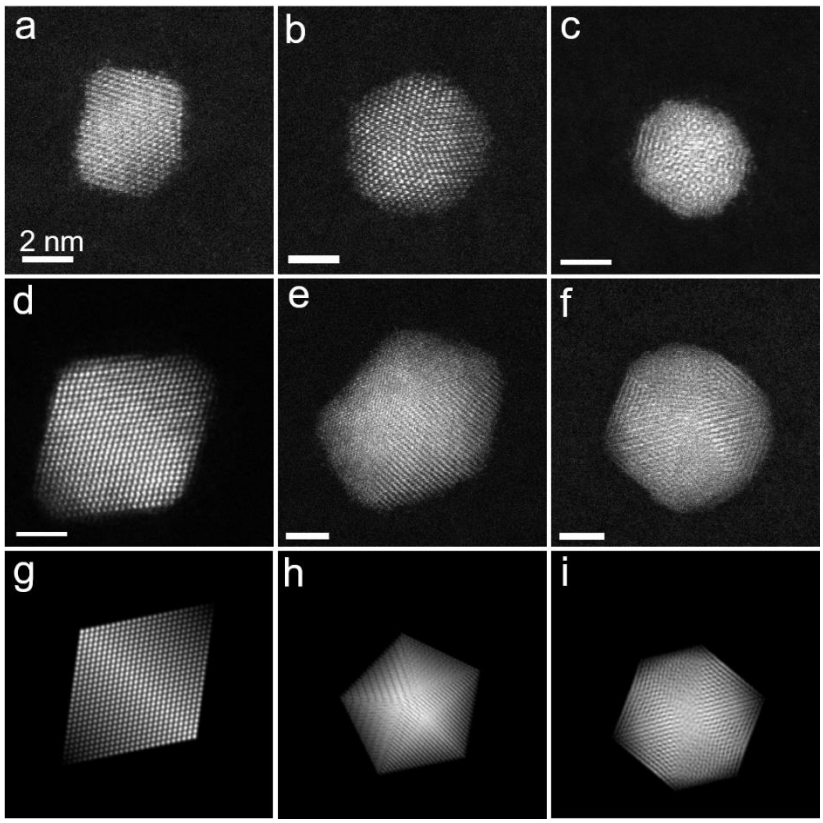


Figure 2.4.1. The representative Pd nanocrystals with octahedral (a, d), decahedral (b, e), and icosahedral (c, f) structures. Pd nanocrystals shown in (a-c) were size-selected with 3800 Pd atoms; the size of Pd nanocrystals in (d-f) were about 12000 Pd atoms. The scale bars are 2 nm. (g-i) The simulated octahedral, decahedral, and icosahedral Pd_{12000} nanocrystals.

The shapes of Pd_{12000} nanoparticles (Figure 2.4.2), which were synthesized using a sputtering power of 135 W under the 90 sccm of Ar gas at room temperature, was classified into four groups: octahedron, decahedron, icosahedron, and other shapes. Octahedral Pd nanoparticles accounted for the majority (88%), followed by decahedra (6.9%) and icosahedra (3.6%). This demonstrates that Pd octahedra are much more easily formed than decahedra and icosahedra in

the gas phase, which agrees with the theoretical prediction[29].

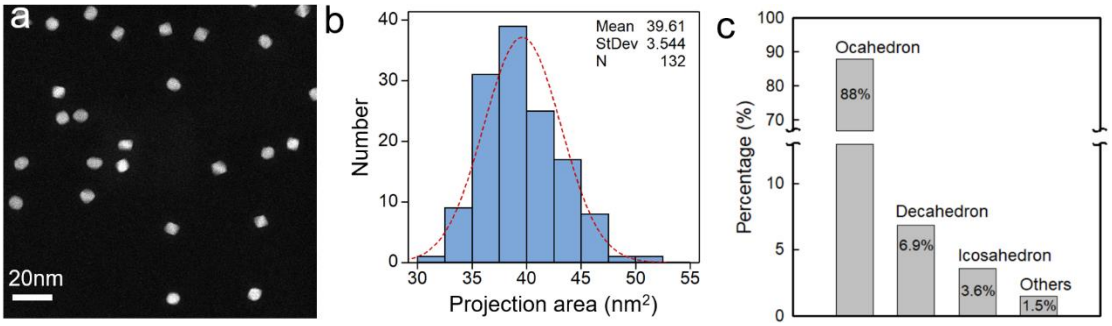


Figure 2.4.2. (a) HAADF-STEM image of Pd_{12000} nanocrystals prepared with 135 W and 90 sccm of Ar gas flow rate at the room temperature, which the Pd nanoparticles show sharp corners and near square shapes. (b) The size distribution of prepared Pd_{12000} nanocrystals, which the projected area of the Pd nanocrystal was used to present the size of octahedral Pd nanocrystals. (c) The population distribution of Pd_{12000} nanocrystals with different shapes, which 392 nanoparticles were atomic imaged for shape identification.

For further investigation into the influence of the sputtering power on the population distribution of Pd nanoparticles, Pd_{3800} nanoparticles were prepared using the same conditions, except for the sputtering power: 75 W and 135 W, respectively. Figure 2.4.3 gives the images of Pd_{3800} nanoparticles prepared with 75 W (a, b) and 135 W (c, d), but there is no obvious difference on their morphologies. Both mass spectra produced by 75 W and 135 W can be fitted well using a normal function as shown in Figure 2.4.3(e), suggesting that Pd nanoparticles grow through adatom condensation by two-body collision rather than particle-particle aggregation, which leads to either dendritic or elongated shapes. A small shift (about 200 atoms) was observed on the peak of the mass spectra accompanied with the increase of beam current at the peak as the sputtering power was strengthened from 75 W to 135 W. This suggests that the sputtering power had minimum impact on the size distribution and the growth mode of Pd nanocrystals, but increasing the number of Pd nanocrystals. 260 nanocrystals and 156

nanocrystals prepared using 75 W and 135 W of sputtering power, respectively, were shape-identified from atom-resolved images. The statistical percentages of Pd_{3800} nanoparticles with octahedral, decahedral, and icosahedral structures are shown in Figure. 2.4.3f. Pd octahedra occupied the most percentages (around 90%) for both Pd nanoparticles, while the population of decahedra and icosahedra had 6-8% and 1-2%, respectively. Taking the error bars (about 2%) of populations into consideration, both 75 W and 135 W prepared the same percentages of octahedral, decahedral, and icosahedral Pd nanoparticles.

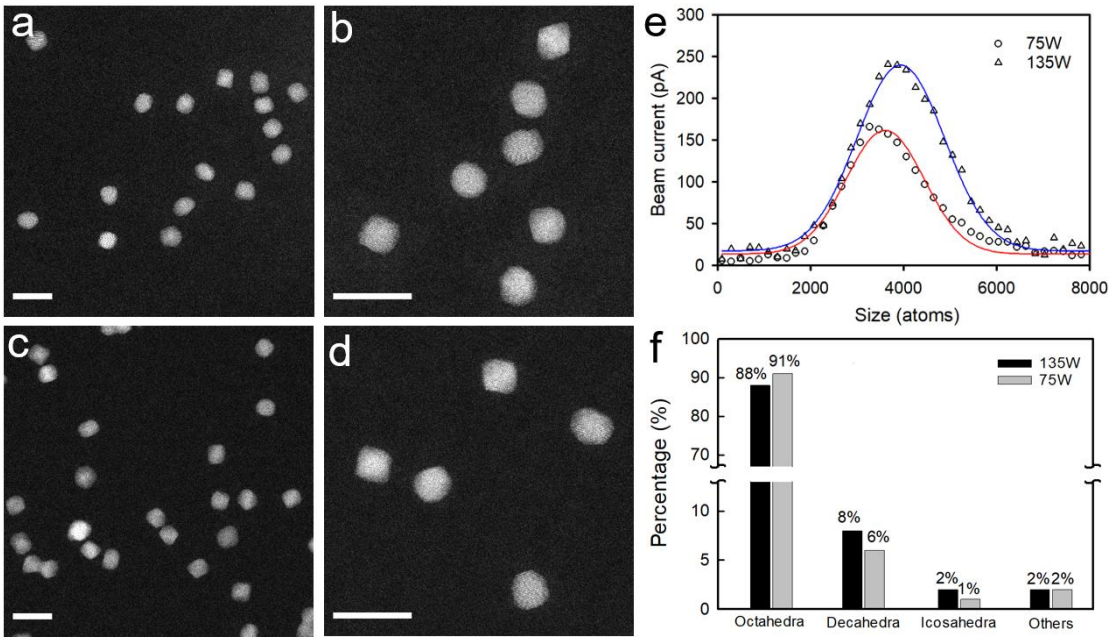


Figure 2.4.3. Influence of sputtering power on the structure of Pd_{3800} nanocrystals. (a) and (b) Pd_{3800} nanocrystals prepared using 75 W. (c) and (d) Pd_{3800} nanocrystals prepared using 135 W. (e) The mass spectra of Pd nanocrystals sputtered using 75 W and 135 W, respectively. (f) The percentages of octahedra, decahedra, icosahedra, and other irregular structure. The scale bars are 10 nm.

The population distribution of Pd_{3800} nanoparticles (Figure 2.4.3f) closely matches that of Pd_{12000} nanoparticles (Figure 2.4.2c), which were both prepared with the sputtering power of 135 W. This suggests that the final size as well as the growth rate have little impact on the shape

formation of Pd nanocrystals.

From the perspective of the thermodynamic Wulff construction[123,132], the Pd nanocrystals growing in the gas environment should form decahedra or truncated octahedra for large sizes[133]. However, the most popular shape in our experiment is octahedra with small vertex-truncations when the high sputtering power and no-chilled argon gas were applied. We believe there are two factors, temperature and the density of atomic vapour, contributing to the octahedra-formation. The high density of atomic Pd vapor produced by the strong sputtering power supported the fast deposition rates. In the previous reports, low sputtering power (no more than 50 W) caused low density atomic Pd vapour, producing Pd nanoparticles with round shapes[130,131]. The temperature has been attributed to the formation mechanism of octahedra using theoretic calculations and simulations[24, 127] in its influence on the diffusion rates of adatoms on the surface of Pd nanocrystals.

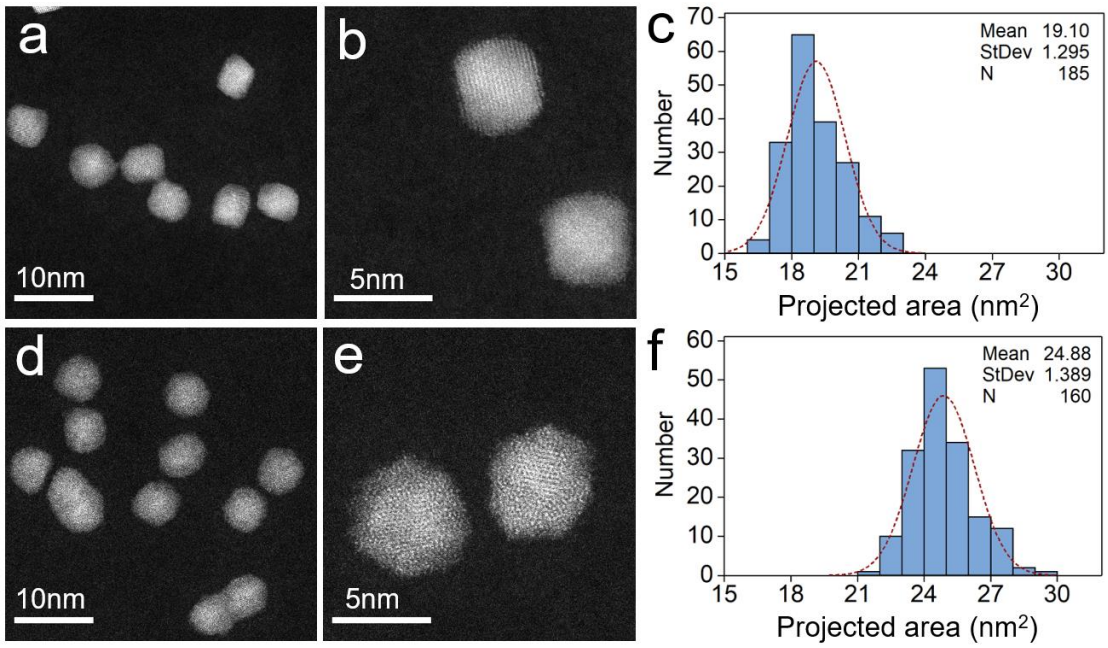


Figure 2.4.4. Naked Pd_{3800} nanoparticles oxidized in the air. (a)-(b) Pd_{3800} nanoparticles imaged after preparation. (c) The size distribution of Pd_{3800} without oxidization, which the average diameter was 4.9 nm. (d)-(e) Pd_{3800} nanoparticles exposed in the air for 7 days. The Pd_{3800} nanoparticles transformed into amorphous structure. (f) The size distribution of oxidized Pd_{3800} nanoparticles, 30% larger than the fresh Pd_{3800} in terms of the projected area.

Naked Pd nanoparticles, different from Pt nanoparticles, can be readily oxidized by the oxygen at ambient pressure. Figure 2.4.4 shows the transformation of naked Pd nanoparticles prepared using the cluster source before and after exposure in the air. The octahedral shapes became rounder and the pristine FCC structure turned amorphous from the exterior layers, as shown in Figure 2.4.4(e). The oxidation process can be monitored by the projected area of particles, as shown in Figure 2.4.4(c, f), with the mean area of naked Pd particles increased from 19.1 nm^2 to 24.9 nm^2, after 7 days exposure in the air.

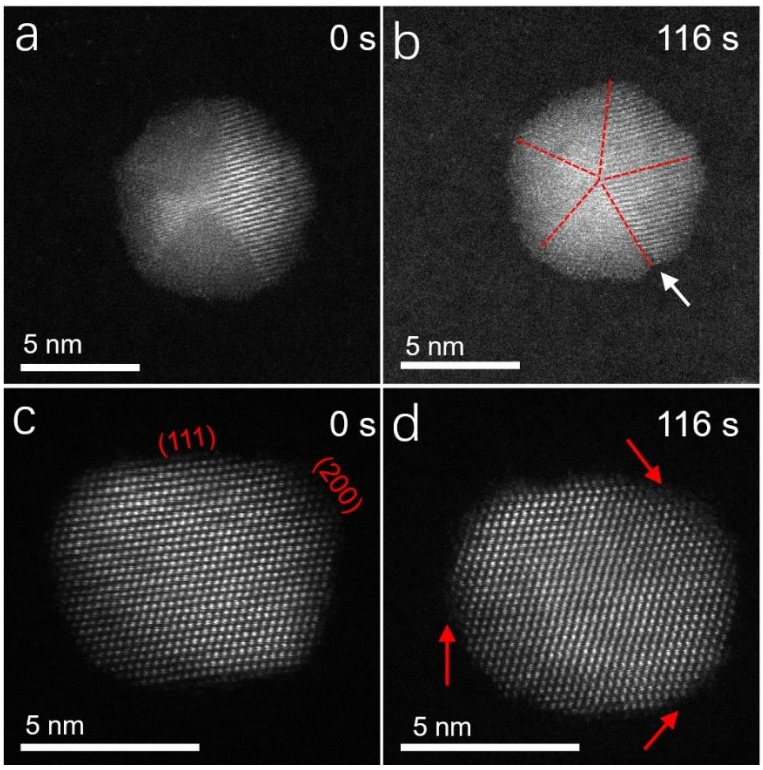


Figure 2.4.5. HAADF-STEM images of Pd_{12000} decahedron (a) and octahedron (c) after the electron beam irradiation with a dose of 1.3×10^4 e- per $Å^2$ per second for 116 seconds (b, d). No structural transformation was observed but the atoms at the edges and vertices of decahedron/octahedron diffused/moved away, making the decahedron/octahedron rounder. (Imaging and beam irradiation conducted in JEM-2100F working at 200 kV)

The structural stability of Pd octahedral and decahedral nanoparticles was investigated by the electron beam irradiation. Figure 2.4.5 displays the shape changes of Pd nanoparticles irradiated for 116 seconds with a dose of 1.3×10^4 e^- per $Å^2$ per second. The Pd decahedron covered with (111) facets in Figure 2.4.5(a, b) experienced small changes, except from the atoms missing at the boundary twin pointed by a white arrow due to the atom diffusion on the surface. However, the octahedron in Figure 2.4.5(c, d) suffered more serious loss of atoms than the decahedron, as shown by the red arrows indicating that atoms at the vertex and (200) facets diffused to neighbor facets (e.g. (111) facets) under the irradiation, making the octahedron rounder.

Therefore, the atoms on the (111) facets may be more stable than atoms on other facets and vertexes.

2.4.2. Nickel nanoparticles: From an icosahedron to an octahedron

The structural motifs of Ni nanoparticles with different sizes was predicted by calculating many-body potentials[134]. There were found that Ni nanoparticles are mainly icosahedral structures when their sizes are less than 1200 atoms[15], while FCC and decahedral structures become energetical favorites at sizes larger than about 2000 atoms[29,134]. With magnetron-sputtering, FCC and decahedral Ni nanoparticles having large sizes (e.g. 5000 atoms and 17000 atoms) can be prepared using 1-inch target when applying high sputtering powers. Figure 2.4.6 shows Ni_{2000} clusters with icosahedral structures, which were prepared using a low sputtering power of 10 W. When the sputtering power was raised to 50 W, decahedral and FCC structural Ni clusters (Figure 2.4.7) appeared with the populations of 10% and 12.4%, respectively.

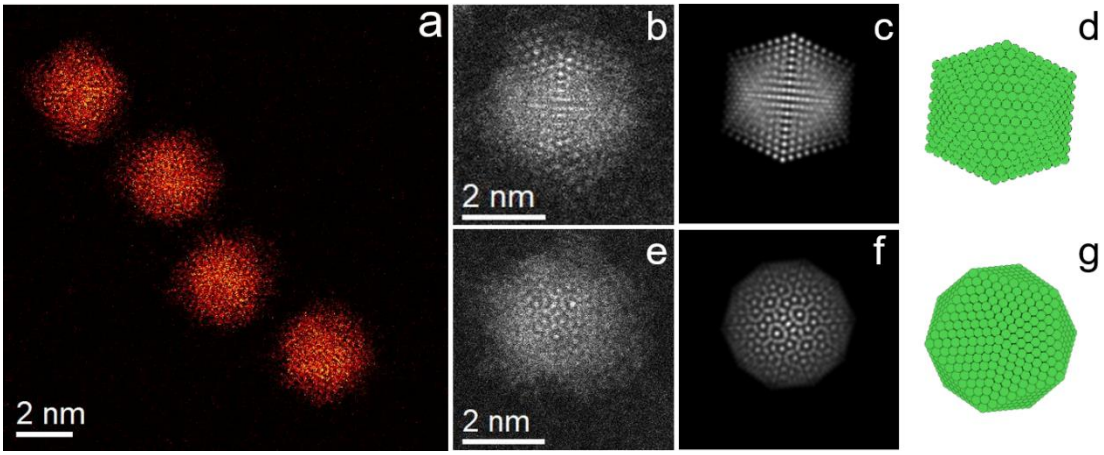


Figure 2.4.6. Ni clusters prepared using 10 W. Clusters mainly show an icosahedral structure. (a) Ni clusters mass-selected with 2000 atoms. (b) and (e) HAADF-STEM images of Ni clusters. (c) and (f) Simulated HAADF images generated by icosahedral models (d) and (g). It indicates that Ni clusters only grow with icosahedral structure as the sputtering power was low (e.g. 10 W).

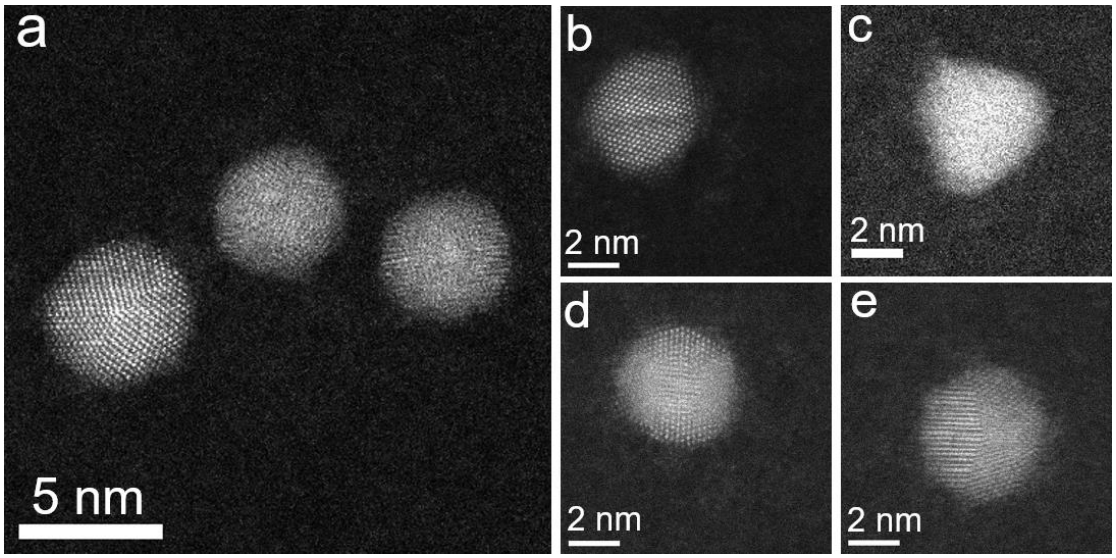
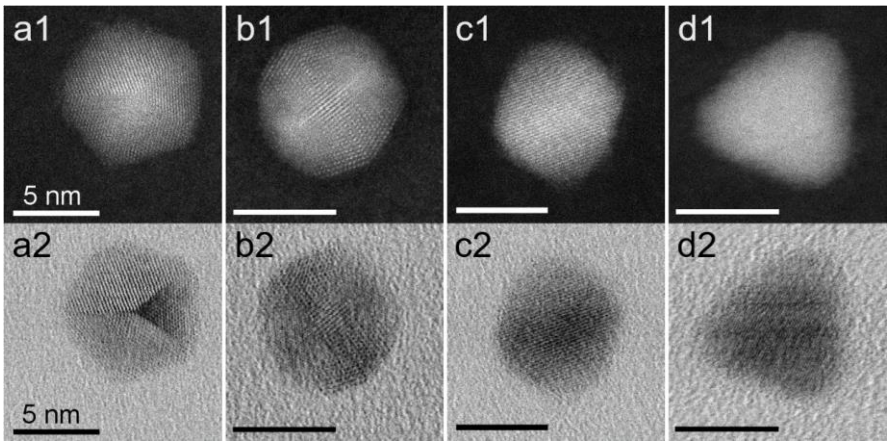


Figure 2.4.7. Pure Ni clusters prepared using 50 W and mass-selected with the nominal size of 5000 Ni atoms. Decahedral (e) and icosahedral (d) Ni clusters were the majority, while octahedral (b) and tetrahedral (c) Ni clusters were formed. Statistically, 77.6% of Ni clusters (169 clusters were structure-identified) have the icosahedral structures, more than the fcc (12.4%) and the decahedra (10.0%).

The population of icosahedral Ni nanoparticles decreased further to about 25% as the sputtering power is increased to 75 W and the size rose to 17000 atoms. For FCC structures, both octahedral and tetrahedral shapes can be observed in Ni_{17000} nanoparticles with 52% and 6%, respectively. As the atoms at the vertexes of octahedra are energetically unstable, the octahedra are truncated to different degrees. This observation agrees with the calculation results from the modified Wulff construction that truncated octahedral Ni nanoparticles are preferred structures for large nanoparticles[19].



Decahedron	Icosahedron	Octahedron	Tetrahedron
17%	25%	52%	6%

Figure 2.4.8. Besides icosahedra (b1, b2), decahedra (a1, a2), fcc structures (octahedra (c1, c2), and tetrahedra (d1, d2)) were observed in Ni_{17000} clusters prepared with 75 W (high sputtering power). 65 of clusters in total were structure-identified, with percentages rounded.

2.5. Structure stability of Pt nanoparticles

In-situ heating. The morphology change of Pt octahedral and tetrahedral nanoparticles was investigated using in-situ heating. Wildfire Nano-chips developed by DENSsolutions, Netherlands (Figure 2.5.1a) were employed for in-situ heating. These chips exhibit 10 windows coated by electron transparent silicon nitride (SiN) films with a total viewing area of 850 μm^2 onto which Pt nanoparticles were deposited. There are four contacts for Joule heating and measuring temperature: two of the contacts are responsible for delivering the current to heat the SiN film, while the other two contacts measure the micro-heater's resistance, which is linearly proportional to its temperature[135]. The metallic heating spiral and the fine control of heating current guarantee a temperature stability within 1 kelvin (K). Both radiative heat loss and heat transfer by conduction through the membrane enable the nano-chip to cool down with

an ultrafast rate (e.g. 2000 ℃/min in this experiment) as shown in Figure 2.5.1(c)[135]. These nano chips can withstand high temperature up to 1100 ℃. Figure 2.5.2 shows the temperature curves set for in-situ heating with the heating rate set to 1000℃/min while a faster cooling rate (2000℃/min) was used to freeze the atoms. Nanoparticles were heated at high temperature for 60 seconds at each heating cycle. Nanoparticles were imaged by the HAADF detector after the temperature had returned to room temperature. The beam density of the microscope was 15 pA for the STEM imaging. For reducing the electron influence, a pixel dwell time of 10 μs with 512×512 pixel area was chosen. The electron dose rate was round 0.7~1×10^4 electrons/$Å^2$ per frame. For reducing the electron irradiation of the nanoparticles, the electron beam was turned off during the heating.

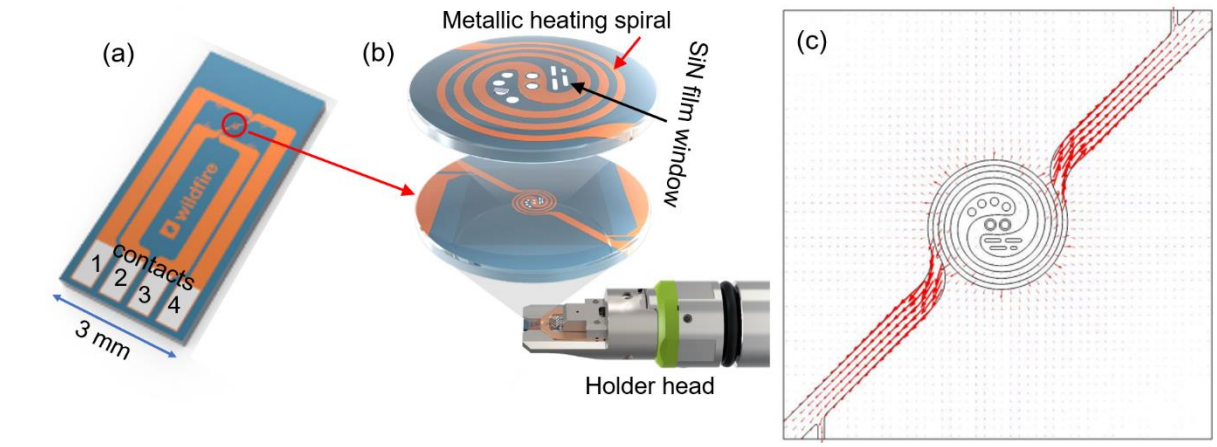


Figure 2.5.1. (a) A Wildfire Nano-chip for in-situ heating. (b) Schematic of the structure of Nano-chip and the head of the holder. (c) Simulation result of the total heat flux across the suspended membrane with the microheater at 1 000 °C. Arrows are proportional to the heat flux that most of heat is conducted through the metal. Figure (a) adapted from https://denssolutions.com/products/wildfire/. Figure (b) adapted from Ref.[135]. Figure (c) and caption adapted from the supplementary material of Ref.[135].

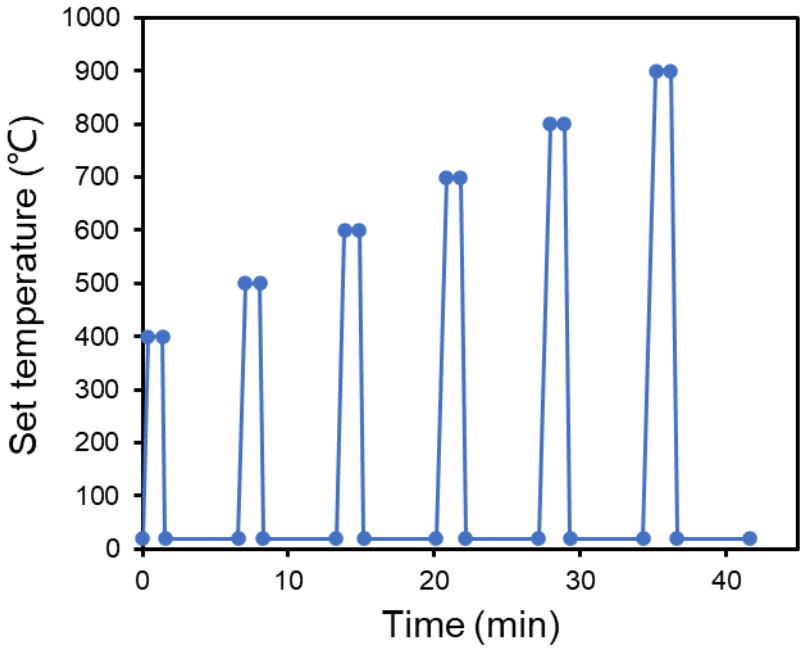


Figure 2.5.2. An example of the temperature settings of the Nano-chip. The heating rate and the cooling rate were 1000 ℃/min and 2000 ℃/min, respectively. Samples were annealed at each temperature for one minute.

Figure 2.5.3 shows the images of tetrahedral (a) and octahedral (b) Pt_{2057} nanoparticles after quenching down to room temperature from different annealing high temperatures. The morphology change of both tetrahedron and octahedron was recorded. Both starting morphologies transformed into truncated octahedron with (100) and (111) facets after annealing at 900 ℃. The tetrahedron in Figure 2.5.3 (a) maintained its shape at least until 700 ℃, even though some atoms rearrange at the vertices. The well-formed tetrahedral tip at the top and the less-well-formed tip on the left bottom of image rounded at 500 ℃. While the truncated corner on the right of the image grew a little bit, which was activated by surface diffusion, indicating autocatalytic growth happening at by modest temperatures. Further heating from 700 ℃ to 900 ℃, yielded (100) facets forming at the tips of the pristine tetrahedron, completed by dramatical mass movement. The surface energies (γ) of (111) and (100) facets are 1.49 and 1.89

J/m^2 (at 0 K), respectively (https://legacy.materialsproject.org/materials/mp-126/). According to the Wulff construction, the ratio of $\gamma(111)/h(111)$ in the annealed nanoparticle after 900 ℃ was 1.49/1.77 = 0.84, which was smaller than $\gamma(100)/h(100)$ = 1.89/1.66 = 1.14, where the distance *h* is measured in nanometers (nm). This indicates that the tetrahedron did not reach an equilibrium shape (Wulff construction with a larger (100) facets than the experimental ones) even after undergoing several annealing cycles at elevated temperatures and transforming into a truncated octahedron. The tetrahedron exhibits different mass transport mechanisms at different facets ((100) and (111) facets) and temperatures. This suggests that the surface diffusion barriers of Pt nanoparticles are heterogeneous. This enables the experimental shape control of Pt nanoparticle synthesis.

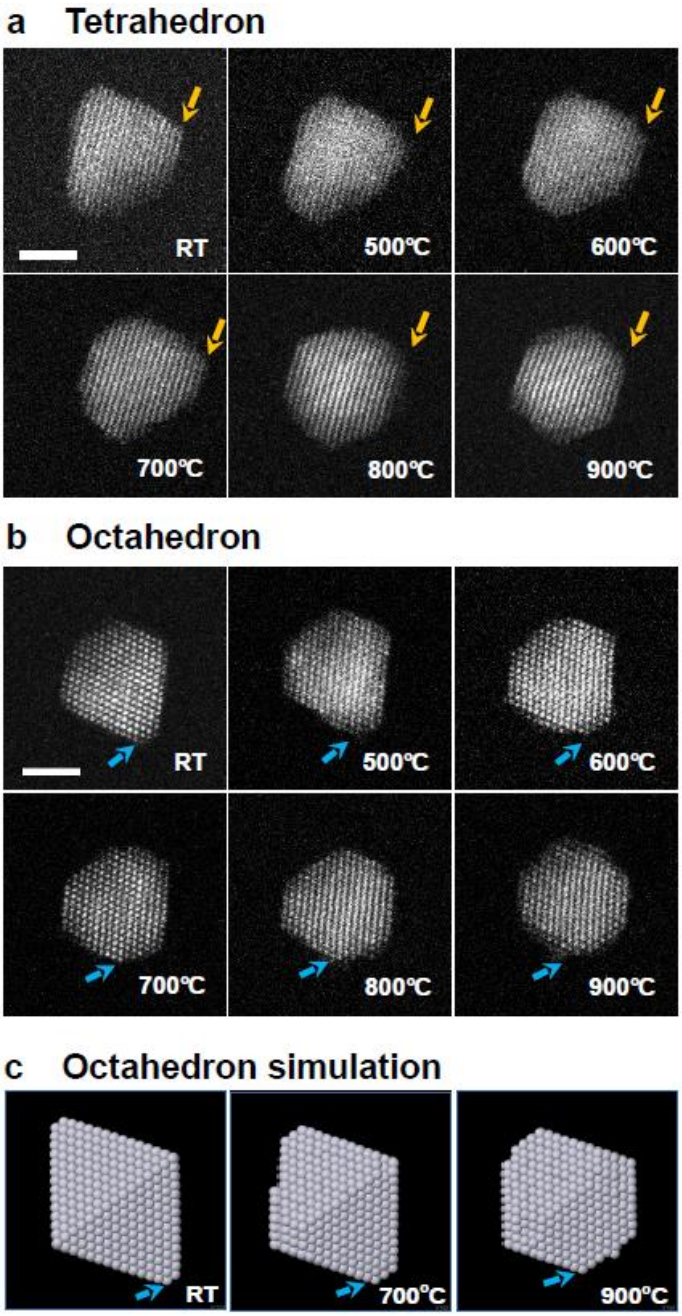


Figure. 2.5.3. Direct visualisation of thermal transformation of Pt_{2057} tetrahedral nanoparticles with *in-situ* heating experiment and comparison with the simulation. HAADF-STEM images of (a) tetrahedral Pt_{2057} and (b) octahedral Pt_{2057}, quenched from various high annealing temperatures as indicated. (c) Simulation of the annealing of an octahedral Pt_{2030} structure, by heating up from RT to 700 and 900°C and cooling back to RT, with rates of 1 K/ns (heating) and -1 K/ns (cooling). The simulation is indicative of the trend of structural evolution, which agrees with the experiment. The arrows indicate the truncated tips. 2 nm-scale bars are used for all the experimental and simulation images. Figure and caption taken from Ref.[120].

The same shape change was observed from the octahedron (Figure 2.5.3b) imaged along the [011]-zone axis. The upper exposed (100) facet extended its area from 500 ℃ to 700 ℃ through surface atoms rearrangement, but the area reduced a little at 800 ℃ and 900 ℃. The other well-formed tip at the bottom of image transformed to a (100) facet in the whole heating process. The asymmetrical mass transports occurring at top and bottom octahedral tips during annealing suggest that atoms on a small (100) facet diffused more easily than on a large (100) facet. After 900 ℃ annealing, the nanoparticle exhibited {111} and {100} planes with distances of 1.59 nm and 1.92 nm, respectively, from its center. Based on the Wulff theorem, the ratio of $\gamma(111)/h(111)$ in the annealed octahedron was 1.49/1.59 = 0.94, which is similar to $\gamma(100)/h(100)$ = 1.89/1.92 = 0.98, suggesting that a Wulff construction was formed. The shape transformations of a tetrahedron and an octahedron under high-temperature annealing demonstrate that the truncated octahedron is the thermodynamic equilibrium shape. Conversely, the octahedral and tetrahedral shapes are non-equilibrium shapes. Moreover, the octahedral shape has a higher tendency to achieve a Wulff construction than the tetrahedral shape. This observation highlights the limitations of using octahedral and tetrahedral Pt nanoparticles at high temperatures (e.g. 500 ℃), where shape transformation can occur and result in worse catalytic performance. Moreover, preparing Pt nanoparticles at high temperatures (e.g. 900 ℃) can obtain thermodynamically equilibrium truncated octahedra.

The annealing simulations (Figure 2.5.3c) conducted by molecular dynamics present the same result as shown in Figure 2.5.3(b). To study the structural evolution of an octahedral Pt_{2030} nanoparticle, the simulation was performed in which the nanoparticle was annealed by elevating

its temperature from room temperature to 700°C and 900°C, followed by cooling back to room temperature at rates of 1 K/ns and -1 K/ns, respectively. Upon annealing at 700°C and 900°C, the morphology of the nanoparticle in Figure 2.5.3c transformed from its original octahedral shape with a slight truncation at its vertex to a truncated octahedron, revealing {100} facets due to the diffusion of atoms from its {100} planes to adjacent {111} surfaces. The outcomes of the simulations are consistent with the experimental findings and offer significant insights into the course of structural alterations that take place during annealing at elevated temperatures, enabling an octahedral structure to reach equilibrium and become a truncated octahedron. This simulation proves that the octahedral and tetrahedral shapes are out-of-equilibrium states for nanoparticles, and that they can reach a thermodynamically stable structure on short annealing time scale at a temperature of above 700 ℃.

Shape-dependent melting behaviours of Pt nanoparticles. The temperature at which a liquid layer forms on the surface of a nanoparticle and moves at a substantial rate into the solid is known as the melting temperature of a nanoparticle[136]. A monotonic decrease in melting temperature has been observed with decreasing nanoparticle size[136,137,138]. The Gibbs-Thomson equation[136,139] describes this relationship between the equilibrium melting temperature (T_m^R) of a nanoparticle and its radius *R*:

$$T_m^R = T_m^{bulk} \cdot exp\left[-\left(\frac{2\gamma_{s,l}V_s}{\Delta H_m^R}\right)\frac{1}{R}\right] = T_m^{bulk} \cdot \left[1-\left(\frac{2\gamma_{s,l}V_s}{\Delta H_m^{bulk}}\right)\frac{1}{R}\right], \quad (2\text{-}5\text{-}1)$$

where T_m^{bulk} is the melting temperature of the bulk material, $\gamma_{s,l}$ is the solid-liquid surface tension, V_s is the molar volume of the solid, and ΔH_m^R is the molar enthalpy of melting at T_m^R, which is approximately equal to ΔH_m^{bulk} of the bulk. In addition to the impact of size, the

melting temperature of nanoparticles is also affected by their shape, which is related to surface tension. For instance, cubic and tetrahedral Pt nanoparticles with an 8 nm diameter, which were coated with capping polymer, exhibited surface melting at an approximate temperature of 600 ℃ much lower than the melting point of bulk platinum (1769 ℃), according to the report in Ref.[140]. This result is in agreement with the predictions of molecular dynamics simulations (Figure 2.5.4), which predicts that the shape of Pt nanoparticles influences their melting temperature, with tetrahedral Pt nanoparticles exhibiting the lowest melting temperature compared to other shapes[141].

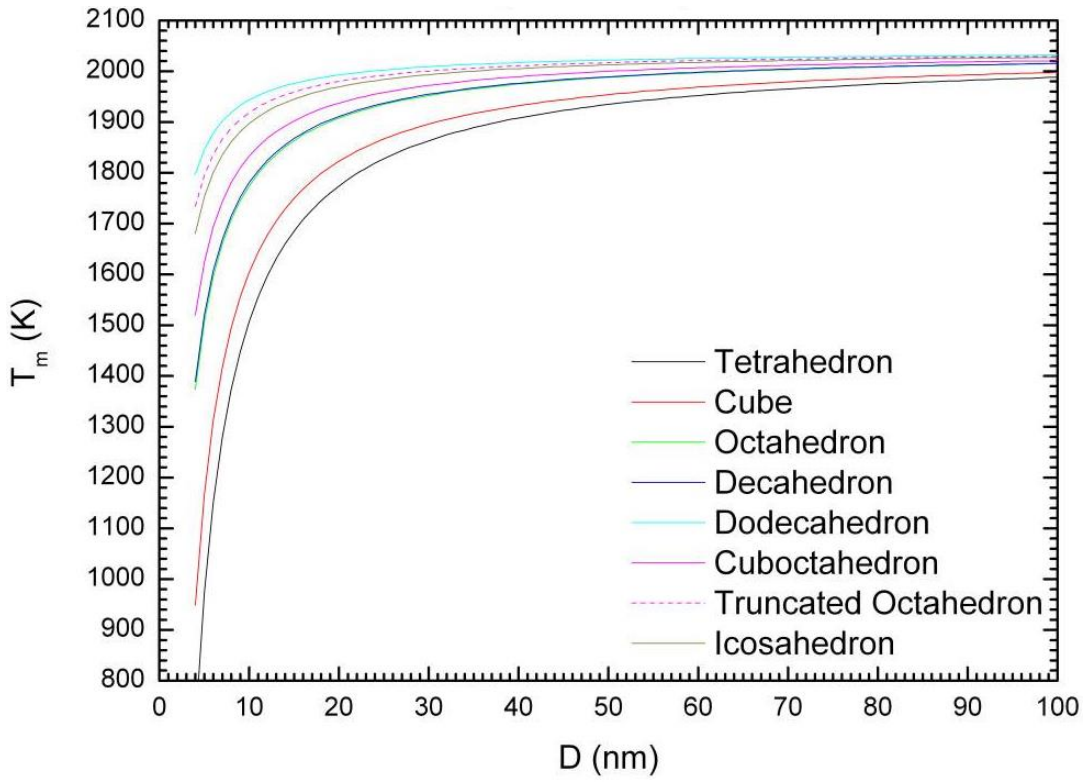


Figure 2.5.4. Size-dependent melting temperature of platinum versus the size for different shapes. Figure and caption adapted from the reference [141].

The present in-situ experiments, as illustrated in Figure 2.5.3(a-b), examine the melting behaviour of tetrahedral and octahedral Pt_{2057} nanoparticles through measuring the

corresponding HAADF intensities. Notably, a sharp change is observed at the interface of the melting surface and the solid core, providing an indicator of melting behaviours of Pt nanoparticles[137]. Figure 2.5.5 shows the HAADF-STEM image of tetrahedral Pt_{2057} nanoparticle after annealed at 700 ℃ and 800 ℃, respectively. Through the implementation of a rapid cooling rate (2000 ℃/min), the molten surface of this nanoparticle was frozen, as marked by red rectangles in Figure 2.5.5(a, c). The corresponding line profiles of the HAADF intensity across the nanoparticle are presented in Figure 2.5.5(b, d), wherein a dramatic change is observed. This change is attributed to the rapid movement of atoms from the surface to the solid core that is induced by the process of melting[136,137]. As increasing the temperature from 700 ℃ to 800 ℃, more melting surfaces were observed as shown in Figure 2.5.5(c, d). It indicates that the melting temperature of tetrahedral Pt_{2057} nanoparticle is no higher than 700 ℃.

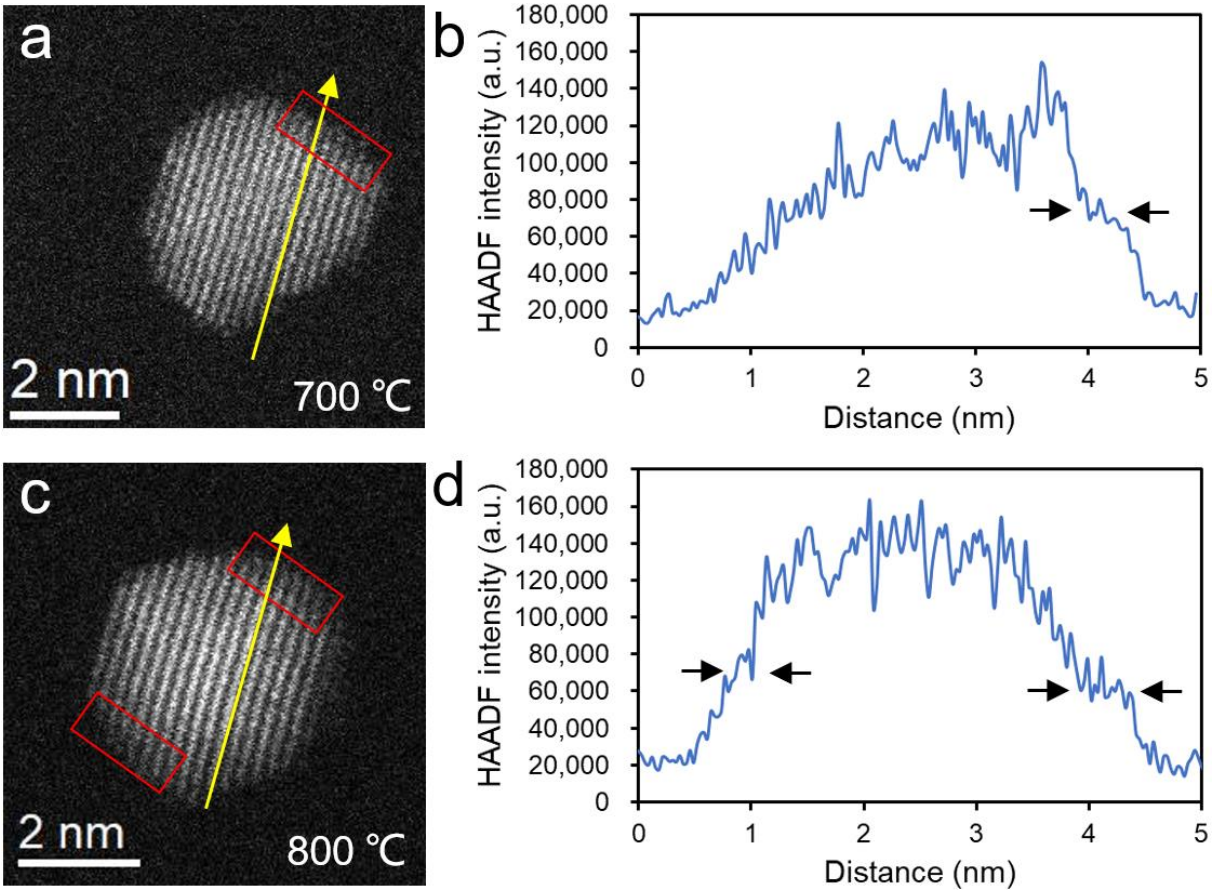


Figure 2.5.5. HAADF-STEM images of tetrahedron, which has been presented in Figure 2.5.3, were captured at RT following cooling from annealing at 700 ℃ and 800 ℃, respectively. The HAADF intensity across the particle was plotted, with the sharp changes in intensity indicated by black arrows suggesting the occurrence of melting behaviour.

The obvious change observed in the HAADF intensity (Figure 2.5.6) of octahedral Pt_{2057} nanoparticle appeared after the heating temperature was raised to 800 ℃, higher than the melting point observed in tetrahedral Pt_{2057} nanoparticles. Despite the observed melting temperatures of octahedral and tetrahedral Pt nanoparticles being 100-200 K lower than the predicted values presented in Figure 2.5.4, it is likely that the discrepancy can be attributed to the relatively short annealing time (1 minute) employed in the experiment. Nevertheless, it is

noteworthy that tetrahedral Pt nanoparticles exhibit a lower melting temperature than their octahedral counterparts, which is consistent with the simulation results[141].

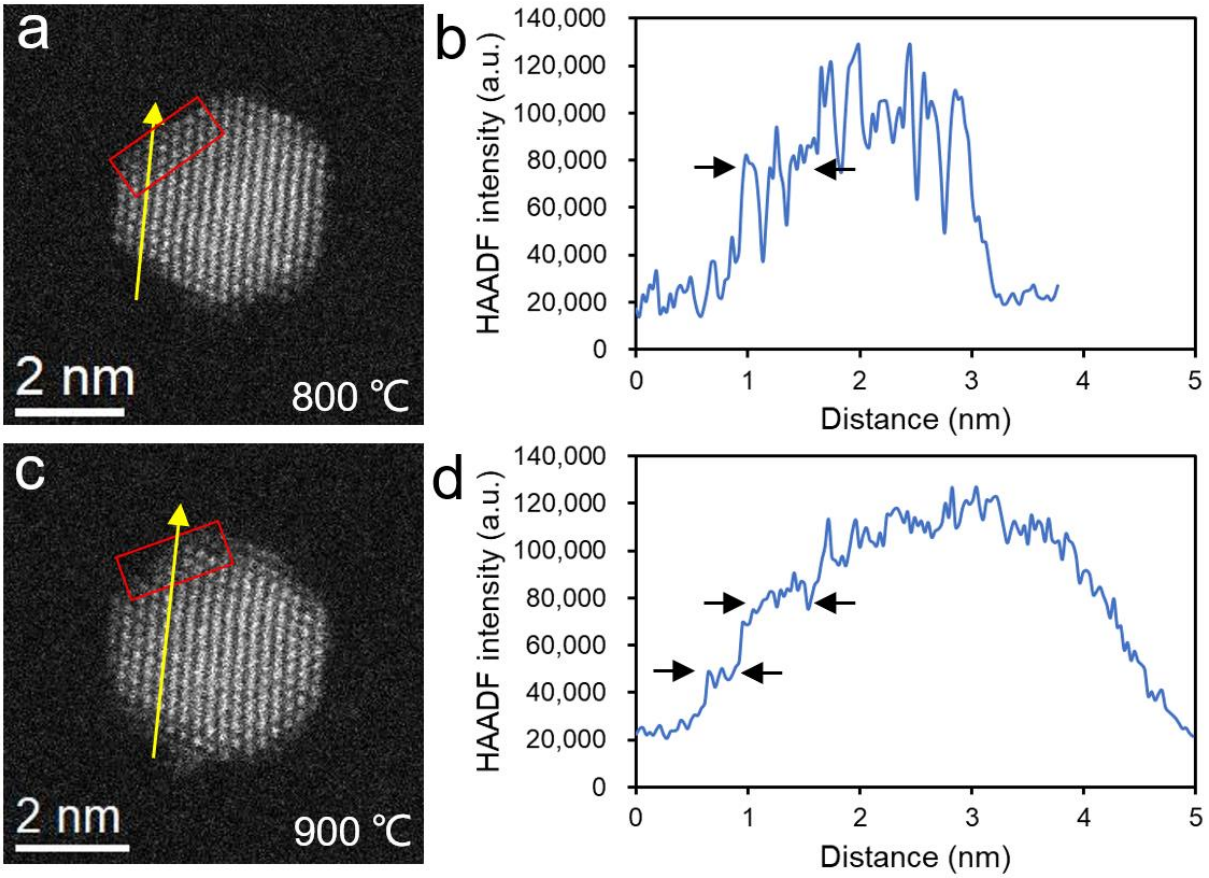


Figure 2.5.6. HAADF-STEM images of the octahedron, as shown in Figure 2.5.3, were acquired at room temperature subsequent to cooling from annealing at 800 ℃ and 900 ℃, respectively. The HAADF intensity was plotted across the particle, and the obvious changes in intensity following the black arrows suggest the occurrence of melting behaviour.

Electron beam irradiation. An electron beam with high energy, e.g. 200 keV or 300 keV, interacts with specimen, which may take place radiation damages to the specimen through three main mechanisms: knock-on displacement, ionization damage (radiolysis), and electrostatic charging effects[142,143,144,145]. As for metallic nanoparticles, especially for small nanoparticles, the knock-on displacement induces the morphology change, which has been simulated by

molecular dynamics and Monte Carlo techniques [146]. The beam scattering process on the atom of nanoparticles can be evaluated by the knock-on cross section (σ_{sd}) for interaction with a nucleus of atom, which is calculated using the Rutherford formula[147,148]:

$$\sigma_{sd} = (0.25barn)FZ^2\left(\frac{1}{sin^2(\theta_{min}/2)} - \frac{1}{sin^2(\theta_{max}/2)}\right) \quad (2\text{-}5\text{-}1)$$

$$F = [1 - (v\ /\ c)^2]\ /\ (^{v}/_{c})^4 \quad (2\text{-}5\text{-}2)$$

$$\theta_{m_{in}} = arc\,sin\left[2(E_{sd}\ /\ E_{max})^{1}/_{2}\right] \quad (2\text{-}5\text{-}3)$$

$$\theta_{max} = \pi - \theta_{min} \quad (2\text{-}5\text{-}4)$$

$$E_{max}(eV) \approx (1.1/A)[2 + E_0/(511keV)]E_0(keV)\ , \quad (2\text{-}5\text{-}5)$$

where v is the incident electron speed and c is the speed of light, Z is the atomic number, θ_{max} and θ_{min} represent the scattering angle range along the surface of nanoparticles, which are determined by the surface diffusion energy (E_{sd}), the incident electron energy (E_0), and the mass number (A). E_{max} is the threshold incident energy, which is 2.70 eV and 4.38 eV for platinum when the E_0 is 200 keV and 300 keV, respectively. In comparison, the binding energy (5.02 eV)[116] of Pt atoms is higher than the E_{max}. When an incident electron transfers energy to an atom, the atom emits a photon or a secondary electron and returns to its ground state. While the photon has minimal momentum in relation to its energy, a secondary electron with kinetic energy (K_e) possesses momentum and transfers an equal and opposite momentum to a Pt atom. The atom receives kinetic energy only if $K_e > K_e^{min}$, which may surpass the surface-displacement energy[147]. For Pt atoms, this value of K_e^{min} can be over 1 KeV. Hence, inelastic scattering by high-energy incident electrons does not lead to displacement (sputtering) when the E_0 is 200 keV and 300 keV[146].

Figure 2.5.7 shows the surface evolution of a decahedron, whose size is around 1850 atoms, calculating from the integrated intensity based on the fitted linear relationship between integrated intensity and sizes shown in Figure 2.1.6(a). The projected area, integrated intensity, and the peak intensity of this decahedron were calculated from the image series under the electron irradiation. Within the irradiation (432 seconds), a small reduction (about 6.7 %) of the projected area was observed. However, the integrated intensity and the peak intensity fluctuates drastically with sharp increases and reductions. Associated with the captured images, the orientation of the decahedron on the carbon film underwent small rotations as demonstrated in Figure 2.5.7 (k), which brought some of the facets on the decahedron close to an on-axis channelling condition (as shown in Figure 2.5.7e), leading to a significant overestimate in the integrated and peak intensity. Compared Figure 2.3.8(a) with Figure 2.3.8(h), the integrated intensity of this decahedron almost kept unchanged during the 432 seconds electron irradiation, which indicates that no atom escaped from this decahedron. However, this decahedron became rounded, which may be caused by the surface atom diffusion[146].

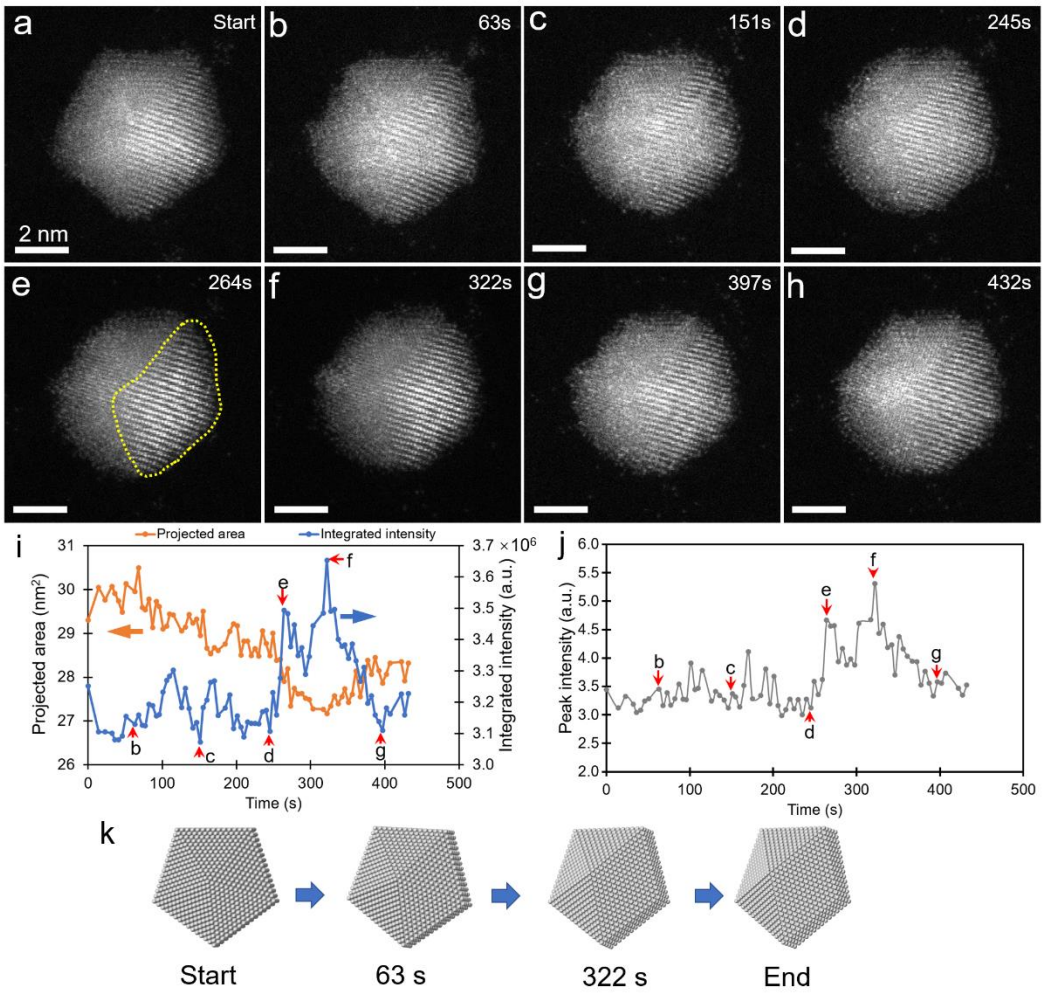


Figure 2.5.7. Electron irradiation on a Pt decahedron. (a-h) HAADF-STEM images of Pt decahedron under the electron beam irradiation with a dose rare of 3.7×10^4 e- per $Å^2$ for 432 seconds, conducting in JEM-2100F with a working voltage of 200 kV. (i) Changes of the projected area and integrated intensity of this decahedron under irradiation. The positions of images shown in (b-g) were labelled. (j) Changes of the peak intensity (the point with the maximum intensity) with time. Combining with the images shown in (a-h), the sharp increase of the peak intensity and the integrated intensity of the decahedron was caused by the rotation of the decahedron to the on-axis channelling condition, which the scattered intensity increased, leading to the increase of the brightness of the image. (k) The demonstration of decahedron rotating its landing angle under the electron irradiation.

The surface atom diffusion caused by the electron irradiation was investigated on a Pt octahedron, as shown in Figure 2.5.8. The first octahedron (Figure 2.5.8a-d) has similar small

truncations marked by yellow arrows. During the 500 s irradiation, the truncated vertices show a similar transformation caused by atom diffusion from (200) facets to their neighbour (111) facets pointed by white arrows. It indicates that atoms at non-close packed facets, e.g. (200) facets, are more easily sputtered by high-energy electron beam and diffused to low index facets, e.g. (111) facets. One more example, supporting this shown in Figure 2.5.8(e-h), this octahedron has different truncations on its left upper corner and the right lower corner. Under electron irradiation, the left vertex (yellow arrow) exposed larger (200) facets than the right one, which more atoms were sputtered from the left (200) facets (yellow arrow) and diffused to the nearby (111) facets.

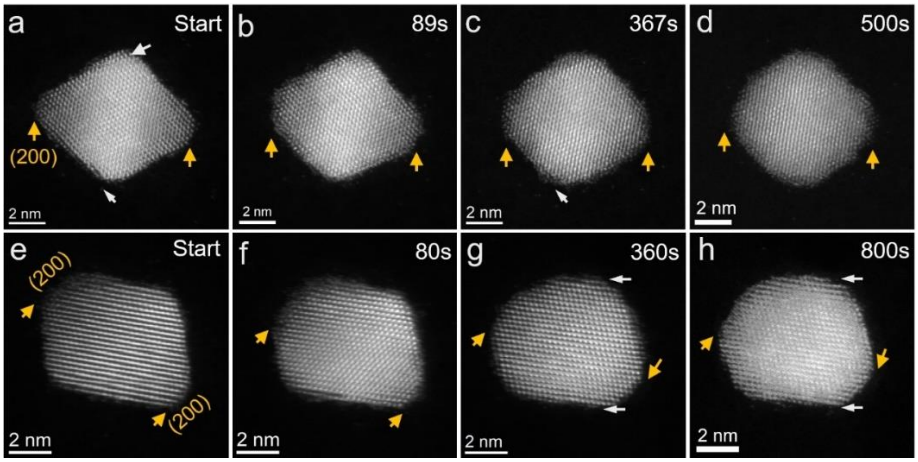


Figure 2.5.8. Pt_{10000} octahedra under the electron irradiation. Images were captured by the machine of FEI Themis G2 with a working voltage of 300kV with a camera length of 145 mm, using a dose rate of 7.6×10^4 e- per $Å^2$, which was calculated based on the screen current (101pA), pixel time (2.5μs per pixel), and the pixel size (0.091Å/pixel).

2.6 Conclusion

Pure nanoparticles of Pt, Pd, and Ni with octahedral, tetrahedral, icosahedral, and decahedral shapes were synthesized using the cluster source. Through controlling the preparation conditions, particularly the sputtering power and the cooling gas flow rates, octahedral and tetrahedral nanoparticles were achieved. For Pt nanoparticles, the population of out-of-equilibrium tetrahedra can be adjusted within a certain range. In addition to the FCC structures (octahedral and tetrahedral shapes), decahedral and icosahedral structures were also observed in Pd and Ni nanoparticles. Decahedral Pt nanoparticles also can be fabricated but with a low population. With the increase of sputtering powers, the number of icosahedral Ni nanoparticles reduced while the population of FCC structures increased. Decahedral Ni nanoparticles occupy a small percentage in the population, consistent with previous calculations.

The growth procedures of octahedral and tetrahedral nanoparticles are interpretated based on the results of the molecular dynamics simulations. The formation of Pt octahedra is contributed by the faster growth rate of (100) facets than (111) facets on the truncated octahedron, which is the representative kinetic Wulff construction. A novel growth pathway is proposed to elucidate the shape transformation from an octahedron to a tetrahedron, whereby the formation of stacking faults on the facets of octahedra causes the loss of symmetry during the growth process. The preparation of naked octahedral and tetrahedral nanoparticles provides further understandings of the out-of-equilibrium growth of metal nanoparticles in the gas-phase. It can be a new route to build the relationship between the physical and chemical properties and the shape/structure of nanoparticles with clean surfaces.

Chapter 3. Ni-Pt alloyed and core-shell nanoparticles

Naked pure metal nanoparticles with non-equilibrium structures, e.g. octahedron and tetrahedron, have been prepared via the cluster source. This chapter will present the synthesis of Ni-Pt alloy and core-shell nanoparticles using the gas condensed magnetron-sputtering method, which fabricates Ni-Pt nanoparticles with octahedral, tetrahedral, decahedral, and icosahedral shapes through precise control of sputtering powers and target condensation lengths. The structures of Ni-Pt nanoparticles are characterised by STEM, while X-ray energy dispersion (EDX) is employed to detect the composition and spatial distributions of Ni and Pt within the nanoparticles. Furthermore, the electron energy loss spectrum (EELS) is used to determine the valence and thus oxidation state of Ni atoms in core-shell Ni-Pt nanoparticles. The results indicate that Pt-shell protects Ni-core against the oxidation. *In-situ* heating experiments demonstrate that the Ni-Pt alloy nanoparticles maintain their crystal structures unchanged up to 900 ℃, while the core-shell structures transformed into the equilibrium alloyed structure. This study demonstrates the synthesis of bare Ni-Pt nanoparticles with different non-equilibrium shapes and structures that have high potential for catalytic and other applications.

3.1. Atomic models of Ni-Pt nanoparticles and the corresponding simulated STEM images

Atomic models of Ni-Pt nanoparticles with alloyed and core-shell structures are built using Python with the ASE package. The sizes of Ni-Pt models are 4.0-8.0×10^5 amu, which are around

the peak of mass spectra measured in the following experiments. In the core-shell Ni-Pt nanoparticles, there are 40-50 at% of Ni atoms to create the models; while the Ni-Pt alloys consist of 90 at% of Pt atoms and 10 at% of Ni atoms. These percentages of Ni and Pt in Ni-Pt nanoparticles were chosen based on the results of as-prepared Ni-Pt nanoparticles measured by STEM-EDX.

The atomic models do not take into consideration the structural relaxation[149] and the interface-lattice mismatch[150] of Ni-Pt. However, they serve usefully to generate the simulated STEM images (shown in Figure 3.1.1) of Ni-Pt nanoparticles, providing reference images for comparison with experimental HAADF-STEM images (Figure 3.1.2). The HAADF-STEM images are formed by the high angle scattered electrons via Rutherford scattering and are called Z-contrast images as the intensity of atom is proportional to Z^{α}, where Z is the atomic number and $1.2<\alpha\leq 2$ [151–154]. Therefore, the intensity of Pt is much higher than that of Ni, which can be used to distinguish the Pt atoms from Ni atoms in the HAADF-STEM images of Ni-Pt nanoparticles. Figure 3.1.1 displays simulated HAADF-STEM images of core-shell Ni-Pt nanoparticles (a1, b1, c1) and Ni-Pt alloys (d1, e1, f1), with the corresponding models shown to their right. Table 3.1 gives the number of Ni and Pt atoms in the core-shell models. In the simulated images, it is apparent that Pt atoms construct the shell (bright skins) around the Ni-cores (a1, b1, c1). Similarly, columns with high Ni faction can be easily observed from the simulated images of Ni-Pt alloys (d1, e1, f1).

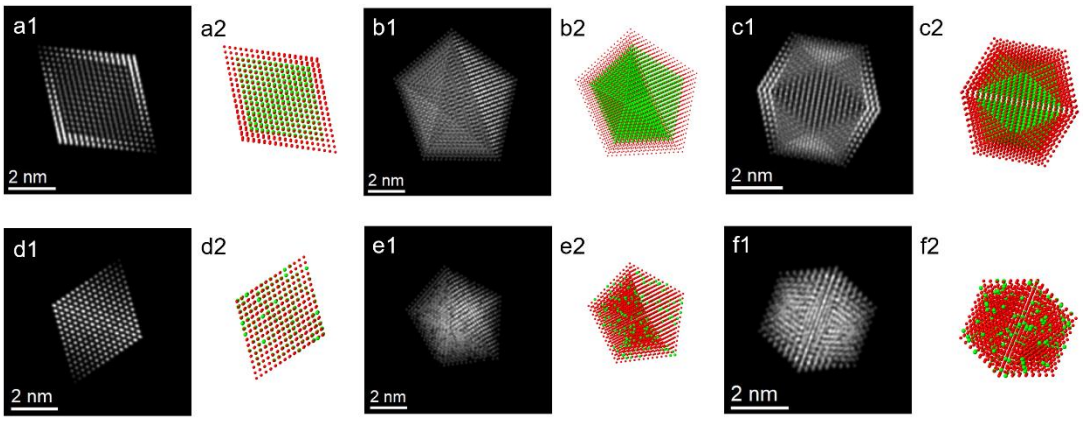


Figure 3.1.1. Atomic models of Ni-Pt nanoparticles. (a1-a2) octahedron with a core (7 layers)-shell (2 layers) structure, which contains 1834 Ni atoms (green) and 2060 Pt atoms (red). (b1-b2) A core-shell decahedron with 2289 Ni atoms and 2574 Pt atoms. (c1-c2) An icosahedron with 2057 Ni atoms in core (9 layers) and 3026 Pt atoms consisting the shell (3 layers). (d1-d2) An octahedral alloy with 210 Ni atoms and 2045 Pt atoms. (e1-e2) A decahedral alloy with 260 Ni atoms and 2029 Pt atoms. (f1-f2) An icosahedral alloy with 209 Ni atoms and 1848 Pt atoms. Due to the difference in the atomic number between Pt and Ni, Pt atoms contribute higher intensity in the HAADF-STEM image (about 5.7 times) than Ni. Therefore, the cores created by Ni atoms look darker than the shell built by Pt atoms as shown in the simulated HAADF-STEM images (a1, b1, and c1). The Ni atoms in the alloys d2, e2, and f2 can be found in d1, e1, and f1.

Table 3.1. Parameters of atomic models of Ni-Pt nanoparticles with core-shell structures

Model	Structure	Core	Shell	Ni (*at* %)	Pt (*at* %)
$Ni_{1834}Pt_{2060}$	Octahedron	7 layers	2 layers	47	53
$Ni_{2289}Pt_{2574}$	Decahedron	8 layers	4 layers	47	53
$Ni_{2057}Pt_{3026}$	Icosahedron	9 layers	3 layers	40	60
$Ni_{2219}Pt_{2574}$	Marks decahedron	11 layers	4 layers	46	54
$Ni_{1896}Pt_{1380}$	Tetrahedron	20 layers	5 layers	58	42

Apart from the octahedral, decahedral, and icosahedral nanoparticles shown in Figure 3.1.1, Marks decahedral and tetrahedral Ni-Pt nanoparticles (Figure 3.1.2) can also be observed in the

experiments, however they occupy low populations. Figure 3.1.3 shows representative images of Ni-Pt nanoparticles with decahedral (first column), icosahedral (second column), octahedral (third column), and tetrahedral (forth column) shapes. Dark points can be found in the images of Ni-Pt alloys (Figure 3.1.3 a-h), indicating the existence of Ni atoms in the nanoparticles. Apparently, core-shell structures are shown in Figure 3.1.3(i-p) with Pt atoms showing bright intensities constituting the shell of the nanoparticles and cores mainly consisting of Ni atoms. Therefore, the core-shell structures can be distinguished from the alloyed structures in the HAADF-STEM images of Ni-Pt nanoparticles.

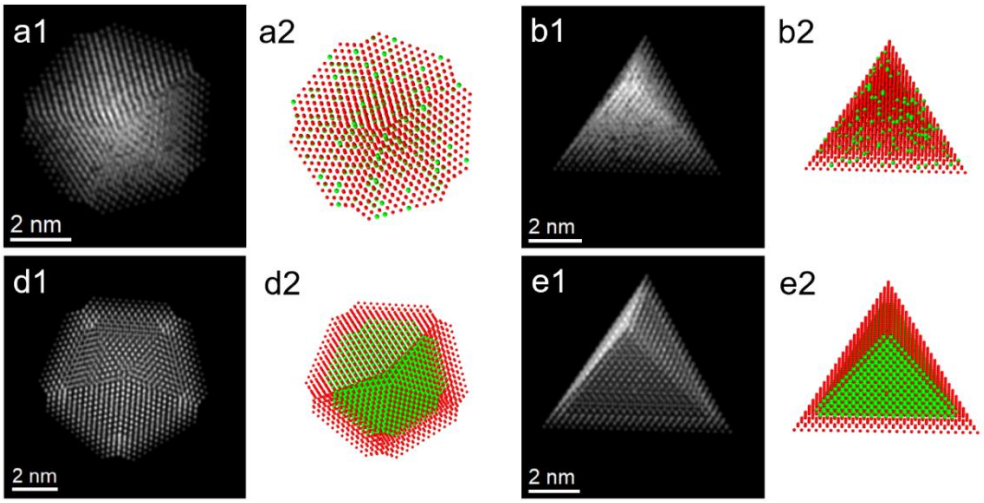


Figure 3.1.2. Simulated HAADF-STEM images of Marks decahedra and tetrahedra, which occupy low populations in the as-prepared samples. (a1-a2) Marks decahedron alloy (266 Ni atoms and 3080 Pt atoms). (b1-b2) tetrahedral alloy with 213 Ni atoms and 2087 Pt atoms. (d1-d2) Core-shell Marks decahedron (2219 Ni atoms(11layers) and 2574 Pt atoms (4 layers)). (e1-e2) core-shell tetrahedron with 1896 Ni atoms (20 layers) and 1380 Pt atoms (5 layers).

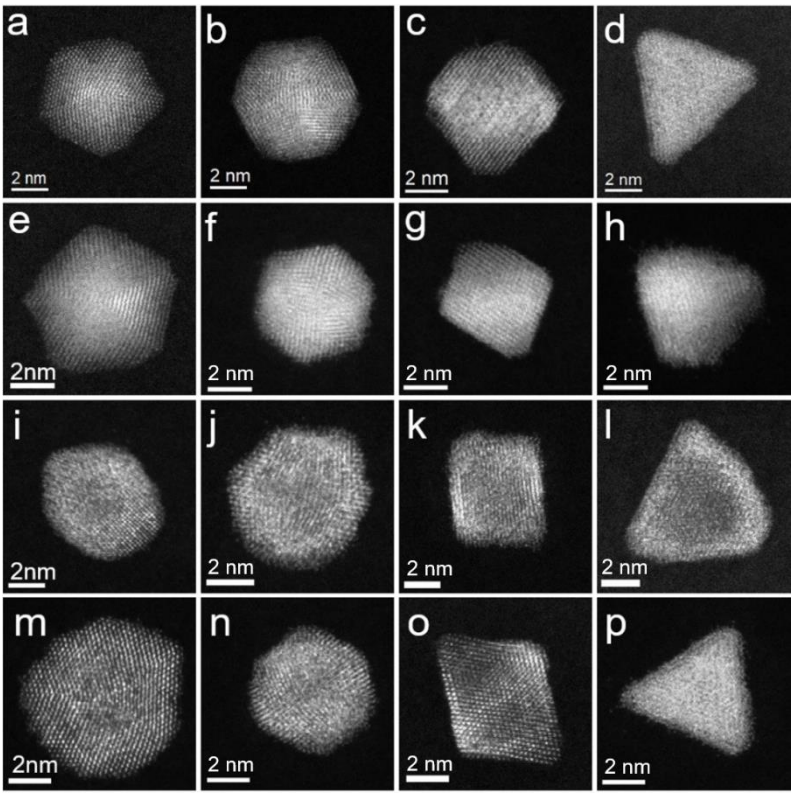
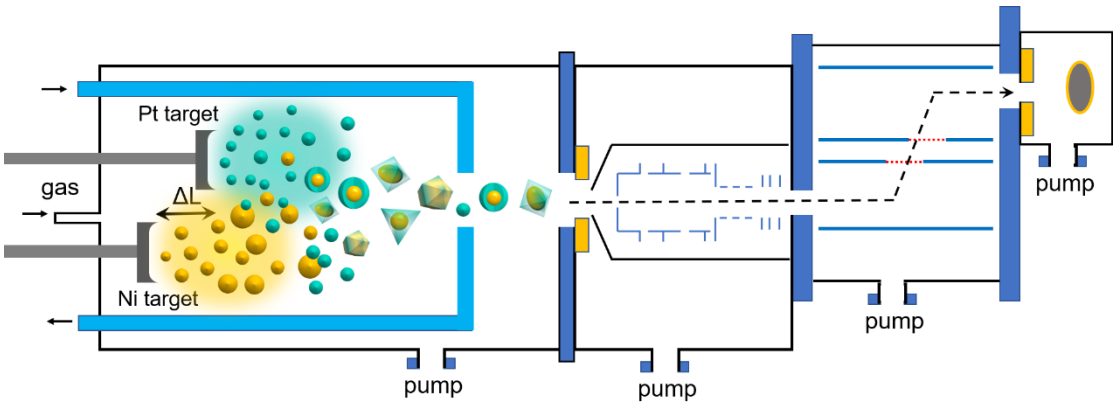


Figure 3.1.3. HAADF-STEM images of Ni-Pt nanoparticles. (a-h) Pt-rich nanoparticles. (i-p) Ni-rich nanoparticles. Nanoparticles shown in (a-d) were prepared with the sputtering power of 50 W for the Pt target and 75 W for the Ni target; (e-h) Pt-rich nanoparticles prepared with the sputtering power of 50 W for the Pt target and 30 W for the Ni target; (i-l) Ni-rich nanoparticles with core-shell structures, prepared by 30 W for Pt target and 75 W for Ni target. (m-p) Ni-rich nanoparticles were prepared using 30 W for Pt target and Ni target. (a, e, i, m) decahedron, (b, f, j, n) icosahedron, (c, g, k, o) octahedron, (d, h, l, p) tetrahedron.

3.2. Condensation lengths of targets



Scheme 3.1. Equipment illustration of the cluster source using magnetron-sputtering, consisting by a sputtering-condensation chamber, a transferring chamber, a mass-filter

chamber, and a deposition chamber (from left to right). A dual-target holder was installed with Pt target and Ni target mounted on the holders. The sputtering power and condensation length of Pt and Ni targets can be tuned separately.

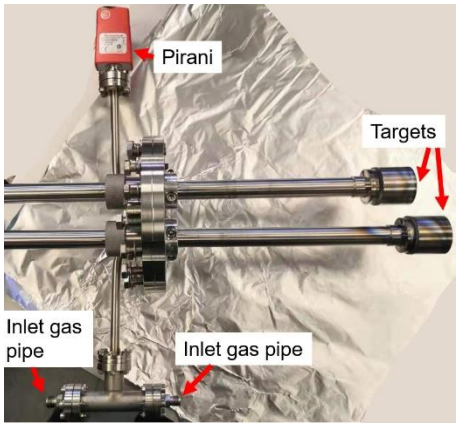


Figure 3.2.1. Photograph of the dual target holder used in this chapter.

A dual target holder was employed to install Ni and Pt targets with 1-inch diameter, as illustrated in Scheme 3.1 and Figure 3.2.1. The condensation length (CL) of each target can be changed separately. The difference between condensation lengths of two targets plays an important role in the structure of Ni-Pt nanoparticles. Figure 3.2.2 shows the images of Ni-Pt nanoparticles prepared with the same condensation length (CL=25 cm). Ni-Pt nanoparticles were collected after the nozzle (not mass filtered). Octahedral (Figure 3.2.2b) and tetrahedral (Figure 3.2.2c) Pt nanoparticles were observed in the images, while Ni atoms were condensed outsides of Pt nanoparticles. Parts of the Pt nanoparticle surface were not covered by Ni clusters as shown in Figure 3.2.2c, indicating that Pt atoms are condensed into nanoparticles much faster than Ni atoms under the same environment of the aggregation zone having the same aggregation length. This difference on the condensation rate is attributed to the higher cohesive energy of Ni (-534 kJ/mol) compared to Pt (-795 kJ/mol)[115,155]. This suggests that sputtered Pt atoms are more prone to condensation into clusters than sputtered Ni atoms, as they release comparatively lower

excess energy through three-body collisions. Therefore, the condensation length of Pt atoms should be shorter than Ni atoms to form Ni clusters before being exposed to Pt atoms for preparing the nanoparticles with Pt shells and Ni cores.

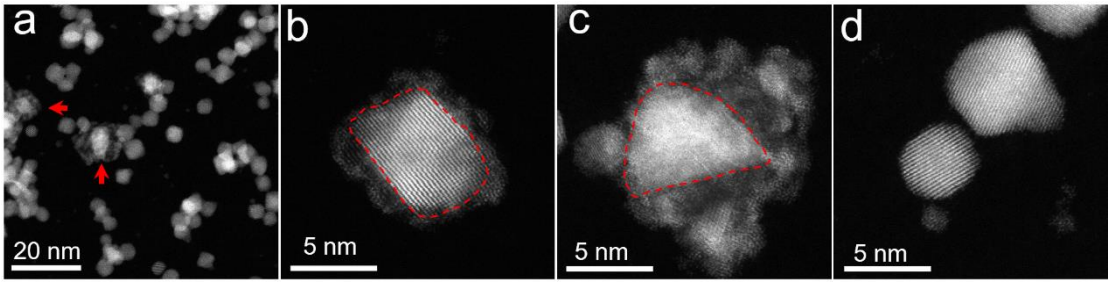


Figure 3.2.2. Ni-Pt nanoparticles were prepared at room temperature, which the aggregation lengths of both Ni and Pt targets are equal to 25 cm. Other preparation conditions include: sputtering power (Pt: 30 W, Ni: 11 W); Ar gas: 140 sccm, He gas: 20 sccm; pressure of chamber (0.49-0.58 mbar); nozzle size (5.7 mm). Pt nanoparticles were circled by dotted red curves.

For fabricating Ni-Pt nanoparticles with core-shell structures, the condensation lengths of 25 cm and 19 cm were used for Ni and Pt targets, respectively. According to the relationship ($I \propto V^n$, where n is a constant within a range of 5 to 15, only impacted by the magnetic field), the discharge current (I) has a much greater impact than the discharge voltage (V) on the sputtering power in a discharge sputtering process[156]. The Ni target weakens the magnetic field, compared with the magnetic field of Pt target. Meanwhile, due to the inverse relationship between sputtering yield and threshold energy of sputtering (21.23 eV and 20.88 eV for Pt and Ni, respectively)[157], sputtering powers of 50 W and 75 W were respectively applied to the Ni and Pt targets to yield comparable numbers of sputtered atoms. Figure 3.2.3 shows the images of as-prepared Ni-Pt nanoparticles demonstrating that nanoparticles are not covered by Ni clusters on the exterior under these conditions. Both core-shell structure (Figure 3.2.3d) and alloyed

structures (Figure 3.2.3c) can be observed. It is interesting that some nanoparticles show weak intensity in Figure 3.2.3(a, b) marked by yellow arrows, while some nanoparticles have bright images, for example, the particle 3 shown in Figure 3.2.3b. Two nanoparticles with low intensities were imaged at higher magnification (Figure 3.2.3e, f). The lattice spacing of the nanoparticle in Figure 3.2.3e is 2.01 Å and the other nanoparticle has a lattice spacing of 1.73 Å. They are close to the structural parameters of pure Ni nanoparticles, which the referred Powder Diffraction File (PDF) are listed in Table 3.2. Therefore, it is reasonable to suppose the existence of pure Ni, Ni-rich, and Pt-rich nanoparticles. As the similar structure of Ni and Pt, there are small differences on the projected area, but there are large differences on the integrated intensities. For example, three nanoparticles shown in Figure 3.2.3b were measured for their projected areas and integrated intensities (Table 3.3) that the maximum intensity is about 2.2 times of the minimum intensity, however, the ratio of the maximum area to the minimum area is 1.3. It suggests that the integrated intensity is more sensitive than the projected area to measure the mass of Ni-Pt nanoparticles.

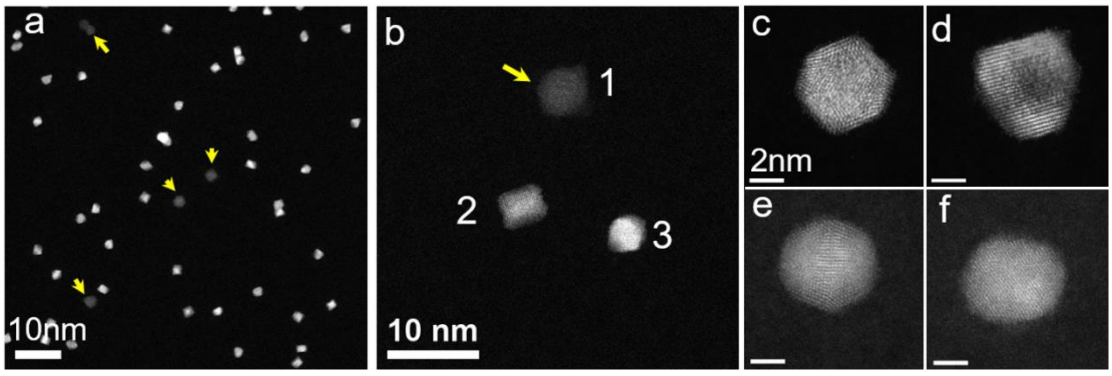


Figure 3.2.3. 25 cm and 19 cm were utilized as the condensation length of Ni and Pt targets, respectively. Ni-Pt nanoparticles were mass-filtered with around 5.0×10^5 amu and prepared using 75 W for Pt target and 50 W for Ni target under the chamber pressure of 0.30-0.32 mbar with the argon gas flow rate of 120 sccm. There are nanoparticles with low intensities marked by yellow arrows in the HAADF-STEM image

(a), which were proposed as Ni nanoparticles. Three octahedral nanoparticles were measured for the integrated intensity, which were listed in the following table. Nanoparticle 1 in Figure b was dimmer than nanoparticle 2 and 3, indicating that nanoparticle 1 contains the most Ni atoms among three nanoparticles. Ni nanoparticles were observed and shown in Figure e (lattice spacing is 2.01 Å, corresponding with (111) plane of Ni FCC) and f (lattice spacing is 1.73 Å, corresponding with (200) plane of Ni FCC). Besides, Ni-Pt core-shell nanoparticles with an icosahedral (Figure c) and FCC structure (Figure d) were shown.

Table 3.2. Parameters of Ni, Pt with faced-center cubic structures. The referred structures of Ni and Pt are from the database of the powder diffraction file (PDF).

Element	Space group	Lattice parameters (a=b=c)	Lattice spacing of (111) facets	PDF (No.)
Ni	Fm-3m (225)	3.516 Å	2.0298 Å	70-0989
Pt	Fm-3m (225)	3.92 Å	2.2632 Å	87-0646

Note: An alloy nanoparticle composed of Ni and Pt atoms can exhibit adjustable crystal cell sizes in comparison to those of pure Ni or Pt, which is stated by Vegard's law[158] that the lattice parameter (a) of an alloy varies following by $a(x) = a_A \cdot x + a_B \cdot (1 - x)$,. Where a_A and a_B are the lattice parameters of the pure systems A and B, respectively. The proportion of nickel (x) and platinum (1-x) atoms in the alloy affects the crystal cell size of the alloy, and it ranges between the crystal cell size of nickel and platinum. For instance, the crystal cell size of the alloy nanoparticle will approach the size of Pt with an increase in the ratio of Pt atoms. In core-shell structures, the lattice mismatch between the shell and core results in atomic strain at the interface[159].

Table 3.3. Sizes of nanoparticles shown in Figure 3.2.3, which were mass-selected with the same size.

Particle	Peak intensity (a.u.)	Integrated intensity (a.u.)	Projected area (nm^2)
1	9.3×10^3	7.6×10^5	18.9
2	2.2×10^5	1.4×10^6	18.2
3	2.9×10^5	1.7×10^6	14.5

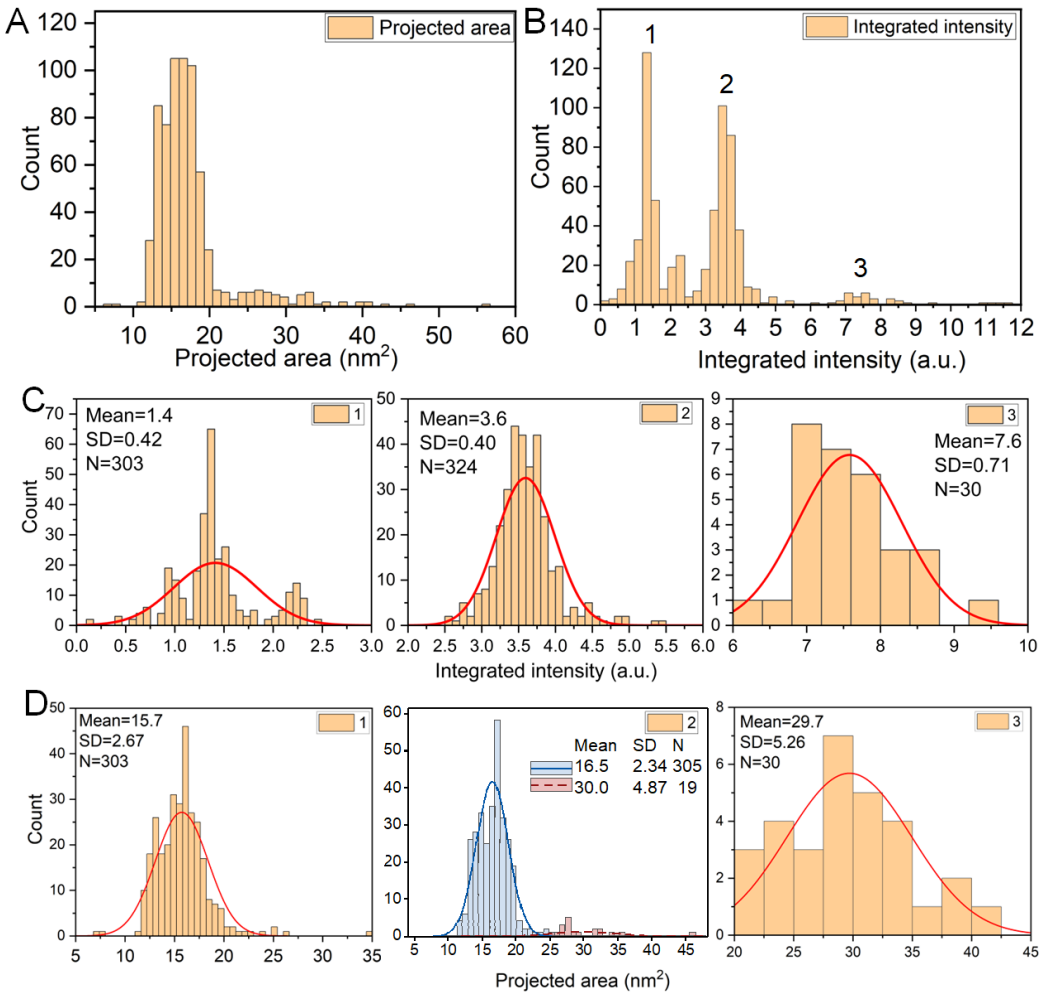


Figure 3.2.4. Size distribution of Ni-Pt nanoparticles with a mass selection 5.0×10^5 amu, as shown in Figure 3.2.3. (A) overview of projected area distribution of nanoparticles; (B) overview of integrated intensity distribution, where there are three separated peaks indicating three different mass distributions of Ni-Pt nanoparticles; (C) Normal fittings of mass distributions shown in (B); (D) the corresponding area distributions of Ni-Pt nanoparticles, whose intensities fall in (C). The Ni-Pt nanoparticles with an intensity distribution as shown in (C) "2" have the same projected area distribution as the nanoparticles shown in (C) "1".

Figure 3.2.4 shows the size distribution of Ni-Pt nanoparticles, whose images are presented in Figure 3.2.3. There is only one peak with a tail in the projected area distribution (Figure 3.2.4a). However, three separated peaks (numbered with 1, 2, and 3) appear in the intensity distribution (Figure 3.2.4b). Among these three peaks, the peak 3 is caused by the aggregated nanoparticles, where the corresponding area (around 29.7 nm^2) is nearly twice as the area of nanoparticles in

peak 2 (shown in Figure 3.2.4d). The area distributions of nanoparticles from peak 1 and 2 were displayed by histograms in Figure 3.2.4D. The projected area of nanoparticles from peak 2 in the intensity distribution has a normal distribution with a mean area of 16.5 nm^2, close to the mean area of nanoparticles from peak 1 (15.7 nm^2). This indicates that peak 1 in the intensity histogram consists of Ni-rich nanoparticles (including pure Ni nanoparticles) while peak 2 mainly consists of Pt-rich nanoparticles. Note that a small population (19/305=6.2%) of nanoparticles in peak 2 consists of aggregated Ni-rich nanoparticles. Therefore, the percentage of Pt-rich nanoparticles in Figure 3.2.3 is no more than 50.2% (=305/(303+305)). Combing the integrated intensity distribution with the projected area distribution of Ni-Pt nanoparticles, it is possible to estimate the populations of Ni-rich and Pt-rich nanoparticles.

For bringing down the population of Pt-rich nanoparticles, the discharging power on the Pt target and the cooling gas flow rate (and thus also the pressure in the condensation chamber) were reduced. An example is illustrated in Figure 3.2.5 where Ni and Pt targets had 75 W and 30 W, respectively, applied. Although the Pt-rich nanoparticles (labelled by yellow arrows) are formed under the reduced Ar gas flow rate of 90 sccm, there were no pure Ni nanoparticles found in the HAADF-STEM images. Ni-rich nanoparticles, showing alloyed structures and core-shell structures, are presented in Figure 3.2.5(c-f). It is interesting that most of the Pt-rich nanoparticles exhibit octahedral shapes (marked by yellow arrows in Figure 3.2.5) while the decahedral and octahedral nanoparticles are alloys or core-shell structures.

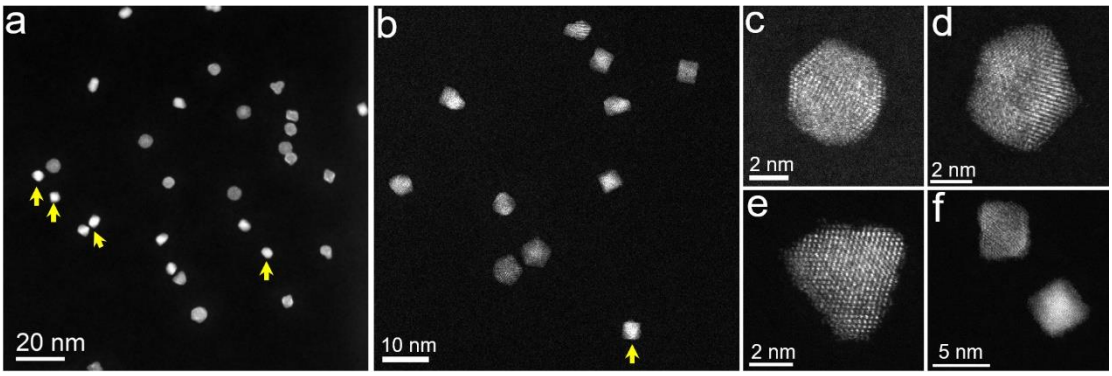


Figure 3.2.5. Ni-Pt nanoparticles, prepared with the condensation lengths of Ni and Pt targets of 25 cm and 19 cm, respectively. Pt-rich octahedral nanoparticles are marked by yellow arrows in (a, b) Core-shell nanoparticles are shown in (c: icosahedron), (d: decahedron), and (upper of f: octahedron). (e) tetrahedral alloy and octahedral alloy in the bottom of f. Preparation conditions: sputtering power of Ni = 75 W, sputtering power of Pt = 30 W; argon gas flow rate = 90 sccm)

The population of Pt-rich and Ni-rich nanoparticles shown in Figure 3.2.5 can be estimated through the area distribution (Figure 3.2.6A) and the corresponding HAADF intensity (Figure 3.2.6B) distribution. HAADF images of 595 as-prepared Ni-Pt nanoparticles were examined, revealing an area histogram with a main peak that fits well with a normal distribution and two minor peaks, as illustrated in Figure 3.2.6A. Meanwhile, the HAADF intensity histogram of the same nanoparticles exhibits two prominent peaks and one minor peak, as indicated by the dotted rectangles in Figure 3.2.6B, with the primary two peaks being re-drawn in Figure 3.2.6C. The minor peaks observed in Figures 3.2.6A and B correspond to a low percentage (42/595 = 7%) of aggregated nanoparticles, which are excluded from structural analysis. The ratio of the mean HAADF intensity of peak 2 to peak 1 is 3.7/1.5=2.5, implying that peak 2 cannot be attributed to the aggregated nanoparticles of peak 1. This indicates that the peak 1 and peak 2 could be attributed to Ni-rich and Pt-rich nanoparticles, respectively. Furthermore, Peak 2 contains aggregated Ni-rich nanoparticles, whose number can be identified by means of the area analysis.

The corresponding area distributions of nanoparticles from peak 1 and peak 2 are illustrated in Figure 3.2.6D. Nanoparticles belonging to the peak 2 of the intensity histogram can be categorized into two groups based on their area distribution, i.e., one main peak distribution and one small group. The average area of nanoparticles from peak 1 of the HAADF intensity histogram is 20.2 nm^2, which is half of the average area (40.6 nm^2) of nanoparticles in the small peak of Figure 3.2.6D2. This suggests that there is an 18.6% (=34/183) population of aggregated Ni-rich nanoparticles in the peak 2 of the intensity distribution. Thus, the population of Pt-rich nanoparticles is estimated to be 26.9% (=149/553) based on the area distribution presented in Figure 3.2.6D. And the percentage of Ni-rich nanoparticles is about 73.1% (=100%-26.9%).

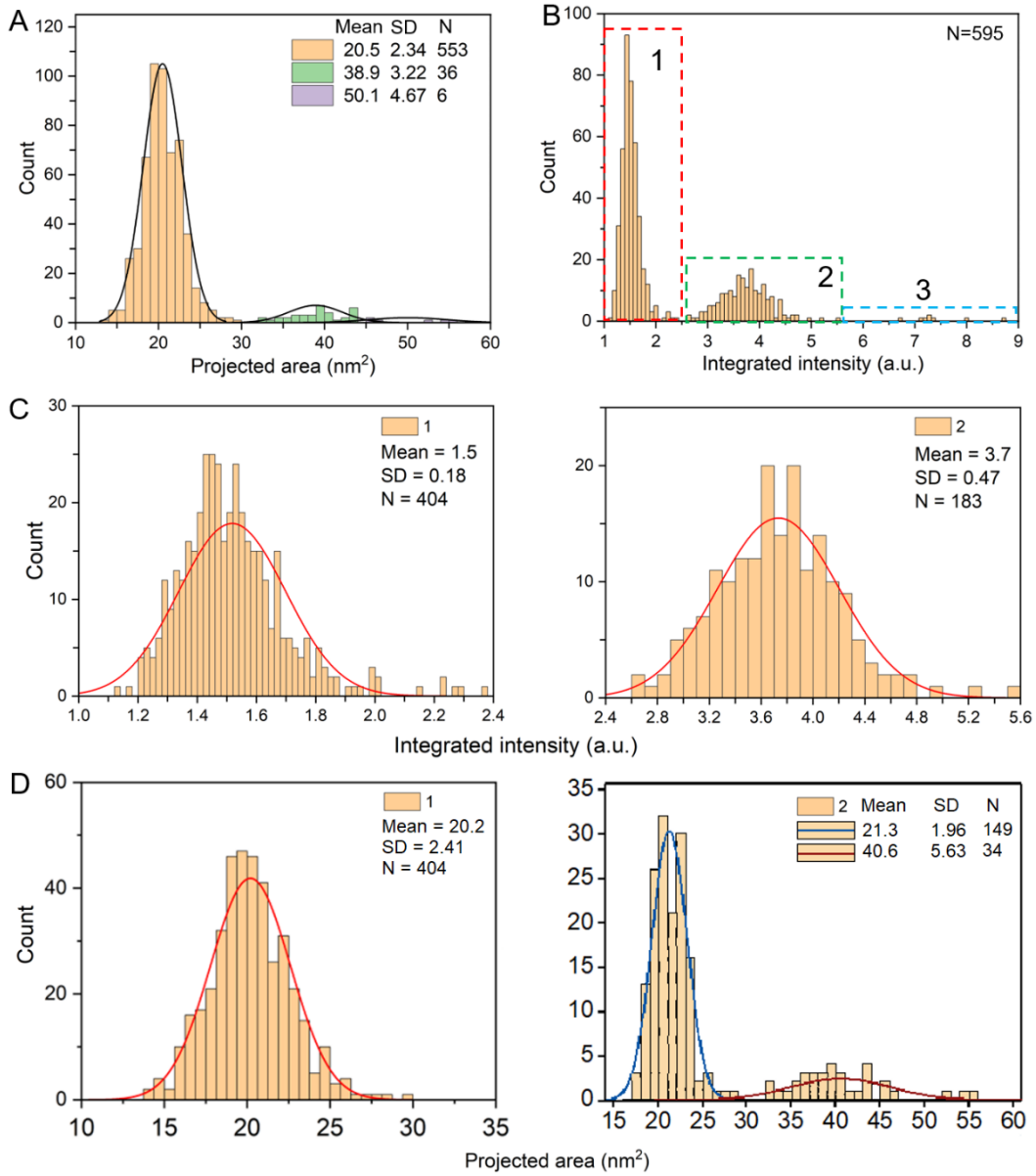


Figure 3.2.6. Size distribution of Ni-Pt nanoparticles, which were prepared under an argon gas flow rate of 90 sccm, using condensation lengths of 25 cm and 19 cm for Ni target and Pt target, respectively. The sizes of nanoparticles were mass-filtered with around 6.0×10^5 amu. (A) Overview of projected area distribution. (B) Overview of integrated intensity distribution, exhibiting three groups. (C) Intensity distribution fitted by normal functions for group 1 and 2. (D) The corresponding projected area distributions of group 1 and 2 fitted by normal functions.

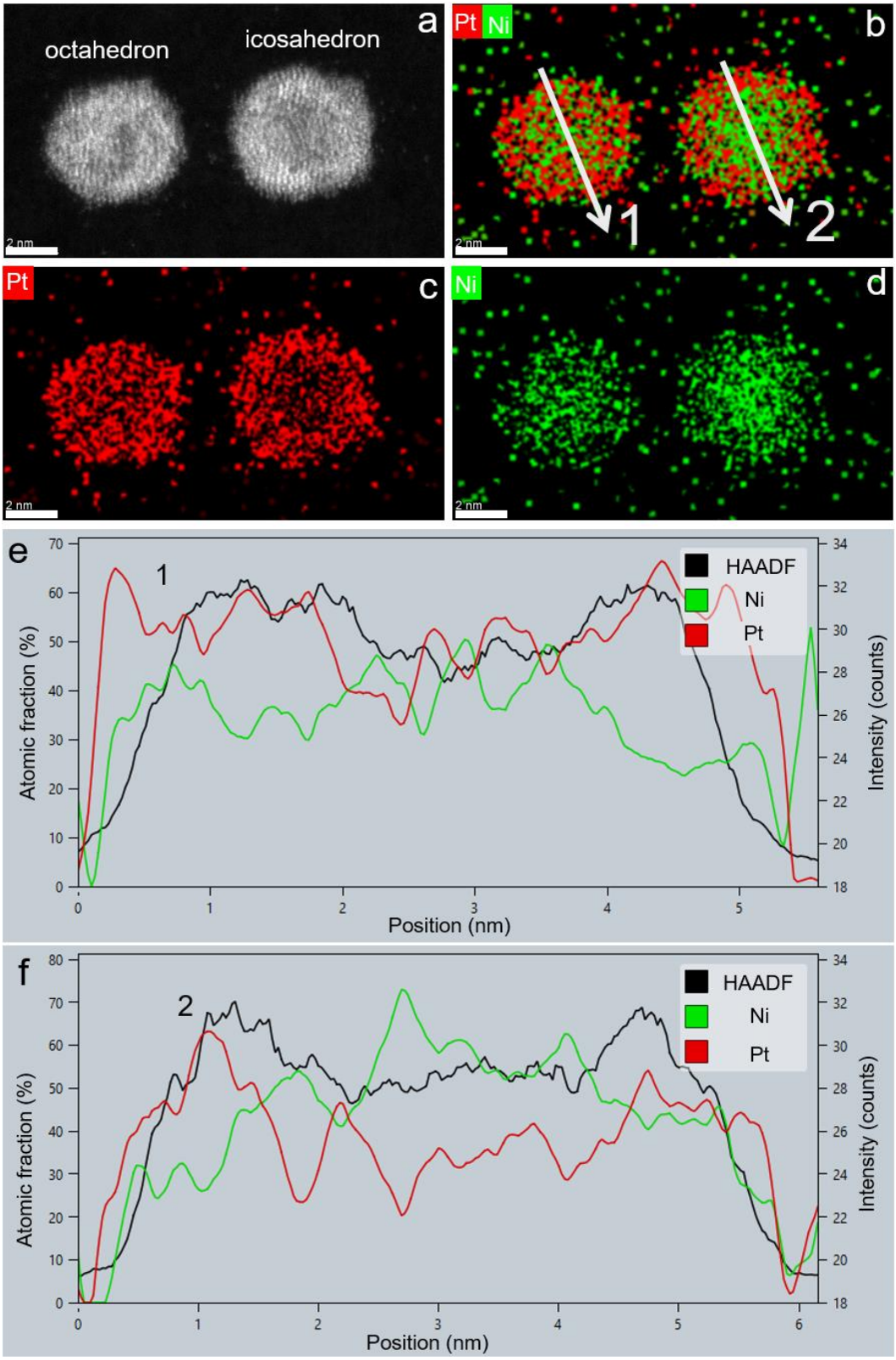


Figure 3.2.7. Elemental mappings of Ni-Pt nanoparticles with core-shell structures. The contents of Ni and Pt are 54.9 at% and 45.1 at%, respectively. Preparation conditions: sputtering power of Ni = 75 W, sputtering power of Pt = 30 W; argon gas flow rate = 90 sccm). All the scale bars are 2 nm. (Images and EDX captured by STEM

mode in FEI Titan Themis G2 60-300 working at 300 kV)

The core-shell structures of Ni-Pt nanoparticles shown in Figure 3.2.5 are confirmed by the elemental mappings (Figure 3.2.7) showing Ni atoms (54.9 at%) encased by Pt atoms (45.1%). The changes of atomic fractions along the lines drawn in Figure 3.2.7b further demonstrate the core-shell structures of the octahedral and icosahedral nanoparticles in Figure 3.2.7a.

In conclusion, the condensation lengths of targets are of importance for the formation of Ni-Pt nanoparticles with core-shell structures. When the Pt target has a 6 cm shorter condensation length than the Ni target, the core-shell structures can be formed even with a sputtering power of the Pt target as high as 75 W. To reduce the fraction of Ni nanoparticles formed, the argon gas flow rate should be low (90 sccm is better than 120 sccm for the formation of core-shell), which reduces the condensation rate of Ni atoms. Due to the fast condensation rate of Pt atoms, Pt-rich nanoparticles can not be avoided in the preparation.

3.3. Pt-rich Ni-Pt alloys

In the following, the preparation conditions of Pt-rich Ni-Pt nanoparticles were studied as a function of sputtering power at fixed condensation length (25 cm for Pt and 22 cm for Ni) and fixed Ar gas flow rate of 90 sccm. The sputtering chamber was not cooled down by flowing liquid nitrogen. The pressure of the chamber was about 0.22 to 0.27 mbar.

For distinguishing the samples easily, the Ni-Pt nanoparticles will be labelled using the sputtering power utilized in the preparation. For example, Ni30W/Pt75W refers to a sample prepared using sputtering powers of 30 W and 75 W for the Ni target and Pt target, respectively.

3.3.1. Mass spectra of Ni-Pt nanoparticles

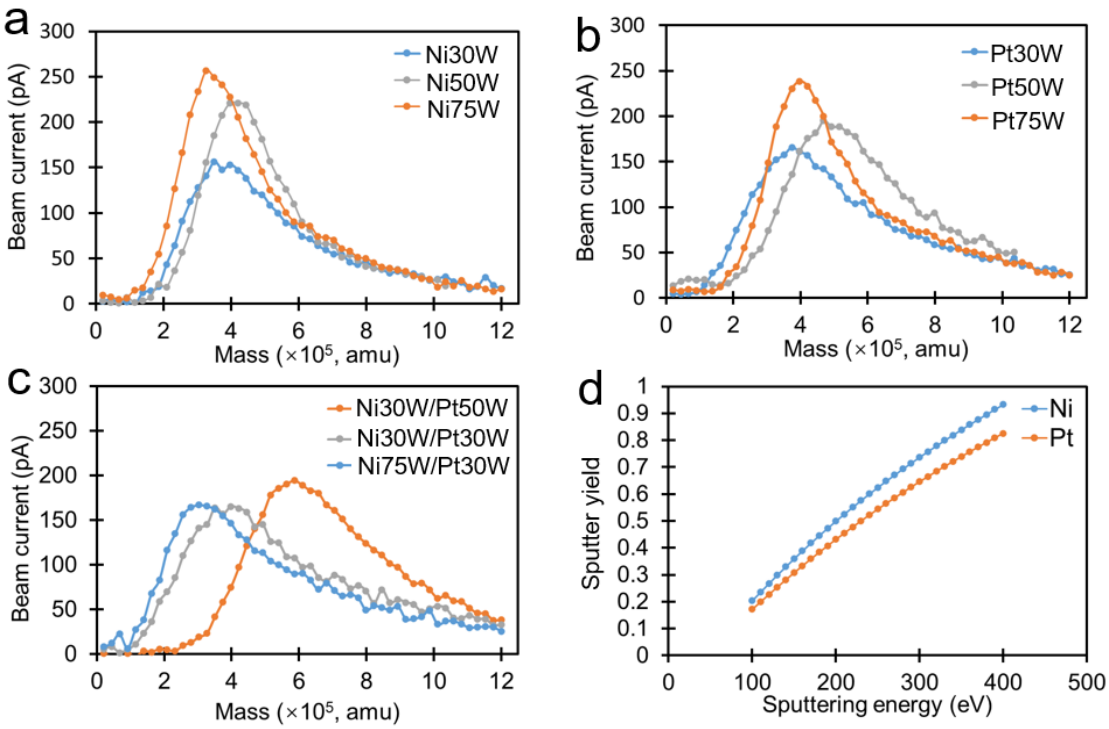


Figure 3.3.1. Mass spectra of nanoparticles prepared with various sputtering powers. (a) pure Pt clusters, (b) pure Ni clusters, (c) Ni-Pt clusters. (d) the sputtering yield of pure Pt and pure Ni under different sputtering power (data from *https://www.iap.tuwien.ac.at/www/surface/sputteryield*). The Pt has an energy threshold of 21.23 eV, higher than Ni (20.88 eV) under the bombarding of Ar ions. Pt and Ni have similar condensation behaviours with the same sputtering powers and chamber environments. The argon gas was controlled at 90 sccm, yielding a corresponding chamber pressure around 0.25 mbar.

There are two different morphologies of Ni-Pt nanoparticles observed in Figure 3.1.3, which are alloys and core-shell structures. The size and structure of nanoparticles is influenced by the preparation parameters, including the sputtering power and the cooling gases supply[130,104]. The mass spectrum, which is recorded by the lateral TOF installed in the mass-filter chamber, presents the size distribution of nanoparticles. Figure 3.3.1(a, b) shows the mass spectra of Ni and Pt nanoparticles with the peaks of the mass spectra observed to stick around 4.0×10^5 amu

as the sputtering power is increased from 30 W to 75 W. In contrast, the beam current maxima rose with increased sputtering powers, attributed to the increase of sputter yield (Figure 3.3.1d). The integration of the mass spectrum can represent the number of nanoparticles formed in the chamber. Under the same cooling gas flow rate (90 sccm), more Pt nanoparticles are formed than Ni nanoparticles when the sputtering power is not higher than 75 W for 1-inch targets, even though the sputtering yield of Ni is higher than Pt. It indicates that Pt atoms are more easily condensed into nanoparticles than Ni atoms.

When the dual targets (Figure 3.2.1) were used for the sputtering, the mass spectra of Ni-Pt nanoparticles as shown in Figure 3.3.1(c), behaved differently compared with the mass spectrum of Ni nanoparticles or Pt nanoparticles. Three curves were displayed in Figure 3.3.1(c) illustrating that the power applied on the Pt target had a stronger impact on the sizes of Ni-Pt nanoparticles than that applied the Ni target. Specifically, the peak (at around 6.0×10^5 amu) of the orange curve produced by 50 W for Pt target and 30 W for the Ni target was significantly higher than those of the blue curve (around 3.0×10^5 amu) and the grey curve (around 4.0×10^5 amu). Combined with the images of Ni-Pt nanoparticles shown in Figure 3.1.3e-h and the following parts, it is found that the orange curve is from Ni-Pt alloys, while the blue and grey curves are produced by the Ni-Pt core-shell nanoparticles.

3.3.2. Elemental contents and mappings of Pt-rich nanoparticles

The sputtering powers were investigated to explore the influence on the structures and compositions of Pt-rich nanoparticles. 30 W and 75 W were utilized for Ni target while the

sputtering power of Pt target was unchanged at 50 W. Figure 3.3.2 shows the EDX mappings of Pt-rich nanoparticles with FCC structure (a-d), decahedral shapes (e-h), and the icosahedral shape (i-l). Compared with about 6 at% of Ni atoms in Pt-rich octahedra, the decahedral and icosahedral nanoparticles contain more Ni (around 10 at%). It is interesting that decahedral and icosahedral nanoparticles, which are rarely observed in the pure Pt nanoparticles (shown in Chapter 2), occupy 1-10% in the population of Pt-rich nanoparticles. The high content of Ni in the decahedra and icosahedra indicates the importance of Ni in the formation of the decahedral and icosahedral shapes.

The same phenomenon was observed in the Pt-rich nanoparticles prepared using 75 W for the Ni target and 50 W for the Pt target. The decahedron (Figure 3.3.3e-h) and the icosahedron (Figure 3.3.3i-l) contain 17 at% of Ni, which is almost twice the Ni content in the nanoparticle with the FCC structure in Figure 3.3.4a-d.

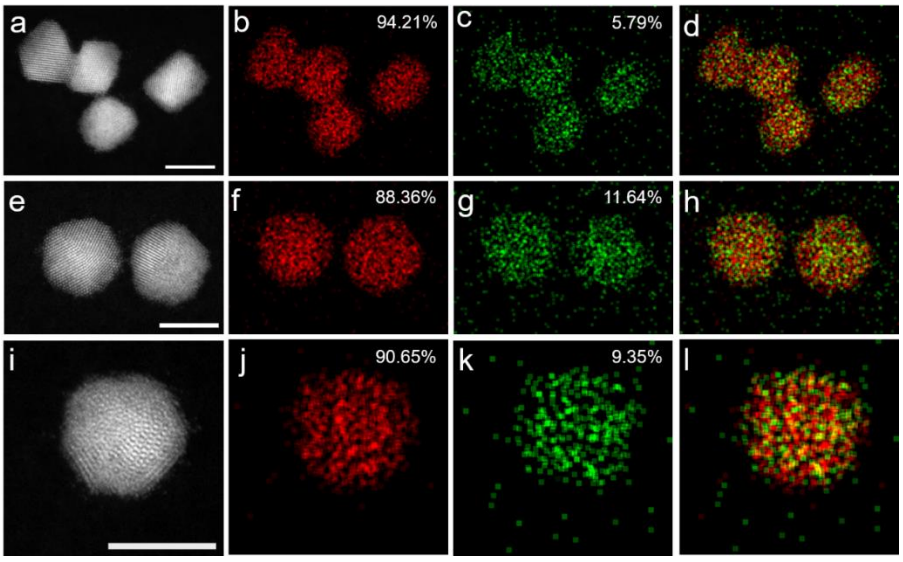


Figure 3.3.2. Elemental mappings of Pt-rich nanoparticles (Ni30W/Pt50W), which 50 W and 30 W were applied on the targets of Pt and Ni respectively. Pt is presented by red dots and Ni is green one. (a-c) four octahedra with a fcc structure; (d-f) two decahedra; (g-i) icosahedron. Decahedral and icosahedral nanoparticles have more

Ni than the alloys with a fcc structure. Scale bars are 5 nm. (Images and EDX captured by STEM mode in FEI Titan Themis G2 60-300 working at 300 kV)

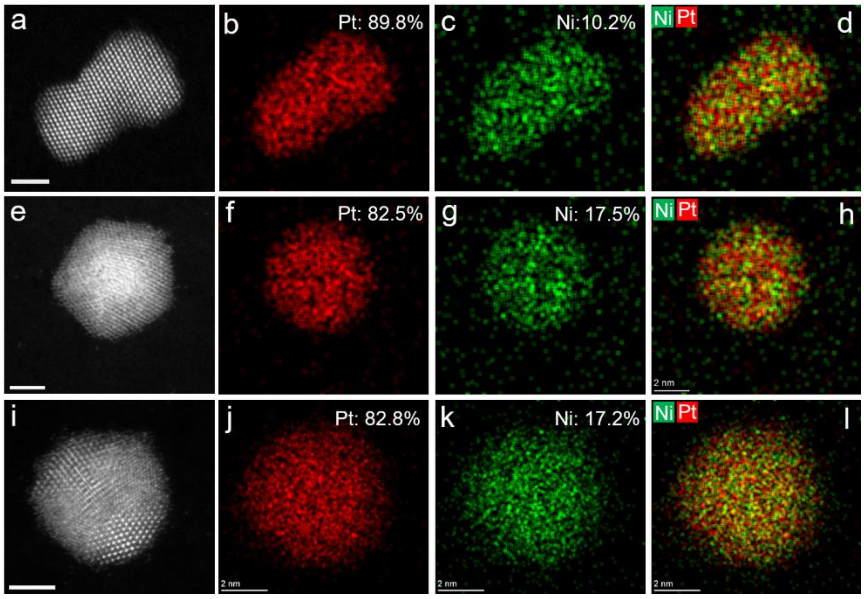


Figure 3.3.3. Elemental mappings of Pt-rich nanoparticles (Ni75W/Pt50W), which 50 W and 75 W were applied on the targets of Pt and Ni respectively for the preparation. Pt distribution was presented by red dots and Ni was green one. (a-c) two aggregated octahedra with a fcc structure; (d-f) decahedron; (g-i) icosahedron. Decahedral and icosahedral nanoparticles occupy higher content of Ni than the alloys with a fcc structure. Scale bars are 2 nm. (Images and EDX captured by STEM mode in FEI Titan Themis G2 60-300 working at 300 kV)

Comparing the Pt-rich nanoparticles shown in Figure 3.3.2 and Figure 3.3.3, a higher sputtering power on the Ni target, bombarding more Ni atoms into the chamber, can provide more Ni atoms to be condensed to form alloys and increase the content of Ni in prepared nanoparticles. The Ni mappings in Figure 3.3.2 and Figure 3.3.3 demonstrate the alloyed structures of the Pt-rich nanoparticles as here is no core-shell structure observed from the EDX mappings and STEM images. The atomic fractions of Ni and Pt along the line in Figure 3.3.4 exhibits similar fluctuations, further demonstrating the alloyed structure. Therefore, Pt-rich nanoparticles tend to form alloyed structures, rather than a core-shell structure.

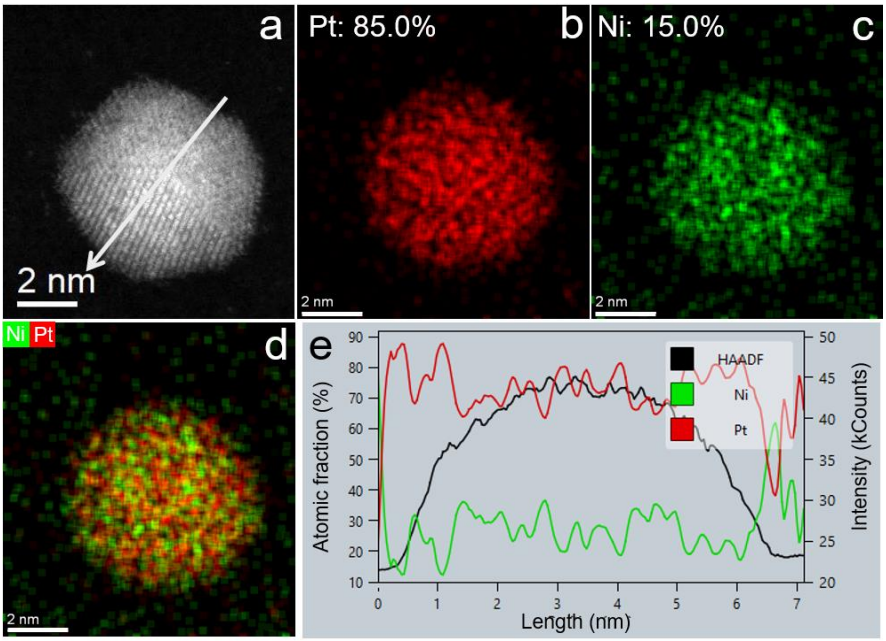


Figure 3.3.4. The linear distribution of elements in Pt-rich nanoparticles (Ni75W/Pt50W), which 50 W and 75 W were applied on the targets of Pt and Ni respectively for the preparation. (a) HAADF-STEM image; (b) Pt mapping; (c) Ni mapping; (d) overlapping of Pt and Ni; (e) atomic fraction distribution of Ni and Pt along the line in (a). (Images and EDX captured by STEM mode in FEI Titan Themis G2 60-300 working at 300 kV)

3.3.3. Size distribution of Pt-rich nanoparticles

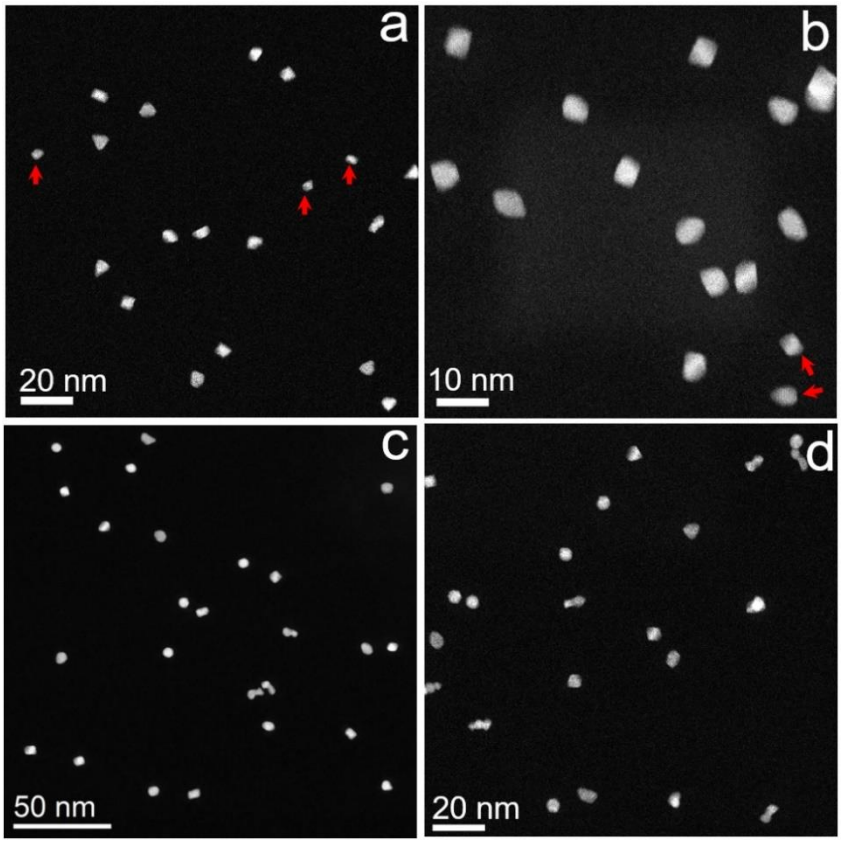


Figure 3.3.5. Ni-Pt alloys prepared with a longer condensation length of Ni atoms (25 cm) than that of Pt atoms (22 cm). Nanoparticles were mass-selected with a mass of 1.0×10^6 amu. (a-b) Pt-rich alloys (Ni30W/Pt50W) prepared using 50 W for the Pt target and 30 W for the Ni target. (c-d) nanoparticles (Ni75W/Pt50W), which 50 W and 75 W were applied on the Pt target and the Ni target, respectively. (Images captured by STEM mode in FEI Titan Themis G2 60-300 working at 300 kV)

STEM images of Pt-rich size-selected nanoparticles as shown in Figure 3.3.5 demonstrate that the majority of nanoparticles have octahedral and tetrahedral shapes. More minority round nanoparticles are observed in Figure 3.3.5(c-d), which is the sample of Ni75W/Pt50W, indicating higher Ni power yields more minority decahedral and icosahedral nanoparticles. Projected areas and integrated intensities, which can be an indicator to estimate the content of Ni in the Ni-Pt nanoparticles, are presented in Figure 3.3.6 and Figure 3.3.7 using the

histograms, which can be fitted well by the normal distribution. There are two peaks (Figure 3.3.6) in both the size distribution and the projected area distribution of the sample Ni30W/Pt50W. The small peak is attributed to the small group (13%) of nanoparticles as marked by red arrows in Figure 3.3.5(a-b). The nanoparticles mass-selected with a mass of 1.0×10^6 amu in the sample of Ni30W/Pt50W present their size distributions shown with rose red histograms in Figure 3.3.6, which the mean integrated intensity (2.9) and the mean area (25.1 nm^2) is a bit larger than that of the sample of Ni75W/Pt50W (Figure 3.3.7) mass-filtered with the same size. It suggests that the nanoparticles of Ni75W/Pt50W contain higher Ni than the nanoparticles of Ni30W/Pt50W, which is in accordance with the results of EDX (Figure 3.3.2 and Figure 3.3.3) that a higher sputtering power on the Ni target yields higher atomic fractions of Ni in Ni-Pt nanoparticles.

The sample of Ni75W/Pt50W has one peak in both the integrated intensity distribution and the projected area distribution (Figure 3.3.7). It is apparent to differentiate the alloyed nanoparticles (e.g. Figure 3.3.7) from the core-shell Ni-Pt nanoparticles (Figure 3.2.6) based on their integrated intensity distribution and the projected area distribution. For alloys, there is one peak in their intensity and area distributions. In contrast, there are two or more peaks in the intensity distribution of core-shell nanoparticles, while there is one peak in their area distribution. Therefore, analysing the area and intensity distribution of Ni-Pt nanoparticles prepared by the cluster source can detect the core-shell nanoparticles.

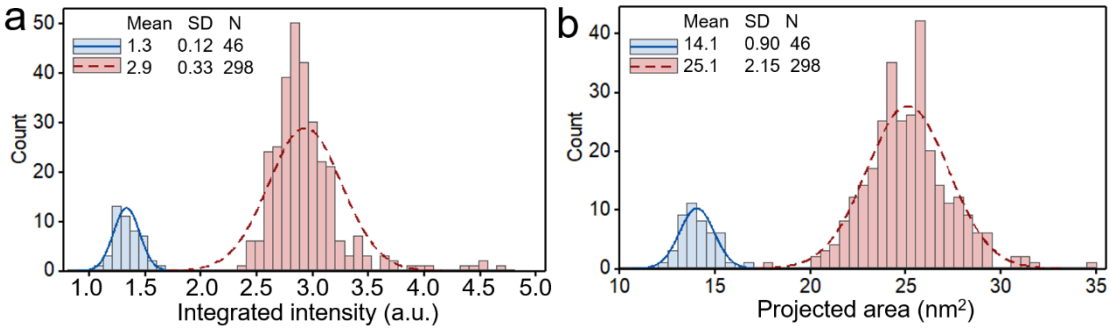


Figure 3.3.6. Size distribution of Ni-Pt alloys (Ni30W/Pt50W) with a mass selection of 1.0×10^6 amu. There are two peaks in both intensity distribution and area distribution of nanoparticles, demonstrating the as-prepared Ni-Pt alloys have two ranges in the size. Some small nanoparticles are marked by red arrows in Figure 3.3.6.

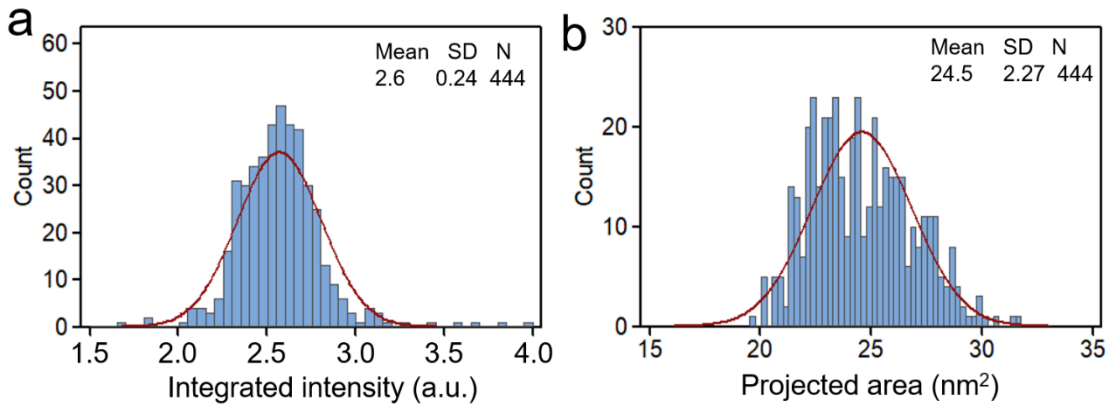


Figure 3.3.7. Size distribution of Ni-Pt alloys with a mass selection of 1.0×10^6 amu (Ni75W/Pt50W), which the sputtering power of Ni target and Pt target was 75 W and 50 W, respectively.

3.4. Ni-rich Ni-Pt core-shell nanoparticles

3.4.1. Elemental contents and mappings of Ni-Pt nanoparticles

The core-shell Ni-Pt nanoparticles have been given as an example in Figure 3.2.5, where a low discharging power on the Pt target (e.g. 30 W) is the key factor for the formation of core-shell structures. Here, two more examples (Figure 3.4.1) illustrate how the sputtering power on the Ni target impacts on the core-shell structures of Ni-rich nanoparticles.

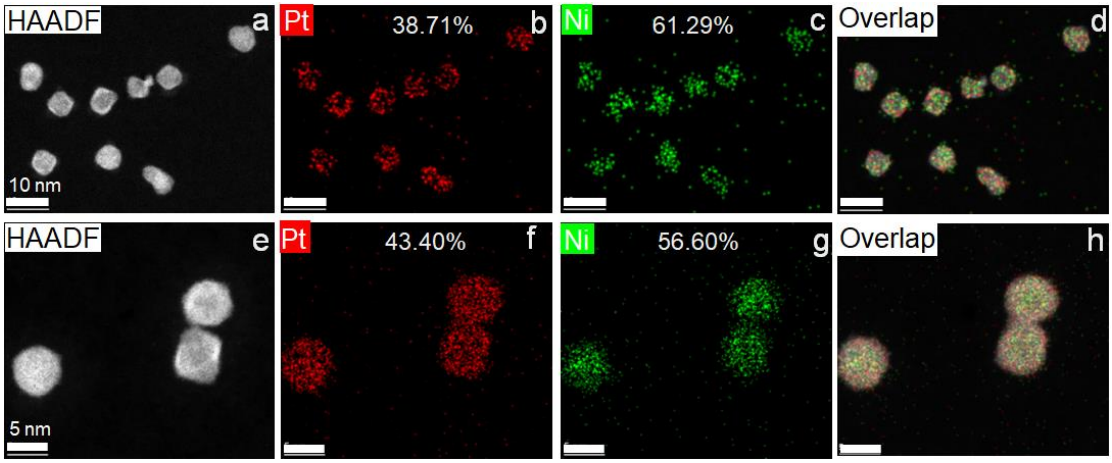


Figure 3.4.1. Elemental mappings of Ni-rich nanoparticles, where red and green dots represent Pt and Ni, respectively. (a-d) Pt-Ni nanoparticles (Ni75W/Pt30W) prepared using the sputtering powers of 30 W and 75 W for Pt and Ni respectively. (e-h) Pt-Ni nanoparticles (Ni30W/Pt30W) prepared using the same sputtering powers (30 W) for Pt and Ni targets. The overlayed elemental mappings and HAADF images shown in (d) and (h) demonstrate that Pt atoms formed the shell of Ni-Pt nanoparticles and Ni atoms are mainly located in the centers. The sputtering power applied on the Pt target plays a more important role than that of Ni target. (Images and EDX captured by STEM mode in FEI Titan Themis G2 60-300 working at 300 kV)

The sputtering power of the Pt target was kept at 30 W for preparing the core-shell nanoparticles, whose structures were confirmed from the elemental mappings shown in Figure 3.4.1. There are two samples, Ni75W/Pt30W (Figure 3.4.1a-d) and Ni30W/Pt30W (Figure 3.4.1e-h) with

the higher sputtering power on the Ni target contributing more Ni atoms (about 61at% in the sample of Ni75W/Pt30W) than the lower power (nearly 57 at% in the sample of Ni30W/Pt30W). The role of the sputtering powers on the contents of Ni-Pt nanoparticles is displayed in Figure 3.4.2, which summarizes the atomic percentages of Ni and Pt in the Ni-Pt nanoparticles prepared with different sputtering powers. The mean atomic fractions (black line in the Figure 3.4.2) of Ni (green bricks) and Pt (red bricks) were averaged from 5-10 nanoparticles. It is interesting that the sputtering power of the Pt target affects the structures and compositions of Ni-Pt nanoparticles more dramatically than that of the Ni target. For example, the Pt contents increase sharply from an average of 38 at% in Ni75W/Pt30W to an average of 84 at% in Ni75W/Pt50W. In contrast, only a small increase (about 6 at%) in the Ni content was observed when the sputtering power of the Ni target was increased from 30 W to 75 W. This demonstrates that sputtered Ni atoms are condensed more slowly than Pt atoms in the same aggregation environment.

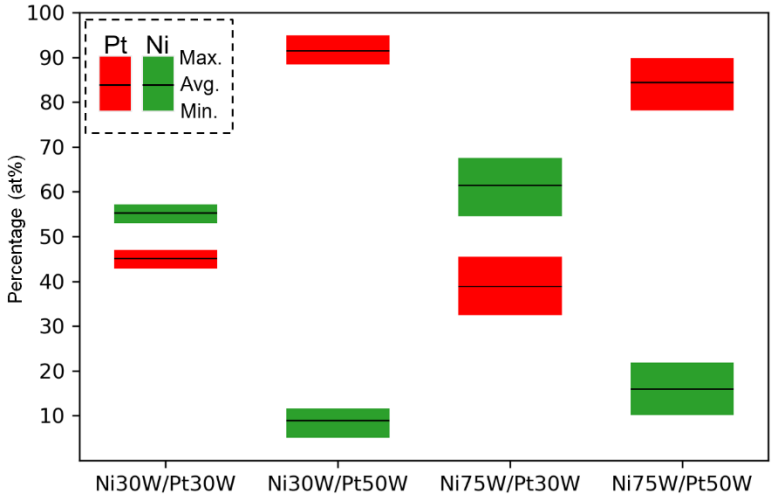


Figure 3.4.2. Atomic fraction of Ni-Pt nanoparticles, which were prepared under the argon flow rate of 90 sccm. The condensation lengths of Ni and Pt targets were 25 cm and 22 cm, respectively. The sputtering powers applied on the targets were labelled such as “Ni30W/Pt30W”.

3.4.2. Size distribution of Ni-rich nanoparticles

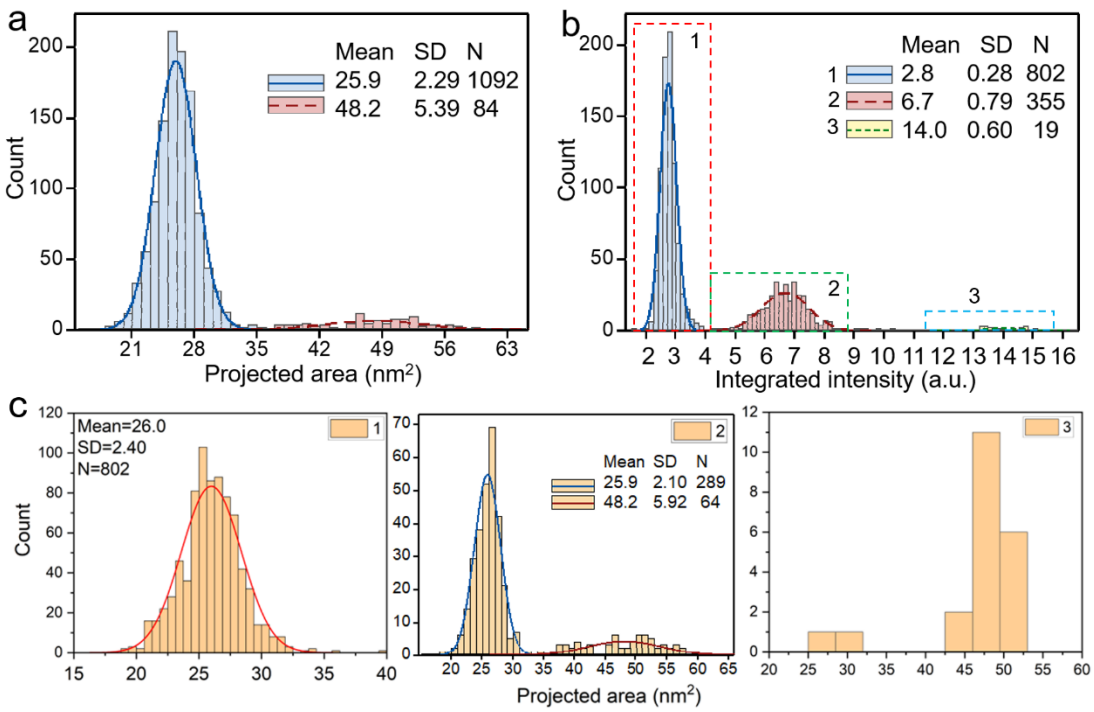


Figure 3.4.3. Size distribution of Ni-Pt nanoparticles (Ni30W/Pt30W). (a) Projected area distribution; (b) Integrated intensity distribution. Based on the distribution of integrated intensity shown in (b), the corresponding projected areas of nanoparticles are (mass-filter with 1.0×10^6 amu) presented in (c), where the "1", "2", and "3" are the area distributions of nanoparticles from the peaks of histogram in (b).

For estimating the population of Ni-rich or core-shell nanoparticles in the sample, projected areas and integrated intensities of Ni-Pt nanoparticles are analyzed and presented in histograms as shown in Figure 3.4.3. The large peak in the projected area distribution (Figure 3.4.3a) illustrates the fine mass selection (M/ΔM=25.9/2.29=11.3) of the mass filter installed in the cluster source. However, there are three peaks in the integrated intensity distribution (Figure 3.4.3b). The mean integrated intensity (6.7) of the peak "2" is larger than twice of the mean integrated intensity (2.8) of the peak "1", indicating that the peak "2" is not created by aggregated nanoparticles. The peak "3" of the intensity distribution is created by the aggregated

nanoparticles, contributing to the minor peak in the projected area distribution. Figure 3.4.3(c) gives the projected area distributions of nanoparticles from the peak "1", "2", and "3", with the rose red peak in Figure 3.4.3(b) containing two types of nanoparticles, Pt-rich nanoparticles and aggregated Ni-rich nanoparticles. Pt-rich nanoparticles have the same mean projected area as the Ni-rich nanoparticles, whose projected areas are presented in Figure 3.4.3(c1), indicating the Pt-rich nanoparticles contain fewer atoms than the Ni-rich nanoparticles due to the large crystal cell of Pt. Combing the projected area distribution with the integrated intensity distribution, the population of Pt-rich nanoparticles can be estimated by the number of nanoparticles from the peak "2" to be (289/(289+802)=26.5%).

Figure 3.4.4 shows the images of Ni30W/Pt30W, where the Pt-rich nanoparticles showing high intensities can be easily distinguished from the Ni-rich nanoparticles. Without exception, Pt-rich nanoparticles exhibit octahedral or tetrahedral (Figure 3.4.4f) shapes. Decahedra and icosahedra, based on their HAADF-STEM images (Figure 3.4.4c,d), are massively more likely to have high Ni contents and core-shell structures. Ni-rich nanoparticles with the core-shell structures can also form as octahedra, e.g. Figure 3.4.4(e).

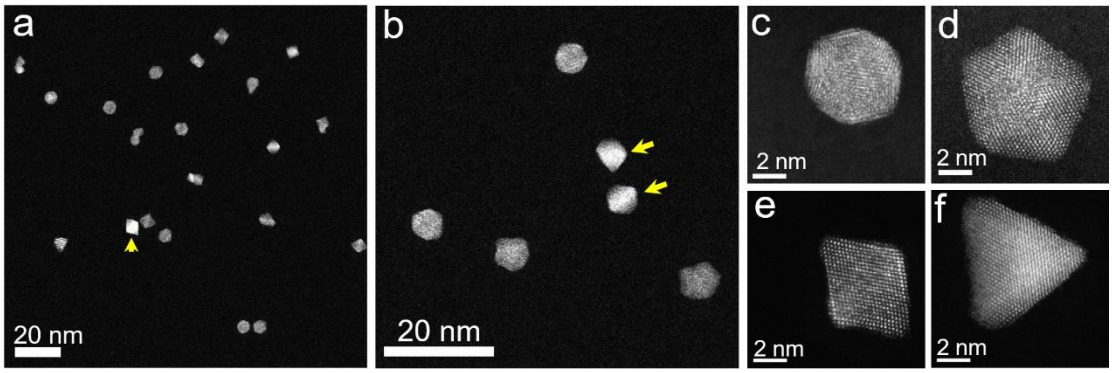


Figure 3.4.4. HAADF-STEM images of Ni-rich nanoparticles **(**Ni30W/Pt30W mass-filter with 1.0×10^6 amu). Pt-rich nanoparticles with octahedral shapes are pointed by yellow arrows in (a-b). The icosahedral (c) and decahedral (d) nanoparticles show

core-shell structures. The core-shell octahedron (e) also can be observed, but the tetrahedral (f) nanoparticles are Pt-rich based on their HAADF-STEM images. The peak “2” in the intensity distribution (Figure 3.4.3) is mainly consisted by octahedral and tetrahedral Pt-rich nanoparticles.

The sample of Ni75W/Pt30W mass-filtered with 1.0×10^6 amu also was analyzed with the same methods as the Ni30W/Pt30W, which both samples have similar values in the average integrated intensity. However, the mean projected area of Ni75W/Pt30W is 31.1 nm^2, 20.1% larger than the nanoparticles of Ni30W/Pt30W. It suggests that the Ni-rich nanoparticles of Ni75W/Pt30W contain more Ni than that of Ni30W/Pt30W, which is in agreement with the results of EDX in Figure 3.4.1. There are two large peaks in the histogram of the integrated intensity as shown in Figure 3.4.5, which means that the Pt-rich nanoparticles occupy over half of the populations in Ni75W/Pt30W, much more than in Ni30W/Pt30W. Considering the same condensation environment of Ni75W/Pt30W and Ni30W/Pt30W, the high percentage of Pt-rich nanoparticles in Ni75W/Pt30W could be caused by the reduction of Ni-rich nanoparticles with large sizes. Although the sputtering power of 75 W on the Ni target produces more Ni clusters (Figure 3.3.1a) than the 30 W on the Ni target, the number of particles in Ni75W/Pt30W is lower than in Ni30W/Pt30W. The mass spectrum of Ni75W/Pt30W (Figure 3.3.1c) peaks at lower mass compared to that of Ni30W/Pt30W, which means the Ni seeds are likely to form Ni-rich nanoparticles with small sizes, rather than large sizes, e.g. 1.0×10^6 amu. For verifying this explanation, the Ni-Pt nanoparticles from the Ni75W/Pt30W were size-selected with a mass of 3.2×10^5 amu as shown in Figure 3.4.7, which corresponds to the peak mass of the mass spectrum of Ni75W/Pt30W (Figure 3.3.1c).

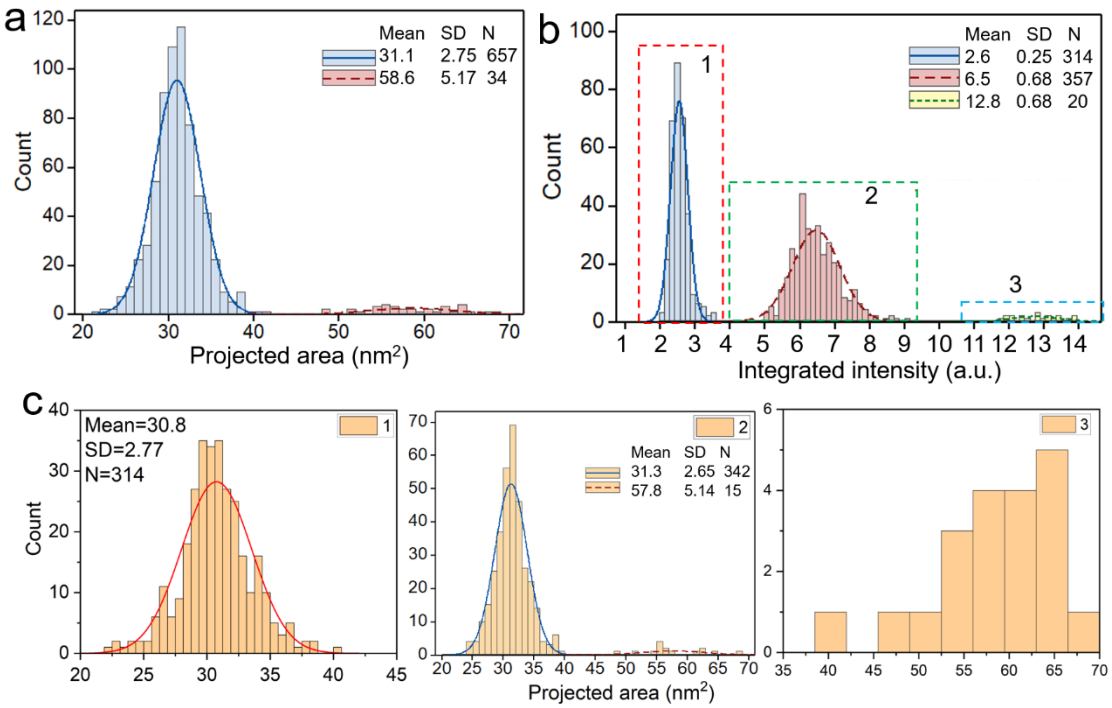


Figure 3.4.5. Size distribution of Ni-Pt nanoparticles (Ni75W/Pt30W with a mass selection of 1.0×10^6 amu). The projected area distribution of nanoparticles from the three peaks of the integrated intensity distribution (b) are presented in (c).

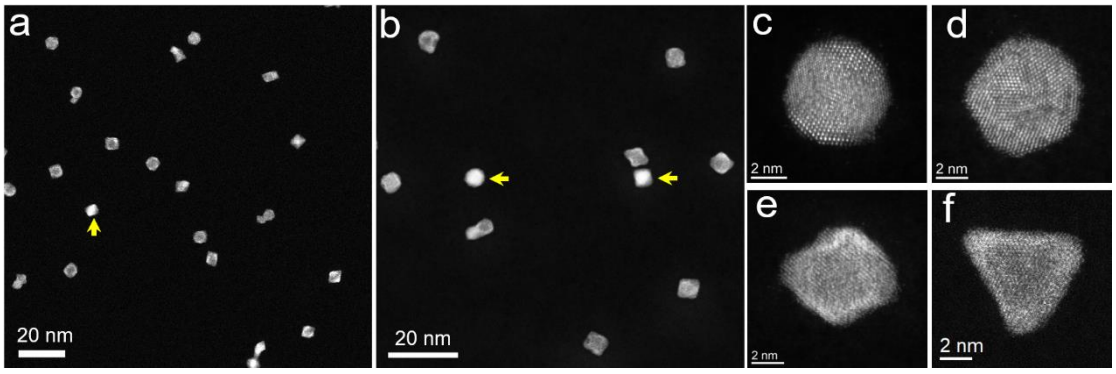


Figure 3.4.6. Images of Ni75W/Pt30W (mass-filter with 1.0×10^6 amu). The Pt-rich nanoparticles, which are octahedra, are marked by yellow arrows. Icosahedron (c), decahedron (d), octahedron (e), and tetrahedron (f) are demonstrated as examples.

The core-shell nanoparticles with various shapes are presented in Figure 3.4.7 that few Pt-rich nanoparticle is observed in the Ni75W/Pt30W with a mass selection of 3.2×10^5 amu (small sizes). The size analysis of nanoparticles (3.2×10^5 amu) (Figure 3.4.8) gives a different distribution with the large size-selected nanoparticles (1.0×10^6 amu) as shown in Figure 3.4.5.

The detailed analysis shows that Pt-rich nanoparticles occupied 52.1% in the large nanoparticles (1.0×10^6 amu). In contrast, only one main peak is observed in both the projected area distribution and the integrated intensity distribution of small nanoparticles (3.2×10^5 amu) (Figure 3.4.8). There are 15 Pt-rich small nanoparticles after careful recognition, which means the population of Ni-rich nanoparticles goes up (555/570) 97.4%. Considering this in light of the size distribution of the large nanoparticles (1.0×10^6 amu) in the Ni75W/Pt30W, it is reasonable to draw an inference that the population of Ni-rich nanoparticles decreases with the mass increase of nanoparticles.

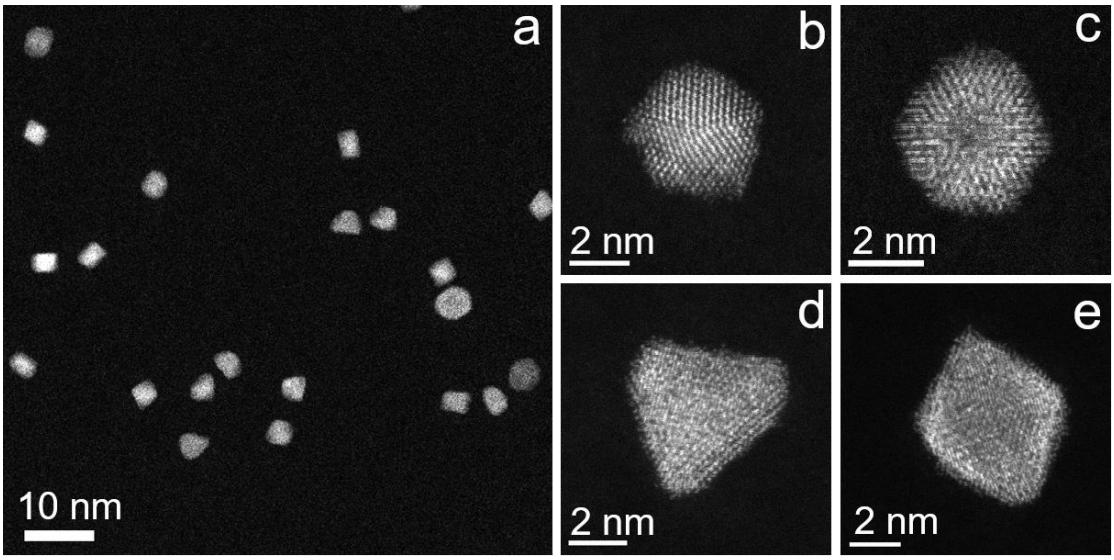


Figure 3.4.7. Images of core-shell Ni-Pt nanoparticles size selected from the Ni75W/Pt30W with a mass of 3.2×10^5 amu. (a) Overview of Ni75W/Pt30W sample; (b) decahedron; (c) icosahedron; (d) tetrahedron; (e) octahedron.

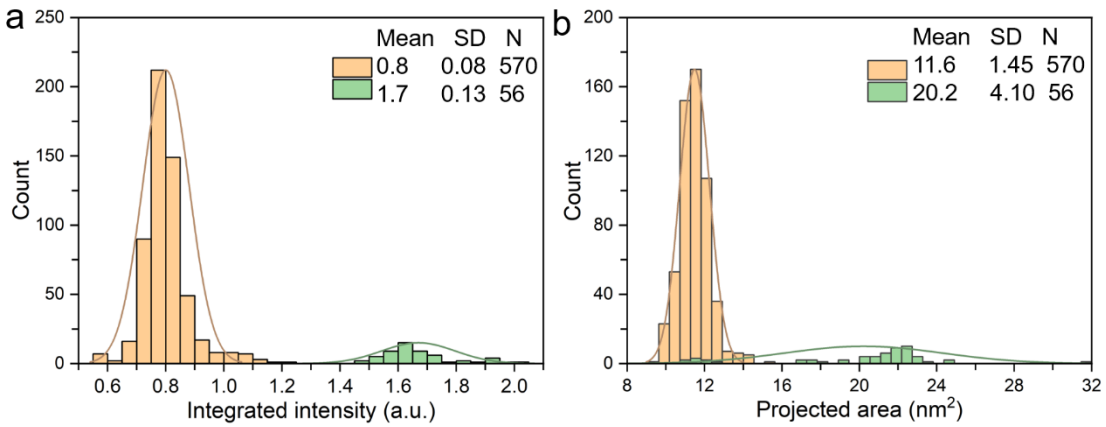


Figure 3.4.8. Size distribution of Ni75W/Pt30W mass selected with a mass of 3.2×10^5 amu. Two peaks are in the integrated intensity distribution (a) and the corresponding projected area distribution is presented in (b). All the peaks are fitted well by the normal distribution.

Table 3.4. Preparation conditions of core-shell nanoparticles with a mass selection of 1.0×10^6 amu.

Sample	Sputtering power (W)	Condensation length (cm)	Ar flow rate (sccm)	Percentage of Pt-rich NPs	Does have pure Ni NPs?
NiPt-1 (Fig. 3.2.3)	Ni(50W) Pt(75W)	Ni(25cm) Pt(19cm)	120	50.2%	Yes
NiPt-2 (Fig. 3.2.5)	Ni(75W) Pt(30W)	Ni(25cm) Pt(19cm)	90	26.7%	No
NiPt-3 (Fig. 3.4.4)	Ni(30W) Pt(30W)	Ni(25cm) Pt(22cm)	90	26.5%	No
NiPt-4 (Fig. 3.4.6)	Ni(75W) Pt(30W)	Ni(25cm) Pt(22cm)	90	52.1%	No

In conclusion, the nanoparticles with core-shell structures should be selected at the peak of the mass spectrum based on the examples of Ni75W/Pt30W. Table 3.4 lists the preparation conditions of Ni-Pt nanoparticles. In terms of the mass-selected nanoparticles with a mass selection of 1.0×10^6 amu, a short condensation length of Pt target (*e.g.* 19 cm) and a relative long gap (e.g. 6 cm) between Ni and Pt targets (NiPt-2 *v.s.* NiPt-4) are beneficial to form Ni-

rich nanoparticles. A low sputtering power rather than high sputtering powers on the Ni target promotes the populations of large Ni-rich nanoparticles. A high gas flow rate (e.g. 120 sccm) enhances the condensation rate of Ni and Pt atoms, which may induce the formation of pure Ni nanoparticles or Pt nanoparticles. In brief, the parameters should be balanced based on the anticipated structure of nanoparticles.

3.5. Structural stability of Ni-Pt nanoparticles

3.5.1. Thermal stability

In-situ heating provides a direct observation to monitor the evolution of the composition and morphology of multi-element metallic nanoparticles and core-shell nanoparticles. The atom diffusion occurring during annealing induces the morphological and compositional evolution, such as the transformation of concave octahedral PtNi to cuboctahedral/spherical PtNi alloys[160] and the structural changes of core-shell octahedral and cubic Pd@Pt nanoparticles to alloys[161]. In this study, the thermal stability of Ni-Pt nanoparticles with various shapes such as octahedral, tetrahedral, icosahedral, and decahedral, was examined using the in-situ heating method. The icosahedral and decahedral Ni-Pt nanoparticles maintain their original shapes even after high-temperature annealing at 900 °C, while the octahedral and tetrahedral Ni-Pt nanoparticles retain their face-centered cubic (fcc) structure but transform into spherical shapes. All of the shapes lose their core-shell structures, resulting in deformations in the alloying structures.

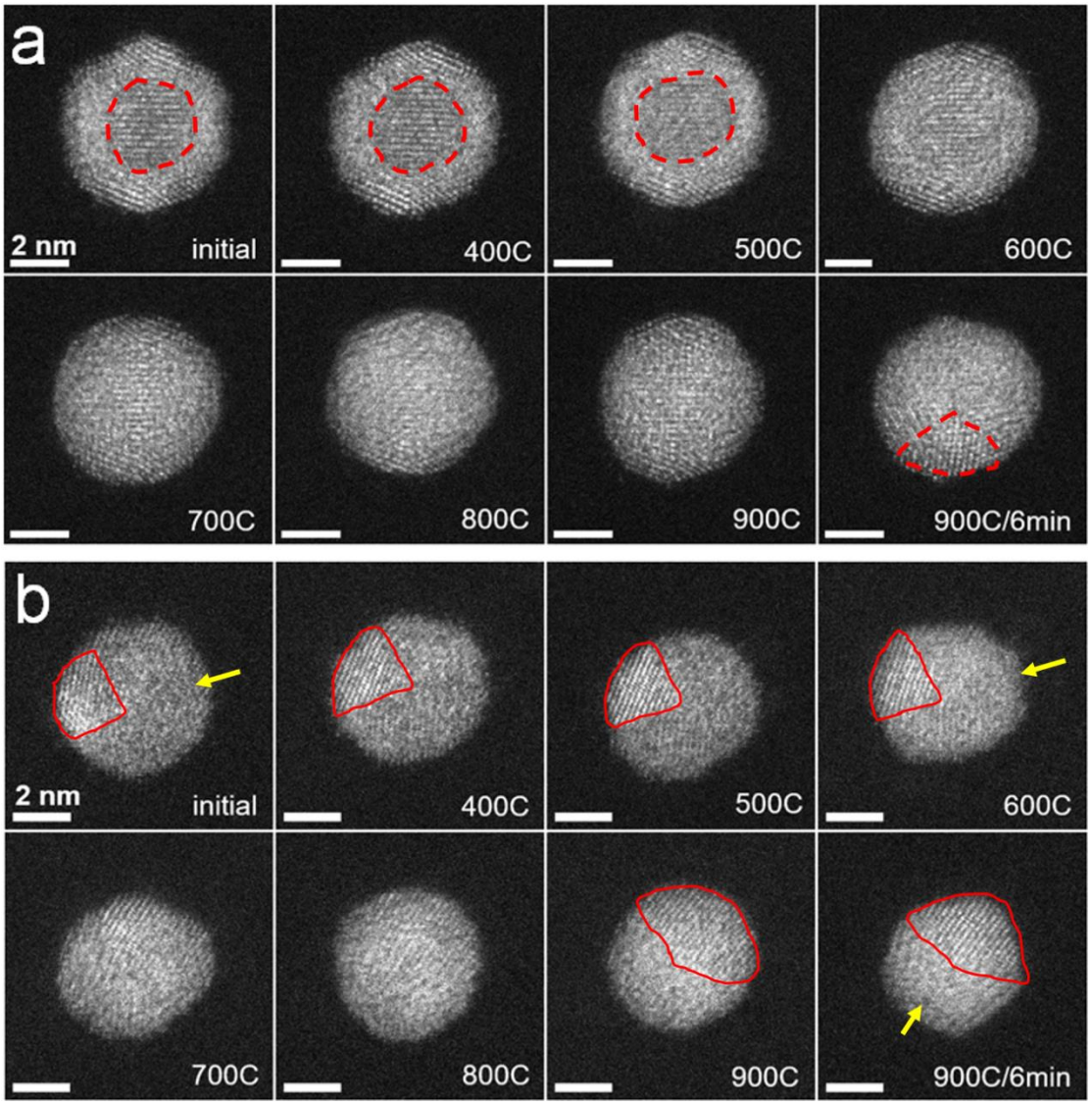


Figure 3.5.1. (a) An icosahedron with a core-shell structure, with the core (*d* spacing is 2.10 Å) consisting of Ni atoms with fcc structure and the shell built by Pt atoms (*d* spacing is 2.28 Å). The fcc-core disappears after annealing at 600 ℃ due to the mutual thermal diffusion of Ni atoms from the core and Pt atoms from the shell. An alloyed icosahedron is formed through annealing at 700 ℃. The icosahedral structure is retained after annealing at 900 ℃ for 6 minutes. (b) A Ni-rich decahedron maintained the structure unchanged over the whole annealing process but the intensity became uniform, suggesting a redistribution of elements in this decahedron. The orientation of decahedron varied, caused by atom diffusion, shape deformation, and rotation of the nanoparticle as a whole. (Images captured by JEM-2100F with a working voltage of 200 kV)

The heating procedure is the same as shown in Figure 2.5.1 with nanoparticles annealed at high temperature (e.g. 400 ℃) for 1 minute each time and images captured at room temperature after

annealing. Figure 3.5.1 illustrates the morphological evolutions of an icosahedron (a) and a decahedron, which were prepared using the same conditions as the Ni75W/Pt30W sample. The elemental mappings displayed in Figure 3.4.1 indicate that the Ni-Pt nanoparticles of Ni75W/Pt30W had a core-shell structure, with a Pt-shell and a Ni-core. This core-shell structure was also verified through HAADF-STEM images, where the Pt atoms in the shell displayed higher HAADF intensities compared to the Ni atoms in the core. This is because the HAADF intensities of Pt atoms and Ni atoms are directly proportional to the Z^{α}, where Z is the atomic number and $1.2<\alpha\leq 2$ Ref.[151–154]. The core-shell structure of the icosahedral Ni-Pt nanoparticle in Figure 3.5.1(a) is marked by a dashed red circle based on the Ni-core shows lower intensity than the Pt-shell in the HAADF-STEM image. After annealing at 400℃ and 500 ℃, the Ni-core maintained the structure but began to disappear at the annealing temperature of 600 ℃ as the Ni and Pt interdiffused. This indicates that the alloying processes took place as the temperature increases up to 600 ℃ or higher. Noting that the Ni and Pt interdiffusion occurred at high temperatures transforming the core-shell structure into alloy, the icosahedral shape covered with (111) facets remained unchanged after annealing at 900 ℃ for 7 minutes. The same phenomenon of atomic interdiffusion was observed in the decahedron shown in Figure 3.5.1(b), with the decahedral shape maintained but the core-shell structure converted into an alloyed structure in which Ni atoms (pointed by yellow arrows) show lower intensities than Pt atoms.

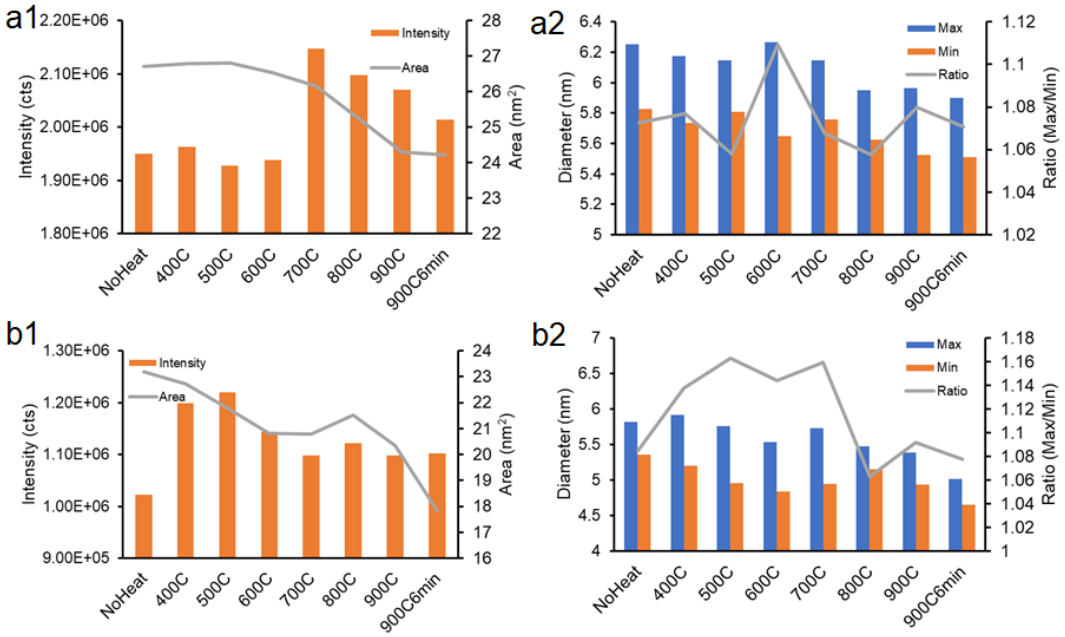


Figure 3.5.2. Changes of integrated intensities and areas of nanoparticles shown in Figure 3.5.1. (a1-a2) shows the variation of icosahedron in Figure 3.5.1(a). (b1-b2) shows the intensities and areas of decahedron in Figure 3.5.1(b).

The morphological evolution of Ni-Pt nanoparticles also was measured by the integrated intensity and the projected area as shown in Figure 3.5.2. As the increase of annealing temperatures, the projected area decreased gradually, accompanied by the decrease of maximum diameter and minimum diameter. This suggests that icosahedron and decahedron in Figure 3.5.1 deformed the morphologies during the annealing.

Figure 3.5.3 gives the morphological evolution of octahedral, tetrahedral, and icosahedral Ni-Pt nanoparticles at thermal annealing. The octahedral Ni-Pt nanoparticles with core-shell structures (a) and (c) began to lose their core-shell structures beyond 600 ℃, suggesting 600 ℃ or higher temperature accelerate the Ni and Pt atomic interdiffusion. The Feret's diameter (a distance between two parallel lines calipering the object) ratio (Figure 3.5.4) demonstrates the shape evolutions of Ni-Pt nanoparticles with the decrease of the Feret's diameter ratio indicating

the shape deformation from octahedra to spheres. The tetrahedron (Figure 3.5.3b) also turned into a round shape through the atomic diffusion from the vertex to neighbour planes. The icosahedron (Figure 3.5.3d), similar to the one shown in Figure 3.5.1a, kept its icosahedral shape but converted the core-shell structure to an alloying structure. Compared with the octahedral and tetrahedral Ni-Pt nanoparticles which were all annealed at 900 ℃, the icosahedral Ni-Pt nanoparticle retains its structure. This indicates that the icosahedron covered by (111) facets owns higher structural stability than octahedral and tetrahedral structures. Note that Ni-Pt nanoparticles with fcc structures in Figure 3.5.3 (a, b, and c) exhibit low resolution in their HAADF images captured after being annealed at 900 ℃. This low resolution in the HAADF images may be induced by the formation of amorphous structures produced during the melting process of nanoparticles. Those amorphous structures were then frozen and preserved due to the ultrafast cooling rate. It is worth noting that the melting temperature of Ni-Pt alloys is predicted to be lower than the pure Pt nanoparticles with the same size[141]. The melting temperature of bulk Pt material is 1769 ℃, higher than that of Ni (1487 ℃) [162,141]. Ni and Pt nanoparticles below 6 nm have been reported to melt at temperature around 900 ℃[162,140]. This difference in melting temperatures likely affects the behavior of Ni-Pt alloys at high temperatures, leading to the observed low resolution in the HAADF images.

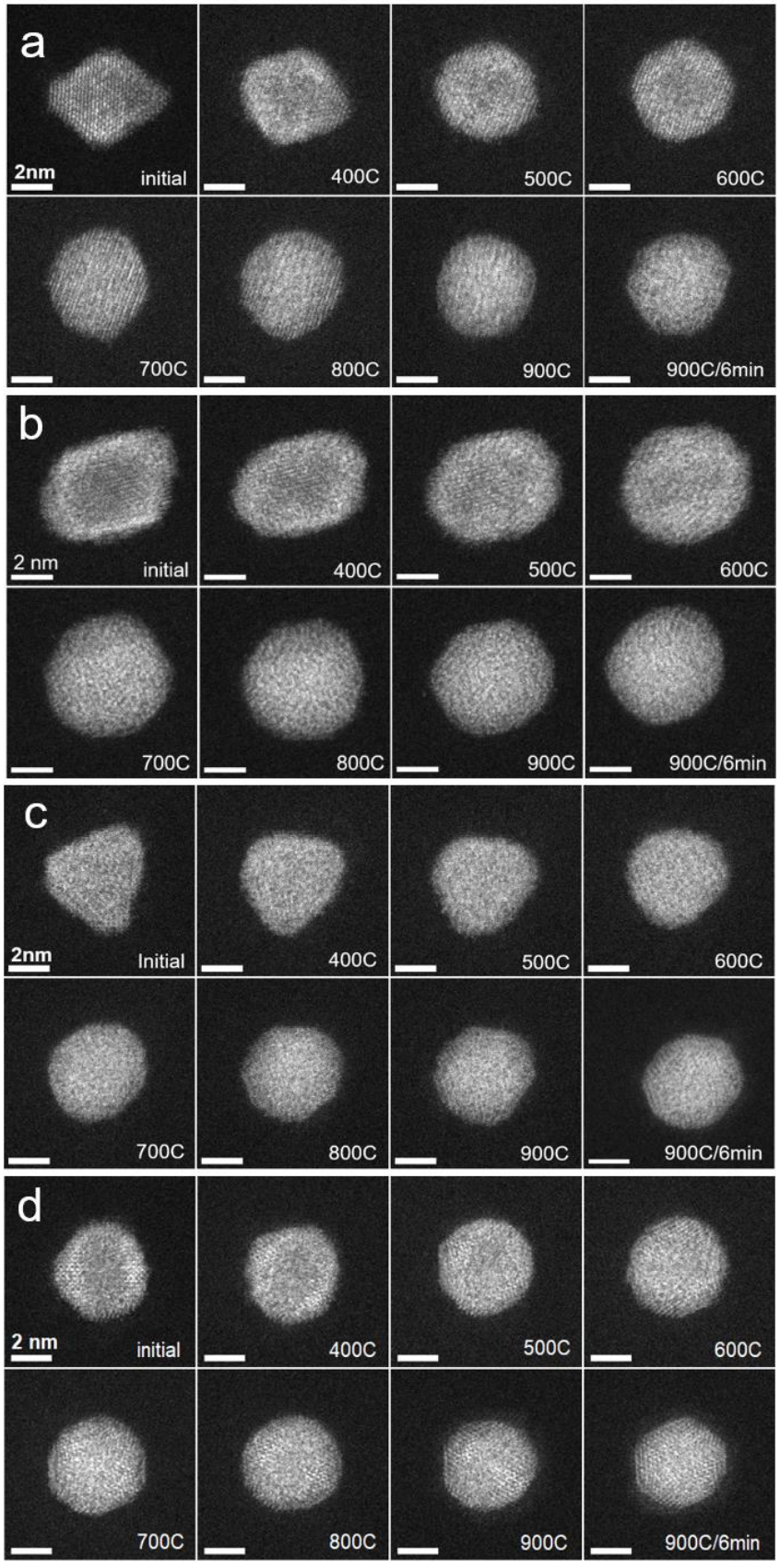


Figure 3.5.3. (a)(b) Core-shell Ni-Pt octahedron; (c) Ni-Pt tetrahedron; (d) Core-shell Ni-Pt icosahedron. The core-shell structures were maintained for annealing

temperatures were below 600 ℃. No structural transformations were observed. (Images captured by JEM-2100F with a working voltage of 200 kV)

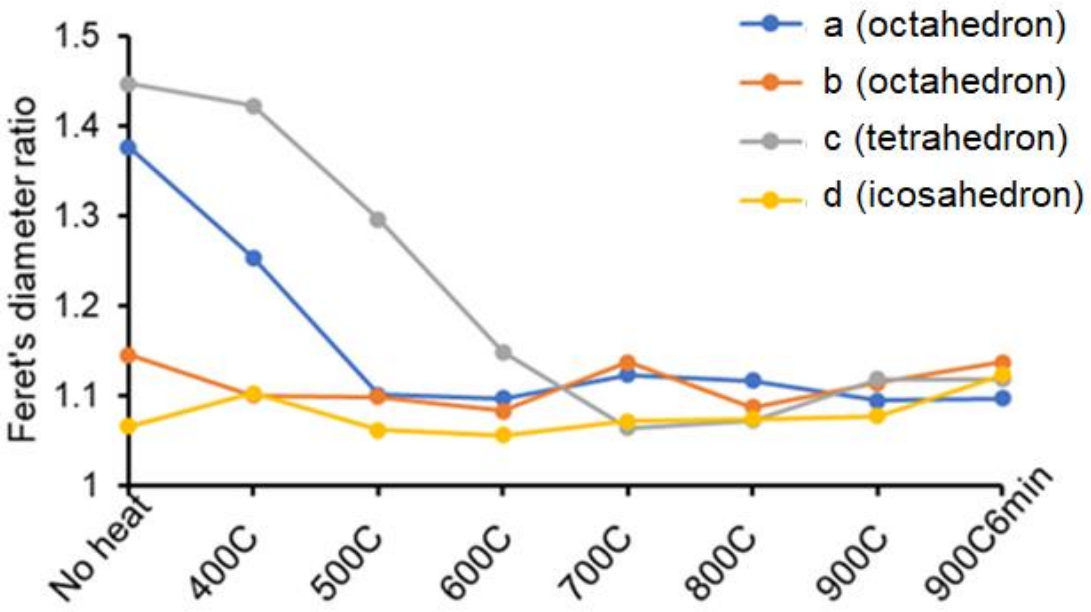


Figure 3.5.4. The ratio of Feret's diameter (the ratio of the maximum to the minimum Feret's diameter) of nanoparticles shown in Figure 3.5.3.

3.5.2. Structural stability of core-shell nanoparticles

The morphology and chemical composition stability are of importance for the applications of core-shell nanoparticles. As Pt atoms are more difficult to be oxidized than Ni atoms, the Pt shell can protect the Ni-core against oxidization. However, the stability of the interface between Pt-shell and Ni-core faces a challenge due to atomic interdiffusion. The elevated-temperature induced atomic diffusion has been discussed in the part 3.5.1. Here, we focus on the atomic diffusion during storage that is also observed to induce the structural change of the core-shell Ni-Pt nanoparticles.

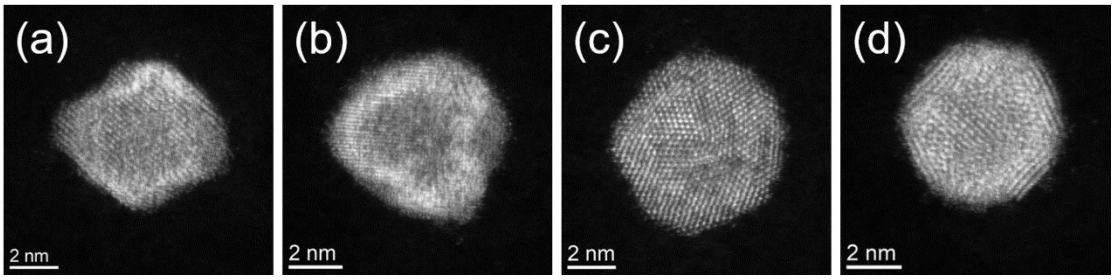


Figure 3.5.5. Core-shell nanoparticles (Pt30W/Ni75W sample) exposed in the air for 8 months. (a, b) Octahedron; (c) decahedron; (d) icosahedron. (Images captured by STEM mode in FEI Titan Themis G2 60-300 working at 300 kV)

Figure 3.5.5 shows images of core-shell nanoparticles, which have been kept for 8 months in the air. The examples of nanoparticles maintain intact core-shell structures, indicating that atomic diffusions did not destroy the core-shell morphology. However, as time passes, the structure of Ni-Pt nanoparticles undergoes changes, including morphology and compositions.

Electron energy-loss spectrometry (EELS) is a technique that can provide chemical information on the nickel in the Ni-Pt nanoparticles. An FEI Titan Themis G2 60-300 working at 300 kV was used to collect the EELS data in STEM mode with a probe semi-angle of 25 mrad and a semi-collection angle of 56.5 mrad. The camera length was 30 mm and the spot number was 6. A probe corrector DCOR+ was employed to correct the spherical aberration of the condenser lens. The Gatan DigitalMicrograph^{TM} software was used to control the microscope for acquisition of the spectrum in dual-EELS mode with the zero energy aligned using the zero-loss peak and the spectrum sharpened before acquisition. The acquired spectra were analyzed quantitatively in the DigitalMicrograph^{TM} with packages (SI and Spectrum). The core-loss spectra were deconvoluted using the Fourier-ratio method, following the background subtraction fitted by a power-law function.

Figure 3.5.6 presents one icosahedron (a) and one octahedron (b) as the examples of how EELS

was used to analyze the valence of Ni by calculating the L_3/L_2 ratio using the second derivative the core-loss spectrum[86]. The icosahedron retains its core-shell structure and the $L_{3,2}$-edges of Ni was recorded as shown in Figure 3.5.6d with Ni-L_3 and Ni-L_2 peak maxima[163] at 860.03 eV and 876.53 eV, respectively. There is no O-K edge detected in the spectrum, indicating the Ni atoms in the core are negligibly oxidized by the oxygen in the air. Compared with the icosahedron in Figure 3.5.6a, the octahedron lost its Ni-core and formed a hole in the center as shown in the line intensity profile (Figure 3.5.6c), which demonstrates that the intensity of the central part is close to the background level. Figure 3.5.6e presents the EELS of Ni from the octahedron with the O-K edge exhibiting a ratio of Ni-$L_{3,2}$ to O-K of 2.96. The Ni-$L_{3,2}$ edges ratio (L_3/L_2) of Ni is 2.07, less than the Ni-L_3/L_2 ratio of the icosahedron (2.67). The lower ratio of Ni-L_3/L_2 and the O-K edge in the octahedron indicate an increased valence of Ni atoms in the octahedron[164,87]. The void formed in the octahedron could be caused by Ni oxidation[165,166] through the Kirkendall effect as illustrated in Figure 2.5.6g[167], which is one of phenomenon caused by interdiffusion[168,169]. The Ni atoms moved outwards from the core of the nanoparticle through exchanging sites with Pt atoms in the shell. When Ni atoms diffused faster than Pt atoms, this process can be regarded as a flux of vacancies towards the core. As the concentration of vacancies in the diffusion zone became supersaturated, they condensed at the interface defects, resulting in the formation of voids. The Ni atoms that diffused to the surface of the Ni-Pt nanoparticles reacted with oxygen and oxidized to form NiO.

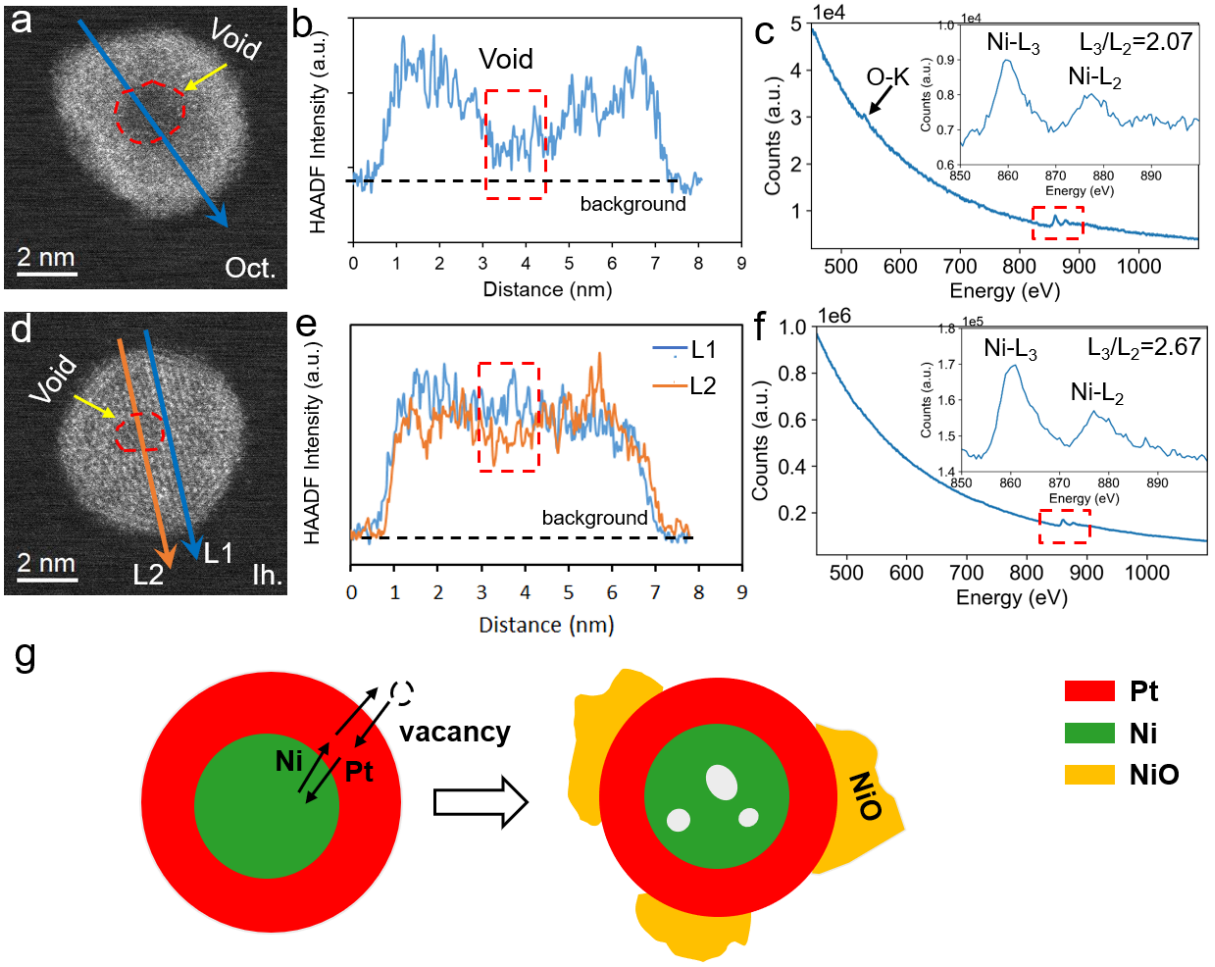


Figure 3.5.6. Storage stability of Pt-Ni nanoparticles with core shell structures, which were kept for 10 months in air. (a) octahedron, (b) line profile of intensity along the blue arrow in (a). A hole with about 1.2 nm diameter formed in the center of octahedron (a) due to the Kirkendall effect. EELS was collected to investigate the valence of Ni. (c) EEL spectrum of octahedral nanoparticle (a), which the ratio of L_3/L_2 is 2.07 and detected oxygen-K edge, indicating that the Ni atoms have been oxidized. (d) Icosahedron, (e) Intensity profiles along the arrows in (d). EELS of icosahedron (d) with the L_3/L_2 ratio of 2.67. The ratio of Ni-$L_{2,3}$ to O-K is 2.96. (g) Schematic of the void formation due to the Kirkendall effect. (Images and EELS captured by STEM mode in FEI Titan Themis G2 60-300 working at 300 kV)

More octahedral Ni-Pt nanoparticles than other shapes (decahedral and icosahedral) were observed to form voids after long-term storage, as shown in Figure 3.5.7. The possible reason could be the existence of twin boundaries in the decahedral and icosahedral Ni-Pt nanoparticles, which suppress Ni diffusion in the nanoparticles.

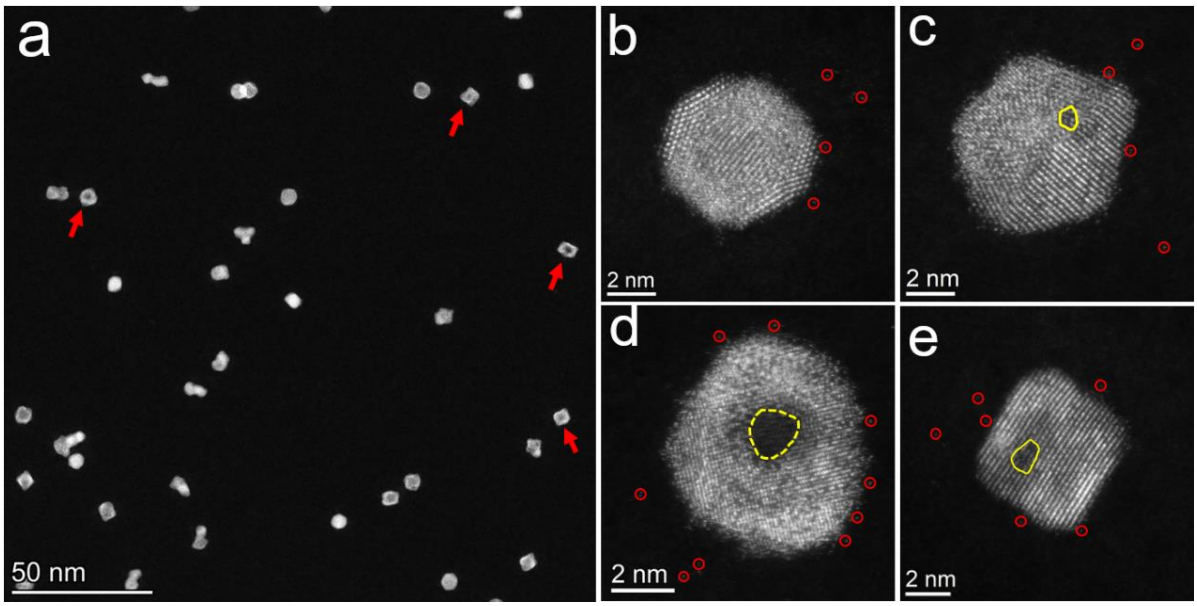


Figure 3.5.7. Core-shell nanoparticles (Pt30W/Ni75W) stored in air for 13 months. (a) Ni-Pt nanoparticles with voids marked by red arrows. (b) Icosahedron with a core-shell structure. (c) Decahedral alloy with a small void. (d) Octahedron with a large void. (e) Octahedral Ni-Pt core-shell nanoparticle with a small void. Single atoms surrounding nanoparticles are circled. (Images captured by STEM mode in FEI Titan Themis G2 60-300 working at 300 kV)

Oxidized Ni is also observed in an atomic image (Figure 3.5.8) with Ni atoms detected between the gap between octahedral nanoparticles (1, 2) and decahedron (3) based on the elemental mappings (Figure 3.5.8(b-d)). Nickel oxide was formed in the green circled area in Figure 3.5.8(a). This is demonstrated by the (111) NiO plane in Figure 3.5.8(e). The bright spots in the image represent individual Pt atoms, with one such atom highlighted by a red circle as an example. In contrast, the very dim spots correspond to single Ni atoms, as indicated by the green circle. The nickel oxide and the dispersed single atoms observed in Figure 3.5.9 further verify that the diffusion of Pt and Ni atoms can break the morphology and composition of Ni-Pt nanoparticles during long-term storage in the air.

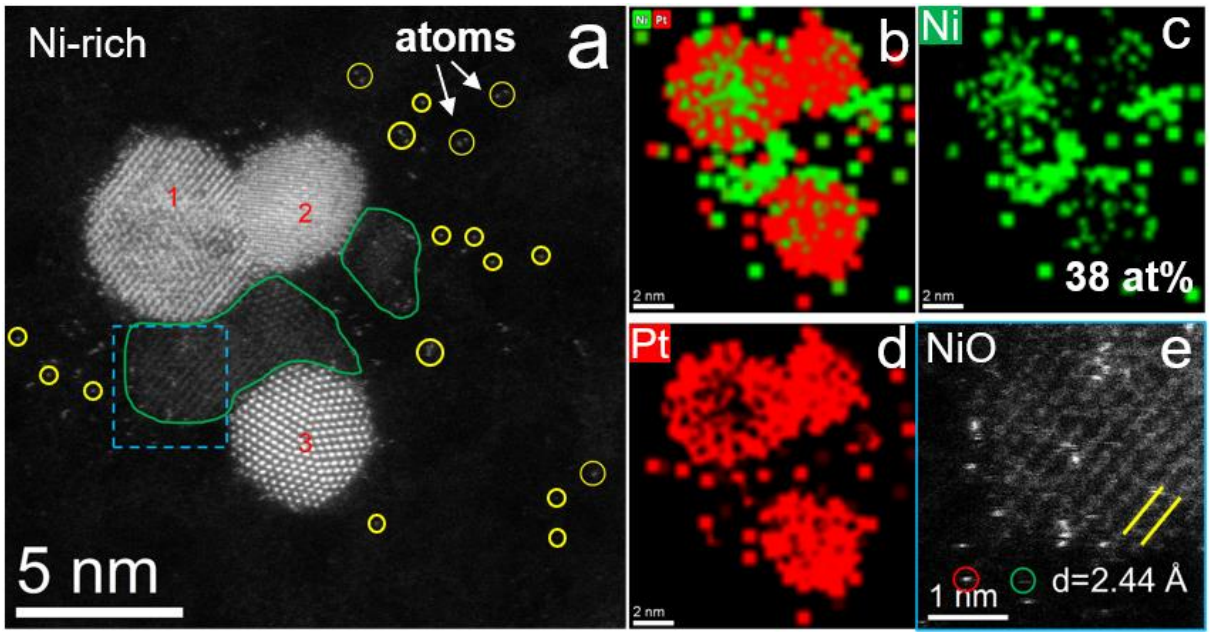


Figure 3.5.8. The structural stability of Ni-Pt nanoparticles in long-term (one-year) storage. (a) The HAADF-STEM image of a core-shell nanoparticle (1), an alloyed octahedron (2), and an alloyed decahedron (3). Single atoms dispersed around the nanoparticles were captured as shown by yellow circles. Elemental mappings in (b-d) showing that Ni atoms were detected in the area encircled by green lines in (a). The area marked by dotted blue line was zoomed in and is shown in (e), exhibiting lattice spacing of 2.44 Å, corresponding to NiO (111) netplane. The bright spots in (e) are Pt atoms circled by red and the green circle marks a single Ni atom. (Images and EDX captured by STEM mode in FEI Titan Themis G2 60-300 working at 300 kV)

The atomic diffusion not only takes place in Ni-rich nanoparticles, as shown in the octahedra and decahedral nanoparticles, but also in Pt-rich nanoparticles. Figure 3.5.9 shows a Pt-rich icosahedral Ni-Pt nanoparticle with dispersed single Ni atoms (encircled by yellow circles) as observed from STEM images and EDS mappings. This indicates that Ni atoms more easily diffuse away from the Pt-rich nanoparticles than Pt atoms.

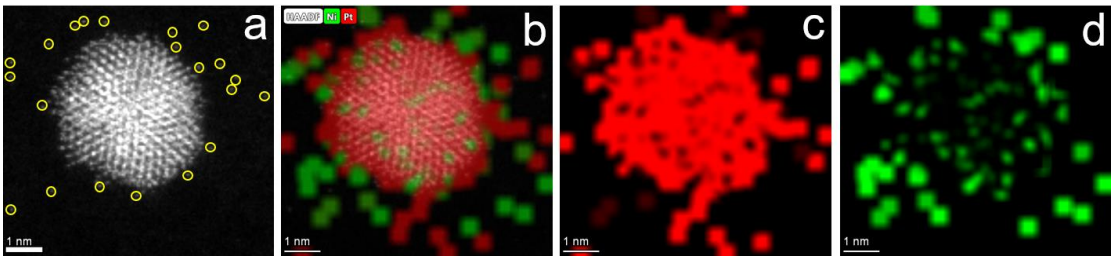


Figure 3.5.9. Ni-Pt alloys (Mass=3.2×10^5 amu, Pt 30W and Ni 75W) stored in the air for 12 months. Ni atoms escaping from the icosahedron with about Ni: 9.8 at% as detected by the EDX. (a) Pt-rich icosahedron and Ni atoms marked by yellow circles. (b) Overlayed image of HAADF-STEM image, Ni mapping, and Pt mapping. (c) Pt mapping. (d) Ni mapping showing that Ni atoms mainly surrounded the icosahedron. The scale bars are 1 nm. (Images and EDX captured by STEM mode in FEI Titan Themis G2 60-300 working at 300 kV)

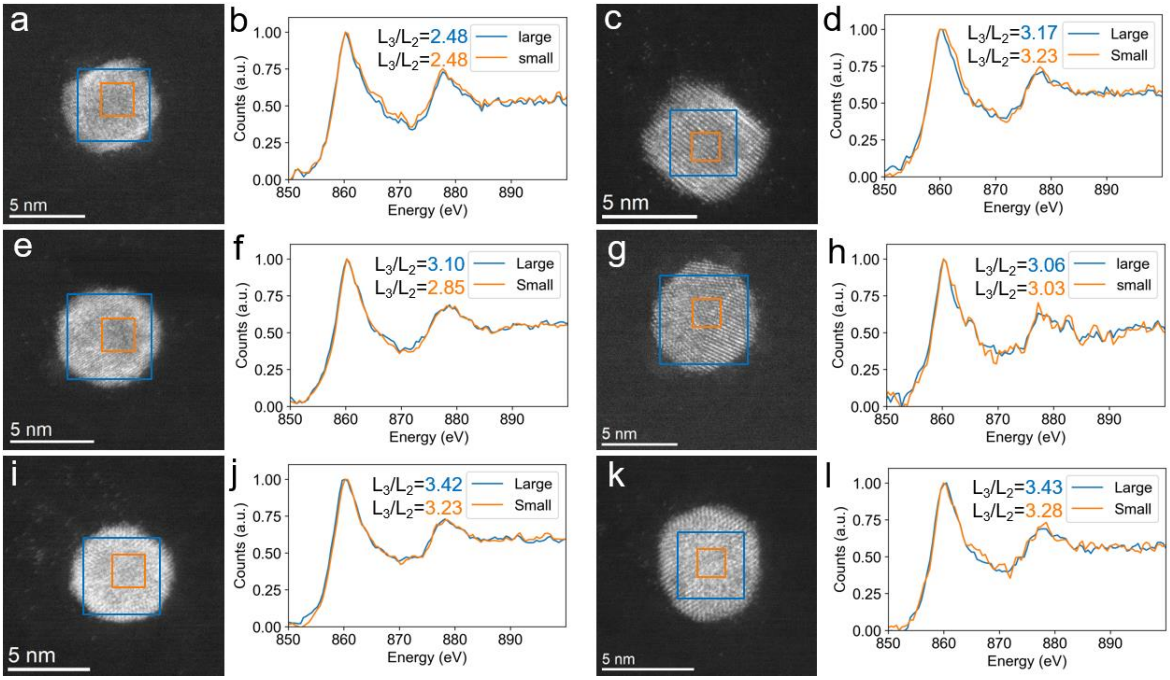


Figure 3.5.10. Examples of background-subtracted, deconvoluted and normalized Ni $L_{3,2}$ edges in core-shell Ni-Pt nanoparticles with (a-f) octahedral, (g, h) decahedral, (i-l) icosahedral shapes. These nanoparticles were stored in the air for 13 months. The rations of Ni-L_3/L_2 were calculated by measuring the integration intensity of the second derivative of L_2 and L_3 peaks[86]. The blue curve of Ni white lines is the sum of signals from the blue square and the origan curves are from orange squares. (Images and EELS captured by STEM mode in FEI Titan Themis G2 60-300 working at 300 kV)

Although Ni atom diffusion occurs in the naked Ni-Pt nanoparticles, causing damage to the

core-shell structure and oxidation of Ni atoms, a subset of Ni-rich nanoparticles can keep their structures intact and protect the Ni-core against oxidation. EELS mapping was utilized to detect the valence states of Ni from the selected ROI (a large blue region and a small orange region) as shown in Figure 3.5.10, giving the $L_{3,2}$-edge ratios of NiPt core-shell nanoparticles. It is found that icosahedra (i, k) have higher intensity ratios (around 3.4) of Ni-L_3/L_2 than the decahedron (h) (3.03) and octahedra (a, c, e) (from 2.48 to 3.23), suggesting that the icosahedron with twin boundaries and (111) facets is more structurally stable and resistant to oxidation than the octahedral and decahedral shapes[87,164].

3.6. Conclusion

Non-spherical Ni-Pt nanoparticles with core-shell structures were prepared using the magnetron-sputtering gas condensation method with shorter condensation length of Pt than Ni as the key prerequisite for the formation of core-shell nanoparticles. With the introduction of Ni atoms, decahedral and icosahedral structures were observed in the Ni-Pt nanoparticles. The sputtering powers applied on the Ni and Pt targets not only determine the contents of Ni and Pt in the formed nanoparticles, but also impact the structures of the nanoparticles dramatically. Nanoparticles mass selected from the peak of the mass spectrum have the highest possibility of forming core-shell structures when no more than 30 W of sputtering powers is employed on the Pt target.

The structural stability of Ni-Pt core-shell nanoparticles was investigated and it is found that the core-shell nanoparticles transform into alloys after annealing at high temperatures. The structures of nanoparticles, e.g. decahedral, icosahedral, and fcc structures, remain unchanged, but they become spherical at high temperatures. The core-shell nanoparticles also suffer from atomic diffusion, which induces the Kirkendall effect and destroys the core-shell structures and oxidizes Ni atoms.

The work in this chapter provides a way to prepare non-spherical alloy and core-shell nanoparticles using the magnetron-sputtering gas condensation method. The Kirkendall effect observed in the naked core-shell Ni-Pt nanoparticles indicate that core-shell nanoparticles face the challenge of retaining their structural stability.

Chapter 4. Nanoparticles synthesis using Joule heating

Joule heating is also called ohmic heating, which is generated by an electric current passing through a resistor converting the electric energy into heat. Recently, Joule heating has been utilized to prepare metal nanoparticles through raising temperature within a short time[27,38,30,31]. Two distinct terms are used in the literature to describe the synthesis involving Joule heating: carbothermal shock synthesis and flash Joule heating synthesis. Carbothermal shock synthesis makes use of the Joule heating generated in carbon films to reduce metal precursors absorbed on the carbon fibers to metal nanoparticles[37]. This method has been successfully synthesized high-entropy alloys[37], intermetallic alloys[41], high-entropy oxides[170,171], and single atoms[172]. Flash Joule heating was employed firstly to prepare metallic glasses[173]. James M. Tour's group introduced flash Joule heating as a bottom-up method for producing gram-scale graphene [39,174] with a quartz tube used to pack the precursor powders, pressed by two electrodes. This synthesis can also prepare transition metal carbide nanoparticles[38].

This chapter employs the carbothermal shock synthesis technique to produce ruthenium (Ru) nanoparticles containing single Pt atoms, which undergo structural transformation from a hexagonal close-packed (HCP) to a face-centered cubic (FCC) structure. Moreover, the flash Joule heating synthesis approach is employed to prepare metal alloy and metal phosphide nanoparticles. Finally, the hydrogen evolution reaction electrocatalytic activity of the single-Pt-atoms Ru nanoparticles is evaluated.

4.1. Structure controlled synthesis of single-Pt-atoms Ru nanoparticles by carbothermal shock

Metal nanoparticles are formed through the carbothermal reduction reaction of metal precursors at ultrahigh temperature (>2000 K) created by the Joule heating when a pulse current passes through carbon fibers. Then flash heating and cooling rates on the order of 10^5 K/s limit particle coarsening[37]. However, the size distribution of the nanoparticles relies heavily on the carbon fiber's surface defect concentration[37]. In this experiment, N, N-dimethyl formamide (DMF), an organic solvent, was utilized to dissolve the metal precursors such as metallic acetyl acetonate, which led to the homogeneous distribution of metal precursors on the carbon fibers. Consequently, this technique was implemented to synthesize Ru nanoparticles with controlled structures of either hexagonal close-packed (hcp) or face-centered cubic (fcc).

4.1.1. Influence of solvent on the nanoparticle sizes

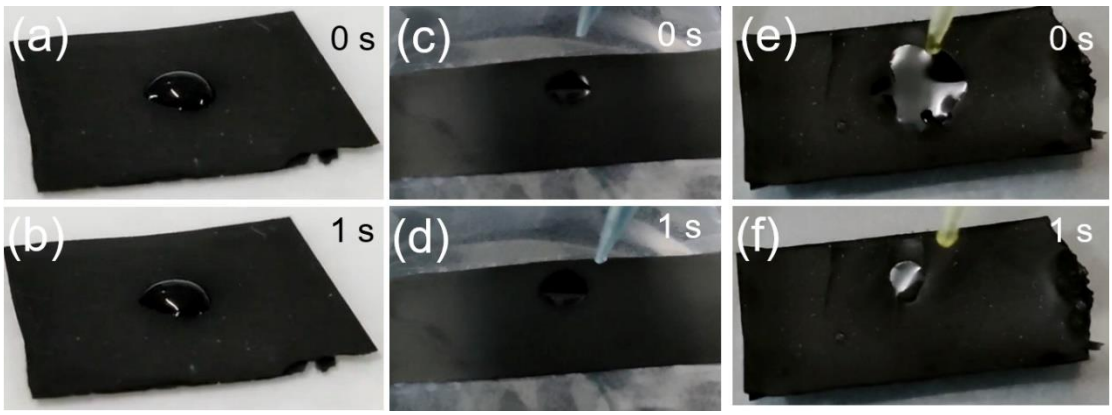


Figure 4.1.1. Wettability of water, ethanol, and N, N-dimethyl formamide (DMF) on the carbon films. (a,b) Water cannot be absorbed but forms a drop on the surface of the carbon films. (c, d) Ethanol infiltrates the carbon films quickly. (e, f) DMF also infiltrates the carbon films but slower than ethanol. The surface tension of water, ethanol, and DMF are 72.8, 22.1, and 37.1 mN/m (at 20 ℃), respectively. (Data taken from *https://www.dataphysics-instruments.com/Downloads/Surface-Tensions-Energies.pdf*)

Electrospun fibers were carbonized at 800℃ for 2 hours in a flowing argon gas atmosphere. In order to absorb the metal salts uniformly on the surface of the carbonized carbon fibers, ethanol, deionized water, and N, N-dimethyl formamide (DMF) were employed as solvents to dissolve the metal precursors. Figure 4.1.1 shows the wettability of metal salts solutions on the carbon film. A water droplet (Figure 4.1.1a, b) cannot infiltrate into carbon films. In contrast, ethanol and DMF can infiltrate carbon fiber films completely. Compared with ethanol, the DMF droplet (Figure 4.1.1e, f) was absorbed by carbon films more slowly. This difference can be explained by the surface tension of ethanol and DMF, as DMF has higher surface tension than ethanol (37.1 mN/m *v.s.* 22.1 mN/m, respectively). Therefore, ethanol and DMF were chosen as the solvents to dissolve metal precursors.

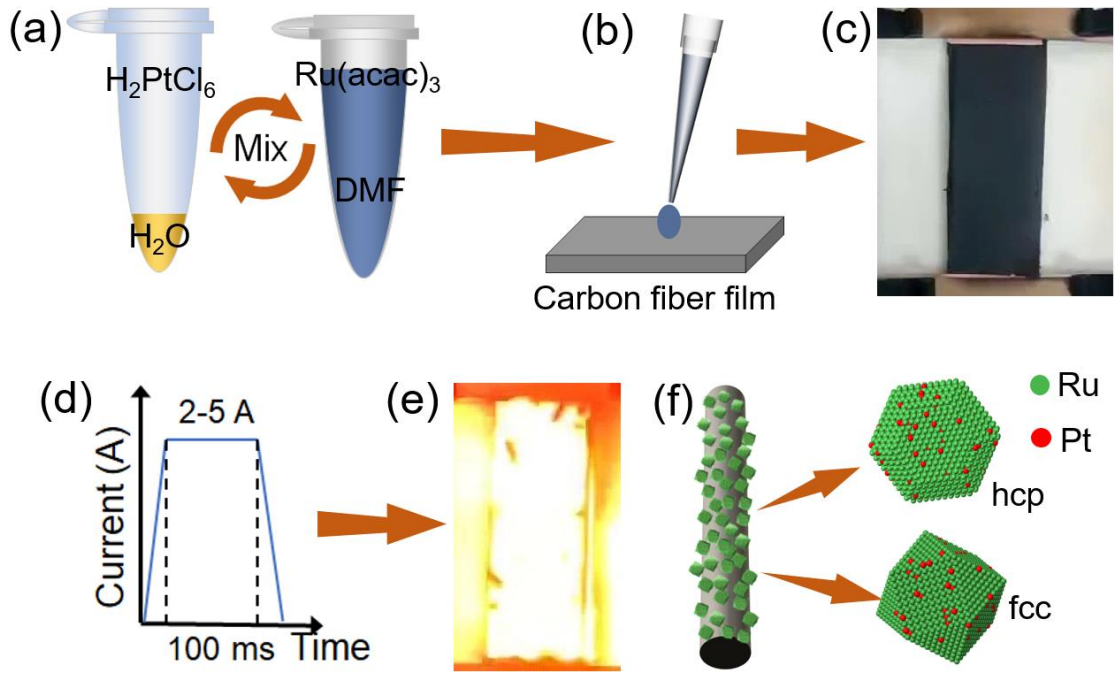


Figure 4.1.2. Carbothermal shock synthesis of nanoparticles on carbon films. (a) Metallic precursors are mixed. (b) The mixture solution is dropped into carbon films, which will be dried in vacuum at 60 ℃. (c) The dried carbon films will be cut into slices with a size of 12 mm × 30 mm and contacted with copper electrodes using silver paste. (d) A pulse current is applied on the carbon film. The temperature of Joule heating is

controlled by the current and the pulse width of the voltage. (e) A snapshot of heating. (f) Model of carbon fiber with nanoparticles, which have hcp and fcc structures.

Figure 4.1.2 demonstrates the procedure of nanoparticle synthesis by the carbothermal shock method, which is modified based on the reference[37]. The metal precursor was dissolved in solvents (DMF or water) to prepare 0.05-0.1 mol/L solutions. Then, the precursor solutions were directly dropped onto 40 mg of carbon films with a loading of 400 μL of solution. Before heating, the carbon fibers were dried in vacuum at 60℃ for 12 hours. As shown in Figure 4.1.2(b), the carbon film was cut into slices of 12 mm×30 mm, which was suspended on an alumina slide. Two copper slides were used as electrodes to connect to the carbon fiber film. An external pulse power source (NOVA POWER) provides the pulse current. The maximum current and voltage can be up to 20 A and 200 V, respectively. The carbothermal shock synthesis was carried out in an argon-filled or evacuated high-vacuum acrylic box.

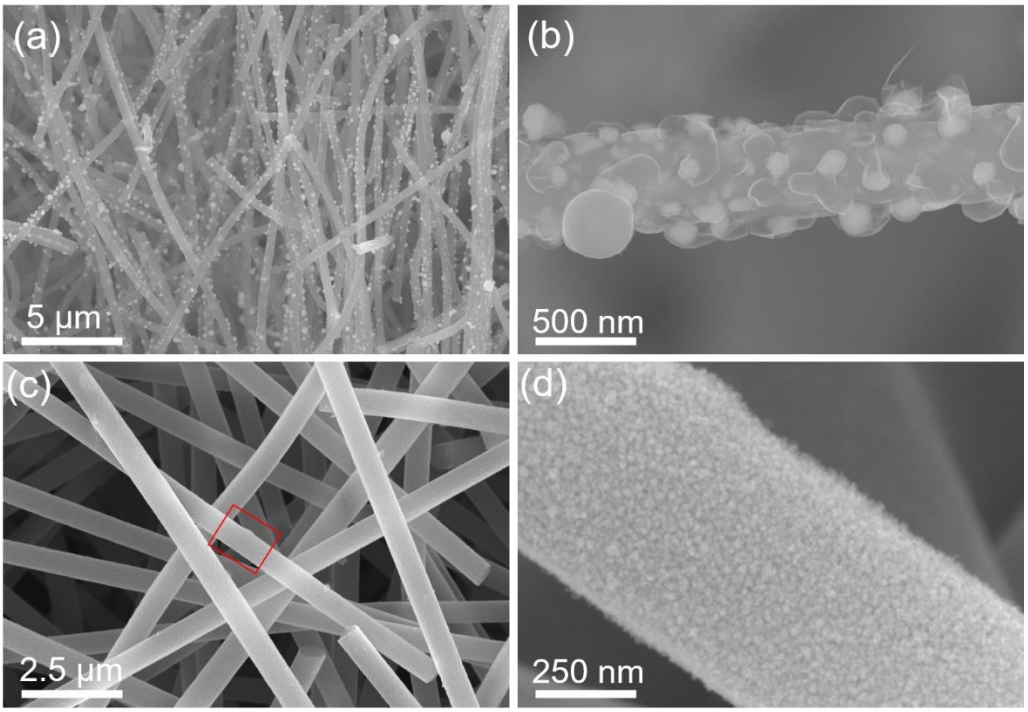


Figure 4.1.3. Influences of solvents on the size of Ru nanoparticles growing on carbon fibers synthesized by flash Joule heating. Ruthenium acetylacetonate was dissolved in different solvents (a-b) Ethanol; (c-d) DMF. The preparation parameters were the same for heating: 3 A of current with a duration of 500 ms.

Figure 4.1.3 shows Ru nanoparticles grows on the surface of the carbon fibers. Ru precursors dissolved by DMF yielded well-dispersed Ru nanoparticles without large nanoparticles, as observed in scanning electron microscope (SEM) images in Figure 4.1.3(c, d). In contrast, large Ru nanoparticles up to 200 nm were observed from the SEM images in Figure 4.1.3(a, b) for samples prepared with deionized water as the solvent to dissolve the Ru precursors. As the same preparation conditions of Ru nanoparticles in the carbothermal shock synthesis had been used (e.g. 3 A for the current, 180 V for the voltage, and 100 ms for the pulse width), the difference in the size distribution can be attributed to the solvents. It is found that DMF is beneficial to form the well-dispersed small nanoparticles by immersing and taking advantage of the surface defects of carbon fibers adequately.

4.1.2 Structure-controlled synthesis of Pt-doped Ru nanoparticles

The hcp structure, rather than the fcc structure, is the more energy-stable structure of Ru both in bulk and at nano dimensions[32,175,176]. The fcc Ru nanoparticles have higher performances than the hcp Ru nanoparticles as catalysts[32,175,176,177]. Ru nanoparticles with fcc structure were synthesized for the first time using the wet-chemical method, in which the cohesive and specific surface free energies of Ru were altered by a stabilizing agent in the organic solvent[176]. Seed-mediated growth also was employed to synthesize the fcc Ru nanoparticles[32,175]. The structural stability of the fcc Ru nanoparticles was measured by in-situ XRD, with the fcc structure transforming into the hcp structure as the temperature is raised 500 ℃ beyond[32]. Here, the carbothermal shock method will be used to prepare fcc Ru nanoparticles, doped by Pt atoms.

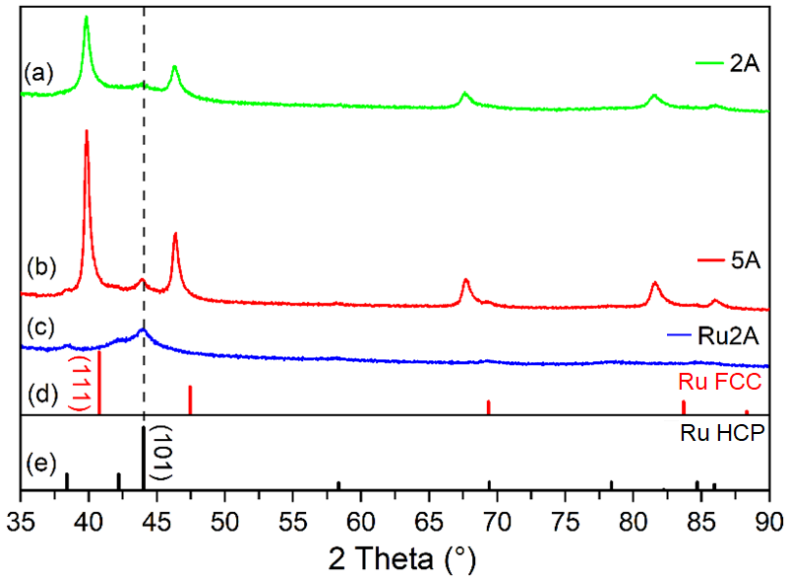


Figure 4.1.4. XRD spectra of Ru and Pt-doped Ru alloys. (a) Ru nanoparticles doped with 10 at% of Pt, prepared using a current of 2 A with 100 ms. (b) $Ru_{90}Pt_{10}$ alloys with an atomic ratio of 10:1, prepared using a current of 5A with 100 ms. (c) Pure Ru nanoparticles prepared with a current of 2A with 100 ms. The reference XRD patterns of Ru nanoparticles with an FCC (fm-3m, ICSD #41515) and an HCP (ICSD #40354 with a space $P6_3/mmc$, a=b=2.7329Å, c=4.3139 Å) structure are presented in (d) and (e), respectively. The peak position of (101) facet in the HCP structure is marked by a dashed line.

The procedure of preparing the Pt doped Ru nanoparticles is described in Figure 4.1.2, with $Ru(acac)_3$ (99.95%) and H_2PtCl_6 (99.99%) used as the precursors, dissolved in DMF or or H_2PtCl_6 in deionized water. The molar ratio of $Ru(acac)_3$ to H_2PtCl_6 was adjusted based on Ru, $Ru_{95}Pt_5$, and $Ru_{90}Pt_{10}$, respectively. 400 µl of 0.1 M mixed solution was dropped on the 40 mg of carbon films. The carbon film was cut with the same size of 12 mm × 35 mm for keeping the resistance of the carbon film the same in the heating. Figure 4.1.4 shows the XRD spectra of as-prepared samples with $Ru_{90}Pt_{10}$ heated using 2 A and 5 A for 100 ms, respectively. Ru2A is the pure Ru nanoparticles prepared by 2 A for 100 ms. Compared with the reference XRD given in Figure 4.1.4, Ru2A shows an hcp structure without fcc structure, while $Ru_{90}Pt_{10}$ nanoparticle samples exhibit both the fcc and the hcp structure. A small peak is observed at 43.4° in the XRD spectrum of the sample 2A ($Ru_{90}Pt_{10}$), indicating the presence of the hcp structure. As the

heating current was increased from 2 A to 5 A, representing a heating temperature increase, the peak at 43.4° became higher, compared with the (111) peak of the fcc structure. It suggests that higher heating temperature may promote the formation of hcp Ru nanoparticles.

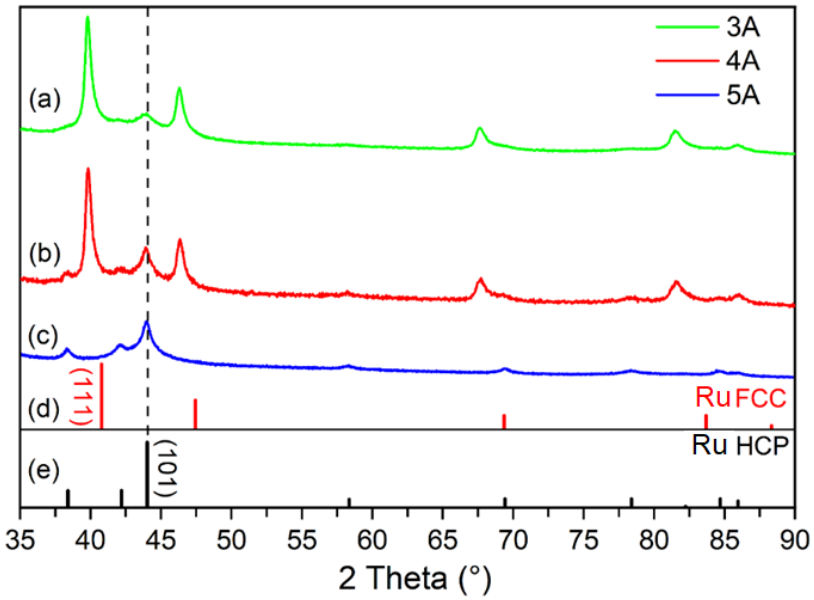


Figure 4.1.5. XRD spectra of 5 at% Pt atom doping Ru nanoparticles. Samples were prepared using different currents (a) 3 A; (b) 4 A; (c) 5A. (d) A reference pattern (ICSD #41515) of Ru with an FCC structure. (e) A reference pattern (ICSD #40354) of Ru with an HCP structure.

For investigating the role of Pt and the heating temperature on the formation of the fcc Ru structure, $Ru_{95}Pt_5$ nanoparticles were prepared using different currents in the preparation. The XRD spectra are displayed in Figure 4.1.5. It is interesting that no peak of fcc structure was detected in the XRD of $Ru_{95}Pt_5$ nanoparticles prepared using 5A. As the current dropped to 4A, both fcc and hcp peaks were detected in the XRD. The intensity ratio of fcc(111) to hcp(101), $I_{fcc(111)}/I_{hcp(101)}$, is used to represent the percentage of the $Ru_{95}Pt_5$ nanoparticles with an fcc structure. $I_{fcc(111)}/I_{hcp(101)}$ increases from 3.32 to 10.31 when the current decreased from 4 A to 3 A, indicating that low heating temperature is preferable for the formation of fcc Ru nanoparticles. More importantly, Pt atoms are important for the formation of fcc Ru nanoparticles with more Pt atoms allowing a higher current to be used in the preparation.

The size and structure of Ru and RuPt alloy nanoparticles were investigated from the STEM images. Figure 4.1.6 shows the images of pure Ru nanoparticles (Ru2A) growing on the surface of carbon fibers with a diameter of about 350 nm. Some fibers (e.g. the fiber with 371 nm in diameter) are loaded with large nanoparticles, whose sizes are up to 80 nm^2 for the projected area. In contrast, some fibers exhibit small nanoparticles, whose average projected area is around 6.8 nm^2. The projected area of Ru nanoparticles are fitted well by the log-normal functions (Figure 4.1.6c,e), suggesting that the Ru nanoparticles are formed by fusion[37]. The size difference of nanoparticles could be caused by the fiber absorbing different amounts of precursors with a higher amount of precursors absorbed on the fiber, yielding larger nanoparticles.

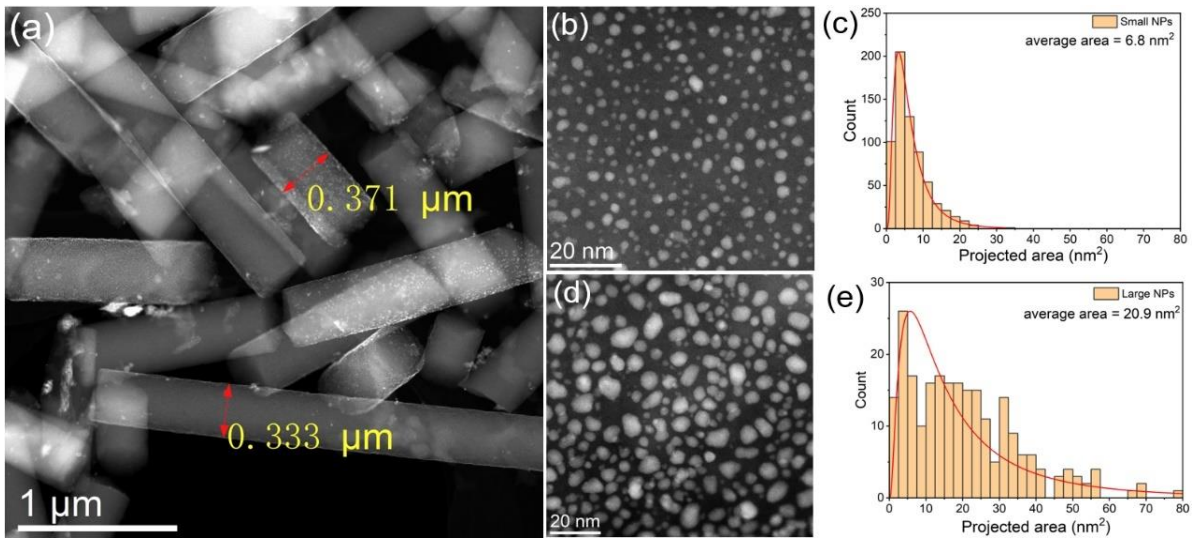


Figure 4.1.6. Pure Ru nanoparticles (Ru2A) growing on the surface of carbon fibers. (a) Overview of Ru nanoparticles on the carbon fibers, in which no large aggregates are observed. (b, c) Small Ru nanoparticles and the size distribution. (d, e) Ru nanoparticles on a different carbon fiber with large sizes and the corresponding size distribution. Both size distributions in (c) and (e) are fitted by the log-normal function. (Images captured by STEM mode in FEI Titan Themis G2 60-300 working at 300 kV)

$Ru_{95}Pt_5$ nanoparticles with 3A and 4A used to heat the carbon films are shown in Figure 4.1.7 and Figure 4.1.8, respectively. Both large and small nanoparticles can be observed from different fibers. The size distribution of nanoparticles follows the log-normal distribution. As

the current is increased to 4A, the large nanoparticles (Figure 4.1.8b) are closer to spheres than the nanoparticles in Figure 4.1.7b. The higher temperature drives the atoms fusion to construct the Wulff shapes, reducing the surface free energies.

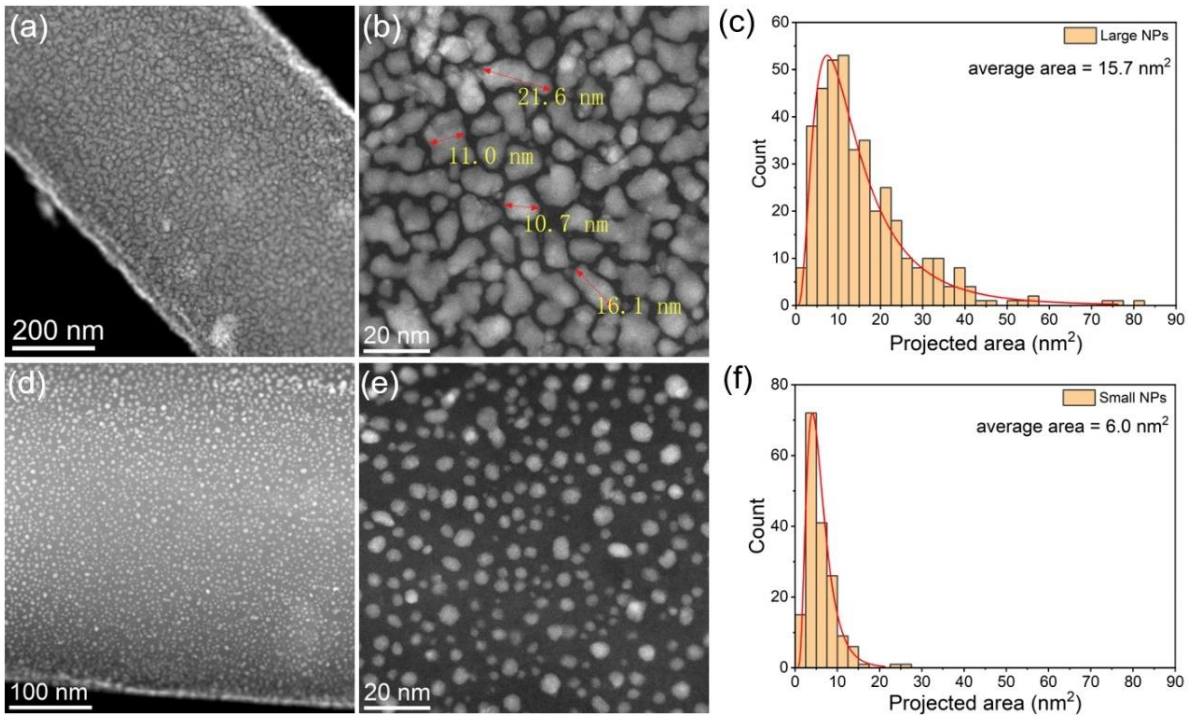


Figure 4.1.7. Images and size distributions of $Ru_{95}Pt_5$ nanoparticles prepared using 3A with 100 ms. (a-c) large nanoparticles; (d-f) small nanoparticles. (Images captured by STEM mode in FEI Titan Themis G2 60-300 working at 300 kV)

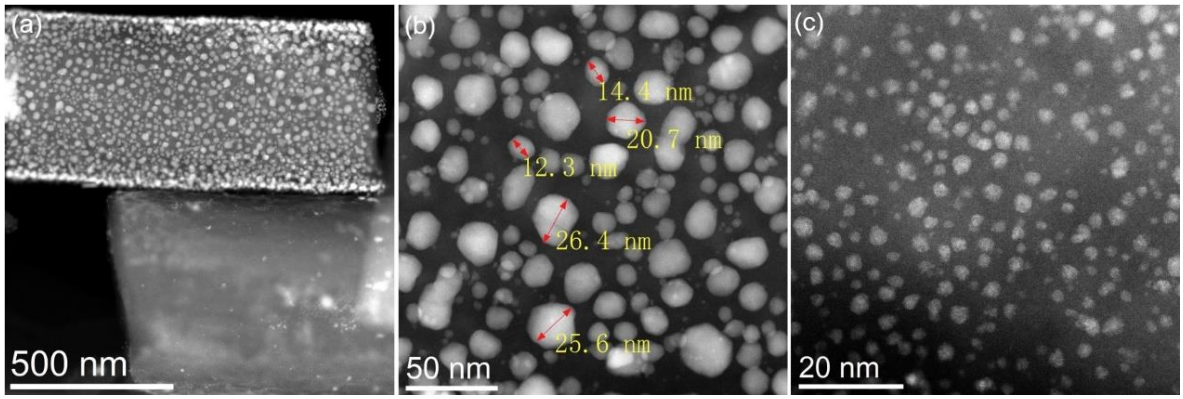


Figure 4.1.8. $Ru_{95}Pt_5$ nanoparticles prepared using 4A with 100 ms. (a) carbon fibers with different sizes of nanoparticles; (b) large nanoparticles, which sizes are marked; (c) small nanoparticles. (Images captured by STEM mode in FEI Titan Themis G2 60-300 working at 300 kV)

There are two structures, icosahedron and hcp, observed from the atomic resolution images of pure Ru nanoparticles, as shown in Figure 4.1.9. The icosahedral structure of the exemplary Ru nanoparticle in Figure 4.1.9b is confirmed by comparison with a simulated image of a Ru icosahedron (Figure 4.1.9d). Yellow arrows point out the icosahedral nanoparticles in Figure 4.1.9a. An icosahedral model is shown in Figure 4.1.9(c). The formation of pure Ru icosahedra confirms that fcc Ru nanoparticles can be prepared by the carbothermal shock synthesis. The hcp nanoparticles can be recognized from the STEM images by comparison with the simulated STEM images of hcp Ru nanoparticles with an hcp Ru nanoparticle with the Wulff shape shown in Figure 4.1.9(f).

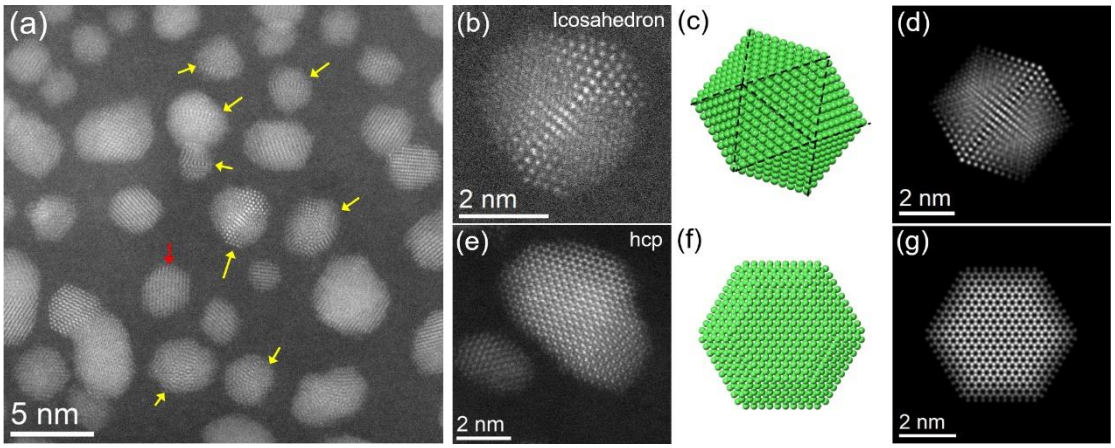


Figure 4.1.9. Pure Ru nanoparticles (Ru2A) prepared with a current of 2A. (b-d) Icosahedron. (e-g) Ru nanoparticle with an HCP structure. (b) and (e) Experimental HAADF-STEM images. (c) Atomic model of an icosahedron with 2869 atoms. (f) Atomic model of a Ru nanoparticle with an HCP stacking built by 4721 atoms. (d) and (g) Simulated STEM images. (Images captured by STEM mode in FEI Titan Themis G2 60-300 working at 300 kV)

The fcc structure of a selected $Ru_{95}Pt_5$ nanoparticle is confirmed by the STEM image and the corresponding FFT, shown in Figure 4.1.10, where a nanoparticle was imaged along the [-112] zone axis. The lattice spacings and the angles between the planes are noted in Figure 4.1.10(a,

c). The atomic ratio of Pt and Ru was measured by EDS, shown in Figure 4.1.10(d-f), yielding a ratio of Pt/Ru close to 4:96. An atomic Wulff model of $Ru_{95}Pt_5$ nanoparticle and its simulated STEM image are shown in Figure 4.1.10(g, h), respectively. In this model, the Pt atoms embed in and replace Ru atoms of Ru nanoparticle. The positions of Pt atoms can be pointed out in the simulated STEM images, where are spots with high intensities (Figure 4.1.10h). The intensity of atomic columns is presented in Figure 4.1.10(i), where the experimental curve is compared with the simulated curve. The higher intensity indicates the position of atomic column containing Pt atoms. Compared with the simulated STEM image of $Ru_{95}Pt_5$ nanoparticle, some of the atomic columns in the experimental nanoparticle were encircled by red, where they include single Pt atoms and show higher intensity than pure Ru columns (Figure 4.1.10i).

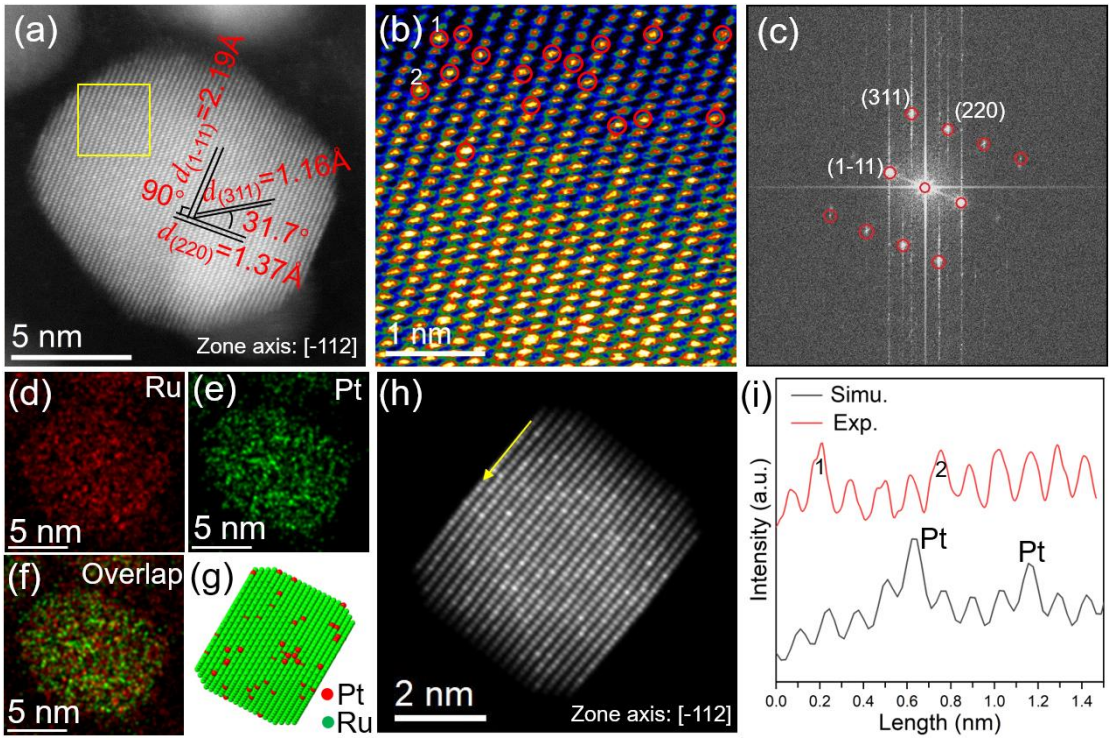


Figure 4.1.10. HAADF-STEM and EDX mapping images of $Ru_{95}Pt_5$ with an fcc structure. (a) An individual nanoparticle with a zone axis [-112]. (b) The atomic resolution image from the yellow square region in (a). Parts of single-Pt-atom embedding in the Ru crystal structures are circled by red. (c) FFT pattern of $Ru_{95}Pt_5$.

EDX mappings of Pt (d), Ru (e), and the overlapping of Pt and Ru (f). (g) An atomic model of $Ru_{95}Pt_5$ nanoparticle with the Wulff shape. (h) The simulated HAADF-STEM image of $Ru_{95}Pt_5$, which the bright spots are the positions of single Pt-atom in the $Ru_{95}Pt_5$ nanoparticle. (i) Line profiles of intensity, which the red profile shows the experimental intensity with single Pt atoms marked by red circles in (b). The black curve shows the intensity profile of the yellow arrow in (h). (Images and EDX captured by STEM mode in FEI Titan Themis G2 60-300 working at 300 kV)

Figure 4.1.11 shows an hcp $Ru_{95}Pt_5$ nanoparticle that was captured along its [1-11] direction. An atomic resolution image is shown in Figure 4.1.11(b), which the model is inserted for marking the atomic positions. The FFT and the simulated hcp image confirm the hcp structure of the experimental $Ru_{95}Pt_5$ nanoparticle. The positions of Pt atoms in the crystal can be located by the intensity, for example, the lattice columns encircled by yellow contain Pt atoms in the simulated image (Figure 4.1.11d) due to the high intensity.

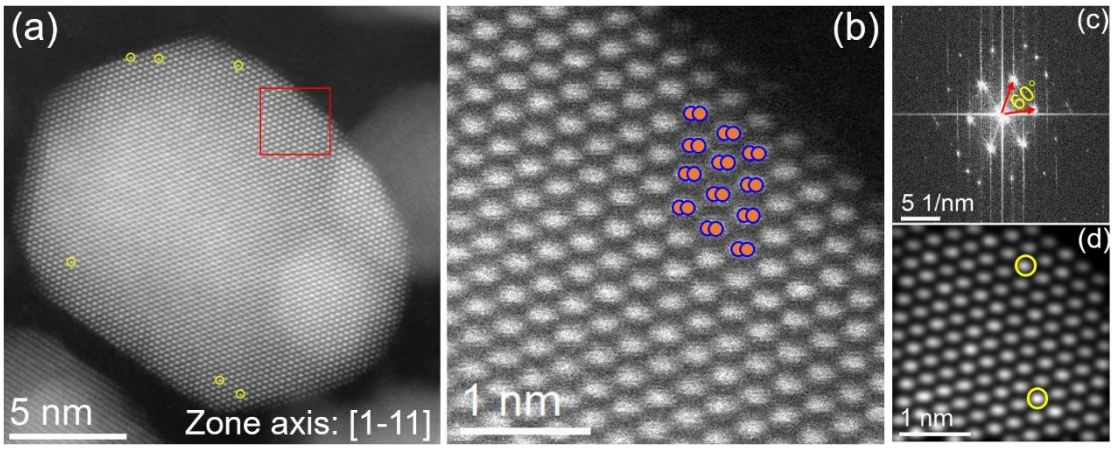


Figure 4.1.11. HAADF-STEM images of $Ru_{95}Pt_5$ with an hcp structure. (a) $Ru_{95}Pt_5$ nanoparticle imaged along the [1-11] direction. Yellow circles mark the positions of Pt atoms embedded in Ru structure. (b) High-resolution image of $Ru_{95}Pt_5$ where shows the atomic model of Ru with the hcp structure. (c) The FFT of $Ru_{95}Pt_5$ nanoparticle in (a). (d) A simulated STEM image of $Ru_{95}Pt_5$ which the positions of Pt atoms are circled. (Images captured by STEM mode in FEI Titan Themis G2 60-300 working at 300 kV)

Except the large nanoparticles shown in Figure 4.1.10 and Figure 4.1.11, small $Ru_{95}Pt_5$ nanoparticles are captured with hcp or fcc structures (Figure 4.1.12). Both the FFT and the simulated STEM images are utilized to recognize the hcp from the fcc structures.

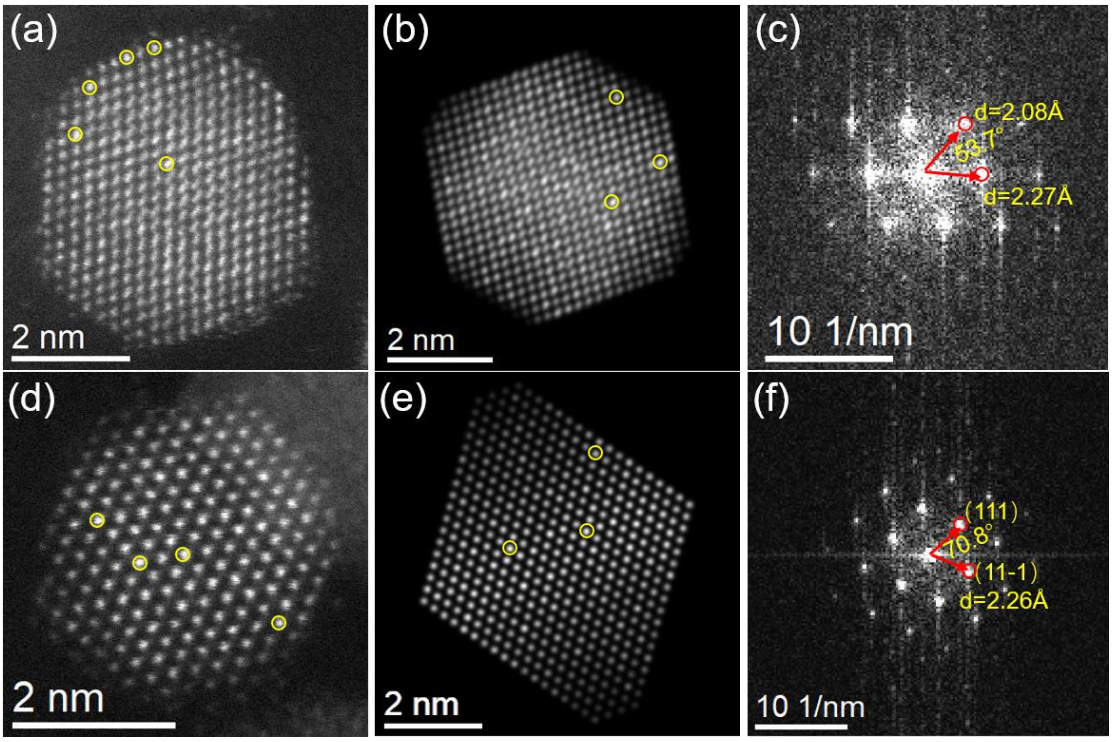


Figure 4.1.12. Structural Recognition of $Ru_{95}Pt_5$ nanoparticles from the HAADF-STEM images. (a) $Ru_{95}Pt_5$ nanoparticle with an hcp structure; (b) A simulated hcp $Ru_{95}Pt_5$ nanoparticle; (c) The FFT of $Ru_{95}Pt_5$ nanoparticle in (a). (d) An fcc $Ru_{95}Pt_5$ nanoparticle and the corresponding simulated STEM image (e) and the FFT (f). Yellow circles give the positions of doped Pt atoms. (Images captured by STEM mode in FEI Titan Themis G2 60-300 working at 300 kV)

4.2. Nanoparticle synthesis using flash Joule heating synthesis

A home-made apparatus as shown in Figure 4.2.1 (a, b) consists of two metallic tungsten cylinders as the electrodes and a quartz tube (5 mm in diameter) as the reaction vessel of sample powders. The power supply (NOVA POWER) can control the output of voltages (0-200 V) and currents (0-20 A) with a pulse width from 1 ms to 999 ms. An example is given in Figure 4.2.1(c, d) to show the process of Joule heating. For this, the light emission intensity of the flash Joule heating was recorded by videos. The carbon powders (coconut shell pyrolyzed at 900 °C for 1 hour) were packed in a quartz tube (5 mm in diameter) and pressed by two electrodes (Figure 4.2.1(b)). The resistance of carbon powders measured by a multimeter was around 5 Ω. The pulse current was 5 A and the maximum voltage applied on the electrode was 180 V with a

pulse duration of 500 ms. A dazzling snapshot was inserted in Figure 4.2.1(c), representing the high temperature. The snapshots displayed in Figure 4.2.1(d) demonstrate the ultrafast ramp rates of heating and cooling.

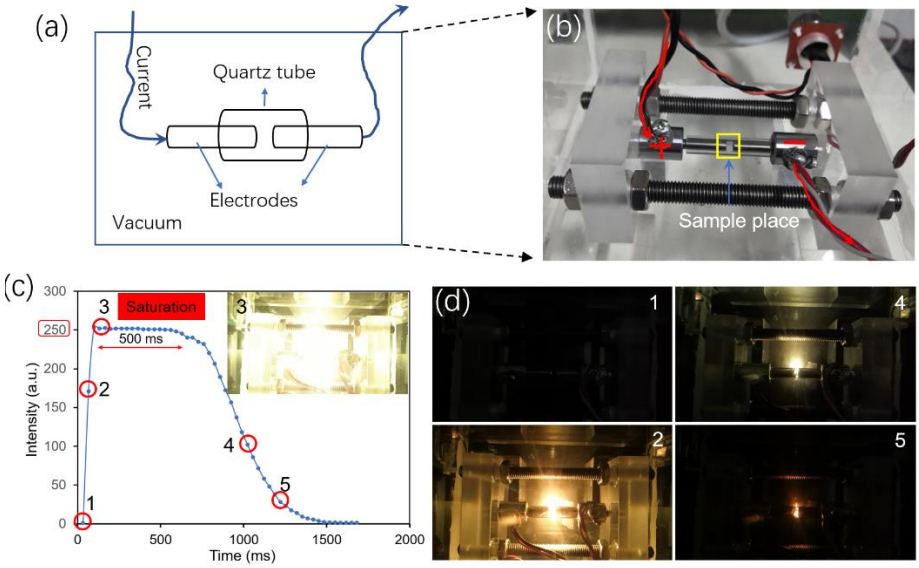


Figure. 4.2.1. (a) Schematic of the flash Joule heating using cylinder electrodes. The sample was placed in the quartz tube, pressed by the electrodes from both sides. (b) A photo of sample holder. (c) A light intensity curve (captured by a smartphone's video) displayed the temperature of the sample in the flash heating process. (d) Photo snapshots were captured in different time of flash heating. Figure and caption taken from Ref.[178].

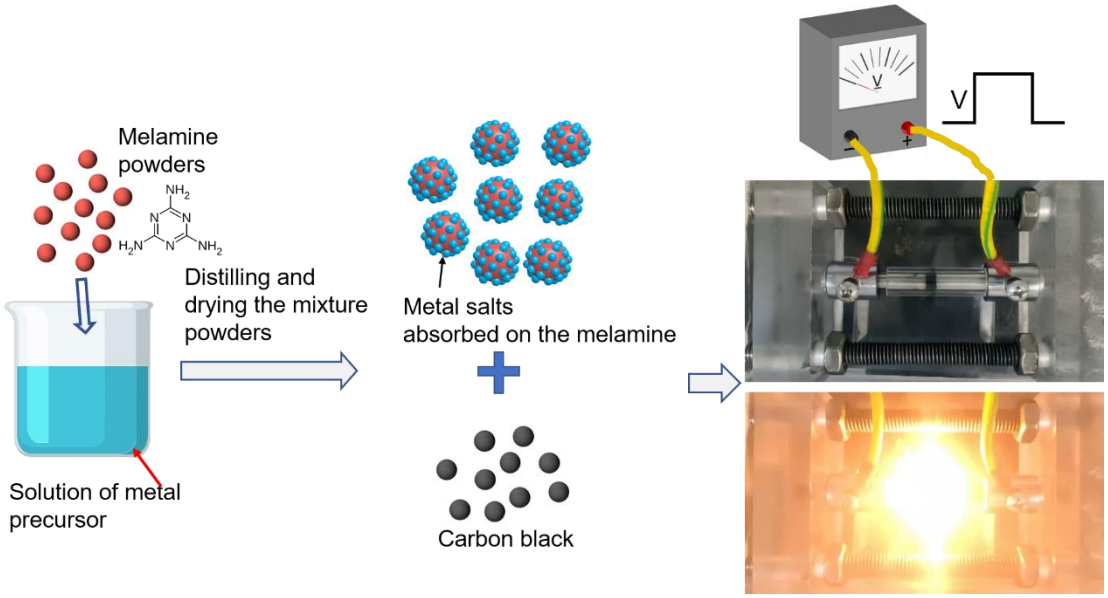


Figure 4.2.2. Schematic of the flash Joule heating synthesis. The sample precursor powders are prepared using melamine and carbon black. The metal salts are absorbed on the surface of melamine. The resistance of sample precursor powders packed in the quartz tube is adjusted in the range of 2-100 Ω. The maximum current passing through the sample is controlled less than 20 A and the pulse voltage applied between the electrodes is not more than 200 V. The pulse width of the applied voltage is from 1 ms to 999 ms.

As the flash Joule heating synthesis requires the sample powders to be packed in a quartz tube, the resistance of sample powders should be controlled in a range of 2-100 Ω, which is the suitable range to produce high Joule heating with the power supply (NOVA POWER). For preparing metal nanoparticles, the metal precursors cannot be mixed with carbon black directly due to the high electrical conductivity of carbon black (10-100 S/cm). Figure 4.2.2 illustrates the preparation of sample precursors, for which carbon black (VXC72) powders are used as the conductive additive to generate Joule heating. Melamine powders, which cannot be dissolved by solvents (e.g. water and DMF), are impregnated in metal precursor solutions to absorb the metal precursors. After the solutions of metal precursors are absorbed by melamine powders, the mixtures are dried using a rotary evaporator. Then, the dried melamine powders are blended uniformly with carbon black for the flash Joule heating synthesis. PtCo alloy nanoparticles

shown in Figure 4.2.3 were prepared using this approach as an example. Figure 4.2.3 (a, b) shows the PtCo nanoparticles with a mean size of 2.35 nm in diameter, which are loaded on graphitic carbon (Figure 4.2.3g). Single Pt/Co metal atoms were observed around the nanoparticles, as shown in Figure 4.2.4. This demonstrates that precious metal alloy nanoparticles (e.g. PtCo alloys) and single atoms can be produced using flash Joule heating.

For transition metals, flash Joule heating can be used to produce carbide nanoparticles at ultrahigh temperature (e.g. 2000 K)[38]. The molybdenum (Mo) as an example is presented in Figure 4.2.5.

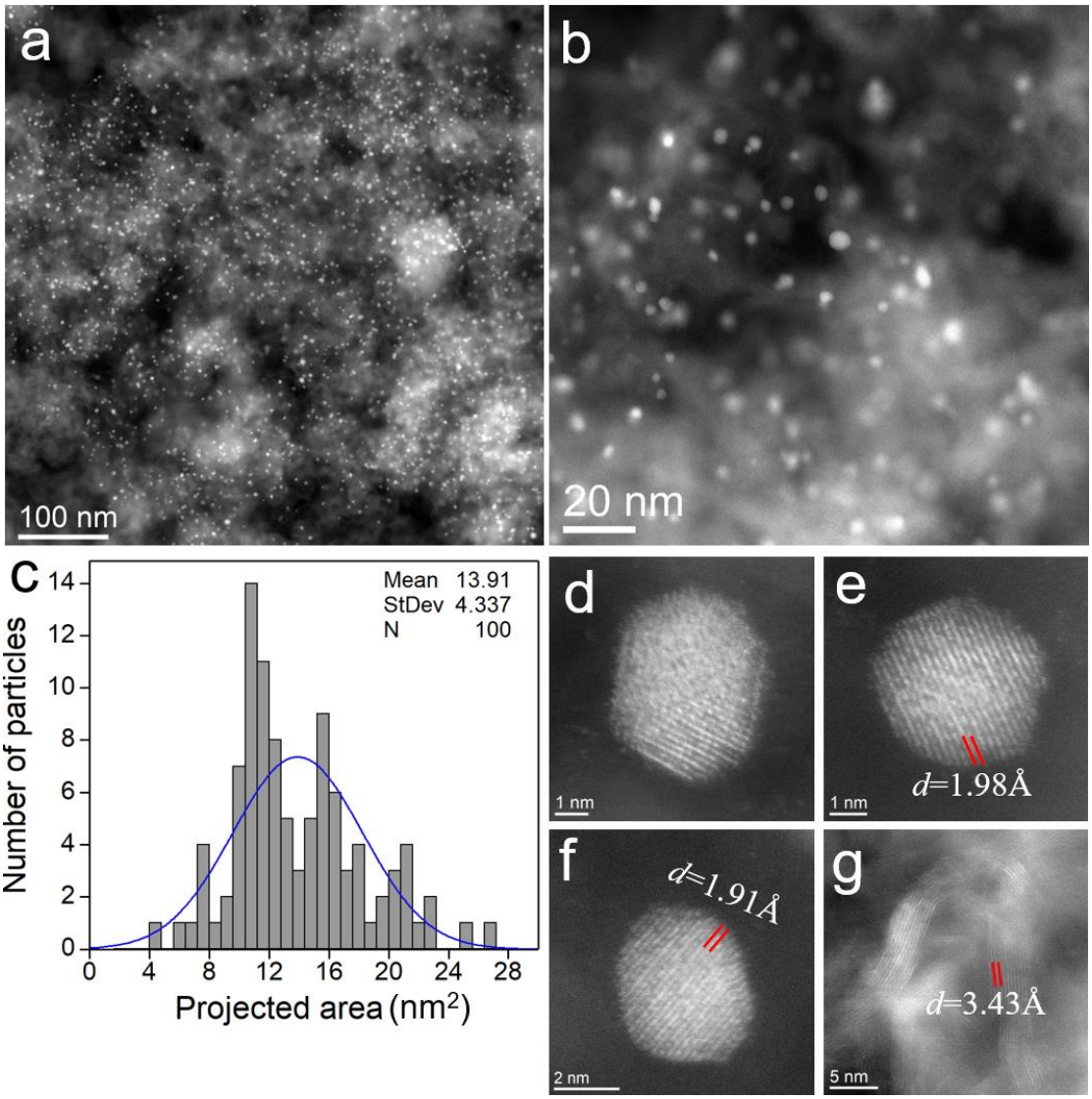


Figure 4.2.3. PtCo nanoparticles prepared using flash Joule heating with a current pulse of 500 ms. (a, b) STEM images of PtCo nanoparticles anchored on graphitic carbon, prepared by the flash Joule heating. (c) Projected area distribution of PtCo nanoparticles in (a). (d-f) High resolution HAADF-STEM images of PtCo nanoparticles. (g) HAADF-STEM image of graphitic carbon with a lattice spacing of 3.43 Å. (Images captured by STEM mode in FEI Titan Themis G2 60-300 working at 300 kV)

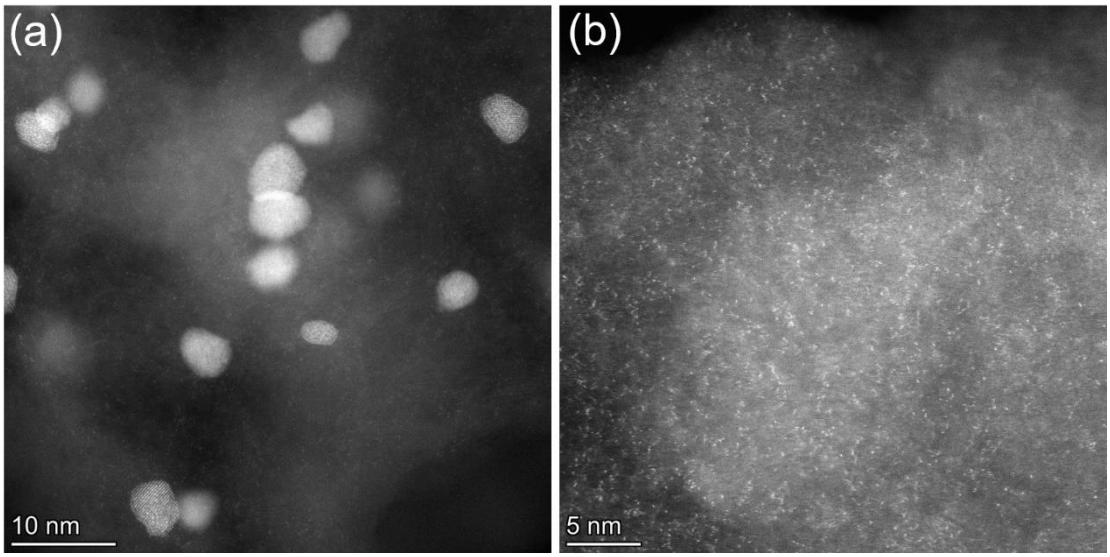


Figure 4.2.4. (a) PtCo alloy nanoparticles and single-Pt/Co-atoms dispersed in the carbon. (b) Single-Pt/Co-atoms in the carbon. (Images captured by STEM mode in FEI Titan Themis G2 60-300 working at 300 kV)

Figure 4.2.5 shows the production of molybdenum carbide (MoC) prepared by the flash Joule heating using a current of 10 A with a pulse width of 500 ms and a 200 V voltage limit. The XRD of the as-prepared MoC (Figure 4.2.5(a)) matches the simulated XRD of MoC with an fcc lattice structure and fm-3m space group. Figure 4.2.5(b, c) give the TEM images of MoC nanoparticles, whose maximum size is roughly 40 nm. The graphitic carbon shown by red arrows can be observed distinctly in Figure 4.2.5(c). Figure 4.2.5(d) presents the radial profile of the selected area electron diffraction (SAED) pattern of MoC (red curve). The black curve in Figure 4.2.5(d) is a simulation based on the crystal cell shown in Figure 4.2.5(a). The experimental SAED pattern in Figure 4.2.5(e) was captured from the region of Figure 4.2.5(b). The SAED confirms the fcc structure of as-prepared MoC. A high-resolution TEM image of a MoC nanocrystal shown in Figure 4.2.5(f) further verifies the fcc structure by the {200} facets with a lattice spacing of 2.13Å.

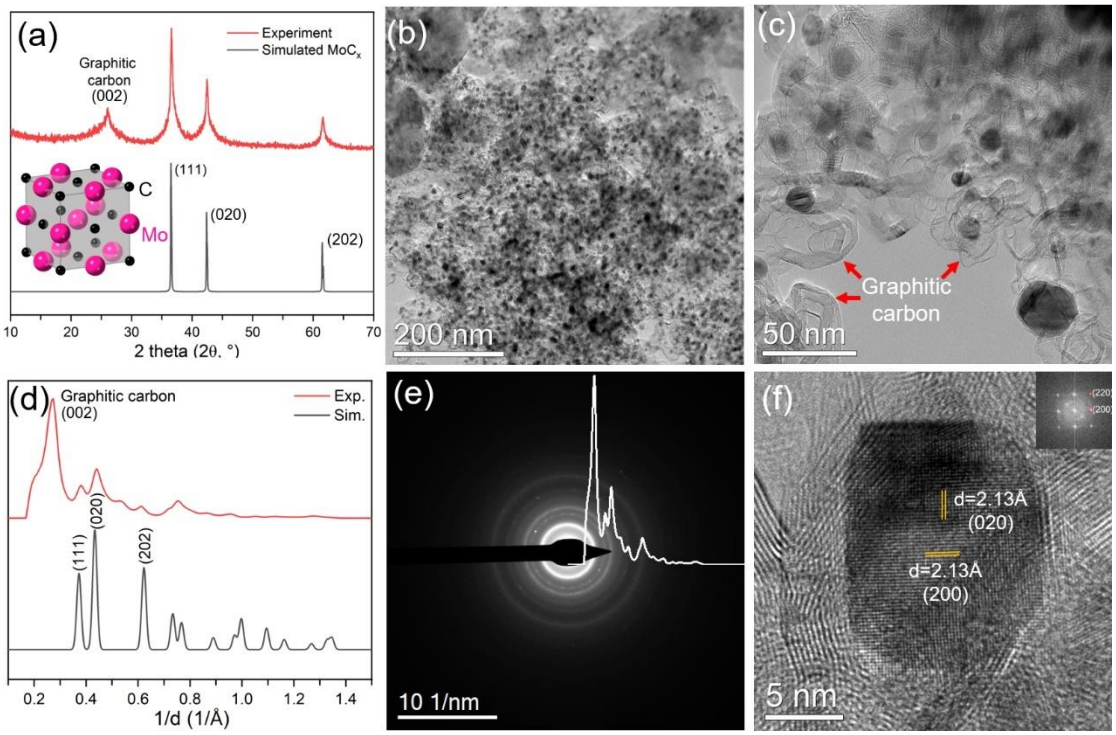


Figure 4.2.5. (a) XRD of as-prepared MoC nanoparticles. The crystal cell of MoC with a space group of fm-3m, where the pink and the black spheres represent Mo and C atoms, respectively. The simulated XRD of MoC is based on the structure of MoC with the unit cell of a=b=c=4.261 Å (ICSD#618306). (b, c) TEM images of MoC nanoparticles and graphitic carbon identified by red arrows. (d) Radial profiles of SAED patterns, which are plotted using the PASAD tools[179] . The red curve is from the experiment and the black one is the simulation based on the structure of fcc-MoC (ICSD#618306). (e) SAED pattern of MoC nanoparticles and graphitic carbon with the radial profile of diffraction pattern shown as the white curve. (f) Atomic resolution TEM image of a MoC nanoparticle with a lattice spacing of 2.13 Å. (Images captured by STEM mode in FEI Titan Themis G2 60-300 working at 300 kV)

4.3. Metallic phosphides synthesis

Metal phosphides have been used as catalysts, gas sensors, energy storage materials, and environmental remediation[180]. In traditional synthesis, the phosphides are prepared using a phosphorization reaction of metal precursors with organic (e.g. trictylphosphine, trioctylphosphine oxide, triphenyl phosphine) or inorganic (e.g. white/red phosphorous, $NH_4H_2PO_4$, NaH_2PO_2) phosphorous sources[180,181,182]. For example, reducing phosphates or hypophosphite at high temperatures (400-1000℃) is a convenient way to prepare metal

phosphides[183]. Another common low-temperature preparation of metal phosphides is using phosphine (PH_3) to reduce the metal precursors, where PH_3 can be produced by decomposition of NaH_2PO_2 or $NH_4H_2PO_2$ at low temperature (e.g. 250 ℃). However, PH_3 is highly toxic and dramatically dangerous due to the spontaneous flammability in air. Red/white phosphorous are also used to react with metal precursors under high temperatures with long reaction times and/or high pressure[181]. Carbothermal shock synthesis has been employed to prepare core-shell metal phosphates ($CoFeP_x$) using trioctylphosphine oxide as the phosphorous source[184]. The mentioned methods not only require harsh preparation conditions but also need expensive precursors (e.g. organic phosphorus sources) and/or involving toxic gas (PH_3).

Joule heating generated by pulse current with a shock duration of less than 1 second has been employed to prepare transition metal carbides, which were synthesized by the carbothermic reaction of carbon black and metal precursors at high temperature (3000 K)[38]. It is possible to prepare metal phosphides using red phosphorous as the phosphorus source by the flash Joule heating synthesis. In the following section, Ruthenium (III) phosphide (RuP), Ruthenium (IV) phosphide (RuP_2) and tungsten (III) phosphide (WP) will be taken as examples to illustrate the synthesis of metal phosphides using flash Joule heating. Figure 4.3.1 shows the unit cells of RuP and WP nanoparticles that belong to the space group of pnma, while the space group of RuP_2 is pnna. Both have an orthorhombic crystal structure.

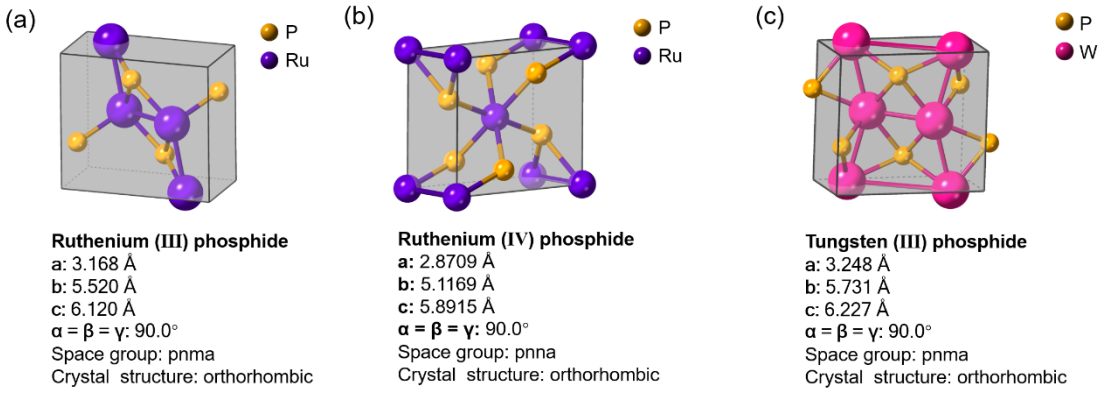


Figure 4.3.1. Unite cells of phosphides prepared by the flash Joule heating method. Ruthenium (Ⅲ) phosphide (RuP) (ICSD#648015) and tungsten (Ⅲ) phosphide (WP) (ICSD#42056) have the same space group of pnma; Ruthenium (Ⅳ) phosphide RuP_2 (ICSD#42607) has a space group of pnna.

4.3.1 Ruthenium phosphide

Glucose-derived carbon, which is prepared by carbonizing glucose at 600 ℃ for 2 hours, is used as the supports of ruthenium phosphide nanoparticles. Firstly, 0.1 m mol of $RuCl_3 \cdot xH_2O$ (99.98%, 38.0-42.0% Ru basis) was dissolved in water (40 ml). Then, 100 mg of glucose-derived carbon was impregnated in the aqueous ruthenium chloride solution. The mixture was sonicated for 1 hour, followed by drying in a rotary evaporator. The dry powders were blended uniformly with red phosphorous powders (10 mg) using an agate mortar to provide the reactants, which were packed in a quartz tube with an inner diameter of 10 mm. Two tungsten cylinders were used as electrodes to compress the reactants with the compression force adjusted to yield an electrical resistance in the range of 2-20 Ω. The electrodes and the quartz tube were loaded on the stage as shown in Figure 4.2.2. The pulse current width was 500 ms, with the maximum voltage and current set to 200 V and 10 A, respectively. The flash Joule heating was conducted in a sealed chamber filled with argon gas.

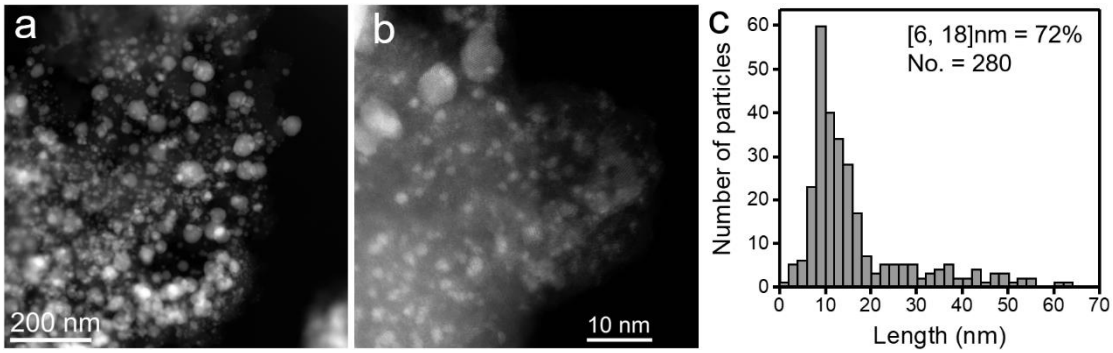


Figure 4.3.2. Size description of RuP_x nanoparticles. (a) RuP_x nanoparticles with large sizes; (b) RuP_x nanoparticles with small sizes; (c) Size distribution of RuP_x nanoparticles. (Images captured by STEM mode in FEI Titan Themis G2 60-300 working at 300 kV)

Figure 4.3.2 shows the HAADF-STEM images of the as-prepared ruthenium phosphide nanoparticles with most (72%) of nanoparticles exhibiting diameters in the range of 6-18 nm. There are large nanoparticles with small populations whose diameters are from 18 nm to 65 nm. Figure 4.3.3 shows the STEM-EDS mappings of a RuPx nanoparticle, which was covered by graphitic layers (Figure 4.3.3a). Uniform spatial distributions were found in the C, P, and Ru EDS maps recorded in STEM mode. The corresponding atomic contents of C, O, P, and Ru listed in Figure 4.3.3(f) show that P is close to Ru in atomic ratio, indicating the formation of RuP.

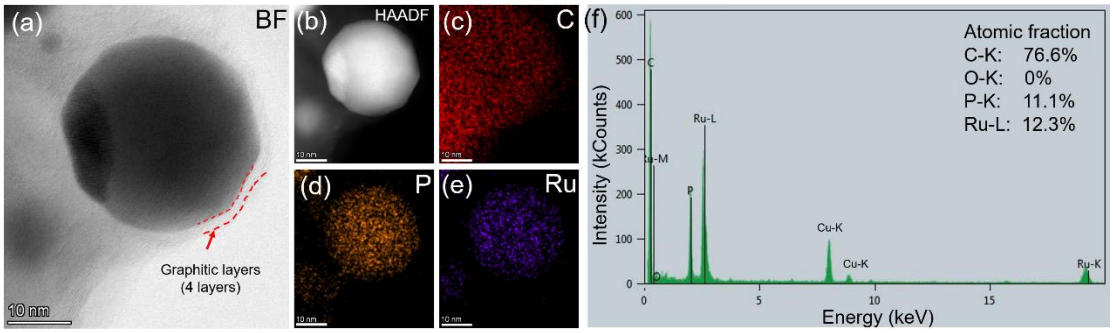


Figure 4.3.3. The EDX mappings of one RuP*x* nanoparticle. (a) Dark field image of RuP*x* nanoparticle. (b) HAADF-image of RuP*x*. (c-e) EDX mapping of C, P, and Ru elements. (f) EDX spectrum of elements. The atomic fraction of elements was given in a list. (Images and EDX captured by STEM mode in FEI Titan Themis G2 60-300 working at 300 kV)

XRD and high-resolution STEM images of as-prepared RuP_x nanoparticles are displayed in Figure 4.3.4 for investigating the structure. Compared with the simulated XRD spectra of RuP and RuP_2 that are numbered in the Inorganic Crystal Structure Database (ICSD) as #648015 and #42607, respectively. The as-prepared RuP_x nanoparticles show two crystal structures: Ruthenium (III) phosphide (RuP) and Ruthenium (IV) phosphide (RuP_2), corresponding to the space group of pnma and pnnm, respectively. This is supported by the high-resolution HAADF-STEM images of RuP_x nanoparticles as shown in Figure 4.3.4 (b,c) and (d-f). A RuP_2 nanoparticle is shown in Figure 4.3.4(b) with a zone axis of [010] and the (100) and (002) planes with 2.82 Å and 2.85 Å, respectively. A false color atomic image of RuP_2 from the yellow area of Figure 4.3.4(b) is presented in Figure 4.3.4(c) where the positions of Ru atoms are in agreement to the atomic model of RuP_2 shown on the right hand. A second RuP nanoparticle is shown in Figure 4.3.4(d-f). The crystal structure of RuP is confirmed by the atomic resolution image in Figure 4.3.4(d, f) with Ru atoms in Figure 4.3.4(f) showing the same pattern as the atomic model with a space group of pnma given on the right hand. Two lattice planes, (101) and (011), show an angle of 74° in Figure 4.3.4(d), in accordance with the structure from the database (ICSD#648015). The chemical reaction leading to the formation of RuP*x* via the reaction between RuCl3 and red phosphorus can be represented as follows:

$$2RuCl_3 \xrightarrow{ultrahigh\ T} 2Ru\ (liquid) + 3Cl_2\ (gas)$$

$$4Ru\ (liquid) + xP_4 \xrightarrow{ultrahigh\ T} 4RuP_x$$

At ultrahigh temperatures, the carbothermal reduction of the $RuCl_3$ precursor yielded metallic ruthenium, which subsequently reacted with phosphorus to form ruthenium phosphide

compounds.

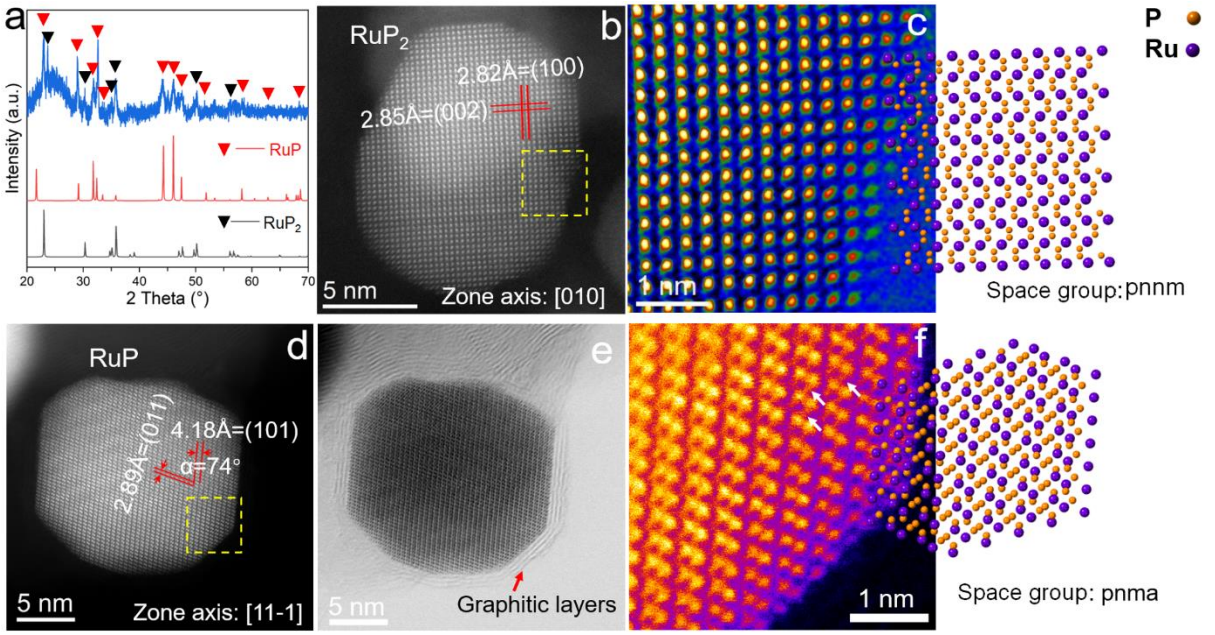


Figure 4.3.4. Structural characterisation of ruthenium phosphide nanoparticles (RuP_x). (a) XRD of RuP_x nanoparticles, where the red and blue curves are simulated XRD spectra of RuP (ICSD#648015) and RuP_2 (ICSD#42607), respectively. The peaks observed in the experimental sample were denoted by inverted triangles, where the red inverted triangles correspond to the diffracted peaks from RuP and the black ones indicate the diffracted peaks from RuP_2. (b) A RuP_2 nanoparticle with the space group pnnm; (c) The image of enlarged area in (b), with the atomic model of RuP_2 was shown on the righthand side. (d) A RuP nanoparticle with the space group pnma; (e) Graphitic layers marked by the red arrow are observed in bright-field image. (f) The area in (d) was magnified and shown with the atomic model of RuP. (Images captured by STEM mode in FEI Titan Themis G2 60-300 working at 300 kV)

The chemical valences of Ru and P in RuP_x nanoparticles are analyzed by the *x*-ray photoelectron spectroscopy (XPS), which was recorded on an Escalab Xi+ X-ray photoelectron spectrometer using an Al Kα excitation source. C 1s and Ru 3d spectra are shown in Figure 4.3.5(a), with the Ru $3d_{5/2}$ and Ru $3d_{3/2}$ subpeaks of RuP located at 280.6 eV and 284.6 eV, respectively. The C1s spectrum is a convolution of three subpeaks at 284.8 eV, 285.3 eV, and 286.6 eV, corresponding to C-C, C-O-C, and C-P[185], respectively. Figure 4.3.5(b) displays the

P 2p core level peaks, with the P 2p peak deconvoluted by P-O (134.8 eV), P-C (133.8 eV), and Ru-P (P $2p_{1/2}$ at 130.3 eV, P $2p_{3/2}$ at 129.5 eV, and 131. 3 eV). The P-O bond can be attributed to the reaction of P with the oxygen-containing functional groups in the glucose-derived carbon[185–187]. The flash Joule heating could also induce the formation of P-C in glucose-derived carbon doped by P[185,187]. For avoiding the interference of C1s, the Ru 3p spectrum (Figure 4.3.5b) is additionally employed to analyze the valence of Ru. Ru 3p3/2 and Ru 3p1/2 are observed at 462.6 eV and 484.8 eV, respectively. This indicates that no Ru-O bonds, whose peaks of spectra are around 464 eV and 469 eV, exist in the as-prepared RuP_x nanoparticles.

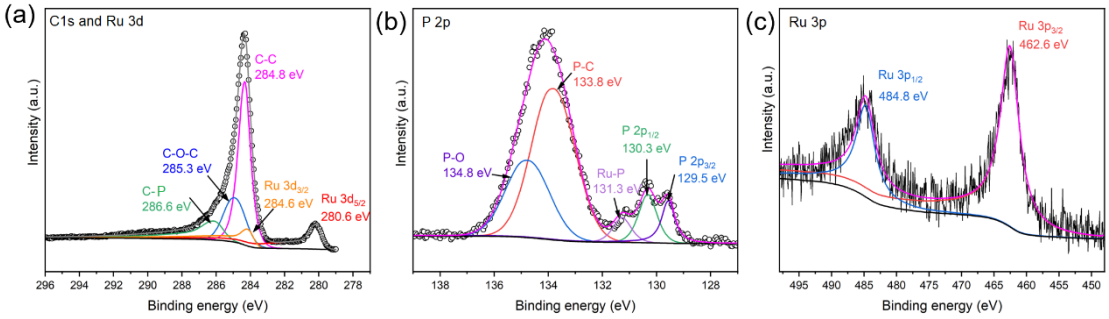


Figure 4.3.5. Chemical state measurement of as-prepared ruthenium phosphide nanoparticles. (a) C1s and Ru 3d XPS spectrum. (b) P 2p XPS spectrum. (c) Ru 3p XPS spectrum.

4.3.2 Tungsten phosphide

The preparation of tungsten phosphide was similar to that of RuP_x, but small changes were made in the preparation of the reactants. Sodium tungstate dihydrate ($Na_2WO_4 \cdot 2H_2O$, 99%) was used as the tungsten source. Melamine (300 mg) was impregnated into 0.1 mmol $Na_2WO_4 \cdot 2H_2O$ aqueous solution (40 ml water). After ultrasonic dispersion of melamine in the Na_2WO_4 aqueous solution for 1 hour, the mixture was dried in a rotary evaporator. The dried

melamine powders (about 332 mg) were blended uniformly with carbon black (about 120 mg) and red phosphorous (30 mg). 150 mg of melamine/carbon black was loaded into a quartz tube with an inner diameter of 10 mm. Pressing the powders using electrodes yielded resistance of 5.5 Ω, measured by a multimeter. The maximum pulse current and voltage were 10 A and 180 V, respectively, with a pulse width of 600 ms.

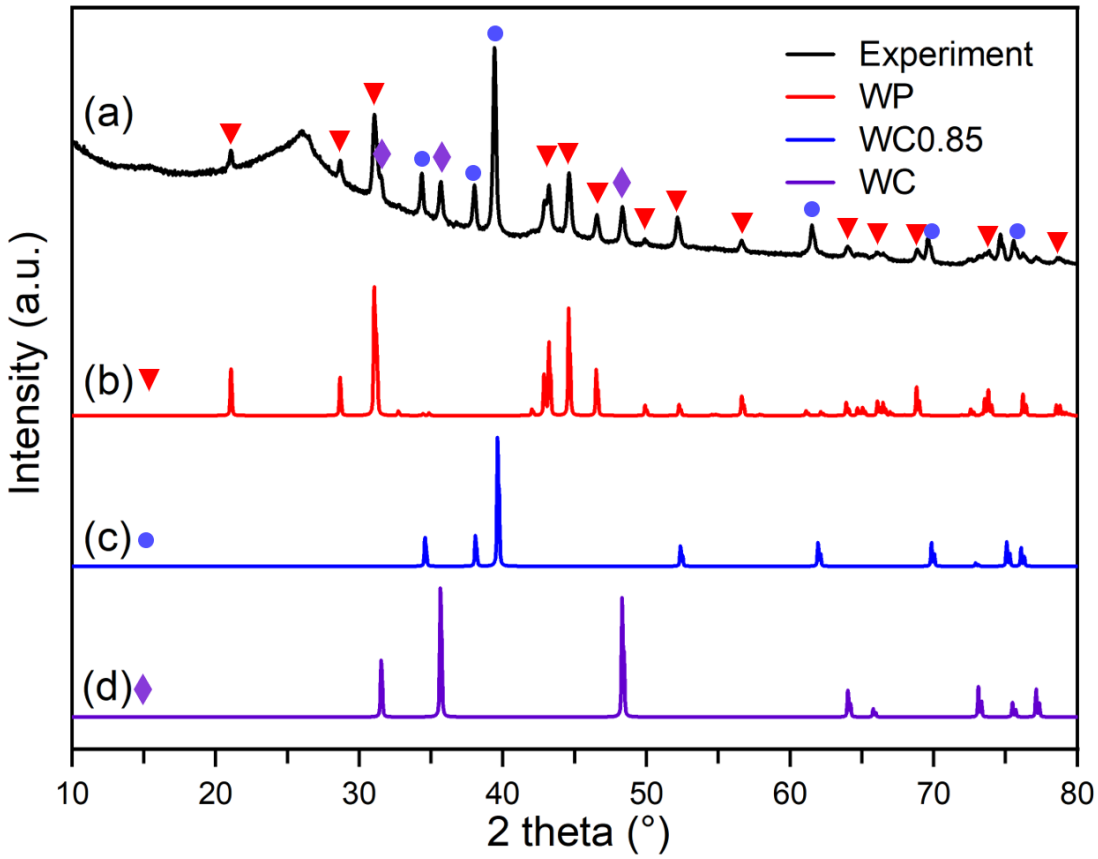


Figure 4.3.6. (a) XRD of as-prepared tungsten phosphide nanoparticles. Simulated powder XRD of (b) WP (tungsten phosphide) showing a space group of pnma (ICSD#42056), (c) $WC_{0.85}$ (tungsten carbide) with a space group of p3-1m (ICSD#30008), and (d) WC (tungsten carbide) belong to the space group of p6-m2 (ICSD#15406).

Figure 4.3.6 shows the XRD of as-prepared tungsten compounds, which was compared with simulated XRD spectra of WP, WC, and $WC_{0.85}$ to identify the structures present in the as-

prepared tungsten compounds. The appearance of tungsten carbides can be attributed to the carbothermal reduction of Na_2WO_4 under flash Joule heating. By comparison with the simulated XRD (Figure 4.3.6b, the red spectrum) of WP (ICSD#42056), the presence of WP with an orthorhombic structure was confirmed in the as-prepared tungsten compounds.

Figure 4.3.7 shows the prepared WP nanoparticles and the EDS mappings of C, P, and W, with the atomic ratio of W: P found to be close to 1:1, indicating tungsten phosphide with a crystal structure of WP. The size of WP nanoparticles given by the HAADF-STEM image is less than 60 nm in terms of the long axis. From the BF-STEM images (Figure 4.3.7(b) and Figure 4.3.8(c)), graphitic layers (marked by a green arrow) are clearly observed surrounding the WP nanoparticles. A lattice spacing of 2.55 Å is shown in the insert image of Figure 4.3.7(c), which corresponds to the net plane spacing of (111) in WP with an orthorhombic structure. The crystal structure of as-prepared WP is further confirmed in Figure 4.3.8, where an atomic model of WP with a space group of pnma and the corresponding simulated STEM image (Figure 4.3.8e), are compared to the experimental image (Figure 4.3.8c).

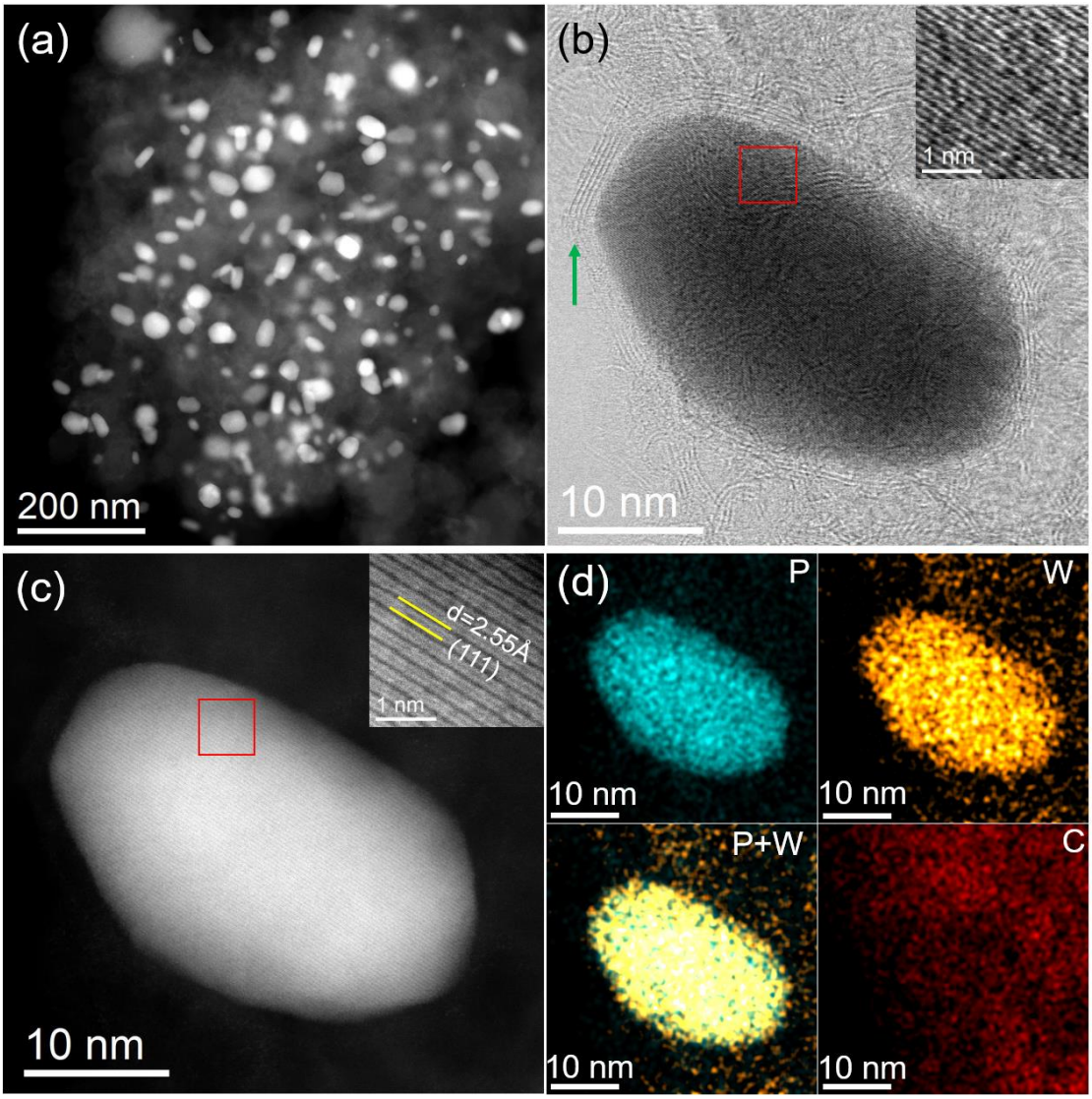


Figure 4.3.7. STEM images and the EDS mappings of WP nanoparticles. (a) HAADF-STEM image of WP and tungsten carbide nanoparticles. (b) BF-STEM image of WP nanoparticle, surrounded by graphitic layers (green arrow). The insert image is a magnification of the red area. (c) HAADF-STEM image of WP nanoparticle, with the insert is a magnification of the red area that the lattice spacing is 2.55Å, indicating (111) net planes of the orthorhombic WP. (Images and EDX captured by STEM mode in FEI Titan Themis G2 60-300 working at 300 kV)

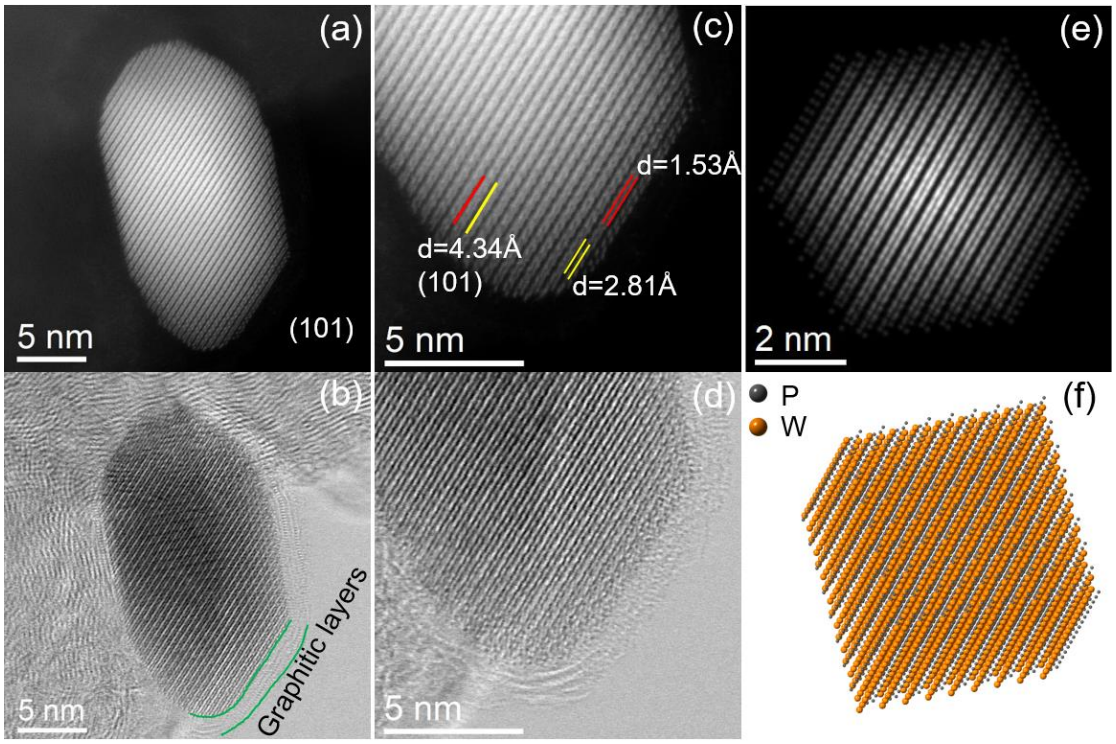


Figure 4.3.8. Atomic resolution STEM images of WP. (a, c) HAADF-STEM images with (101) plane. (b, d) BF-STEM images. (e) Simulated STEM image of WP. (f) Atomic model of WP nanoparticle with a space group of pnma. (Images captured by STEM mode in FEI Titan Themis G2 60-300 working at 300 kV)

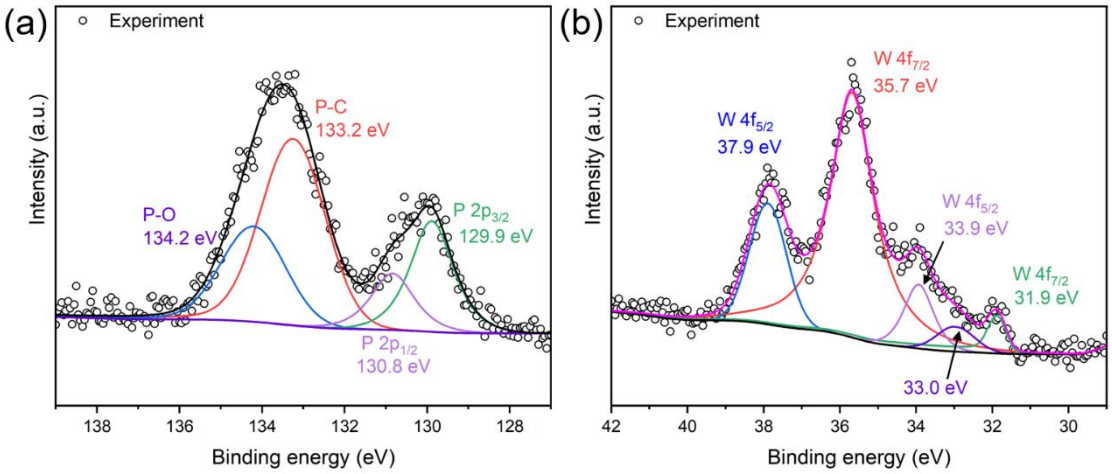


Figure 4.3.9. High-resolution XPS of P 2p (a) and W 4f (b) in the as-prepared WP and WC_x.

The chemical states of as-prepared tungsten compounds are confirmed by XPS in Figure 4.3.9.

Two separated peaks are recorded in the high-resolution XPS of P 2p (Figure 4.3.9a), with the

binding energies of P $2p_{1/2}$ and P $2p_{3/2}$ obtained from the deconvoluted peaks located at 130.8 eV and 129.9 eV, respectively. The P $2p_{1/2}$ and P $2p_{3/2}$ can be assigned to bonds of P-W. The other peak at round 134 eV can be attributed to P-C and P-O bonds, which were formed by P bonded to carbon and the oxidized phosphorus species. In the W 4f region, the experimental spectrum can be deconvoluted with five peaks belonging to W $4f_{7/2}$ and W $4f_{5/2}$. The small peaks located at 33.9 eV of W $4f_{5/2}$ and 31.9 eV of W $4f_{7/2}$ are assigned to W-C bonds. The pair of peaks at 33.0 eV and 35.7 eV are assigned to W-P[188]. The highest peaks at 37.9 eV corresponds to the W^{6+}-based material, which could be generated by WO_3 due to the residual of Na_2WO_3[189].

4.4. Stacking faults in the nanoparticles

The ultrafast heating-quenching in the flash Joule heating synthesis or carbothermal shock synthesis enable defects to be maintained such as stacking faults which create strains. Figure 4.4.1 shows one Ru nanoparticle doped with 5 at% Pt atoms. There are two stacking sequences in the nanoparticle, the ABAB stacking of the hcp structure and the ABC stackings create the fcc structure, as shown in Figure 4.4.1(a). The interfaces between hcp and fcc stackings create the stacking faults, which generate strains. For analyzing the strain fields, the geometrical phase analysis[190] was employed using two non-colinear Fourier components (vectors) as shown in Figure 4.4.1(b). FRWRtools installed in DM as a plugin was used to analyse the strain fields. After choosing the reference reciprocal lattice described by the vectors in Figure 4.4.1(b), the deviations of the local reciprocal lattice are calculated, which produces the displacement field. The strain tensor e(**r**) is with reference to the undistorted (selected) area, which is the lattice

circled by red with the ABAB stackings in the upper part of Figure 4.4.1(a). The strain e(**r**) is separated into *x*-component and *y*-component. Figure 4.4.1(c-e) show e_{xx}, e_{yy}, and e_{xy}, respectively, with the color bar presented on the right with red representing tensile stress and green representing compressive stress. Small uniform distortions are observed in e_{xx}, which may be induced by the doped Pt atoms into the Ru nanoparticle. Three green strips in e_{yy} and red strips in e_{xy} are observed, reflecting the stacking faults induced by the hcp and fcc stackings. The e_{xy}, representing the shear strain, is overlapped with the HAADF-STEM image, shown in Figure 4.4.1(f). This image demonstrates that the tensile stress is observed at the stacking faults. As the reference area was selected in the hcp stacking, the fcc area marked by yellow box in Figure 4.4.1(a) show compressive stress in e_{xy}.

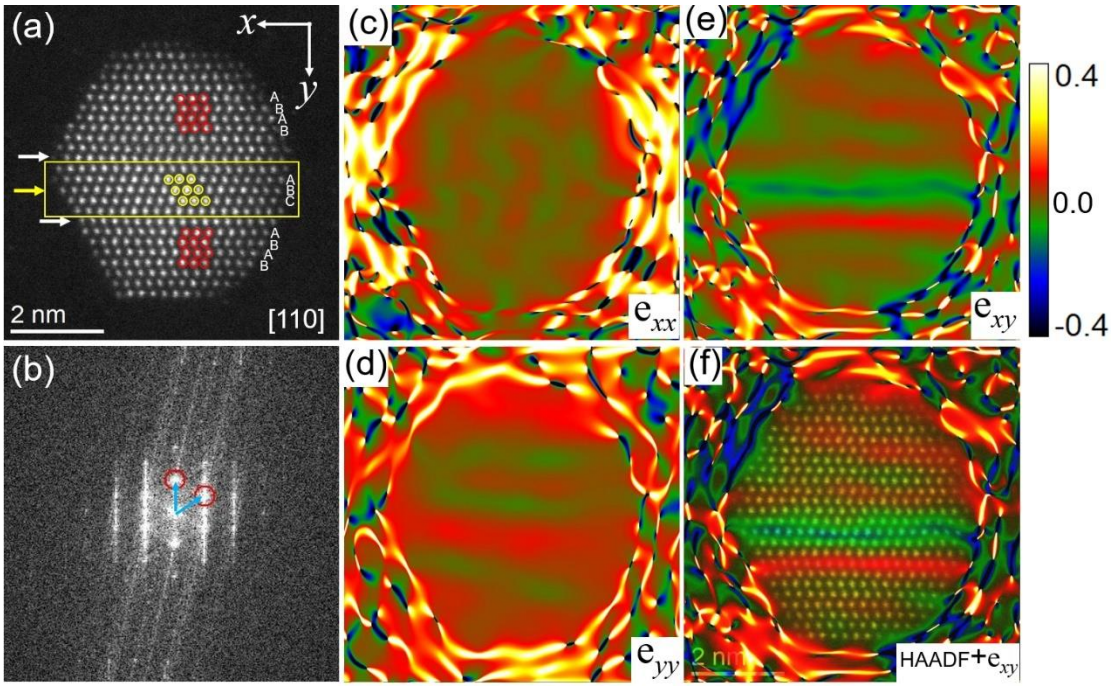


Figure 4.4.1. Single-Pt-atoms Ru nanoparticle with an FCC and an HCP structures. (a) HAADF-STEM image, where the ABC stackings is highlighted by a yellow rectangle and the interfaces of the ABC and ABAB stacking are pointed by white arrows. (b) FFT of STEM image with two non-linear vectors for calculating the strain field. Strain mappings in e_{xx} (c), e_{yy} (d), and e_{xy} (e). (f) overlap of STEM image and the strain

mapping of e_{xy}. (Images captured by STEM mode in FEI Titan Themis G2 60-300 working at 300 kV)

The stacking faults also were observed in the WP nanoparticle. The BF-STEM image (Figure 4.4.2b) clearly shows the dislocations created by stacking faults, as marked by red arrows. The high resolution images (Figure 4.4.2c,d) exhibit the dislocations from the area of red box, indicating the dislocations are successive. The distribution of dislocations are marked by green in the BF-intensity image of Figure 4.4.2e, demonstrating that higher density of dislocations are observed in the interior than the exterior of the nanoparticle. The generation of dislocations can be attributed to the heating-quenching in the flash Joule heating synthesis, where the strain cannot be released and the stacking faults are frozen in the nanoparticle. In addition, WP was produced by the reaction of WO_4^{2-} with red phosphorous. Therefore, the new-generated phase can also create strains. The strain close to the exterior of the nanoparticle can be released, but the strain generated on the interior of the nanoparticle is kept and expanded across the nanoparticle.

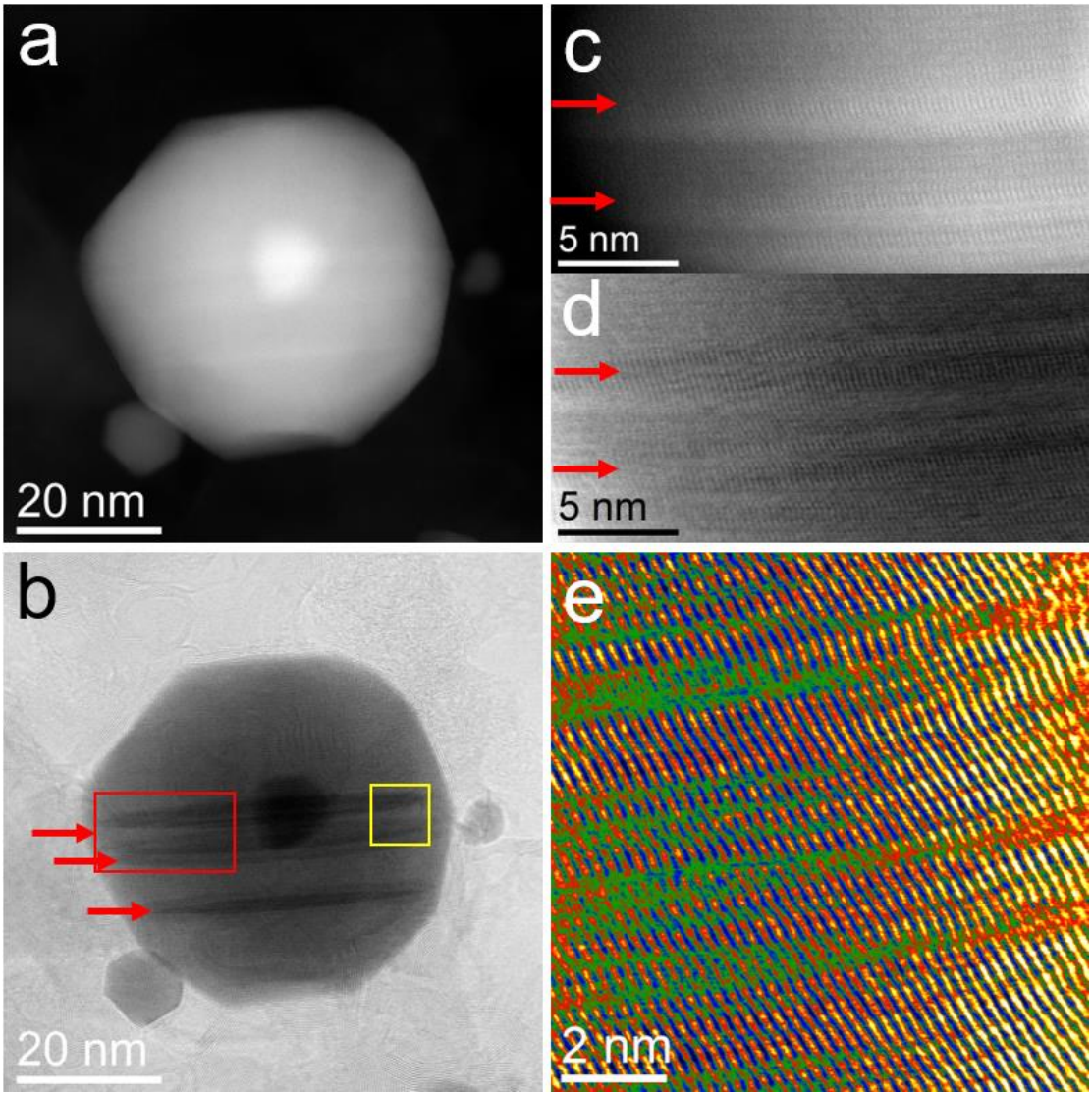


Figure 4.4.2. WP nanoparticle with stacking faults. (a) HAADF-STEM image of WP nanoparticle with a diameter around 48 nm. (b) BF-STEM image of WP nanoparticle, where the red and yellow areas are magnified to show the details in (c, d) and (e), respectively. (c, d) Stacking faults marked by red arrows in the HAADF (c) and BF (d) images, respectively. (e) Atomic resolution image with stacking faults (green). (Images captured by STEM mode in FEI Titan Themis G2 60-300 working at 300 kV)

4.5. Catalytic performances of Ru-based nanoparticles

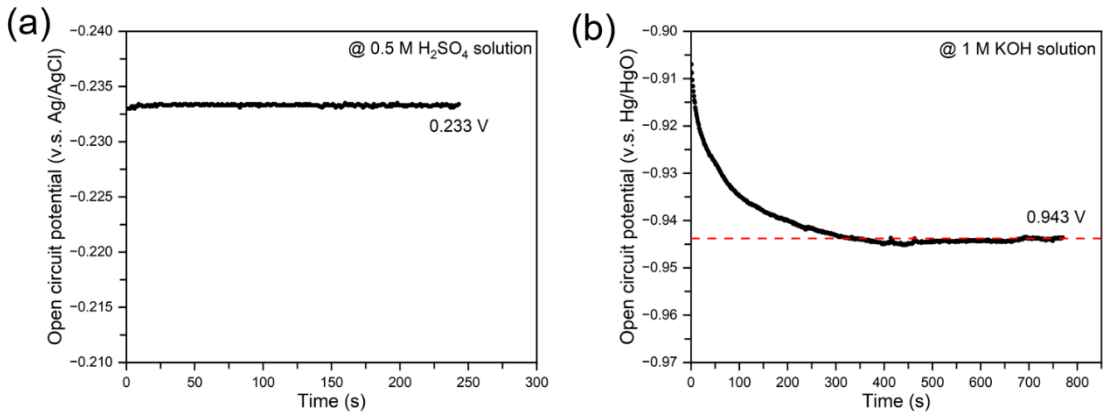


Figure 4.5.1. Calibration of the reference electrodes by measuring the reversible hydrogen electrode versus Ag/AgCl (a) or Hg/HgO (b) electrodes at hydrogen saturated electrolyte.

For testing the electrocatalytic performances of catalysts, an electrochemical workstation (e.g. CHI 660) is utilized to conduct the electrochemical measurements using a three-electrode system. The reference electrode (RE) should be calibrated in H_2 saturated electrolytes before tests[191]. The open circuit potential is recorded to measure the potential of the reference electrode with reference to the reversible hydrogen electrode (RHE) in a three-electrode system, where Pt wire is used as the working electrode (WE) and counter electrode (CE). Figure 4.5.1 shows the potentials (v.s. RHE) of reference electrodes in 0.5 M sulfuric acid (H_2SO_4) (a) and 1 M potassium hydroxide (KOH) (b). Therefore, the experimental electrode potential versus RHE can be calculated using the equation: E(RHE) = E(WE) + E(RE), where E(RE)=0.059·pH + E^0(RE). E^0(RE) is the potential versus normal hydrogen electrode (NHE) at room temperature (25 °C). For example, the reference electrode Ag/AgCl has a potential of 0.233 V versus RHE in 0.5 M H_2SO_4 solution. Then, the experimental electrode potential is (E(WE) + 0.233) V in the same electrolyte.

The working electrode is prepared by loading 60 μl of the catalyst ink onto a square carbon cloth with an area of 1 cm^2. The carbon cloth is clamped by a glassy carbon electrode for electrochemical tests. Typically, 5 mg catalyst is dispersed in 500 μl of 3:1 V/V water/ isopropanol solution containing 25 μl of 5 *wt*% Nafion for preparing the ink. Linear sweep voltammetry (LSV) was conducted at a scan rate of 5 $mV \cdot s^{-1}$ in the voltage range of 50 mV to -200 mV (v.s. RHE) at room temperature. Cyclic voltammograms were tested at scan rate of 20 $mV \cdot s^{-1}$ in the potential range of 0 V to 0.94 V versus RHE. The compensated resistance (R) of the circuit was measured by electrochemical impedance spectroscopy (EIS), which was performed from 100 kHz to 0.1 Hz with an alternating current amplitude of 5 mV at the overpotential ($\eta_{10\ mA \cdot cm\text{-}2}$) with a current density of 10 $mA \cdot cm^{-2}$. The stability evaluation of catalysts in HER was tested using the accelerated CV method with a scan rate of 20 $mV \cdot s^{-1}$.

Figure 4.5.2 shows the HER performances of as-prepared Ru-based catalysts, whose structures have been displayed in Figure 4.1.4 and Figure 4.1.5. $Ru_{95}Pt_5$ (3A) and $Ru_{95}Pt_5$ (4A) exhibit high electrocatalytic activity in HER in both acidic and alkaline electrolytes. $Ru_{95}Pt_5$ (3A), which has more fcc nanoparticles ($I_{fcc(111)}/I_{hcp(101)}$=10.31) than $Ru_{95}Pt_5$ (4A) ($I_{fcc(111)}/I_{hcp(101)}$=3.32), shows an overpotential $\eta_{10\ mA \cdot cm\text{-}2}$ of 19 mV in the LSV curve (Figure 4.5.2 (a)) measured in 1 M KOH electrolyte, which is the lowest overpotential observed among the tested catalysts. This suggests that $Ru_{95}Pt_5$ (3A) has the highest activity of HER. $Ru_{95}Pt_5$ (3A) also had the highest activity in 0.5 M H_2SO_4 solution with only $\eta_{10\ mA \cdot cm\text{-}2}$=8 mV required to produce the current density of 10 mA/cm^2. Ru(2A) with hcp structure shows the highest overpotentials 77 mV and 83 mV at 10 mA/cm^2 of current density in 1 M KOH and 0.5 M

H_2SO_4 media, respectively, indicating a much lower activity of HER. The slower kinetics on hcp Ru compared to fcc Ru was explained by higher adsorption energy barriers of protons (H^+) and hydroxyl groups (OH^-) calculated on the hcp structure than the fcc structure[175]. However, $Ru_{95}Pt_5$ (5A) with hcp structures shows much lower overpotentials (33 mV in alkaline and 26 mV in acidic media). This demonstrates that Pt single atoms embed in Ru nanoparticles (Figure 4.1.11) can enhance the electrochemical activity of HER.

The Tafel slopes derived from the LSV curves, which are indicators to evaluate the activity of catalysts, are displayed in Figure 4.5.2(b, e). $Ru_{95}Pt_5$ (3A) exhibits the smallest Tafel slope (30 $mV \cdot dec^{-1}$ in alkaline and 22 $mV \cdot dec^{-1}$ in acidic electrolytes) among the four catalysts. This verifies that single-Pt-atom substituted Ru nanoparticles can improve the reaction kinetics of HER, compared with the pure Ru nanoparticles with hcp structure. Furthermore, the metastable fcc structure boosts the activity of single-Pt-atom doped Ru catalysts in the HER, supported by the smaller Tafel slope achieved in the catalyst of $Ru_{95}Pt_5$ (3A) than that of $Ru_{95}Pt_5$ (4A) and $Ru_{95}Pt_5$ (5A). This system exhibits a phase-dependent catalytic performance[177]. Figure 4.5.2(c, f) evaluate the electrocatalytic activity of as-prepared Ru-based catalysts by considering both the overpotential and the Tafel slope value. $Ru_{95}Pt_5$ (3A) shows the lowest values located in the left bottom, demonstrating the fastest reaction kinetics in HER.

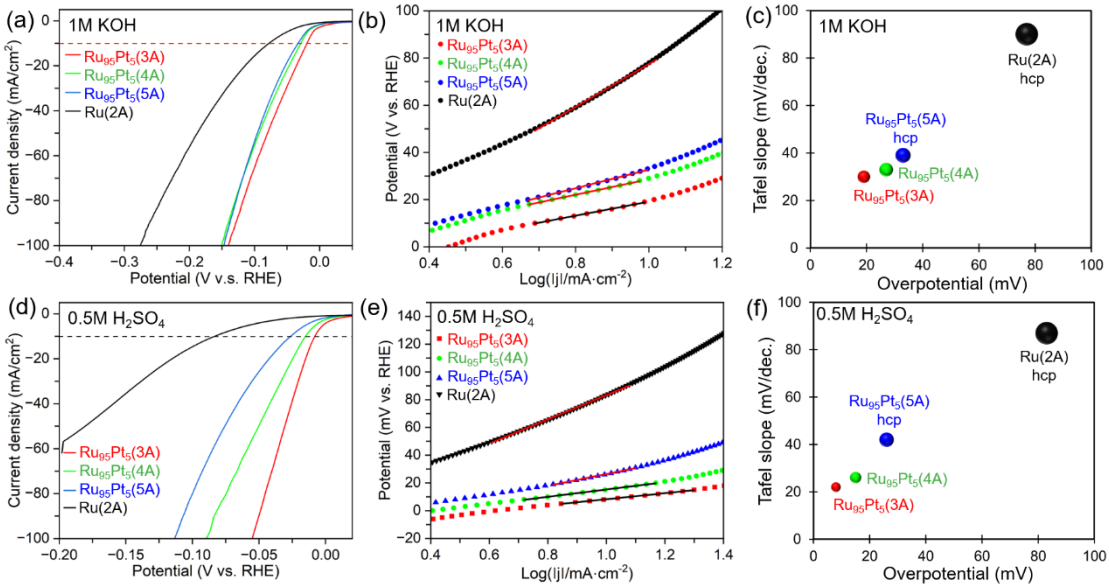


Figure 4.5.2. HER activity measurements in acidic and alkaline electrolytes. (a, d) LSV polarization curves with iR compensation measured at scan rate of 5 $mV \cdot s^{-1}$. (b, e) Tafel slopes calculated from (a, d). (c, f) Comparison of overpotentials and Tafel slopes of as-prepared samples. The lower of overpotential (Tafel slope), the better of HER performance.

The HER performances of as-prepared Ru-based catalysts are compared with recently reported catalysts, summarized in Figure 4.5.3, where both overpotentials and the Tafel slopes are taken into consideration. The catalysts shown in Figure 4.5.3 and Table 4.1 and 4.2 are Ru-based and/or Pt-based catalysts reported in high-impacted journals within the latest 4 years. The values of commercial Pt/C and commercial Ru/C also are presented in Figure 4.5.3(a) and Table 4.1. The home-made Ru-based catalysts locate in the left bottom of Figure 4.5.3 (a, b), highlighting the better HER performances compared with the reported catalysts for HER.

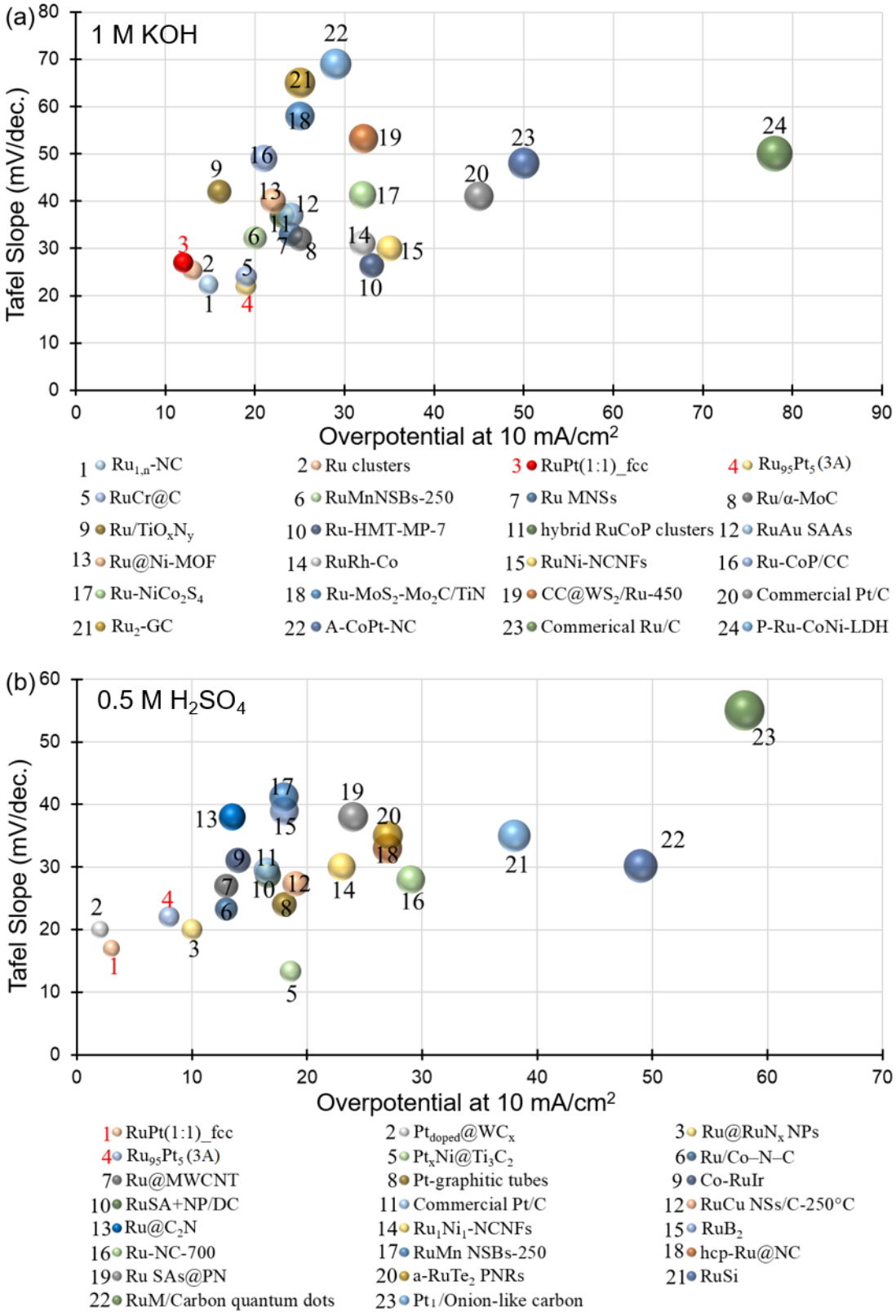


Figure 4.5.3. Comparison of overpotentials at η_{10} and Tafel slopes of recently reported Ru or Pt-contained electrocatalysts for HER in the electrolyte of 1 M KOH (a), and 0.5 M H_2SO_4 (b). RuPt(1:1)_fcc and $Ru_{95}Pt_5$(3A) are prepared in this thesis. The details of values are listed in Table 4.1.and Table 4.2. The diameter of spheres represents the

performance of catalysts on HER. The smaller in the diameter, the better of electrocatalytic performance.

Table 4.1. Summary of recently reported Ru or Pt-contained catalysts for HER in 1 M KOH electrolyte.

No.	Electrocatalysts	Overpotential at 10mA/cm^2	Tafel slope (mV/dec)	Reference
1	$Ru_{1,n}$-NC	14.8	22.3	Adv. Mater. **2022**, 34, 2110604
2	Ru clusters	13	25.3	Nature Commun. **2022**, 13, 3958
3	RuPt(1:1)_fcc	12	27	This work
4	$Ru_{95}Pt_5$(3A)	19	22	This work
5	RuCr@C	19	24	Adv. Funct. Mater., **2021**, 32, 2108991.
6	RuMnNSBs-250	20	32.2	Adv. Mater. **2021**, 33, 2105308
7	Ru MNSs	24	33	Angew. Chem. Int. Ed. Engl., **2022**, e202116867.
8	Ru/α-MoC	25	32	Appl. Catal. B: Environ., **2022**, 318, 121867.
9	Ru/TiO_xN_y	16	42	J. Mater. Chem. A, **2022**, 10 , 11205 — 11212
10	Ru-HMT-MP-7	33	26.4	Small, **2022**, 2105168
11	hybrid RuCoP clusters	23	37	Energ. Environ. Sci., **2018**, 11,1819-1827.
12	RuAu SAAs	24	37	Adv.Energy Mater., **2019**, 9 ,1803913.
13	Ru@Ni-MOF	22	40	Angew. Chem. Int. Ed. Engl., **2021**, 60, 22276-22282.
14	RuRh-Co	32	31	Nano Energy, **2021**, 90, 106579.
15	RuNi-NCNFs	35	30	Adv. Sci., **2020**, 7, 1901833.
16	Ru-CoP/CC	21	49	Mater. Today Phys., **2020**, 12, 100182.
17	Ru-$NiCo_2S_4$	32	41.3	Adv. Funct. Mater., **2021**, 2109731.
18	Ru-MoS_2-Mo_2C/TiN	25	58	Nano Energy, **2021**, 88, 106277.
19	CC@WS_2/Ru-450	32.1	53.2	Adv. Funct. Mater., **2022**, 2109439.
20	Commercial Pt/C	45	41	Appl. Catal. B: Environ., **2022**, 318, 121867.
21	Ru_2-GC	25	65	ACS Catal., **2018**, 8, 11094-11102.
22	P-Ru-CoNi-LDH	29	69	Small, **2022**, 18, e2104323.
23	A-CoPt-NC	50	48	Angew. Chem. Int. Ed. Engl., **2019**, 58, 9404-9408.
24	Commerical Ru/C	78	50	Appl. Catal. B: Environ., **2022**, 318, 121867.

Table 4.2. Summary of recently reported Ru or Pt-contained catalysts for HER in 0.5 M H_2SO_4 electrolyte.

No.	Electrocatalysts	Overpotential at 10mA/cm^2	Tafel slope (mV/dec)	Reference
1	RuPt(1:1)_fcc	3	17	This work
2	Pt_{doped}@WC_x	2	20	Adv.Mater.**2022**, 34, 2206368
3	Ru@RuNx NPs	10	20	Adv. Energy. Mater. **2019**, 9, 1900931.
4	$Ru_{95}Pt_5$(3A)	8	22	This work
5	Pt_xNi@Ti_3C_2	18.55	13.3	Small **2019**, 15, 1805474.
6	Ru/Co–N–C	13	23.3	Adv.Mater.**2022**, 34, 2110103
7	Ru@MWCNT	13	27	Nat. Commun. **2020**, 11, 1278.
8	Pt-graphitic tubes	18	24	Nat. Energy **2018**, 3, 773.
9	Co-RuIr	14	31.1	Adv. Mater. **2019**, 31, 1900510.
10	RuSA+NP/DC	16.6	28.7	Adv. Sci. **2021**, 8, 2004516
11	Commercial Pt/C	16.5	29.5	Adv. Sci. **2021**, 8, 2004516
12	RuCu NSs/C-250°C	19	27.3	Angew. Chem. Int. Ed. **2019**, 58, 13983.
13	Ru@C_2N	13.5	38	Nat. Nanotech. **2017**, 12, 441.
14	Ru_1Ni_1-NCNFs	23	30	Adv. Sci. **2020**, 7, 1901833.
15	RuB_2	18	38.9	Adv. Energy. Mater. **2019**, 9, 1803369.
16	Ru-NC-700	29	28	Nat. Commun. **2019**, 10, 631.
17	RuMn NSBs-250	18	41.2	Adv. Mater. **2021**, 33, 2105308
18	hcp-Ru@NC	27	33	ACS Catal. **2018**, 8, 5714.
19	Ru SAs@PN	24	38	Angew. Chem. Int. Ed. **2018**, 130, 9639.
20	a-$RuTe_2$ PNRs	27	35	Nat. Commun. **2019**, 10, 5692.
21	Pt_1/Onion-like carbon	38	35	Nat. Energy **2019**, 4, 512.
22	RuSi	49	30.2	Angew. Chem. Int. Ed. **2019**, 58, 11409.
23	RuM/Carbon quantum dots	58	55	Angew. Chem. Int. Ed. **2020**, 20, 1718.

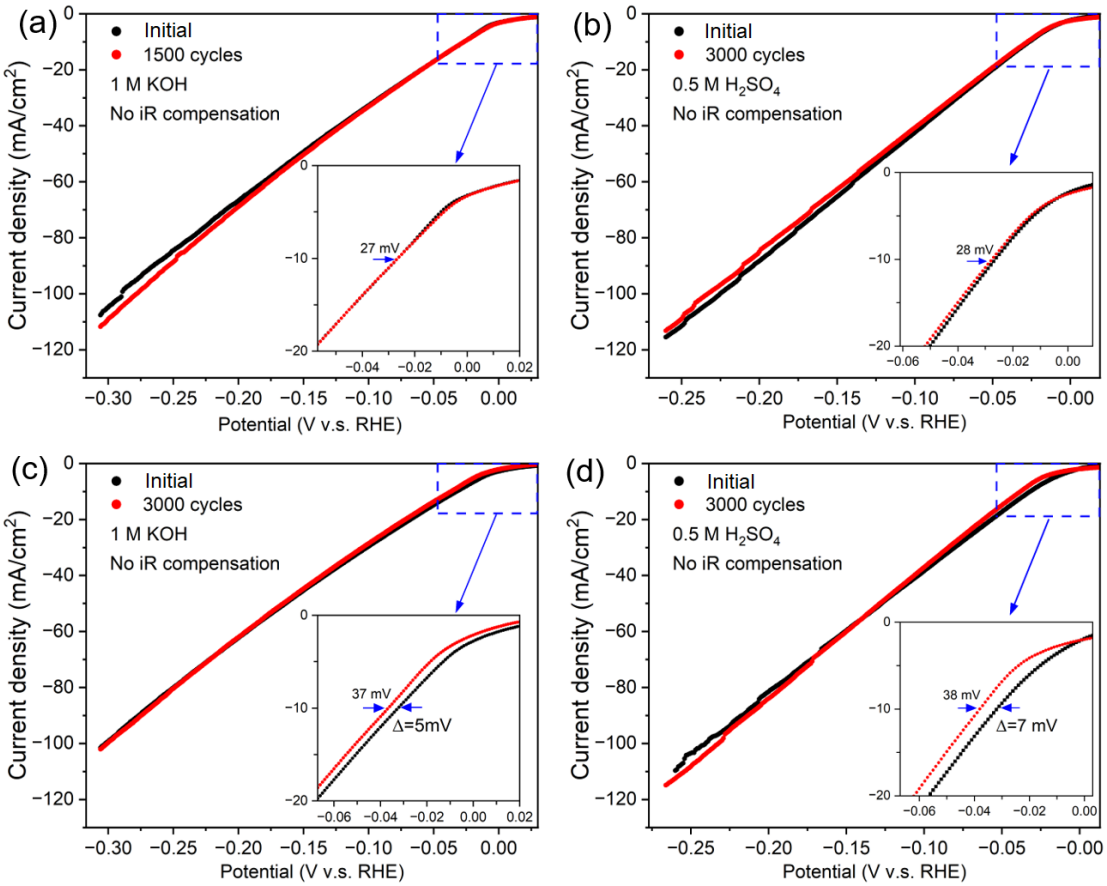


Figure 4.5.4. Durability tests by accelerated cyclic voltammetry tests. A scan rate of 20 mV·s^{-1} was used to run the cyclic voltammetry measurements. The tests were not compensated on the voltage caused by resistances of circuit (iR). (a, b) Accelerated durability tests of $Ru_{95}Pt_5$ (3A) in the electrolyte of 1 M KOH and 0.5 M H_2SO_4, respectively. (c, d) Accelerated durability tests of $Ru_{95}Pt_5$ (4A) in the electrolyte of 1 M KOH and 0.5 M H_2SO_4, respectively.

Long-term CV tests were conducted to evaluate the durability of $Ru_{95}Pt_5$ (3A) and $Ru_{95}Pt_5$ (4A). As shown in Figure 4.5.4, $Ru_{95}Pt_5$ (3A), whose structures are more fcc than hcp, exhibits negligent shifts on the polarization curves after 1500 and 3000 continuous CV tests in 1 M KOH and 0.5 M H_2SO_4, respectively, with the change of the overpotential $\eta_{10\ mA\cdot cm\text{-}2}$ less than 0.5 mV. In contrast, small shifts (5-7 mV) are observed from the polarization curves of $Ru_{95}Pt_5$ (4A) in Figure 4.5.4(c, d) after 3000 cycles. This demonstrates that the metastable fcc phase can retain its structure during the long-term tests of HER.

The high HER activity induced by the fcc structure is verified by RuPt(1:1), which are prepared with fcc structures or hcp structures shown in Figure 4.5.5 (a). The atomic ratio of RuPt(1:1) was measured by EDX (Figure 4.5.5c, d) and the fcc structure was confirmed by the lattice spacing in Figure 4.5.5(b).

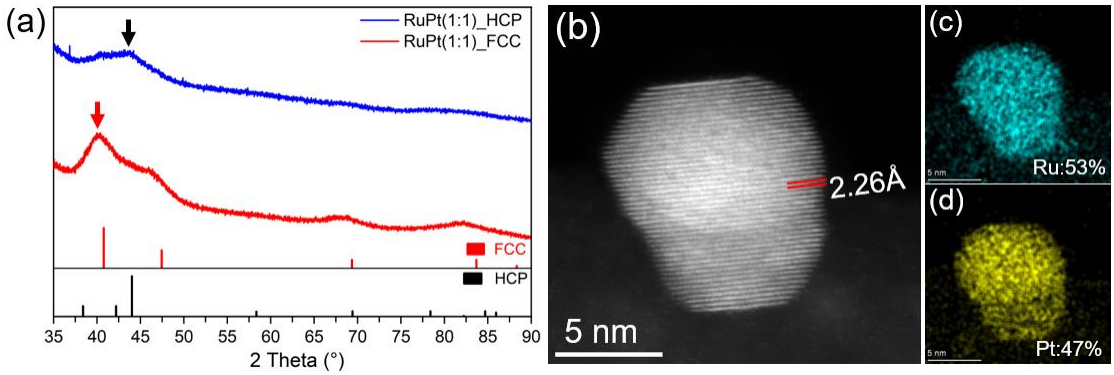


Figure 4.5.5. Structure of RuPt(1:1). (a) XRD of RuPt(1:1) with an hcp (blue) or an fcc (red) structure. (b) STEM image of an fcc RuPt(1:1). (c, d) EDS mappings of Ru and Pt, respectively. (Images and EDX captured by STEM mode in FEI Titan Themis G2 60-300 working at 300 kV)

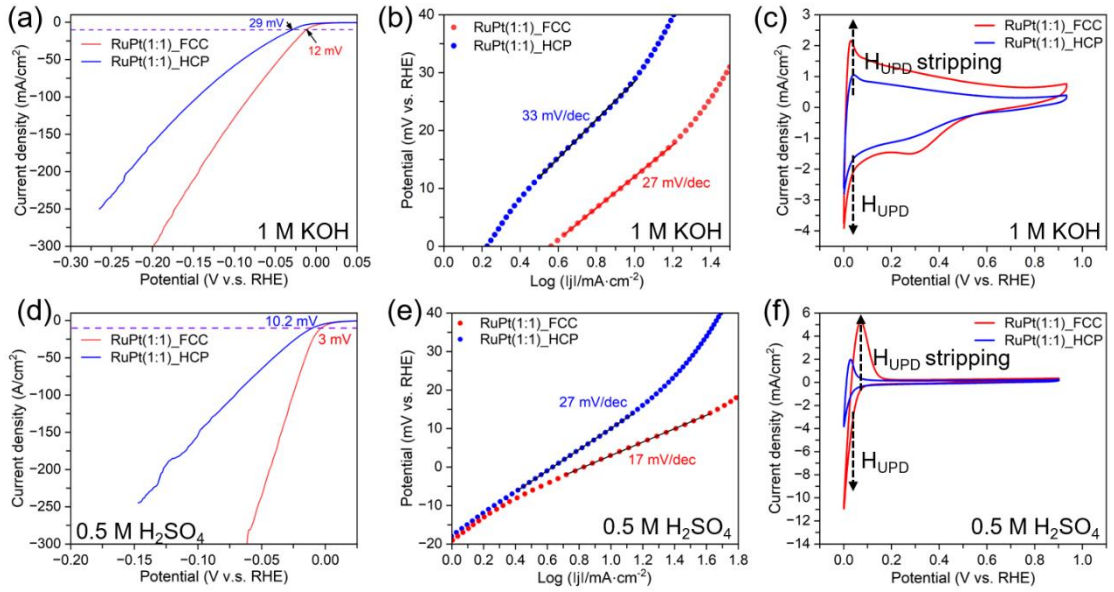


Figure 4.5.6. HER performance tests of RuPt(1:1)_FCC and RuPt(1:1)_HCP. (a, d) LSV tests in 1 M KOH and 0.5 M H_2SO_4, respectively. (b, e) Tafel slopes derived from (a, d), with the linear parts fitted to calculate the slope. (c, f) CV tests at scan rate of 20 $mV \cdot s^{-1}$.

The HER performance of RuPt(1:1) catalysts is displayed in Figure 4.5.6. RuPt(1:1)_FCC with a fcc structure exhibits a higher catalytic activities than the catalyst of RuPt(1:1)_hcp with a hcp structure in both alkaline and acidic electrolytes. It is worth mentioning that RuPt(1:1)_FCC exhibits the lowest overpotential (3 mV) in 0.5 M H_2SO_4 solution, compared with the reported catalysts in Figure 4.5.3(b). The strong activity of HER can be observed from the CV measured in the range of 0-0.94 V versus RHE (Figure 4.5.6c, f). The peaks in the range of 0-0.2 V vs. RHE are caused by underpotential deposition hydrogen (H_{UPD})[192]. A small peak around 0.35 V vs. RHE is observed in alkaline media, which is caused by the electrical double layer that adsorbed OH is replaced by H_2O[192]. The stronger H_{UPD} peak implies the larger amount of H adsorption on the catalyst, providing more proton for the reaction[193]. The stronger H_{UPD} peak in RuPt(1:1)_FCC than RuPt(1:1)_HCP indicates faster kinetics in HER.

The stability of the chemical states of single Pt atom substituted Ru catalysts was measured by XPS (Figure 4.5.7) before and after the specimen was tested in 1 M KOH at voltage of -0.1 V vs. RHE for 400 s. There are two peaks at 280.4 eV and 284.7 eV in high-resolution XPS of Ru 3d, which are assigned to the metallic Ru^0 Ref.[193]. The metallic Ru^0 is also observed in the Ru 3p XPS spectrum (Figure 4.5.7c, f) with 461.8 eV and 484.1 eV for Ru $3p_{3/2}$ and Ru $3p_{1/2}$, respectively. Pt $4f_{7/2}$ and $4f_{5/2}$ are located at 71.9 eV and 75.1 eV, respectively, which are higher than the binding energies of the metallic Pt^0 located at 71.2 eV and 74.5 eV, respectively[194]. The positive shifts of Pt 4f orbitals indicate the partially positive charge of Pt atoms ($Pt^{\delta+}$)[194]. Compared with the XPS of the initial specimen, no shift is observed on the XPS peaks of the

specimen post-reaction at -0.1 V vs. RHE for 400 s, indicating that the chemical states of Pt and Ru remained the same before and after HER tests.

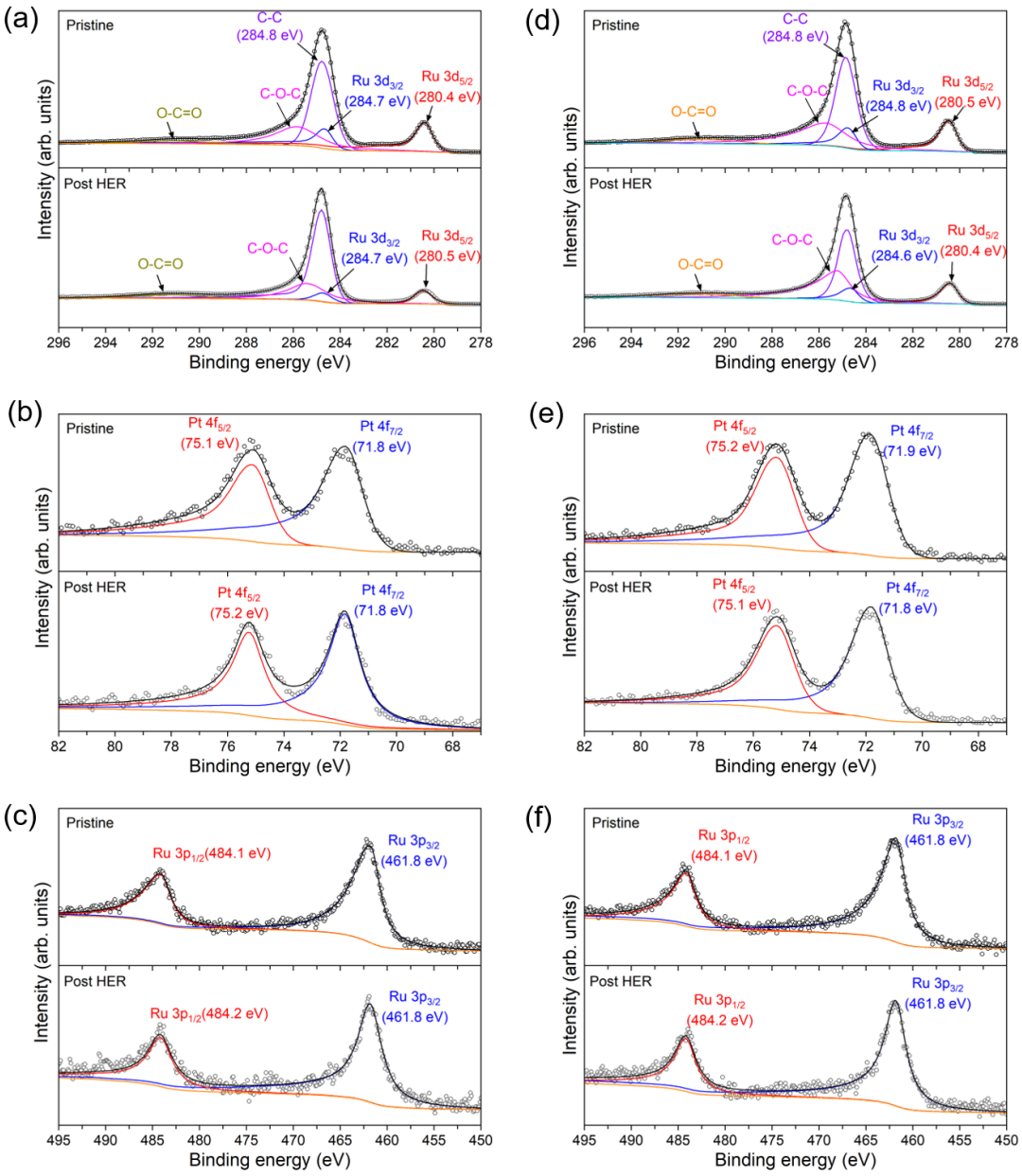


Figure 4.5.7. High-resolution XPS of $Ru_{95}Pt_5$ (a-c) and $Ru_{90}Pt_{10}$ (a-c) nanoparticles before and after HER tests (working at -0.1 V v.s. RHE for 400 s). (a, d) XPS of C 1s and Ru 3d; (b, e) XPS of Pt 4f; (c, f) XPS of Ru 3p.

4.6 Conclusion

This chapter explores the synthesis of Pt-doped Ru nanoparticles and phosphides using Joule heating. The key benefits of this method are the utilization of shock heating from flash pulse currents and the ultrafast cooling rate, which can freeze nonequilibrium structures and pin stacking faults in the nanoparticles. The synthesis of fcc-structured Pt-doped Ru nanoparticles on carbon fiber surfaces is demonstrated, with both single Pt atoms and pulse currents playing important roles in their formation. The flash Joule heating technique is also applied to prepare metal compounds, including carbides and phosphides, with examples such as molybdenum carbide, ruthenium phosphide, and tungsten phosphide presented, with stacking faults pinned in the as-prepared nanoparticles. PtCo alloy nanoparticles with single Pt/Co atoms grown on graphitic carbon hosts are also prepared using flash Joule heating. The Pt-doped Ru nanoparticles are then tested as electrocatalysts for HER, with RuPt alloys with an fcc structure displaying high activity with an ultralow overpotential and small Tafel slope. The flash Joule heating synthesis method provides a simple approach to rapidly prepare nanoparticles, from metals to compounds.

Chapter 5. Conclusion and outlook

Nanoparticle preparation. Nanoparticles have been employed as catalysts in various catalytic reactions such as electrochemical water splitting and fuel cells. Structures, shapes, and sizes are of importance for promoting of catalytic activitiy[195]. Stacking faults, introduced in the process of synthesis, have been shown to boost the catalytic reactions[4,196–199]. Magnetron sputtering gas condensation and flash Joule heating syntheses are described and employed in this thesis for preparing nanoparticles with thermodynamically nonequilibrium structures and shapes. Firstly, tetrahedral and octahedral Pt nanoparticles were prepared in the gas-phase method. The faster growth rates of (111) facets than that of (100) facets produce octahedral Pt nanoparticles. Thanks to the formation of stacking faults between the FCC stackings and the HCP stackings, tetrahedral Pt nanoparticles are prepared with the transformation from octahedra to tetrahedra. The formation of tetrahedra and octahedra demonstrates the strategies of controlling the growth path of nanoparticles in the gas phase by the preparation conditions, revealing the vital role of kinetics in the formation of nanoparticles. Another strategy for preparing non-equilibrium structures is introducing heterogenous atoms (e.g. Ni atoms) in the growth of Pt nanoparticles. Ni atoms trigger the formation of icosahedral and decahedral Pt-Ni nanoparticles with core-shell or alloy structures.

Conventional nanoparticle synthesis involves complicate operations and/or instruments[132]. For example, different reductants and conditions are required in the synthesis of metal nanoparticles using wet-chemical methods. The magnetron-sputtering is versatile in the preparation from single-atoms to nanoparticles, but the instrument is complicated and expensive[55,66]. This

motivates developing an operation-friendly and economic synthesis. The flash Joule heating synthesis is a time-saving and energy-saving approach to prepare nanoparticles, where pulse currents are converted into Joule heating within milliseconds, driving the synthesis reaction of nanoparticles. Two routes were introduced in this thesis using carbon films and conductive powders to load nanoparticles, respectively. The ultrahigh temperature with flash heating and high cooling rates makes it possible to create and maintain metastable structures (e.g. fcc for Ru nanoparticles) and/or defects (e.g. dislocation) in nanoparticles. Formation of Pt-doped Ru nanoparticles with an fcc structure was demonstrated, with these nanoparticles showing excellent performance in the HER. Strains were observed in phosphide nanoparticles and Ru nanoparticles. It was found that the residual strains were generated by stacking faults in the formation of nanoparticles in flash Joule heating.

Precious-metal nanoparticles (e.g. PtCo), transition metal carbides (e.g. MoC and WC_x), metallic phosphides (e.g. RuP_x and WP) were fabricated using flash Joule heating, demonstrating the versatility of this synthesis strategy. Joule heating also shows potentials on the preparation of high-entropy alloys[37] and compounds with arbitrary elements and contents, such as high-entropy phosphides and high-entropy carbides, which have potential applications in catalytic reactions.

As graphene with few layers can be fabricated using various organics containing N, S, P etc., the graphene can be doped with various non-metal elements. Therefore, it is possible to prepare single-atoms catalysts with M-N-C structure, which M represents metal atom, N is non-metal atom (e.g. nitrogen, sulfur, phosphorus, boron). An example (PtCo) was shown in this thesis

that the single-atoms (Pt/Co) catalyst is grown in N-doped graphitic carbons, prepared using the flash Joule heating.

Structure stability. The *in-situ* experiment heating conducted in microscope illustrated the morphological evolution of nonequilibrium structures from tetrahedral and octahedral shapes to the Wulff constructions. In contrast, icosahedral and decahedral Ni-Pt nanoparticles presented high structure stability at elevated temperatures. However, the core-shell structure of Ni-Pt nanoparticles disappeared after long-term storage due to the Kirkendall effect, induced by atom diffusions. The oxidation of Ni atoms was detected by the changes of Ni valence from the EELS spectrum.

Naked surfaces of nanoparticles prepared using the magnetron sputtering method make it possible to investigate the role of atoms on the surfaces in structure reconstructions and catalytic mechanisms. Employing an environmental TEM, the roles of different facets (e.g. (111) or (100)) on the catalytic reactions, such as ammonia oxidation, ammonia decomposition, and carbon monoxide oxidation were investigated. The naked nanoparticles also enable researchers to observe directly the evolution of morphologies in working gases (e.g. oxygen, ammonia, or hydrogen).

Graphene layers were observed to cover the nanoparticles prepared using the flash Joule heating or carbothermal shock synthesis. The graphene layers, in some cases, can protect the active sites of nanoparticles against poison, oxidation and reconstruction at elevated temperature, such as Pt catalysts that are easily deactivated by CO. However, the graphene layers also block the surface of nanoparticles to be exposed in the reaction environment, which may impact their

catalytic performance.

Using in-situ techniques, the impacts of structural stability of high-entropy compounds on the catalytic activities can be investigated. For example, how the catalytic reactions affect the elemental distributions of high-entropy compounds? Do the reactions induce the structure transformation?

Potential applications. The Materials Genome Initiative (MGI) attempts to accelerate the discovery of new materials, integration of computation, synthesis, analytical theory, and experiment[200,201]. Both magnetron-sputtering gas-condensation and flash Joule heating (carbothermal shock) synthesis provide a high-throughput pathway to synthesize new materials. Magnetron-sputtering with a mass-filter can prepare size selected nanoparticles with clean surfaces. Using multi-targets, core-shell or alloy structures can be obtained. The flash Joule heating synthesis enables scientists to fabricate materials from single element to high-entropy compounds including high-entropy alloys, high-entropy phosphides, and high-entropy oxidates. Both syntheses have wide applications for materials discovery.

Reference

(1) Mistry, H.; Varela, A. S.; Kühl, S.; Strasser, P.; Cuenya, B. R. Nanostructured Electrocatalysts with Tunable Activity and Selectivity. *Nat. Rev. Mater.* **2016**, *1*, 1–15.

(2) Burkart, M. D.; Hazari, N.; Tway, C. L.; Zeitler, E. L. Opportunities and Challenges for Catalysis in Carbon Dioxide Utilization. *ACS Catal.* **2019**, *9* (9), 7937–7956.

(3) Mahata, A.; Nair, A. S.; Pathak, B. Recent Advancements in Pt-Nanostructure-Based Electrocatalysts for the Oxygen Reduction Reaction. *Catal. Sci. Technol.* **2019**, *9* (18), 4835–4863.

(4) Strasser, P.; Koh, S.; Anniyev, T.; Greeley, J.; More, K.; Yu, C.; Liu, Z.; Kaya, S.; Nordlund, D.; Ogasawara, H.; et al. Lattice-Strain Control of the Activity in Dealloyed Core-Shell Fuel Cell Catalysts. *Nat. Chem.* **2010**, *2* (6), 454–460.

(5) Zhang, L.; Doyle-Davis, K.; Sun, X. Pt-Based Electrocatalysts with High Atom Utilization Efficiency: From Nanostructures to Single Atoms. *Energy Environ. Sci.* **2019**, *12* (2), 492–517.

(6) Huang, X.; Li, Z.; Yu, Z.; Deng, X.; Xin, Y. Recent Advances in the Synthesis, Properties, and Biological Applications of Platinum Nanoclusters. *J. Nanomater.* **2019**, *2019*, 1–31.

(7) Ferrando, R.; Jellinek, J.; Johnston, R. L. Nanoalloys: From Theory to Applications of Alloy Clusters and Nanoparticles. *Chem. Rev.* **2008**, *108* (3), 845–910.

(8) Liu, L.; Corma, A. Metal Catalysts for Heterogeneous Catalysis: From Single Atoms to Nanoclusters and Nanoparticles. *Chem. Rev.* **2018**, *118* (10), 4981–5079.

(9) Tyo, E. C.; Vajda, S. Catalysis by Clusters with Precise Numbers of Atoms. *Nat. Nanotechnol.* **2015**, *10* (7), 577–588.

(10) Wu, J.; Qi, L.; You, H.; Gross, A.; Li, J.; Yang, H. Icosahedral Platinum Alloy Nanocrystals with Enhanced Electrocatalytic Activities. *J. Am. Chem. Soc.* **2012**, *134* (29), 11880–11883.

(11) Rizo, R.; Roldan Cuenya, B. Shape-Controlled Nanoparticles as Anodic Catalysts in Low-Temperature Fuel Cells. *ACS Energy Lett.* **2019**, *4* (6), 1484–1495.

(12) Devivaraprasad, R.; Nalajala, N.; Bera, B.; Neergat, M. Electrocatalysis of Oxygen Reduction Reaction on Shape-Controlled Pt and Pd Nanoparticles—Importance of Surface Cleanliness and Reconstruction. *Front. Chem.* **2019**, *7* (October), 1–25.

(13) Nicolae Strambeanu, Laurentiu Demetrovici, D. D. and M. L. Nanoparticles. Definition, Classification, General Physical Properties. In *Nanoparticles' Promises and Risks: Characterization, Manipulation, and Potential Hazards to Humanity and the Environment*; 2015; pp vii–viii.

(14) Yacamán, M. J.; Ascencio, J. A.; Liu, H. B.; Gardea-Torresdey, J. Structure Shape and Stability of Nanometric Sized Particles. *J. Vac. Sci. Technol. B Microelectron. Nanom. Struct.* **2001**, *19* (4), 1091.

(15) Baletto, F.; Ferrando, R. Structural Properties of Nanoclusters: Energetic, Thermodynamic, and Kinetic Effects. *Rev. Mod. Phys.* **2005**, *77* (1), 371–423.

(16) Xia, Y.; Xia, X.; Peng, H. C. Shape-Controlled Synthesis of Colloidal Metal Nanocrystals: Thermodynamic versus Kinetic Products. *J. Am. Chem. Soc.* **2015**, *137* (25), 7947–7966.
(17) Liang, J.; Ma, F.; Hwang, S.; Wang, X.; Sokolowski, J.; Li, Q.; Wu, G.; Su, D. Atomic Arrangement Engineering of Metallic Nanocrystals for Energy-Conversion Electrocatalysis. *Joule* **2019**, *3* (4), 956–991.
(18) Wulff, G. On the Question of Speed of Growth and Dissolution of Crystal Surfaces. *Zeitschrift für Kryst. und Mineral.* **1901**, No. 34, 449–530.
(19) Marks, L. D. Modified Wulff Constructions for Twinned Particles. *J. Cryst. Growth* **1983**, *61* (3), 556–566.
(20) Ringe, E.; Van Duyne, R. P.; Marks, L. D. Kinetic and Thermodynamic Modified Wulff Constructions for Twinned Nanoparticles. *J. Phys. Chem. C* **2013**, *117* (31), 15859–15870.
(21) Vernieres, J.; Steinhauer, S.; Zhao, J.; Grammatikopoulos, P.; Ferrando, R.; Nordlund, K.; Djurabekova, F.; Sowwan, M. Site-Specific Wetting of Iron Nanocubes by Gold Atoms in Gas-Phase Synthesis. *Adv. Sci.* **2019**, *6* (13).
(22) Vernieres, J.; Chapelle, A.; Nordlund, K.; Menini, P.; Sowwan, M.; Diaz, R. E.; Steinhauer, S.; Dufour, N.; Djurabekova, F.; Grammatikopoulos, P.; et al. Gas Phase Synthesis of Multifunctional Fe-Based Nanocubes. *Adv. Funct. Mater.* **2017**, *27* (11), 1605328.
(23) Rahm, J. M.; Erhart, P. Beyond Magic Numbers: Atomic Scale Equilibrium Nanoparticle Shapes for Any Size. *Nano Lett.* **2017**, *17* (9), 5775–5781.
(24) Zhao, J.; Baibuz, E.; Vernieres, J.; Grammatikopoulos, P.; Jansson, V.; Nagel, M.; Steinhauer, S.; Sowwan, M.; Kuronen, A.; Nordlund, K.; et al. Formation Mechanism of Fe Nanocubes by Magnetron Sputtering Inert Gas Condensation. *ACS Nano* **2016**, *10* (4), 4684–4694.
(25) Ahmadi, T. S.; Wang, Z. L.; Green, T. C.; Henglein, A.; El-Sayed, M. A. Shape-Controlled Synthesis of Colloidal Platinum Nanoparticles. *Science (80-.).* **1996**, *272* (5270), 1924–1925.
(26) Petroski, J. M.; Wang, Z. L.; Green, T. C.; El-Sayed, M. A. Kinetically Controlled Growth and Shape Formation Mechanism of Platinum Nanoparticles. *J. Phys. Chem. B* **1998**, *102* (18), 3316–3320.
(27) Wang, Y.; Xie, S.; Liu, J.; Park, J.; Huang, C. Z.; Xia, Y. Shape-Controlled Synthesis of Palladium Nanocrystals: A Mechanistic Understanding of the Evolution from Octahedrons to Tetrahedrons. *Nano Lett.* **2013**, *13* (5), 2276–2281.
(28) Marks, L. D.; Marks, L. D. Surface Structure and Energetics of Multiply Twinned Particles. *Philos. Mag. A Phys. Condens. Matter, Struct. Defects Mech. Prop.* **1984**, *49* (1), 81–93.
(29) Baletto, F.; Ferrando, R.; Fortunelli, A.; Montalenti, F.; Mottet, C. Crossover among Structural Motifs in Transition and Noble-Metal Clusters. *J. Chem. Phys.* **2002**, *116* (9), 3856–3863.
(30) Xia, Y.; Xiong, Y.; Lim, B.; Skrabalak, S. E. Shape-Controlled Synthesis of Metal Nanocrystals: Simple Chemistry Meets Complex Physics? *Angew. Chemie - Int. Ed.*

2009, *48* (1), 60–103.
(31) An, K.; Somorjai, G. A. Size and Shape Control of Metal Nanoparticles for Reaction Selectivity in Catalysis. *ChemCatChem* **2012**, *4* (10), 1512–1524.
(32) Zhao, M.; Chen, Z.; Lyu, Z.; Hood, Z. D.; Xie, M.; Vara, M.; Chi, M.; Xia, Y. Ru Octahedral Nanocrystals with a Face-Centered Cubic Structure, {111} Facets, Thermal Stability up to 400 °C, and Enhanced Catalytic Activity. *J. Am. Chem. Soc.* **2019**, *141* (17), 7028–7036.
(33) Meziane, L.; Salzemann, C.; Aubert, C.; Gérard, H.; Petit, C.; Petit, M. Hcp Cobalt Nanocrystals with High Magnetic Anisotropy Prepared by Easy One-Pot Synthesis. *Nanoscale* **2016**, *8* (44), 18640–18645.
(34) Tao, A. R.; Habas, S.; Yang, P. Shape Control of Colloidal Metal Nanocrystals. *Small* **2008**, *4* (3), 310–325.
(35) Niu, Z.; Li, Y. Removal and Utilization of Capping Agents in Nanocatalysis. *Chem. Mater.* **2014**, *26* (1), 72–83.
(36) Liu, Y.; Sun, C.; Bolin, T.; Wu, T.; Liu, Y.; Sternberg, M.; Sun, S.; Lin, X. M. Kinetic Pathway of Palladium Nanoparticle Sulfidation Process at High Temperatures. *Nano Lett.* **2013**, *13* (10), 4893–4901.
(37) Xie, H.; Chen, F.; Nie, A.; Pu, T.; Rehwoldt, M.; Yu, D. Carbothermal Shock Synthesis of High-Entropy-Alloy Nanoparticles. *Science (80-.).* **2018**, *1494* (March), 1489–1494.
(38) Deng, B.; Wang, Z.; Chen, W.; Li, J. T.; Luong, D. X.; Carter, R. A.; Gao, G.; Yakobson, B. I.; Zhao, Y.; Tour, J. M. Phase Controlled Synthesis of Transition Metal Carbide Nanocrystals by Ultrafast Flash Joule Heating. *Nat. Commun.* **2022**, *13* (1), 1–10.
(39) Luong, D. X.; Bets, K. V.; Algozeeb, W. A.; Stanford, M. G.; Kittrell, C.; Chen, W.; Salvatierra, R. V.; Ren, M.; McHugh, E. A.; Advincula, P. A.; et al. Gram-Scale Bottom-up Flash Graphene Synthesis. *Nature* **2020**, *577* (7792), 647–651.
(40) Song, J. Y.; Kim, C.; Kim, M.; Cho, K. M.; Gereige, I.; Jung, W. Bin; Jeong, H.; Jung, H. T. Generation of High-Density Nanoparticles in the Carbothermal Shock Method. *Sci. Adv.* **2021**, *7* (48).
(41) Cui, M.; Yang, C.; Hwang, S.; Yang, M.; Overa, S.; Dong, Q.; Yao, Y.; Brozena, A. H.; Cullen, D. A.; Chi, M.; et al. Multi-Principal Elemental Intermetallic Nanoparticles Synthesized via a Disorder-to-Order Transition. *Sci. Adv.* **2022**, *8* (4), eabm4322.
(42) Chong, L.; Wen, J.; Kubal, J.; Sen, F. G.; Zou, J.; Greeley, J.; Chan, M.; Barkholtz, H.; Ding, W.; Liu, D. J. Ultralow-Loading Platinum-Cobalt Fuel Cell Catalysts Derived from Imidazolate Frameworks. *Science (80-.).* **2018**, *362* (6420), 1276–1281.
(43) Yang, C. L.; Wang, L. N.; Yin, P.; Liu, J.; Chen, M. X.; Yan, Q. Q.; Wang, Z. S.; Xu, S. L.; Chu, S. Q.; Cui, C.; et al. Sulfur-Anchoring Synthesis of Platinum Intermetallic Nanoparticle Catalysts for Fuel Cells. *Science (80-.).* **2021**, *374* (6566), 459–464.
(44) Wang, L.; Chen, M. X.; Yan, Q. Q.; Xu, S. L.; Chu, S. Q.; Chen, P.; Lin, Y.; Liang, H. W. A Sulfur-Tethering Synthesis Strategy toward High-Loading Atomically Dispersed Noble Metal Catalysts. *Sci. Adv.* **2019**, *5* (10).
(45) Bilger, D.; Homayounfar, S. Z.; Andrew, T. L. A Critical Review of Reactive Vapor

Deposition for Conjugated Polymer Synthesis. *J. Mater. Chem. C* **2019**, *7* (24), 7159–7174.

(46) Perrotta, A.; Werzer, O.; Coclite, A. M. Strategies for Drug Encapsulation and Controlled Delivery Based on Vapor-Phase Deposited Thin Films. *Adv. Eng. Mater.* **2018**, *20* (3).

(47) Swihart, M. T. Vapor-Phase Synthesis of Nanoparticles. *Curr. Opin. Colloid Interface Sci.* **2003**, *8* (1), 127–133.

(48) Mackus, A. J. M.; Weber, M. J.; Thissen, N. F. W.; Garcia-Alonso, D.; Vervuurt, R. H. J.; Assali, S.; Bol, A. A.; Verheijen, M. A.; Kessels, W. M. M. Atomic Layer Deposition of Pd and Pt Nanoparticles for Catalysis: On the Mechanisms of Nanoparticle Formation. *Nanotechnology* **2015**, *27* (3).

(49) Dubkov, S.; Gromov, D.; Savitskiy, A.; Trifonov, A.; Gavrilov, S. Alloying Effects at Bicomponent Au-Cu and In-Sn Particle Arrays Formation by Vacuum-Thermal Evaporation. *Mater. Res. Bull.* **2019**, *112* (July 2017), 438–444.

(50) Shishino, Y.; Yonezawa, T.; Kawai, K.; Nishihara, H. Molten Matrix Sputtering Synthesis of Water-Soluble Luminescent Au Nanoparticles with a Large Stokes Shift. *Chem. Commun.* **2010**, *46* (38), 7211–7213.

(51) Morita, K.; Sakuma, K.; Miyajima, K.; Mafuné, F. Thermally and Chemically Stable Mixed Valence Copper Oxide Cluster Ions Revealed by Post Heating. *J. Phys. Chem. A* **2013**, *117* (40), 10145–10150.

(52) Li, Z.; Fu, J. Y.; Feng, Y.; Dong, C. K.; Liu, H.; Du, X. W. A Silver Catalyst Activated by Stacking Faults for the Hydrogen Evolution Reaction. *Nat. Catal.* **2019**, *2* (12), 1107–1114.

(53) Tabrizi, N. S.; Ullmann, M.; Vons, V. A.; Lafont, U.; Schmidt-Ott, A. Generation of Nanoparticles by Spark Discharge. *J. Nanoparticle Res.* **2009**, *11* (2), 315–332.

(54) Reinmann, R.; Akram, M. Temporal Investigation of a Fast Spark Discharge in Chemically Inert Gases. *J. Phys. D. Appl. Phys.* **1997**, *30* (7), 1125–1134.

(55) Pratontep, S.; Carroll, S. J.; Xirouchaki, C.; Streun, M.; Palmer, R. E. Size-Selected Cluster Beam Source Based on Radio Frequency Magnetron Plasma Sputtering and Gas Condensation. *Rev. Sci. Instrum.* **2005**, *76* (4).

(56) Hihara, T.; Sumiyama, K. Formation and Size Control of a Ni Cluster by Plasma Gas Condensation. *J. Appl. Phys.* **1998**, *84* (9), 5270–5276.

(57) Nguyen, M. T.; Zhang, H.; Deng, L.; Tokunaga, T.; Yonezawa, T. Au/Cu Bimetallic Nanoparticles via Double-Target Sputtering onto a Liquid Polymer. *Langmuir* **2017**, *33* (43), 12389–12397.

(58) Zheng, Y. R.; Vernieres, J.; Wang, Z.; Zhang, K.; Hochfilzer, D.; Krempl, K.; Liao, T. W.; Presel, F.; Altantzis, T.; Fatermans, J.; et al. Monitoring Oxygen Production on Mass-Selected Iridium–Tantalum Oxide Electrocatalysts. *Nat. Energy* **2022**, *7* (1), 55–64.

(59) Gudmundsson, J. T.; Hecimovic, A. Foundations of DC Plasma Sources. *Plasma Sources Sci. Technol.* **2017**, *26* (12).

(60) Behrisch, R.; Eckstein, W. Sputtering by Particle Bombardment, Experiments and Computer Calculations from Threshold to MeV Energies. In *Topics in Applied Physics*;

Springer Berlin, 2007; pp 1–19.
(61) Gudmundsson, J. T. Physics and Technology of Magnetron Sputtering Discharges. *Plasma Sources Sci. Technol.* **2020**, *29* (11).
(62) Gudmundsson, J. T.; Fischer, J.; Hinriksson, B. P.; Rudolph, M.; Lundin, D. Ionization Region Model of High Power Impulse Magnetron Sputtering of Copper. *Surf. Coatings Technol.* **2022**, *442* (February), 128189.
(63) Smirnov, B. M. Processes Involving Clusters and Small Particles in a Buffer Gas. *Uspekhi Fiz. Nauk* **2011**, *181* (7), 713.
(64) Smirnov, B. M. Cluster Plasma. *Uspekhi Fiz. Nauk* **2000**, *170* (5), 532–534.
(65) Grammatikopoulos, P.; Steinhauer, S.; Vernieres, J.; Singh, V.; Sowwan, M. Nanoparticle Design by Gas-Phase Synthesis. *Adv. Phys. X* **2016**, *1* (1), 81–100.
(66) Von Issendorff, B.; Palmer, R. E. A New High Transmission Infinite Range Mass Selector for Cluster and Nanoparticle Beams. *Rev. Sci. Instrum.* **1999**, *70* (12), 4497–4501.
(67) D.E. Jesson; S. J. Pennycook. Incoherent Imaging of Crystals Using Thermally Scattered Electrons. *Proc. R. Soc. London A* **1995**, *449* (1936), 273–293.
(68) Williams, David B., C. C. B. *Transimission Electron Microscopy-A Textbook for Materials Science*; Springer US: New York, 2008.
(69) Nellist, P. D.; Pennycook, S. J. *The Principles and Interpretation of Annular Dark-Field Z-Contrast Imaging*; 2000; Vol. 113.
(70) Pennycook, S. J. Structure Determination through Z-Contrast Microscopy. *Adv. Imaging Electron Phys.* **2002**, *123* (C), 173–206.
(71) Rafferty, B.; Nellist, D.; Pennycook, J. On the Origin of Transverse Incoherence in Z-Contrast STEM. *J. Electron Microsc. (Tokyo).* **2001**, *50* (3), 227–233.
(72) Nellist, P. D.; Behan, G.; Kirkland, A. I.; Hetherington, C. J. D. Confocal Operation of a Transmission Electron Microscope with Two Aberration Correctors. *Appl. Phys. Lett.* **2006**, *89* (12), 87–90.
(73) Haider, M.; Braunshausen, G.; Schwan, E. Correction of the Spherical Aberration of a 200 KV TEM by Means of a Hexapole-Corrector. *Optik (Stuttg).* **1995**, *99* (4), 167–179.
(74) Haider, M.; Rose, H.; Uhlemann, S.; Schwan, E.; Kabius, B.; Urban, K. A Spherical-Aberration-Corrected 200 KV Transmission Electron Microscope. *Ultramicroscopy* **1998**, *75* (1), 53–60.
(75) Kisielowski, C.; Freitag, B.; Bischoff, M.; Van Lin, H.; Lazar, S.; Knippels, G.; Tiemeijer, P.; Van Der Stam, M.; Von Harrach, S.; Stekelenburg, M.; et al. Detection of Single Atoms and Buried Defects in Three Dimensions by Aberration-Corrected Electron Microscope with 0.5-Å Information Limit. *Microsc. Microanal.* **2008**, *14* (5), 469–477.
(76) Lin, Y.; Zhou, M.; Tai, X.; Li, H.; Han, X.; Yu, J. Analytical Transmission Electron Microscopy for Emerging Advanced Materials. *Matter* **2021**, *4* (7), 2309–2339.
(77) Egerton, R. F. *Electron Energy-Loss Spectroscopy in the Electron Microscope*, Third edit.; Springer New York, 2011.
(78) E, H.; MacArthur, K. E.; Pennycook, T. J.; Okunishi, E.; D'Alfonso, A. J.; Lugg, N.

R.; Allen, L. J.; Nellist, P. D. Probe Integrated Scattering Cross Sections in the Analysis of Atomic Resolution HAADF STEM Images. *Ultramicroscopy* **2013**, *133*, 109–119.

(79) Martinez, G. T.; Rosenauer, A.; De Backer, A.; Verbeeck, J.; Van Aert, S. Quantitative Composition Determination at the Atomic Level Using Model-Based High-Angle Annular Dark Field Scanning Transmission Electron Microscopy. *Ultramicroscopy* **2014**, *137* (2014), 12–19.

(80) Jones, L. Quantitative ADF STEM: Acquisition, Analysis and Interpretation. *IOP Conf. Ser. Mater. Sci. Eng.* **2016**, *109* (1).

(81) Langlois, C.; Wang, Z. W.; Pearmain, D.; Ricolleau, C.; Li, Z. Y. HAADF-STEM Imaging of CuAg Core-Shell Nanoparticles. *J. Phys. Conf. Ser.* **2010**, *241*.

(82) Hovden, R.; Cueva, P.; Mundy, J. A.; Muller, D. A. The Open-Source Cornell Spectrum Imager. *Micros. Today* **2013**, *21* (1), 40–44.

(83) Yedra, L.; Xuriguera, E.; Estrader, M.; López-Ortega, A.; Baró, M. D.; Nogués, J.; Roldan, M.; Varela, M.; Estradé, S.; Peiró, F. Oxide Wizard: An EELS Application to Characterize the White Lines of Transition Metal Edges. In *Microscopy and Microanalysis*; 2014; Vol. 20, pp 698–705.

(84) Wang, Z. L.; Yin, J. S.; Jiang, Y. D. EELS Analysis of Cation Valence States and Oxygen Vacancies in Magnetic Oxides. In *Micron*; 2000; Vol. 31, pp 571–580.

(85) Pearson, D. H.,Ahn,C. C., Fultz, B. White Lines and D-Electron Occupancies for the 3d and 4d Transition Metals. *Phys. Rev. B* **1993**, *47* (14), 8471.

(86) BOTTON, G. A.; APPEL, C. C.; HORSEWELL, A.; STOBBS, W. M. Quantification of the EELS Near-edge Structures to Study Mn Doping in Oxides. *J. Microsc.* **1995**, *180* (3), 211–216.

(87) Bawane, K.; Manganaris, P.; Wang, Y.; Sure, J.; Ronne, A.; Halstenberg, P.; Dai, S.; Gill, S. K.; Sasaki, K.; Chen-Wiegart, Y. chen K.; et al. Determining Oxidation States of Transition Metals in Molten Salt Corrosion Using Electron Energy Loss Spectroscopy. *Scr. Mater.* **2021**, *197*.

(88) Zhu, J.; Hu, L.; Zhao, P.; Lee, L. Y. S.; Wong, K. Y. Recent Advances in Electrocatalytic Hydrogen Evolution Using Nanoparticles. *Chem. Rev.* **2020**, *120* (2), 851–918.

(89) Zeng, M.; Li, Y. Recent Advances in Heterogeneous Electrocatalysts for the Hydrogen Evolution Reaction. *J. Mater. Chem. A* **2015**, *3* (29), 14942–14962.

(90) Allen J. Bard, L. R. F. *Electrochemical Methods: Fundamentals and Applications*; John Wiley & Sons, 2000.

(91) McCrory, C. C. L.; Jung, S.; Peters, J. C.; Jaramillo, T. F. Benchmarking Heterogeneous Electrocatalysts for the Oxygen Evolution Reaction. *J. Am. Chem. Soc.* **2013**, *135* (45), 16977–16987.

(92) Walter, M. G.; Warren, E. L.; McKone, J. R.; Boettcher, S. W.; Mi, Q.; Santori, E. A.; Lewis, N. S. Solar Water Splitting Cells. *Chem. Rev.* **2010**, *110* (11), 6446–6473.

(93) Sheng, W.; Gasteiger, H. A.; Shao-Horn, Y. Hydrogen Oxidation and Evolution Reaction Kinetics on Platinum: Acid vs Alkaline Electrolytes. *J. Electrochem. Soc.* **2010**, *157* (11), B1529.

(94) Zhao, G.; Rui, K.; Dou, S. X.; Sun, W. Heterostructures for Electrochemical Hydrogen Evolution Reaction: A Review. *Adv. Funct. Mater.* **2018**, *28* (43).
(95) Wei, J.; Zhou, M.; Long, A.; Xue, Y.; Liao, H.; Wei, C.; Xu, Z. J. Heterostructured Electrocatalysts for Hydrogen Evolution Reaction Under Alkaline Conditions. *Nano-Micro Lett.* **2018**, *10* (4), 1–15.
(96) Wu, Z. P.; Lu, X. F.; Zang, S. Q.; Lou, X. W. Non-Noble-Metal-Based Electrocatalysts toward the Oxygen Evolution Reaction. *Adv. Funct. Mater.* **2020**, *30* (15), 1–20.
(97) Anantharaj, S.; Ede, S. R.; Karthick, K.; Sam Sankar, S.; Sangeetha, K.; Karthik, P. E.; Kundu, S. Precision and Correctness in the Evaluation of Electrocatalytic Water Splitting: Revisiting Activity Parameters with a Critical Assessment. *Energy Environ. Sci.* **2018**, *11* (4), 744–771.
(98) Young, N. P.; Li, Z. Y.; Chen, Y.; Palomba, S.; Di Vece, M.; Palmer, R. E. Weighing Supported Nanoparticles: Size-Selected Clusters as Mass Standards in Nanometrology. *Phys. Rev. Lett.* **2008**, *101* (24), 28–31.
(99) Li, Z. Y.; Young, N. P.; Di Vece, M.; Palomba, S.; Palmer, R. E.; Bleloch, A. L.; Curley, B. C.; Johnston, R. L.; Jiang, J.; Yuan, J. Three-Dimensional Atomic-Scale Structure of Size-Selected Gold Nanoclusters. *Nature* **2008**, *451* (7174), 46–48.
(100) Yang, J. C.; Bradley, S.; Gibson, J. M. Rapid and Semi-Automated Method for Analysis of the Number of Atoms of Ultra-Small Platinum Clusters on Carbon. *Microsc. Microanal.* **2000**, *6* (4), 353–357.
(101) House, S. D.; Chen, Y.; Jin, R.; Yang, J. C. High-Throughput, Semi-Automated Quantitative STEM Mass Measurement of Supported Metal Nanoparticles Using a Conventional TEM/STEM. *Ultramicroscopy* **2017**, *182*, 145–155.
(102) Xia, Y.; Harrison, P.; Ornelas, I. M.; Wang, H. L.; Li, Z. Y. HAADF-STEM Image Analysis for Size-Selected Platinum Nanoclusters. *J. Microsc.* **2020**, *279* (3), 229–233.
(103) He, D. S.; Li, Z. Y. A Practical Approach to Quantify the ADF Detector in STEM. *J. Phys. Conf. Ser.* **2014**, *522* (1).
(104) Khojasteh, M.; Kresin, V. V. Influence of Source Parameters on the Growth of Metal Nanoparticles by Sputter-Gas-Aggregation. *Appl. Nanosci.* **2017**, *7* (8), 875–883.
(105) YAMAMURA, Y.; MATSUNAMI, N.; ITOH, N. New Empirical Formula for the Sputtering Yield. *Radiat Eff Lett* **1982**, *V 68* (N 3), 83–87.
(106) Quesnel, E.; Pauliac-Vaujour, E.; Muffato, V. Modeling Metallic Nanoparticle Synthesis in a Magnetron-Based Nanocluster Source by Gas Condensation of a Sputtered Vapor. *J. Appl. Phys.* **2010**, *107* (5).
(107) Kashtanov, P. V.; Smirnov, B. M.; Hippler, R. Magnetron Plasma and Nanotechnology. *Physics-Uspekhi* **2007**, *50* (5).
(108) Blažek, J.; Kousal, J.; Biederman, H.; Kyliá N, O.; Hanuš, J.; Slavinská, D. Charging of Nanoparticles in Stationary Plasma in a Gas Aggregation Cluster Source. *J. Phys. D. Appl. Phys.* **2015**, *48* (41).
(109) Ding, R.; Padilla Espinosa, I. M.; Loevlie, D.; Azadehranjbar, S.; Baker, A. J.; Mpourmpakis, G.; Martini, A.; Jacobs, T. D. B. Size-Dependent Shape Distributions of Platinum Nanoparticles. *Nanoscale Adv.* **2022**, *4* (18), 3978–3986.
(110) Schebarchov, D.; Hendy, S. C. Thermal Instability of Decahedral Structures in

Platinum Nanoparticles. *Eur. Phys. J. D* **2007**, *43* (1–3), 11–14.
(111) Zeng, K.; Zhang, J.; Gao, W.; Wu, L.; Liu, H.; Gao, J.; Li, Z.; Zhou, J.; Li, T.; Liang, Z.; et al. Surface-Decorated High-Entropy Alloy Catalysts with Significantly Boosted Activity and Stability. *Adv. Funct. Mater.* **2022**, *2204643*, 1–12.
(112) Liu, D. L. *Particle Deposition onto Enclosure Surfaces*, First Edit.; Elsevier Inc., 2009.
(113) Ounis, H.; Ahmadi, G.; McLaughlin, J. B. Brownian Diffusion of Submicrometer Particles in the Viscous Sublayer. *J. Colloid Interface Sci.* **1991**, *143* (1), 266–277.
(114) Zhang, L.; Shao, J.; Chen, X. Numerical Simulation of Nanocluster Motion through a DC Magnetron Nanocluster Source. *Vacuum* **2016**, *128*, 137–145.
(115) Turchanin, M. A.; Agraval, P. G. Cohesive Energy, Properties, and Formation Energy of Transition Metal Alloys. *Powder Metall. Met. Ceram.* **2008**, *47* (1–2), 26–39.
(116) Kudriavtsev, Y.; Villegas, A.; Godines, A.; Asomoza, R. Calculation of the Surface Binding Energy for Ion Sputtered Particles. *Appl. Surf. Sci.* **2005**, *239* (3–4), 273–278.
(117) Richard Tran, Zihan Xu, Balachandran Radhakrishnan, Donald Winston, Wenhao Sun, K. A. P. & S. P. O. Data Descriptor: Surface Energies of Elemental Crystals. *Sci. Data* **2016**, *3*, 160080.
(118) Masini, F.; Hernández-Fernández, P.; Deiana, D.; Strebel, C. E.; McCarthy, D. N.; Bodin, A.; Malacrida, P.; Stephens, I.; Chorkendorff, I. Exploring the Phase Space of Time of Flight Mass Selected PtxY Nanoparticles. *Phys. Chem. Chem. Phys.* **2014**, *16* (48), 26506–26513.
(119) Hjorth Larsen, A.; JØrgen Mortensen, J.; Blomqvist, J.; Castelli, I. E.; Christensen, R.; Dułak, M.; Friis, J.; Groves, M. N.; Hammer, B.; Hargus, C.; et al. *The Atomic Simulation Environment - A Python Library for Working with Atoms*; 2017; Vol. 29.
(120) Xia, Y.; Nelli, D.; Ferrando, R.; Yuan, J.; Li, Z. Y. Shape Control of Size-Selected Naked Platinum Nanocrystals. *Nat. Commun.* **2021**, *12* (1), 1–8.
(121) Zhang, W. B.; Chen, C.; Zhang, S. Y. Equilibrium Crystal Shape of Ni from First Principles. *J. Phys. Chem. C* **2013**, *117* (41), 21274–21280.
(122) He, D. S.; Li, Z. Y.; Yuan, J. Kinematic HAADF-STEM Image Simulation of Small Nanoparticles. *Micron* **2015**, *74*, 47–53.
(123) Marks, L. D.; Peng, L. Nanoparticle Shape, Thermodynamics and Kinetics. *J. Phys. Condens. Matter* **2016**, *28* (5).
(124) Shi, Y.; Lyu, Z.; Zhao, M.; Chen, R.; Nguyen, Q. N.; Xia, Y. Noble-Metal Nanocrystals with Controlled Shapes for Catalytic and Electrocatalytic Applications. *Chem. Rev.* **2021**, *121* (2), 649–735.
(125) Pearmain, D.; Park, S. J.; Abdela, A.; Palmer, R. E.; Li, Z. Y. The Size-Dependent Morphology of Pd Nanoclusters Formed by Gas Condensation. *Nanoscale* **2015**, *7* (46), 19647–19652.
(126) Nelli, D.; Krishnadas, A.; Ferrando, R.; Minnai, C. One-Step Growth of Core–Shell (PtPd)@Pt and (PtPd)@Pd Nanoparticles in the Gas Phase. *J. Phys. Chem. C* **2020**.
(127) Baletto, F.; Mottet, C.; Ferrando, R. Molecular Dynamics Simulations of Surface Diffusion and Growth on Silver and Gold Clusters. *Surf. Sci.* **2000**, *446* (1–2), 31–45.
(128) Villarba, M.; Jónsson, H. Diffusion Mechanisms Relevant to Metal Crystal Growth: Pt/Pt(111). *Surf. Sci.* **1994**, *317* (1–2), 15–36.

(129) Gölzhäuser, A.; Ehrlich, G. Atom Movement and Binding on Surface Clusters: Pt on Pt(111) Clusters. *Phys. Rev. Lett.* **1996**, *77* (7), 1334–1337.
(130) Ayesh, A. I.; Thaker, S.; Qamhieh, N.; Ghamlouche, H. Size-Controlled Pd Nanocluster Grown by Plasma Gas-Condensation Method. *J. Nanoparticle Res.* **2011**, *13* (3), 1125–1131.
(131) Liu, C.; Zhang, L.; Zhang, S.; Liu, F.; Wang, G.; Han, M. Influence of Discharge Power on the Size of the Pd Cluster Generated with a Magnetron Plasma Gas Aggregation Cluster Source. *Vacuum* **2020**, *179* (February), 109486.
(132) Xia, Y.; Xia, X.; Peng, H. C. Shape-Controlled Synthesis of Colloidal Metal Nanocrystals: Thermodynamic versus Kinetic Products. *J. Am. Chem. Soc.* **2015**, *137* (25), 7947–7966.
(133) Baletto, F.; Ferrando, R.; Fortunelli, A.; Montalenti, F.; Mottet, C. Crossover among Structural Motifs in Transition and Noble-Metal Clusters. *J. Chem. Phys.* **2002**, *116* (9), 3856–3863.
(134) Cleveland, C. L.; Landman, U. The Energetics and Structure of Nickel Clusters: Size Dependence. *J. Chem. Phys.* **1991**, *94* (11), 7376–7396.
(135) van Omme, J. T.; Zakhozheva, M.; Spruit, R. G.; Sholkina, M.; Pérez Garza, H. H. Advanced Microheater for in Situ Transmission Electron Microscopy; Enabling Unexplored Analytical Studies and Extreme Spatial Stability. *Ultramicroscopy* **2018**, *192*, 14–20.
(136) Couchman, P. R.; Jesser, W. Thermodynamic Theory of Size Dependence. *Nature* **1977**, *269* (5628), 481–483.
(137) Foster, D. M.; Pavloudis, T.; Kioseoglou, J.; Palmer, R. E. Atomic-Resolution Imaging of Surface and Core Melting in Individual Size-Selected Au Nanoclusters on Carbon. *Nat. Commun.* **2019**, *10* (1), 1–8.
(138) Samsonov, V. M.; Vasilyev, S. A.; Nebyvalova, K. K.; Talyzin, I. V.; Sdobnyakov, N. Y.; Sokolov, D. N.; Alymov, M. I. Melting Temperature and Binding Energy of Metal Nanoparticles: Size Dependences, Interrelation between Them, and Some Correlations with Structural Stability of Nanoclusters. *J. Nanoparticle Res.* **2020**, *22* (8).
(139) Gunawan, L.; Johari, G. P. Specific Heat, Melting, Crystallization, and Oxidation of Zinc Nanoparticles and Their Transmission Electron Microscopy Studies. *J. Phys. Chem. C* **2008**, *112* (51), 20159–20166.
(140) Wang, Z. L.; Petroski, J. M.; Green, T. C.; El-Sayed, M. A. Shape Transformation and Surface Melting of Cubic and Tetrahedral Platinum Nanocrystals. *J. Phys. Chem. B* **1998**, *102* (32), 6145–6151.
(141) Guisbiers, G.; Abudukelimu, G.; Hourlier, D. Size-Dependent Catalytic and Melting Properties of Platinum-Palladium Nanoparticles. *Nanoscale Res. Lett.* **2011**, *6* (1), 1–5.
(142) Egerton, R. F. Radiation Damage to Organic and Inorganic Specimens in the TEM. *Micron*. Elsevier Ltd April 1, 2019, pp 72–87.
(143) Wang, Z.; Gui, L.; Han, D.; Xu, Z.; Han, L.; Xu, S. Measurement and Evaluation of Local Surface Temperature Induced by Irradiation of Nanoscaled or Microscaled Electron Beams. *Nanoscale Res. Lett.* **2019**, *14*.
(144) Jones, L.; Macarthur, K. E.; Fauske, V. T.; Van Helvoort, A. T. J.; Nellist, P. D. Rapid

Estimation of Catalyst Nanoparticle Morphology and Atomic-Coordination by High-Resolution Z-Contrast Electron Microscopy. *Nano Lett.* **2014**, *14* (11), 6336–6341.
(145) Banhart, F. Irradiation Effects in Carbon Nanostructures. *Reports Prog. Phys.* **1999**, *62* (8), 1181–1221.
(146) Knez, D.; Schnedlitz, M.; Lasserus, M.; Schiffmann, A.; Ernst, W. E.; Hofer, F. Modelling Electron Beam Induced Dynamics in Metallic Nanoclusters. *Ultramicroscopy* **2018**, *192* (May), 69–79.
(147) Egerton, R. F. Beam-Induced Motion of Adatoms in the Transmission Electron Microscope. *Microsc. Microanal.* **2013**, *19* (2), 479–486.
(148) Van Aert, S.; De Backer, A.; Jones, L.; Martinez, G. T.; Béché, A.; Nellist, P. D. Control of Knock-On Damage for 3D Atomic Scale Quantification of Nanostructures: Making Every Electron Count in Scanning Transmission Electron Microscopy. *Phys. Rev. Lett.* **2019**, *122* (6), 1–6.
(149) Aveyard, R.; Ferrando, R.; Johnston, R. L.; Yuan, J. Modeling Nanoscale Inhomogeneities for Quantitative HAADF STEM Imaging. *Phys. Rev. Lett.* **2014**, *113* (7), 1–5.
(150) Ding, Y.; Fan, F.; Tian, Z.; Wang, Z. L. Atomic Structure of Au-Pd Bimetallic Alloyed Nanoparticles. *J. Am. Chem. Soc.* **2010**, *132* (35), 12480–12486.
(151) Wang, Z. W.; Li, Z. Y.; Park, S. J.; Abdela, A.; Tang, D.; Palmer, R. E. Quantitative Z-Contrast Imaging in the Scanning Transmission Electron Microscope with Size-Selected Clusters. *Phys. Rev. B - Condens. Matter Mater. Phys.* **2011**, *84* (7), 2–4.
(152) Weyland, M.; Midgley, P. A.; Thomas, J. M. Electron Tomography of Nanoparticle Catalysts on Porous Supports: A New Technique Based on Rutherford Scattering. *J. Phys. Chem. B* **2001**, *105* (33), 7882–7886.
(153) S.J. PENNYCOOKMayr, G. Z-Contrast Stem for Materials Science. *Ultramicroscopy* **1989**, *143* (1), 82–97.
(154) Spence, J. C. H.; Spence, J. C. H. Scanning Transmission Electron Microscopy and Z-Contrast. *High-Resolution Electron Microsc.* **2014**, No. 3, 233–263.
(155) Förster, G. D.; Benoit, M.; Lam, J. Alloy, Janus and Core-Shell Nanoparticles: Numerical Modeling of Their Nucleation and Growth in Physical Synthesis. *Phys. Chem. Chem. Phys.* **2019**, *21* (41), 22774–22781.
(156) Rossnagel, S. M.; Kaufman, H. R. Current – Voltage Relations in Magnetrons Current-Voltage Relations in Magnetrons. **2017**, *223* (1988).
(157) Grais, K. I.; Shaltout, A. A.; Ali, S. S.; Boutros, R. M.; El-behery, K. M.; El-Sayed, Z. A. A New Formula for Sputtering Yield as Function of Ion Energies at Normal Incidence. *Phys. B Condens. Matter* **2010**, *405* (7), 1775–1781.
(158) Denton, A. R.; Ashcroft, N. W. Vegards Law. *Phys. Rev. A* **1991**, *43* (6), 3161–3164.
(159) Mukherjee, D.; Gamler, J. T. L.; Skrabalak, S. E.; Unocic, R. R. Lattice Strain Measurement of Core@Shell Electrocatalysts with 4D Scanning Transmission Electron Microscopy Nanobeam Electron Diffraction. *ACS Catal.* **2020**, *10* (10), 5529–5541.
(160) Gocyla, M.; Kuehl, S.; Shviro, M.; Heyen, H.; Selve, S.; Dunin-Borkowski, R. E.; Heggen, M.; Strasser, P. Shape Stability of Octahedral PtNi Nanocatalysts for Electrochemical Oxygen Reduction Reaction Studied by in Situ Transmission Electron

Microscopy. *ACS Nano* **2018**, *12* (6), 5306–5311.
(161) Vara, M.; Roling, L. T.; Wang, X.; Elnabawy, A. O.; Hood, Z. D.; Chi, M.; Mavrikakis, M.; Xia, Y. Understanding the Thermal Stability of Palladium-Platinum Core-Shell Nanocrystals by in Situ Transmission Electron Microscopy and Density Functional Theory. *ACS Nano* **2017**, *11* (5), 4571–4581.
(162) Van Teijlingen, A.; Davis, S. A.; Hall, S. R. Size-Dependent Melting Point Depression of Nickel Nanoparticles. *Nanoscale Adv.* **2020**, *2* (6), 2347–2351.
(163) Graetz, J.; Ahn, C. C.; Ouyang, H.; Rez, P.; Fultz, B. White Lines and D-Band Occupancy for the 3d Transition-Metal Oxides and Lithium Transition-Metal Oxides. *Phys. Rev. B - Condens. Matter Mater. Phys.* **2004**, *69* (23), 1–6.
(164) Potapov, P. L.; Kulkova, S. E.; Schryvers, D. Study of Changes in L32 EELS Ionization Edges upon Formation of Ni-Based Intermetallic Compounds. *J. Microsc.* **2003**, *210* (1), 102–109.
(165) Lewis, E. A.; Slater, T. J. A.; Prestat, E.; Macedo, A.; O'Brien, P.; Camargo, P. H. C.; Haigh, S. J. Real-Time Imaging and Elemental Mapping of AgAu Nanoparticle Transformations. *Nanoscale* **2014**, *6* (22), 13598–13605.
(166) Railsback, J. G.; Johnston-Peck, A. C.; Wang, J.; Tracy, J. B. Size-Dependent Nanoscale Kirkendall Effect during the Oxidation of Nickel Nanoparticles. *ACS Nano* **2010**, *4* (4), 1913–1920.
(167) Smigelskas A, K. E. Zinc Diffusion in Alpha Brass. *Trans. AIME* **1947**, *171*, 130–142.
(168) Chee, S. W.; Wong, Z. M.; Baraissov, Z.; Tan, S. F.; Tan, T. L.; Mirsaidov, U. Interface-Mediated Kirkendall Effect and Nanoscale Void Migration in Bimetallic Nanoparticles during Interdiffusion. *Nat. Commun.* **2019**, *10* (1), 1–8.
(169) Yang, Z.; Yang, N.; Pileni, M. P. Nano Kirkendall Effect Related to Nanocrystallinity of Metal Nanocrystals: Influence of the Outward and Inward Atomic Diffusion on the Final Nanoparticle Structure. *J. Phys. Chem. C* **2015**, *119* (39), 22249–22260.
(170) Li, T.; Yao, Y.; Huang, Z.; Xie, P.; Liu, Z.; Yang, M.; Gao, J.; Zeng, K.; Brozena, A. H.; Pastel, G.; et al. Denary Oxide Nanoparticles as Highly Stable Catalysts for Methane Combustion. *Nat. Catal.* **2021**, *4* (1), 62–70.
(171) Abdelhafiz, A.; Wang, B.; Harutyunyan, A. R.; Li, J. Carbothermal Shock Synthesis of High Entropy Oxide Catalysts : Dynamic Structural and Chemical Reconstruction Boosting the Catalytic Activity and Stability toward Oxygen Evolution Reaction. **2022**, 10–15.
(172) Yao, Y.; Huang, Z.; Xie, P.; Wu, L.; Ma, L.; Li, T.; Pang, Z.; Jiao, M.; Liang, Z.; Gao, J.; et al. High Temperature Shockwave Stabilized Single Atoms. *Nat. Nanotechnol.* **2019**.
(173) Okulov, I. V.; Soldatov, I. V.; Sarmanova, M. F.; Kaban, I.; Gemming, T.; Edström, K.; Eckert, J. Flash Joule Heating for Ductilization of Metallic Glasses. *Nat. Commun.* **2015**, *6*, 1–6.
(174) Algozeeb, W. A.; Savas, P. E.; Luong, D. X.; Chen, W.; Kittrell, C.; Bhat, M.; Shahsavari, R.; Tour, J. M. Flash Graphene from Plastic Waste. *ACS Nano* **2020**, *14* (11), 15595–15604.
(175) Li, L.; Liu, C.; Liu, S.; Wang, J.; Han, J.; Chan, T.-S.; Li, Y.; Hu, Z.; Shao, Q.; Zhang,

Q.; et al. Phase Engineering of a Ruthenium Nanostructure toward High-Performance Bifunctional Hydrogen Catalysis. *ACS Nano* **2022**, *16* (9), 14885–14894.
(176) Kusada, K.; Kobayashi, H.; Yamamoto, T.; Matsumura, S.; Sumi, N.; Sato, K.; Nagaoka, K.; Kubota, Y.; Kitagawa, H. Discovery of Face-Centered-Cubic Ruthenium Nanoparticles: Facile Size-Controlled Synthesis Using the Chemical Reduction Method. *J. Am. Chem. Soc.* **2013**, *135* (15), 5493–5496.
(177) Axet, M. R.; Philippot, K. Catalysis with Colloidal Ruthenium Nanoparticles. *Chem. Rev.* **2020**, *120* (2), 1085–1145.
(178) Wei, B.; Xia, Y.; Chen, S.; Wang, H. L. Modified Separator with Nitrogen-Doped High-Graphitized Carbon for Lithium-Sulfur Batteries. *Electroanalysis* **2022**, 1–7.
(179) Gammer, C.; Mangler, C.; Rentenberger, C.; Karnthaler, H. P. Quantitative Local Profile Analysis of Nanomaterials by Electron Diffraction. *Scr. Mater.* **2010**, *63* (3), 312–315.
(180) Li, S. H.; Qi, M. Y.; Tang, Z. R.; Xu, Y. J. Nanostructured Metal Phosphides: From Controllable Synthesis to Sustainable Catalysis. *Chem. Soc. Rev.* **2021**, *50* (13), 7539–7586.
(181) Liu, Y.; McCue, A. J.; Li, D. Metal Phosphides and Sulfides in Heterogeneous Catalysis: Electronic and Geometric Effects. *ACS Catal.* **2021**, *11* (15), 9102–9127.
(182) Prins, R.; Bussell, M. E. Metal Phosphides: Preparation, Characterization and Catalytic Reactivity. *Catal. Letters* **2012**, *142* (12), 1413–1436.
(183) Oyama, S. T.; Gott, T.; Zhao, H.; Lee, Y. K. Transition Metal Phosphide Hydroprocessing Catalysts: A Review. *Catal. Today* **2009**, *143* (1–2), 94–107.
(184) Yang, C.; Cui, M.; Li, N.; Liu, Z.; Hwang, S.; Xie, H.; Wang, X.; Kuang, Y.; Jiao, M.; Su, D.; et al. In Situ Iron Coating on Nanocatalysts for Efficient and Durable Oxygen Evolution Reaction. *Nano Energy* **2019**, *63* (June), 1–8.
(185) Du, H.; Du, Z.; Wang, T.; Li, B.; He, S.; Wang, K.; Xie, L.; Ai, W.; Huang, W. Unlocking Interfacial Electron Transfer of Ruthenium Phosphides by Homologous Core–Shell Design toward Efficient Hydrogen Evolution and Oxidation. *Adv. Mater.* **2022**, *2204624*, 1–9.
(186) Li, Y.; Zhang, J.; Liu, Y.; Qian, Q.; Li, Z.; Zhu, Y.; Zhang, G. Partially Exposed RuP2 Surface in Hybrid Structure Endows Its Bifunctionality for Hydrazine Oxidation and Hydrogen Evolution Catalysis. *Sci. Adv.* **2020**, *6* (44).
(187) Yu, J.; Guo, Y.; She, S.; Miao, S.; Ni, M.; Zhou, W.; Liu, M.; Shao, Z. Bigger Is Surprisingly Better: Agglomerates of Larger RuP Nanoparticles Outperform Benchmark Pt Nanocatalysts for the Hydrogen Evolution Reaction. *Adv. Mater.* **2018**, *30* (39), 1–10.
(188) Pu, Z.; Ya, X.; Amiinu, I. S.; Tu, Z.; Liu, X.; Li, W.; Mu, S. Ultrasmall Tungsten Phosphide Nanoparticles Embedded in Nitrogen-Doped Carbon as a Highly Active and Stable Hydrogen-Evolution Electrocatalyst. *J. Mater. Chem. A* **2016**, *4* (40), 15327–15332.
(189) Fei, H.; Yang, Y.; Fan, X.; Wang, G.; Ruan, G.; Tour, J. M. Tungsten-Based Porous Thin-Films for Electrocatalytic Hydrogen Generation. *J. Mater. Chem. A* **2015**, *3* (11), 5798–5804.

(190) Hÿtch, M. J.; Snoeck, E.; Kilaas, R. Quantitative Measurement of Displacement and Strain Fields from HREM Micrographs. *Ultramicroscopy* **1998**, *74* (3), 131–146.
(191) Niu, S.; Li, S.; Du, Y.; Han, X.; Xu, P. How to Reliably Report the Overpotential of an Electrocatalyst. *ACS Energy Letters*. 2020, pp 1083–1087.
(192) Shah, A. H.; Zhang, Z.; Huang, Z.; Wang, S.; Zhong, G.; Wan, C.; Alexandrova, A. N.; Huang, Y.; Duan, X. The Role of Alkali Metal Cations and Platinum-Surface Hydroxyl in the Alkaline Hydrogen Evolution Reaction. *Nat. Catal.* **2022**, *5* (10), 923–933.
(193) He, Q.; Zhou, Y.; Shou, H.; Wang, X.; Zhang, P.; Xu, W.; Qiao, S.; Wu, C.; Liu, H.; Liu, D.; et al. Synergic Reaction Kinetics over Adjacent Ruthenium Sites for Superb Hydrogen Generation in Alkaline Media. *Adv. Mater.* **2022**, *34* (20), 1–9.
(194) Jiang, K.; Liu, B.; Luo, M.; Ning, S.; Peng, M.; Zhao, Y.; Lu, Y. R.; Chan, T. S.; de Groot, F. M. F.; Tan, Y. Single Platinum Atoms Embedded in Nanoporous Cobalt Selenide as Electrocatalyst for Accelerating Hydrogen Evolution Reaction. *Nat. Commun.* **2019**, *10* (1), 1–9.
(195) Cuenya, B. R. Synthesis and Catalytic Properties of Metal Nanoparticles: Size, Shape, Support, Composition, and Oxidation State Effects. *Thin Solid Films* **2010**, *518* (12), 3127–3150.
(196) Liu, S.; Hu, Z.; Wu, Y.; Zhang, J.; Zhang, Y.; Cui, B.; Liu, C.; Hu, S.; Zhao, N.; Han, X.; et al. Dislocation-Strained IrNi Alloy Nanoparticles Driven by Thermal Shock for the Hydrogen Evolution Reaction. *Adv. Mater.* **2020**, *32* (48), 1–8.
(197) Bu, L.; Zhang, N.; Guo, S.; Zhang, X.; Li, J.; Yao, J.; Wu, T.; Lu, G.; Ma, J. Y.; Su, D.; et al. Biaxially Strained PtPb/Pt Core/Shell Nanoplate Boosts Oxygen Reduction Catalysis. *Science (80-.).* **2016**, *354* (6318), 1410–1414.
(198) Wang, L.; Zeng, Z.; Gao, W.; Maxson, T.; Raciti, D.; Giroux, M.; Pan, X.; Wang, C.; Greeley, J. Tunable Intrinsic Strain in Two-Dimensional Transition Metal Electrocatalysts. *Science (80-.).* **2019**, *363* (6429), 870–874.
(199) Luo, M.; Guo, S. Strain-Controlled Electrocatalysis on Multimetallic Nanomaterials. *Nat. Rev. Mater.* **2017**, *2* (September), 1–14.
(200) De Pablo, J. J.; Jones, B.; Kovacs, C. L.; Ozolins, V.; Ramirez, A. P. The Materials Genome Initiative, the Interplay of Experiment, Theory and Computation. *Curr. Opin. Solid State Mater. Sci.* **2014**, *18* (2), 99–117.
(201) de Pablo, J. J.; Jackson, N. E.; Webb, M. A.; Chen, L. Q.; Moore, J. E.; Morgan, D.; Jacobs, R.; Pollock, T.; Schlom, D. G.; Toberer, E. S.; et al. New Frontiers for the Materials Genome Initiative. *npj Comput. Mater.* **2019**, *5* (1), 1–23.